



UNIVERSITAT^{DE}
BARCELONA

Band gap grading strategies for high efficiency kesterite based thin film solar cells

Jacob Antonio Andrade Arvizu



Aquesta tesi doctoral està subjecta a la llicència **Reconeixement 4.0. Espanya de Creative Commons.**

Esta tesis doctoral está sujeta a la licencia **Reconocimiento 4.0. España de Creative Commons.**

This doctoral thesis is licensed under the **Creative Commons Attribution 4.0. Spain License.**

Tesi doctoral

Band gap grading
strategies for
high efficiency
kesterite based
thin film solar cells

Autor/a: Jacob Antonio Andrade Arvizu

Director/a: Prof Dr Edgardo Saucedo Silva



UNIVERSITAT DE
BARCELONA

Band gap grading strategies for high efficiency kesterite based thin film solar cells

Memòria presentada per optar al grau de doctor per la
Universitat de Barcelona

Programa de Doctorat en Física

Autor/a: MSc Jacob Antonio Andrade Arvizu 

Director/a: Prof Dr Edgardo Saucedo Silva

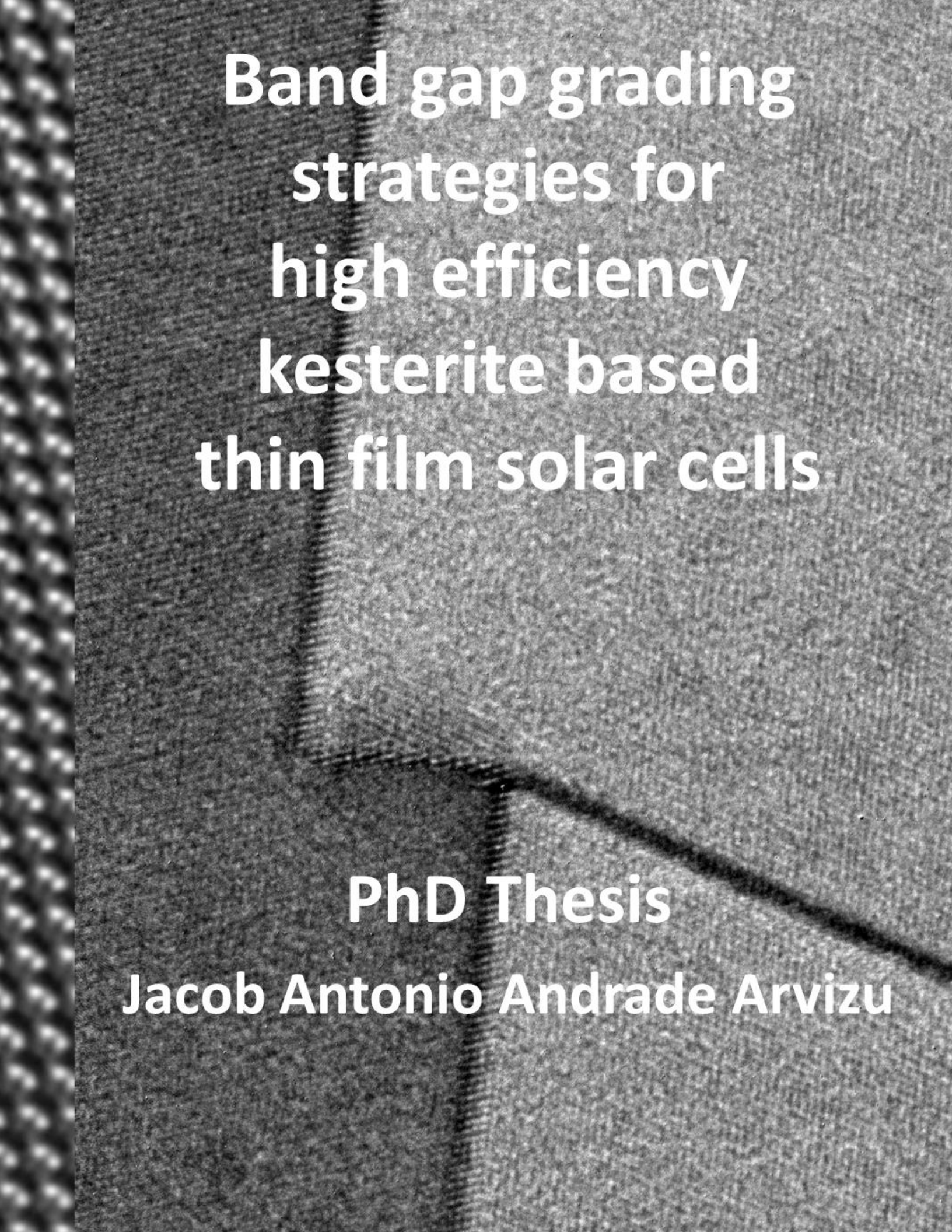
Tutor/a: Prof Dr Blas Garrido Fernández

Lloc on s'ha dut a terme la tesi:

L'Institut de Recerca en Energia de Catalunya (IREC) i La Universitat de Barcelona (UB)



UNIVERSITAT_{DE}
BARCELONA



**Band gap grading
strategies for
high efficiency
kesterite based
thin film solar cells**

PhD Thesis

Jacob Antonio Andrade Arvizu



UNIVERSITAT DE
BARCELONA

University of Barcelona
Faculty of Physics
Electronic materials, sensors,
micro- and nanosystems
Department of Electronic and
Biomedical Engineering



Shaping Energy for a Sustainable Future

Catalonia Institute for
Energy Research
(Institut de Recerca en
Energia de Catalunya)
Solar Energy Materials and
Systems Group (SEMS)

Band gap grading strategies for high efficiency kesterite based thin film solar cells

Physics program Doctoral Thesis

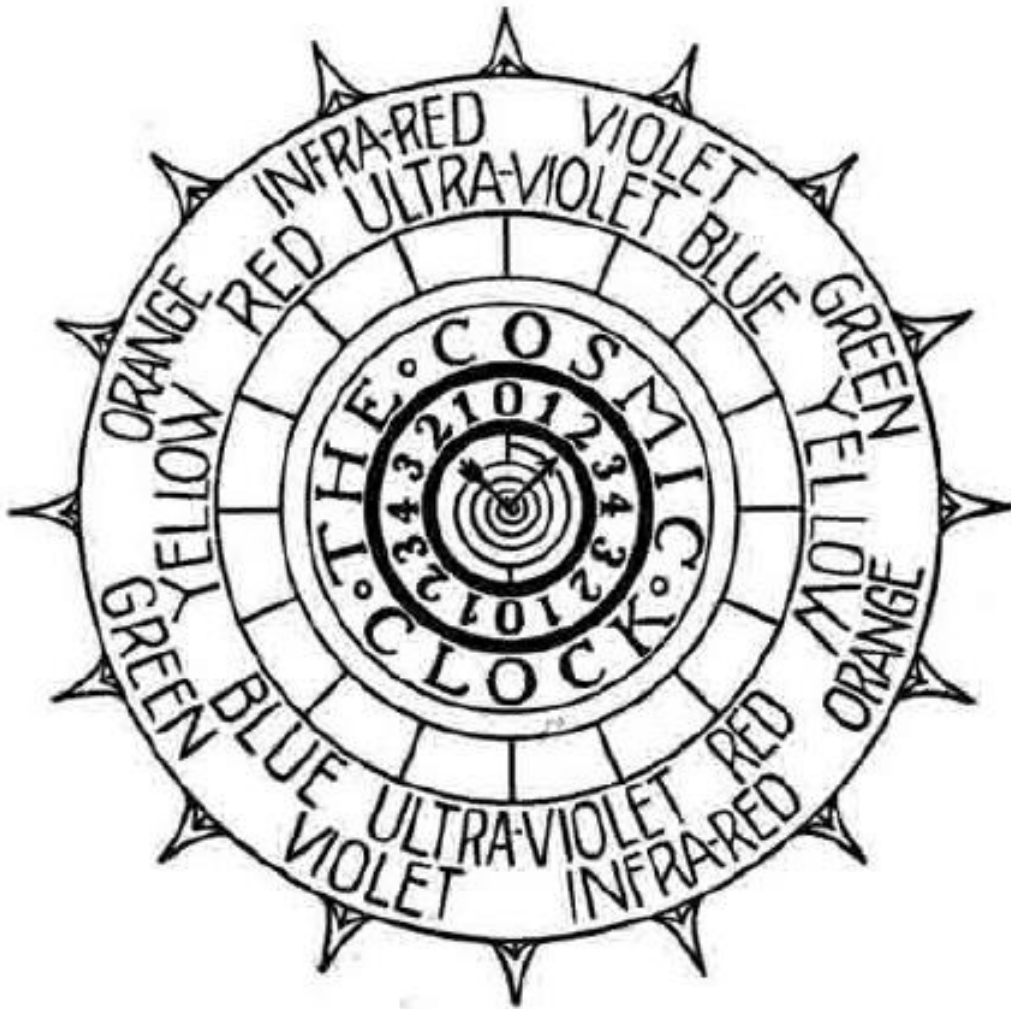
Author: MSc Jacob Antonio Andrade Arvizu



Supervisor: Prof Dr Edgardo Saucedo Silva

Tutor: Prof Dr Blas Garrido Fernández

To the One God, the Universal One,
this codex is humbly dedicated



Con especial dedicación...

*A mí amada esposa, mejor amiga y siempre confidente:
Dra. Irene Romera Sánchez.*

*A mi amada madre Carmen Aida y a mi amado padre Raúl Benigno.
A mis amados hermanos Raúl Armando y Carmen Elizabeth.*

*Con todo mi cariño y muchísimo amor a mi
Abuela Paz Esthela Ortiz y a mi Nana Nena Villarreal[†].*

Resumen

Los suministros de energía renovable basados en celdas solares de película fina, y enfocados en materiales sostenibles como la kesterita (CZTS), podrían desenvolverse de manera muy exitosa en una amplia variedad de escenarios de aplicaciones energéticas. Esto se debe a su potencial para ser depositadas sobre sustratos flexibles, su estética y transparencia selectiva para integraciones en sectores como el de construcción y la automoción. Así como su uso en nuevos conceptos energéticos tales como agrovoltaicos o portabilidad energética, como lo es el Internet de las cosas (IoT).

Las celdas solares actuales de kesterita y de una sola capa absorbente con perfiles de banda prohibida no variables limitan la plenitud en la obtención de mejores eficiencias de conversión energética para una unión PN. Ante esto, esta Tesis demuestra que la eficiencia de conversión energética de la próxima generación de celdas solares de kesterita (y calcopiritas) puede verse potenciada tras desarrollar nuevas metodologías más estratégicas de recolección de energía fotónica. Por tanto, se propone el graduado del perfil de banda prohibida como una estrategia sostenible para mejorar la utilización del espectro solar, mediante la generación de campos cuasi-eléctricos internos a lo largo de las películas finas, consiguiendo incrementar las longitudes de deriva y difusión de los portadores de carga minoritarios y así aumentar la eficiencia del dispositivo fotovoltaico. De esta manera, esta Tesis desarrolla técnicas avanzadas de síntesis y caracterización de superficies, que al integrarse con la complejidad estructural de la kesterita (CZTGSSe), permiten a la Naturaleza revelarnos varias disruptivas y novedosas propiedades de la materia, deliberadamente manipulables cuando se trabaja en condiciones fuera del equilibrio termodinámico.

Abstract

Renewable energy supplies based on thin film solar cells, and focused on sustainable materials such as kesterite (CZTS), could perform very successfully in a wide variety of energy application scenarios. This is due to its potential to be deposited on flexible substrates, its aesthetics and selective transparency for integrations in construction and automotive sectors. As well as its use in new energy concepts such as agrovoltatics or energetic portability like the Internet of Things (IoT).

The actual kesterite thin film devices hinder the actual energy conversion efficiencies of a single absorber layer PN junction. With all this in mind, the next generation of kesterite and chalcopyrite solar cells power energy efficiency improvements can be enhanced after developing novel and more strategic methodologies for collecting photon energy. Therefore, graded bandgap profiling in kesterites is proposed as a sustainable strategy to improve the use of the solar spectrum, through the generation of internal quasi-electric fields situated along the thin films, increasing the drift and diffusion lengths of minority charge and finally improving the power conversion efficiency of the photovoltaic device. In this way, this Thesis develops advanced material synthesis techniques and surface characterization, which, when integrated with the structural complexity of kesterite (CZTGSSe), allow Nature to reveal several disruptive and novel and properties of matter, deliberately manipulable when working in conditions out-of-thermodynamic equilibrium.

Agradecimientos/Acknowledgments

Primordialmente quisiera agradecer a toda mi familia Andrade & Arvizu en México, y ahora a mi familia Romera & Sánchez aquí en España. Pero fundamentalmente, a la amada esposa Irene por toda su comprensión, apoyo y amor siempre compartido, ¡Muchas Gracias por todo cari!

Agradeciendo de una muy especial y profunda manera a mi amigo, asesor y director de Tesis, Prof. Dr. Edgardo Saucedo Silva, y al BB & PI del SEMS-IREC, el Prof. Dr. Alejandro Pérez-Rodríguez, así como al tutor: Prof. Dr. Blas Garrido, por permitirme y ayudarme por todos los medios posibles durante la realización de estos estudios e investigaciones en el IREC y en la UB. Adicionalmente, especiales agradecimientos para el Prof. Dr. Joaquín Puigdollers, a la Prof. Dr. Teresa Andreu Arbella, al Prof. Dr. Levent Gütay, al Prof. Dr. Lorenzo Calvo-Barrio, al Prof. Dr. Cristóbal Voz, y al Prof. Dr. Joan Bertomeu por su apoyo y aceptar ser miembros del tribunal de esta Tesis doctoral. Desde lo más profundo de mi corazón: ¡Muchas Gracias! A la Dra. Georgina Arrambide y al Dr. Xavier Montalban, así como a todo el equipo del *Cemcat* en el *Vall d'Hebron*, por tan cálido recibimiento y toda su atención en el centro: ¡Gracias Totales!

A todos mis colegas de los proyectos (STARCELL, INFINITE-CELL & MASTERPV), así como a todos los investigadores de mis todas mis inter- y naciones por todo lo que me han enseñado. Natural y orgánicamente, con un mucho cariño y afecto para el grupo *Solar Energy Materials and Systems* (SEMS) del IREC por fundamentar y estructurar esta tan maravillosa y grandiosa aventura. A todos y cada uno de ustedes mis maestros y mentores por regalar y compartir conmigo su luz, enseñanzas y sincera amistad. Muchas gracias Victor Izquierdo Roca, Marcel Placidi, Ignacio Becerril, Zacharie Jehl Li-Kao, Diouldé Sylla, Yudenia Sánchez, Maxim Guc, Robert Fonoll, Pedro Vidal, Sergio Giraldo, Markus Neuschitzer, Mohamed Ould Salem, Florian Oliva, Laia Arqués, Alejandro Hernández, Oriol Blazquez, Alejandro Navarro, Fabien Atlan, Alex López, Alex Jiménez, Iván Caño, Josep Maria Herrera, Francesc Torregrosa, Matias Valdes, y Alfredo Blázquez. Muchas gracias Osvaldo Vigil, Maykel Courel, Mario García, Fabián Pulgarín, Moisés Espíndola y Victor Rangel. Muchas gracias de verdad mis compadres, panas, patas, colegas y parceros: Arturo Pajares, Cesar Macías, Edwin A. Ramírez, Roberto González y Esteban Ojeda. LP!

Also, many and special thanks: Nada Benhaddou, Ikram Anefnaf, Claudia Malerba, Eleonora Isotta, Matteo Valentini, Syafiq Mustaffa, Paolo Scardi, Martynas Bertašius, Rokas Kondrotas, Teoman Taskesen, Marco González, Devendra Pareek, Zakaria Oulad Elhmaidi, Laghfour Zakaria, Filipe Martinho, Willi Kogler, Thierry Khol, Ingrid Amer Cid, Ivan Gordon, Bart Vermang, David Mitzi, Teodor Todorov, Dieter Meissner, Hajime Shibata, Yaroslav Romanyuk, Yi Ren, Louis Grenet, Fabrice Emieux, Maria Pilar Ascencio, Sara Niedenzu, Leo Chubrac, Matthias Maiberg, Paul Pistor y Gerardo Larramona. Sorry if I missed somebody but thank you so much if you feel like it! 😊. And last but not least, thank you Alexandra Elbakyan for removing barriers in the name of science.



TOC: Table of Contents

		Page
C H A P T E R	<i>Dedicatoria</i>	I
	<i>Resumen</i>	II
	Abstract	III
	<i>Agradecimientos/Acknowledgments</i>	IV
	TOC: Table of Contents	V
	List of Symbols, Acronyms and Abbreviations	VIII
	<i>Prefacio y Publicaciones</i>	XII
	Preface and Publications	XIX
	Introduction	
	1.1 General Introduction.....	1
I	1.2 Solar Photovoltaic (PV) Technology.....	8
	1.3 Solar PV Technology Classification by Material Complexity.....	11
	1.4 Chapter References.....	16
	Kesterite: State of the Art and Thesis Objectives	
II	2.1 Kesterite: Main Properties of a Complex Material.....	19
	2.2 Defects.....	24
	2.3 V_{OC} deficit in Kesterite Thin Film Solar Cells.....	30
	2.4 Possible Technological Solutions of Kesterite Thin Film Solar Cells V_{OC} deficit.....	33
	2.5 Graded Bandgap in Kesterite	
	2.5.1 Front Graded Bandgap Through Anion Replacement.....	34
	2.5.2 Rear Graded Bandgap Through Cationic Substitution.....	39
	2.5.3 Rear Ge-Sn Graded Bandgap as a BSF in Kesterites.....	41
	2.6 Thesis Objectives*	44
	2.7 Chapter References.....	45
III	Experimental Procedures and Theoretical Studies on Kesterite Based Thin Film Solar Cells: From Glass to Alloyed Brass	
	3.1 Soda Lime Glass Substrate Cleaning and Preparation.....	53
	3.2 Molybdenum (Mo) Back Contact Sputtering Deposition.....	56
	3.3 Kesterite Precursor Metallic Layer Sputtering Deposition.....	57

	3.4 Absorber Synthesis and Device Fabrication	
	3.4.1 Absorber Material Development.....	59
	3.4.2 Front Graded Bandgap on Kesterite.....	59
	3.5 Absorber Surface Cleaning and Passivation: Chemical Etchings.....	60
	3.6 Thin Film Material and Systems Characterization	
	3.6.1 General Overview.....	62
III	3.7 Theoretical Solar PV Physics	
	3.7.1 Semiconductor Materials and the PN Junction.....	66
	3.7.2 Heterojunction.....	69
	3.7.3 Optoelectronic PV Physics.....	73
	3.7.4 Characteristic JV curves.....	76
	3.7.5 Shockley–Queisser Efficiency Limit and the JV- E_g Dependence.....	81
	3.7.6 Spectral Response and Quantum Efficiency.....	82
	3.7.7 Capacitive-Voltage Profiling.....	86
	3.8 Chapter References.....	90
	Results Part I: Kesterite Graded Bandgap - Theoretical Numerical Modeling Simulations (SCAPS-1D):	
	4.0 Introduction and Chapter Presentation	93
	4.1 First Bandgap Grading Attempts	
	4.1.1 Influence of Sulfurization in CZTSSe Solar Cells.....	94
	4.1.2 Impact of the Contact's Ohmicity with Rear Sulfur Segregation	97
	4.1.3 Linear Bandgap Profiles in CZTSSe.....	99
IV	4.1.4 Front Surface Sulfurization Profiles in CZTSSe.....	103
	4.2 Discussion on the Sulfur Content and Band Diagram Implications	
	4.2.1 CZTSSe: Front Sulfurization with a Layer ($d < 300$ nm)...	104
	4.2.2 CZTSSe: Front Sulfurization with a (300 nm $< d < 800$ nm) Layer.....	105
	4.2.3 CZTSSe: Deep Bulk Sulfurization ($d > 800$ nm).....	106
	4.3 Frontal Graded Bandgap Profile in CZTSSe	
	4.3.1 Variations of the Defect Density with the Sulfur Content.....	106
	4.4 Effect of the Front Sulfurization of CZTSe Solar Cell with a Realistic (Experimental) Compositional Profile.....	110
	4.5 Chapter References.....	113
	Results Part II: Experimental Front Graded Bandgap on CZTSSe	
	5.1 Introduction and Chapter Presentation.....	115
	5.2 Sulfur Pulse (Shoot) Analysis by Thermo-Gravimetric Analysis.....	117
	5.3 CZTSSe structures: Raman Methodology and System Calibration...	121
V	5.4 First Insights on the Experimental Superficial Chalcogenization of CZTSSe*	122
	5.5 Superficial Chalcogenization: Experimental Setup Optimization.....	126
	5.6 Investigations on Chalcogenide Evaporation Dynamics	
	5.6.1 Case of S and Shoot Introduction Scenario.....	130
	5.6.2 Accessing the Back (Rear) Interface.....	133
	5.6.3 Case of SeS ₂ -Shoot Introduction at Different Cooling Down Times.....	140

	5.7 Sulfur Introduction and Creation of Sharp Compositional Gradients by Distinct Chalcogenide Materials.....	145
V	5.7.2 Raman Analyses of Zn(S,Se) Presence in CZTSSe Samples..	158
	5.8 Fabrication and Analysis of CZTSSe Solar Cell Devices.....	161
	5.9 Device Impedance spectroscopy analyses.....	165
	5.10 Chapter Main Conclusions.....	168
	5.11 Chapter References.....	169
	Results Part III, Case A: Experimental Rear Bandgap Grading Strategy in CZTGSe Alloyed Kesterite Solar Cells	
	6.1 Introduction and Chapter Presentation.....	171
	6.2 Tin (Sn) – Germanium (Ge) Alloyed Sputtered Layers.....	172
	6.3 Thermal annealing: Chalcogenization Process.....	173
	6.4 Planar (Top) and Cross Sectional SEM Morphological Details on CZTG and CZTGSe.....	174
	6.5 XRD Structural Studies on CZTGSe.....	176
VI	6.6 Compositional Studies by GDOES and Auger Spectroscopy.....	178
	6.7 Structural and Compositional Analysis by Raman Spectroscopy.....	182
	6.8 Fabrication and Analysis of CZTGSe Solar Cell Devices.....	185
	6.9 Chapter VI, Part III, Case A Main Conclusions.....	195
	Results Part III, Case B: Dual Anionic and Cationic Bandgap Grading Profiles in Kesterite.....	197
	6.11 Experimental Double Graded U-Shaped Bandgap in CZTGSSe Solar Cells.....	200
	6.12 Chapter References.....	205
	Thesis Conclusions, Closing Remarks and Outlook	
VII	7.1 Kesterite technologies optimized during the development of this Thesis: CZTS, CZTSe, CZTSSe, CZTSe:Ge, CZTGSe, and CZTGSSe	207
	7.2 Thesis Outlook: The Arrow of Time.....	211
	7.3 Chapter References.....	215
	Appendix: Additional and Supporting Information	i
	i.1 Kesterite technologies optimized during the development of this Thesis: CZTS, CZTSe, CZTSSe, CZTSe:Ge, CZTGSe, and CZTGSSe	ii
i	i.2 Absorber Surface Cleaning: Chemical Etchings	v
	i.3 Appendix References	ix
	RESEARCH EXPERIENCE	
	Publications during Doctoral Thesis development	xi
	Journal Reviewer at:	xv
	Oral lectures at congresses and conferences	xvi
	Conference attendance, poster presentation and collaborative lectures	xvii
	Miscellaneous Thesis derivatives	xix

Libertas perfundet omnia luce

La libertad ilumina todas las cosas con su luz

List of Symbols, Acronyms and Abbreviations

Chapter I

IEO	International Energy Outlook
BTU	British Thermal Units
OECD	Organisation for Economic Co-operation and Development
GHG	Greenhouse Gases
SRES	Special Report on Emissions Scenarios
IPCC	Intergovernmental Panel on Climate Change
SRREN	Special Report on Renewable Energy
COP	Conference of the Parties
UNFCCC	United Nations Framework Convention on Climate Change
IEA	International Energy Agency
COVID-19	Coronavirus Disease. Formerly, this disease was referred to as '2019 novel coronavirus' or '2019-nCoV'
USA	United States of America
PV	Photovoltaics / Solar Photovoltaics
NREL	National Renewable Energy Laboratory
a-Si:H	Hydrogenated Amorphous Silicon
CdTe	Cadmium telluride
CIGS	Copper indium gallium (di)sulfo/selenide
TFPV	Thin Film Photovoltaics
DSSC	Dye-sensitized Solar Cell
QDs	Quantum-dot Solar Cell
BIPV	Building Integrated Photovoltaics
AIPV	Automotive Integrated Photovoltaics
IoT	Internet of Things
CRM	Critical Raw Materials
CZTS	$\text{Cu}_2\text{ZnSnS}_4$
CZTSe	$\text{Cu}_2\text{ZnSnSe}_4$
CZGSe	$\text{Cu}_2\text{ZnGeSe}_4$
CZTSe:Ge	Ge doped $\text{Cu}_2\text{ZnSnSe}_4$
CZTSSe	$\text{Cu}_2\text{ZnSn(S,Se)}_4$
CZGSe	$\text{Cu}_2\text{ZnGeSe}_4$
CZ(T,G)Se	$\text{Cu}_2\text{ZnSn}_x\text{Ge}_{1-x}\text{Se}_4$
CZ(T,G)(S,Se)	$\text{Cu}_2\text{ZnSn}_x\text{Ge}_{1-x}(\text{S,Se})_4$

Chapter II

V_{oc}	Open Circuit Voltage
VB	Valance Band
CB	Conduction Band
V_{Cu}	Cu Vacancies
Zn_{Cu}	Zn-Cu Antisite Defects
$E_g/E_g/E_g$	Bandgap / Band Gap

IBM	International Business Machines Corporation
DGIST	Daegu Gyeongbuk Institute of Science and Technology
SQ	Shockley–Queisser
CBO	Conduction Band Offset
RPN	Risk Priority Number
EMPA	Swiss Federal Laboratories for Materials Science and Technology
WIRE	Weee Internacional Recycling S.L.
UDUKE	Duke University
AIST	National Institute of Advanced Industrial Science and Technology
MIDS	Midsummer
HZB	Helmholtz-Zentrum Berlin für Materialien und Energie
UU	Uppsala University
CEA	Commissariat à l'Énergie Atomique et aux Énergies Alternatives
ICL	Imperial College London
IREC	Institut de Recerca de l'Energia de Catalunya
FOM	Figure of Merit
I_{sc}	Short Circuit Current Intensity
FF	Fill Factor
GIXRD	Grazing Incidence X-Ray Diffraction
RTP	Rapid Thermal Process
H_F	Enthalpy of Formation
CBM	Conduction Band Minimum
BSF	Back Surface Field
PCE / η / Eff.	Energy Power Conversion Efficiency
Ref.	Reference
CHON	Chonnam National University
INU	Incheon National University
UW	University of Washington
PRUD	Purdue University

Chapter III

SLG	Soda Lime Glass
SEMS	Solar Energy Material and Systems
DC	Direct Current
sccm	Standard Cubic Centimetres per Minute
XRF	X-Ray Fluorescence
CBD	Chemical Bath Deposition
iZnO / i-ZnO	Intrinsic Zinc Oxide
ARC	Antireflective Coating Layer
TGA	Thermal Gravimetric Analysis
ICP-MS	Inductively Coupled Plasma Mass Spectrometry
ICP-OES	Inductively Coupled Plasma coupled Optical Emission Spectroscopy
GDOES	Glow Discharge Optical Emission Spectroscopy
XRD	X-Ray Diffraction
SEM	Secondary Electron Microscopy
EDX	Energy Dispersive X-Ray Spectroscopy
FESEM	Field Emission Scanning Electron Microscopy
STEM	Scanning Transmission Electron Microscopy
CV	Capacitance-Voltage
SCR	Space-Charge Region
EQE	External Quantum Efficiency
TCO	Transparent Conductive Oxide Layer
JV	Current Density-Voltage
AM1.5	Air Mass Representing the Overall Yearly Standardized Average for Mid-Latitudes (Sun $\approx 41^\circ$ above the Horizon)

E	Energy
h	Planck's Constant
ν	Frequency
E_C	Conduction Band Energy Position
E_V	Valance Band Energy Position
N_A	Acceptor Level Carrier Concentration
N_D	Donor Level Carrier Concentration
n_i	Intrinsic Carrier Concentration
V_{bi}	Built-in Voltage
\vec{E}_{bi}	Built-in Electric Field
E_F	Fermi Energy Level
ϵ	Permittivity
Φ / W	Work Function
χ	Electron Affinity
q	Elemental Charge
N_A^-	Ionized Acceptor Concentration
N_D^+	Ionized Donor Concentration
d	Space Charge Region Depletion Width
J_{ph}	Short-Circuit Photocurrent Density
J_d	Diode Current Density
n	Diode Quality Factor
k_B	Boltzmann Constant
P_{max}	Maximum Power
MPP	Maximum Power Point
J_{mp}	Maximum Power Short-Circuit Current Density
V_{mp}	Maximum Power Open Circuit Voltage
P_{theo}	Maximum Theoretical Power
P_{in}	Incident Power
PV	Power-Voltage curve
R_S	Series Resistance
R_{SH}	Shunt Resistance
SRH	Shockley-Read-Hall
G_{SH}	Shunt Conductance
J_0	Dark Diode Current Density
STC	Standard Test Conditions
QE	Quantum Efficiency
SR	Spectral Response
λ	Wavelength
R	Reflectance
IQE	Internal Quantum Efficiency
$J_{SC,MAX}$	Maximum Theoretical Short Circuit Density Photo-Current
Φ	Photon Flux
α	Absorption Coefficient
L	Minority Carrier Diffusion Length

Chapter IV

SCAPS	Solar Cell Capacitance Simulator
OVC	Order Vacancy Compound

Chapter V

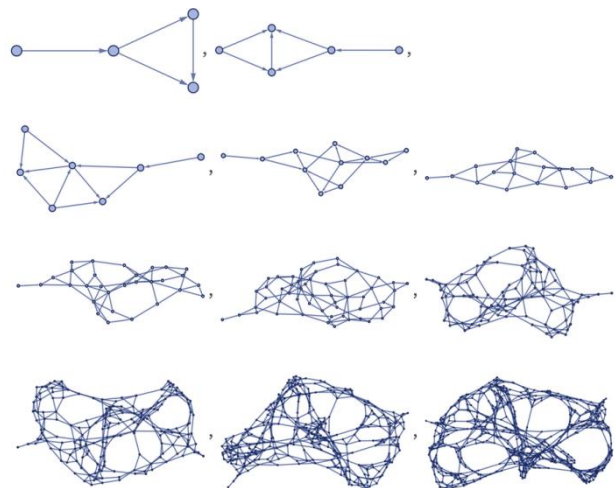
DTA	Differential Thermal Analysis
PL	Photoluminescence
Φ_{ext}	External diameter
T	Temperature
SE2	Secondary Electron Emission Type 2
ESB	Backscattered electrons
FM_x	Reactivity
E_x	Formation Energy
M_x	Molar Mass
HCl	Hydrochloridric Acid
KCN	Potassium Cyanide
UV	Ultraviolet
KMnO₄	Potassium Permanganate
(NH₄)₂S	Ammonium Hydrosulfide
ITO	Indium Tin Oxide

Chapter VI

GGT	$[\text{Ge}]/([\text{Ge}]+[\text{Sn}]) = \text{Ge}/(\text{Ge}+\text{Sn})$ ratio
FWHM	Full Width at Half Maximum
ω	Raman Band Shift
HAADF-STEM	High-Angle Annular Dark-Field Scanning Transmission Electron Microscopy

Chapter VII

FTO	Fluorine doped Tin Oxide
CE	Chemical Etching



If you take two successive terms of the series, a , b and $a + b$ so that

$$\begin{aligned}\frac{b}{a} &\approx \frac{a+b}{b} \\ &\approx \frac{a}{b} + 1\end{aligned}$$

Thus, define phi (φ) as the limit of $\frac{b}{a}$, so:

$$\varphi = \frac{1}{\varphi} + 1$$

→

$$\varphi^2 - \varphi - 1 = 0$$

→

$$\varphi = \frac{1 + \sqrt{5}}{2} \approx 1.6180339887498948482045868343656381177203 \dots$$

$$\varphi = 1 + \frac{1}{\varphi} \quad \rightarrow \quad \varphi = 1 + \frac{1}{1 + \frac{1}{1 + \frac{1}{1 + \frac{1}{1 + \dots}}}}$$

En todo caos hay un cosmos,

En todo desorden un orden secreto.

-Carl Gustav Jung

Prefacio y Publicaciones

El trabajo de investigación presentado en esta Tesis Doctoral se realizó en el *Institut de Recerca en Energía de Catalunya* en *Sant Adrià de Besòs*, Barcelona, España desde el año 2017 al 2021, esto bajo el marco del proyecto: “*Advanced strategies for substitution of critical raw materials in photovoltaics*” **STARCELL** (H2020-NMBP-03-2016-720907); el proyecto: “*International cooperation for the development of cost-efficient kesterite/c-Si thin film next generation tandem solar cells*” **INFINITE-CELL** (H2020-MSCA-RISE-2017-777968); y el proyecto “*Innovative manufacturing solutions for cost-efficient semi-transparent BIPV*” **MASTER-PV** (MICINN-PCI2018-092945), todos proyectos de la Comisión Europea. El tema principal de la Tesis se centra en el desarrollo de novedosas y avanzadas estrategias tecnológicas respecto a la ingeniería de perfilado de la brecha de banda prohibida en celdas solares de película delgada basadas en estructuras tipo kesterita ($\text{Cu}_2\text{Zn}(\text{Sn,Ge})(\text{S}_x\text{Se}_{1-x})_4$), los cuales son materiales amigables con el medio ambiente y cuyos elementos constituyentes son abundantes en la corteza Terrestre. Esto con el primordial objetivo de potencialmente optimizar y mejorar la eficiencia de conversión energética de los dispositivos fotovoltaicos basados en estos materiales. Esta Tesis se encuentra estructurada en torno a 22 (16, Q1) artículos científicos publicados en revistas JCR-indexadas, revisadas a pares, y de altos factores de impacto; incluidos los siguientes que se presentan de acuerdo con los requisitos para obtener el título de Doctor en Física por la Facultad de Física en la Universidad de Barcelona; de esta manera ensamblando el producto final de esta investigación como una Tesis de 7 capítulos:

El primer capítulo proporciona una introducción y descripción general donde se exponen las motivaciones principales detrás de las tecnologías fotovoltaicas, el segundo capítulo describe la problemática abordada, describiendo los objetivos de esta Tesis. Seguidamente, el tercer capítulo expone la metodología experimental utilizada, proporcionando además, un esquema general sobre la física detrás de la energía fotovoltaica. Los tres capítulos siguientes cubren los principales resultados obtenidos a lo largo del desarrollo de esta Tesis y, finalmente, el último capítulo resume y destaca los resultados y conclusiones principales de esta investigación.

A continuación se presenta una descripción más detallada de los diferentes capítulos que componen la estructura de la Tesis:

El **primer capítulo** comienza con una descripción general y una introducción a las tecnologías fotovoltaicas exponiendo los problemas del actual consumo energético mundial y su implicación directa con el “desequilibrio de calefacción”, alias “calentamiento global” producido por las emisiones actuales de gases de efecto invernadero. Por lo tanto, se presenta la clasificación tecnológica de la energía solar fotovoltaica por su complejidad estructural material con el fin de introducir la kesterita como un material amigable con el medio ambiente y abundante en la corteza Terrestre; cuya disponibilidad permita el pleno desarrollo de tecnologías fotovoltaicas emergentes.

El **segundo capítulo** dispone de una breve introducción a la kesterita como un material complejamente estructurado. De ahí que al exponer los defectos más relevantes en una extensa y crítica revisión literaria; se revelan las razones que dan lugar al “déficit del voltage a circuito abierto (V_{OC})”, por lo que se proporcionan las correspondientes resolutivas tecnológicas. De esta manera, se señala y puntualiza por primera vez el graduado del perfil de la brecha de banda prohibida (*bandgap*) en películas finas y/o delgadas de kesterita. Asimismo, se exploran varios perfiles graduados aniónicos y catiónicos, lo que sugiere la viabilidad de una combinación de un graduado aniónico frontal (S-Se) junto con una sustitución catiónica posterior (Ge-Sn) dentro de la misma matriz estructural del grano de kesterita, para generar perfiles graduados en forma de U sobre la brecha de banda prohibida del material absorbedor. Finalmente, se revelan los **objetivos de esta Tesis** como una estrategia plausible para superar las limitaciones de eficiencia reales en las celdas solares de película delgada basadas en kesteritas.

El **tercer capítulo** presenta un “viaje por carretera” desde el inicio experimental, es decir, desde la limpieza del sustrato de soporte (vidrio), pasando por el depósito del contacto trasero (Mo), hacia la pulverización catódica de las capas precursoras metálicas de cobre (Cu), zinc (Zn) y estaño (Sn), hasta a la síntesis de aleaciones de kesterita con graduados en diversos perfiles de brecha de banda prohibida.

Asimismo, se comenta y describe la correcta adecuación y preparación de diversos ataques químicos (*chemical etchings*) de superficies para la subsecuente completitud del dispositivo fotovoltaico, i.e., el depósito de las capas de contacto frontal y amortiguador (*capa buffer*). Por lo tanto, se detalla a fondo el proceso de fabricación seguido para el desarrollo de células solares de kesterita. Asimismo, se resume con una descripción general sobre la síntesis de material de película delgada (kesterita), así como correcta y adecuada caracterización. Finalmente, se proporciona una breve compilación sobre la teoría física con respecto a la energía solar fotovoltaica, desde los materiales semiconductores y la unión PN, hasta las técnicas de caracterización optoelectrónica utilizadas en esta Tesis.

El **cuarto capítulo** desarrolla la simulación de modelado numérico para una celda solar de referencia (kesterita, CZTSe) del SEMS-IREC, utilizando los parámetros principales de los materiales recopilados del conocimiento y experiencia de dispositivos propia del grupo de Energía Solar y Sistemas Solares (SEMS), basado fundamentalmente en SCAPS-1D (Simulador de capacitancia de celdas solares), junto con la actual literatura existente respecto al modelado de dispositivos de kesterita de última generación. De esta manera, la primera parte de este capítulo, aborda los primeros intentos de modelado respecto al gradado del perfil de la brecha de banda prohibida, en los que se proporcionan factores como la influencia de la sulfurización sobre celdas solares basadas en kesterita (CZTSSe); así como el impacto de la ohmicidad del contacto trasero debido a segregaciones de azufre posteriores como una comparación entre los perfiles de la brecha de banda prohibida lineales contra perfiles superficialmente graduados. Por tanto, se proporciona una discusión sobre el contenido de azufre y el posicionamiento en las implicaciones del diagrama de bandas para varios escenarios de sulfurización. Por último, se analiza y discute el efecto de la sulfurización frontal de la celda solar de CZTSe con un perfil de composición “real”. Los tres capítulos siguientes cubren principalmente los resultados recopilados experimentalmente con respecto al gradado del perfil de la brecha de banda prohibida para distintas tecnologías de kesterita.

Los capítulos quinto (gradiente frontal aniónico) y sexto (gradiente posterior catiónico) se basan en artículos científicos publicados en revistas revisadas a pares con alto factor de impacto, como se detallará a continuación, mientras que la investigación presentada al final del sexto capítulo (graduación del perfil de banda prohibida en forma de U) es primordialmente presentada en esta Tesis y será publicada posteriormente a la defensa de la misma.

El **quinto capítulo** se basa en las siguientes publicaciones (reproducidas con permiso de *Copyright* © American Chemical Society):

i) [“Is It Possible To Develop Complex S–Se Graded Band Gap Profiles in Kesterite-Based Solar Cells?”](#). **Jacob Andrade-Arvizu**, Víctor Izquierdo-Roca, Ignacio Becerril-Romero, Pedro Vidal-Fuentes, Robert Fonoll-Rubio, Yudania Sánchez, Marcel Placidi, Lorenzo Calvo-Barrio, Osvaldo Vigil-Galán, and Edgardo Saucedo. **ACS Applied Materials & Interfaces** 11 (36), 32945-32956 (2019). DOI: 10.1021/acsami.9b09813. Factor de Impacto: **8.758 (Q1)**

ii) [“Controlling the anionic ratio and gradient in kesterite technology”](#) **Jacob Andrade-Arvizu**, Robert Fonoll Rubio, Victor Izquierdo-Roca, Ignacio Becerril-Romero, Diouldé Sylla, Pedro Vidal-Fuentes, Zacharie Jehl Li-Kao, Angélica Thomere, Sergio Giraldo, Kunal Tiwari, Shahaboddin Resalati, Maxim Guc, Marcel Placidi. **ACS Applied Materials & Interfaces**. En revisión desde 23/02/2021. Factor de Impacto: **8.758 (Q1)**

Este capítulo demuestra el desarrollo de un novedoso y disruptivo proceso de calcogenización para la fabricación de celdas solares de $\text{Cu}_2\text{ZnSn}(\text{S},\text{Se})_4$ (CZTSSe) que permiten la generación de perfiles brecha de banda prohibida complejos, presentando una graduación composicional aniónica de manera superficial y súbitamente abrupta. Particularmente enfocado en generar altos contenidos de S en la superficie frontal del material absorbedor, disminuyendo abruptamente (tanto como sea posible) hacia la parte posterior dentro del mismo grano cristalino de kesterita y depositado en forma de película fina o delgada. Logrando esto mediante la optimización de los parámetros de recocido, incluido el estudio de varias fuentes de azufre con diferentes reactividades (S elemental, tiourea, SnS y SeS_2).

Como resultado, dependiendo de la fuente de azufre empleada, se obtienen dispositivos celdas solares de kesterita de alta eficiencia con un contenido máximo de azufre localizado superficialmente entre el 50% y el 20% dentro de la zona de agotamiento de carga y entre el 10% y el 30% hacia el bulto (*bulk*) o volumen del material. Por lo tanto, demostrando experimentalmente la factibilidad de realizar perfiles de graduado aniónico teorizado y modelado en el cuarto capítulo. Haciendo claramente notar que estos resultados representan un paso adelante hacia la graduación aniónica de la brecha de banda prohibida en celdas solares de kesterita.

El **sexto capítulo** se basa en la siguiente publicación (reproducida con permiso de *Copyright* © American Chemical Society):

iii) [“Rear Band gap Grading Strategies on Sn–Ge Alloyed Kesterite Solar Cells”](#). **Jacob Andrade-Arvizu**, R. Fonoll-Rubio, Y. Sánchez, I. Becerril-Romero, C. Malerba, M. Valentini, L. Calvo-Barrio, V. Izquierdo-Roca, M. Placidi, O. Vigil-Galán, A. Pérez-Rodríguez, Edgardo Saucedo, Z. Jehl Li-Kao. **ACS Applied Energy Materials** 3 (11), 10362–10375 (2020). DOI: 10.1021/acsaem.0c01146. Factor de Impacto: **4.473 (Q1)**

En este capítulo, se demuestra una estrategia de ingeniería de bandas para asistir la recolección de portadores de carga en kesterita, inspirándose en celdas solares de calcopirita. Para este propósito, un proceso secuencial basado en una combinación de pulverización catiónica de precursores metálicos y su posterior recocido reactivo con calcogenuro, permitió el control de sustituciones catiónicas reemplazando parcialmente Sn por Ge, y por tanto, adaptando varios perfiles de graduado posterior de la brecha de banda prohibida a lo largo del espesor del absorbedor de kesterita (CZTGSe). Se realizan las pertinentes caracterizaciones de las propiedades estructurales, morfológicas, topográficas y composicionales de muestras que van desde compuestos puros de estaño (Sn) hasta compuestos puros de germanio (Ge), pasando por algunas sus respectivas aleaciones. Por lo tanto, la formación de un graduado posterior en el perfilado del ancho de la banda prohibida es ascertivamente determinado a través de un análisis avanzado de caracterización correlacional, específicamente a través de la combinación de la emisión óptica de descarga luminiscente (GDOES) y espectroscopias tipo Auger junto con estudios de espectroscopía Raman para múltiples longitudes de onda llevados a cabo en las superficies frontal y trasera de las películas delgadas de kesterita.

Accediendo a la interfaz posterior mediante un proceso termo-mecánico de despegue o arrancado (*lift off process*).

Como tal, se demuestra la factibilidad de un enriquecimiento preferencial de Ge hacia la parte posterior del absorbedor (kesterita) de manera inequívoca y se adicionalmente se aplican en dispositivos fotovoltaicos para deliberadamente generar distintos perfiles del gradado posterior de la brecha de banda prohibida. Finalmente, esto conduce a la generación de un campo de superficie posterior (BSF, de *back surface field*) muy eficiente que potencialmente mejora la selectividad de los portadores de carga colectados en la interfaz posterior.

De esta manera, las celdas solares de kesterita (CZTGeSe) demuestran una interacción compleja entre los beneficios del gradado de banda prohibida y los posibles defectos relacionados con la interacción Sn-Ge en el absorbedor.

Optimizando las condiciones de síntesis, se observa un contundente aumento de la eficiencia absoluta para el dispositivo campeón de kesterita ($\approx 10\%$); Esto sin la necesidad de recubrimiento o capa anti-reflectante (ARC), ni rejilla metálica alguna.

Por lo tanto, la mejora del rendimiento se atribuye principalmente a la presencia de un campo eléctrico de deriva que asiste la recolección de portadores de carga, al tiempo que evita su recombinación en la interfaz posterior.

Consiguientemente, estos resultados confirman la posibilidad de generar un gradado posterior del perfil de brecha de banda prohibida en celdas solares de kesterita, abriendo así el camino a un mayor desarrollo de la tecnología fotovoltaica con mayores eficiencias de conversión energética a través de estrategias de gradado e ingeniería en el perfilado de la brecha de banda prohibida.

iv) [“U-Shaped Graded Bandgap Profile on Kesterite Thin Film Solar Cells”](#).

Jacob Andrade-Arvizu, Z. Jehl, M. Courel, R. Fonoll-Rubio, V. Izquierdo-Roca, Y. Sánchez, M. Guc, D. Sylla, I. Becerril, M. Placidi, A. Pérez-Rodríguez, Osvaldo Vigil-Galán and E. Saucedo. En preparación.

Además, este capítulo reúne ambas estrategias de perfilado de brecha de banda prohibida para desarrollar de manera simultánea una graduación aniónica y catiónica dentro de la misma estructura matriz de kesterita depositada en forma de película fina.

Así, proporcionando por primera vez una conjunta sinergia entre la pasivación de defectos así como la modificación en los desplazamientos energéticos de las bandas en la interfaz a través de estrategias de graduado de brecha de banda prohibida en kesterita conduce a considerables mejoras en cuanto a la estabilidad y eficiencia de los dispositivos fotovoltaicos basados en este material.

En el caso de esta particular aleación (CZTGSSe), la compensación de energía bandas se puede controlar de forma independiente a través de los contenidos de azufre (S) y germanio (Ge), lo que se explicaría mediante un modelo del perfil doblemente graduado (en forma de U) de la brecha de banda prohibida.

Finalmente, el **séptimo capítulo** resume los principales resultados y conclusiones desarrollados por esta Tesis sugiriendo la urgencia de las aplicaciones materialistas directas en el escrutinio de las propiedades complejas de la Naturaleza expuestas bajo condiciones lejanas o circundantes, pero fuera del equilibrio termodinámico.

Además de las anteriormente mencionadas, las siguientes publicaciones que son coautoradas por el **M. en C. Jacob Antonio Andrade Arvizu**, contribuyeron en la preparación de esta Tesis, pero no se incluyen específicamente en el texto: **(Ver de Preface and Publications):**

In all chaos there is a cosmos,

In all disorder a secret order.

-Carl Gustav Jung

Preface and Publications

The research work presented in this Doctoral Thesis was performed at the Catalanian Institute for Energy Research (IREC) in Sant Adrià de Besòs, Barcelona, Spain from 2017 to 2021 in the framework of the “Advanced strategies for substitution of critical raw materials in photovoltaics” **STARCELL** project (H2020-NMBP-03-2016-720907); the “International cooperation for the development of cost-efficient kesterite/c-Si thin film next generation tandem solar cells” **INFINITE-CELL** project (H2020-MSCA-RISE-2017-777968); and the “Innovative manufacturing solutions for cost-efficient semi-transparent BIPV” **MASTER-PV** project (MICINN-PCI2018-092945), all projects of the European Commission.

The main subject of the Thesis focuses the development of advanced technological strategies for bandgap profile engineering on Earth-abundant and eco-friendly $\text{Cu}_2\text{Zn}(\text{Sn},\text{Ge})(\text{S}_x\text{Se}_{1-x})_4$ (kesterite) thin film solar cells which potentially optimize and enhance the energy power conversion efficiency of the devices.

This Thesis is structured around 22 (16, Q1 quartile) scientific articles published in high impact factor peer-reviewed JCR-indexed journals, including the following which are submitted in accord with the requirements for the Doctor of Philosophy in Physics Degree at the Physics Faculty of the University of Barcelona; this way assembling the product of this research as a 7-chaptered Thesis:

The first chapter provides a general overview and introduction by exposing the main motivations behind solar photovoltaic technologies, the second chapter describes the tackled problematic by describing the Thesis objectives. The third chapter states the experimental methodology employed, and provides a general outline on theoretical solar photovoltaic physics.

The three following chapters cover the main results obtained throughout the development of this Thesis and, and finally, the last chapter summarizes and highlights the outcomes and conclusions of this investigation.

In this regards, a more detailed description of the different chapters that comprise the structure of the Thesis is presented below:

The first chapter starts by providing a general overview and introduction to solar photovoltaic technologies by exposing the actual world energy consumption hassles and the direct implication with the heating imbalance produced by the current greenhouse gas emissions. Therefore, the solar PV technological classification by its material structural complexity is presented in order to introduce kesterite as an Earth abundant and eco-friendly material for emerging photovoltaic technologies.

The **second chapter** extends a brief introduction to kesterite as a complex structured material. Hence, by exposing the most relevant defects in an extensive and critical literature review; the identification of the V_{OC} deficit is revealed. Therefore the corresponding technological resolute is provided. In this fashion, graded bandgap profiling is sharply pointed out for the first time. Several anionic and cationic graded profiles are explored, suggesting the feasibility of a combination of a frontal anionic (S-Se) replacement together with a rear cationic (Ge-Sn) substitution inside the kesterite structure matrix in order to generate dual U-shaped graded bandgap profiles. As follows, advertised as this **Thesis objectives** as a plausible strategy to overcome the actual efficiency limitations in thin film kesterite solar cells.

The **third chapter** offers a road trip from the experimental very beginning, i.e., from the cleaning of the supporting substrate (glass), passing through the back contact deposition (Mo), to the sputtering of the Cu, Zn and Sn metallic precursor layers, up to the synthesis of the graded bandgap kesterite structured alloyed compounds.

Also, its adequation and surface etching and cleaning preparation for the completion of the solar device structure (buffer and front contact layers) are outlined. Thus, the fabrication process followed for the development of kesterite solar cells is thoroughly detailed. Hence, a general overview on the thin film material synthesis and system characterization is summarized.

Finally, a brief compilation on theoretical solar PV physics from the semiconductor materials and the PN junction to several of the optoelectronic characterization techniques utilized in this Thesis is provided.

The **fourth chapter** develops the standard numerical modelling simulation of a SEMS-IREC's baseline pure selenium kesterite solar cell by utilizing the gathered material parameters from the Solar Energy Materials and Solar Systems (SEMS) group device knowledge, which is mainly based on SCAPS-1D (Solar Cell Capacitance Simulator) numerical modelling simulation, along with the current state of the art kesterite device modelling literature.

In this way, the first part of this chapter tackles the first bandgap profile modeled grading attempts, in which factors such as the influence of sulfurization in kesterite (CZTSSe) solar cell devices and the impact of the contact ohmicity due rear sulfur segregations are provided as a comparative between linear and front surface bandgap profiles. Hence, a discussion on the sulfur content and positioning on the band diagram implications is provided for several sulfurization scenarios. Lastly, the effect of the front sulfurization of CZTSe solar cell with a realistic experimental compositional profile is analysed and discussed.

The next two chapters mainly cover the experimentally gathered results regarding the bandgap grading profiling in kesterite. The fifth (front anionic gradient) and sixth (rear cationic gradient) chapters are based on scientific papers published in high impact factor peer-reviewed journals, as will be detailed below, while the investigation presented at the final part of the sixth chapter (U-shaped graded bandgap) its primarily presented in this Thesis and will be posteriorly published.

The **fifth chapter** is based on the following publications (reproduced with permission, Copyright © American Chemical Society):

i) [“Is It Possible To Develop Complex S–Se Graded Band Gap Profiles in Kesterite-Based Solar Cells?”](#) **Jacob Andrade-Arvizu**, Víctor Izquierdo-Roca, Ignacio Becerril-Romero, Pedro Vidal-Fuentes, Robert Fonoll-Rubio, Yudania Sánchez, Marcel Placidi, Lorenzo Calvo-Barrio, Osvaldo Vigil-Galán, and Edgardo Saucedo. **ACS Applied Materials & Interfaces** 11 (36), 32945-32956 (2019). DOI: 10.1021/acsami.9b09813. Impact factor: **8.758 (Q1)**

ii) [“Controlling the anionic ratio and gradient in kesterite technology”](#) **Jacob Andrade-Arvizu**, Robert Fonoll Rubio, Victor Izquierdo-Roca, Ignacio Becerril-Romero, Diouldé Sylla, Pedro Vidal-Fuentes, Zacharie Jehl Li-Kao, Angélica Thomere, Sergio Giraldo, Kunal Tiwari, Shahaboddin Resalati, Maxim Guc, Marcel Placidi. **ACS Applied Materials & Interfaces**. Under review since 23/02/2021. Impact factor: **8.758 (Q1)**

This chapter demonstrates the development of a novel and disruptive chalcogenization process for the fabrication of $\text{Cu}_2\text{ZnSn}(\text{S},\text{Se})_4$ (CZTSSe) solar cells that enable the generation of complex and sharp graded anionic compositional profiles. Particularly focused in generating high S contents at the very top or front surface of the absorber, abruptly diminishing (as much as possible) to the rear side inside the same kesterite crystalline structured grain deposited over a thin film. This is achieved through the optimization of the annealing parameters including the study of several sulfur sources with different predicted reactivities (elemental S, thiourea, SnS, and SeS_2).

As a result, depending on the sulfur source employed, high efficiency kesterite solar cell devices with superficially localized maximum sulfur content between 50 and 20% within the charge depletion zone and between 10% and 30% towards the bulk material are obtained.

Hence, experimentally demonstrating the anionic graded profile theorized and modelled in the fourth chapter. These results represent one step forward toward anionic bandgap grading in kesterite solar cells.

The **sixth chapter** is based on the following publication (reproduced with permission, Copyright © American Chemical Society):

iii) [“Rear Band gap Grading Strategies on Sn–Ge Alloyed Kesterite Solar Cells”](#)

Jacob Andrade-Arvizu, R. Fonoll-Rubio, Y. Sánchez, I. Becerril-Romero, C. Malerba, M. Valentini, L. Calvo-Barrio, V. Izquierdo-Roca, M. Placidi, O. Vigil-Galán, A. Pérez-Rodríguez, Edgardo Saucedo, Z. Jehl Li-Kao. **ACS Applied Energy Materials** 3 (11), 10362–10375 (2020). DOI: 10.1021/acsaem.0c01146. Impact factor: **4.473 (Q1)**

In this chapter, a proven strategy of band engineering to assist charge carrier collection in kesterite, taking inspiration from chalcopyrite solar cells is demonstrated. For this purpose, a sequential process based on a combination of metallic precursor sputtering and chalcogenide reactive thermal annealing, allowed to control of cationic substitutions by partly replacing Sn by Ge, hence tailoring several rear bandgap grading profiles along the kesterite (CZTGSe) absorber thickness.

A complete set of structural, morphological, topographical and compositional characterization techniques, with samples ranging from pure Sn to pure Ge compounds are firstly discussed.

Therefore, the formation of a rear bandgap grading is determined through an advanced correlational characterization analysis, specifically through a combination of glow discharge optical emission (GDOES) and Auger spectroscopies along with multiwavelength Raman spectroscopy studies carried out at the front and rear sides of the films using thermomechanical a lift-off process.

As such, a preferential Ge enrichment toward the back of the absorber is unequivocally demonstrated in kesterite absorbers and further applied to complete devices for deliberately generating distinct rear bandgap profiles, leading to an efficient back surface field that potentially enhances the carrier selectivity of the back interface. In this way, the fabricated kesterite CZTGSe solar cells demonstrate a complex interplay between the benefits of bandgap grading and possible Sn-Ge interplay related defects in the absorber.

By optimizing the synthesis conditions, an absolute increase in bare efficiency is obtained for the champion device ($\approx 10\%$) without any antireflective coating (ARC) neither any metallic grid.

Therefore, the performance enhancement is mostly ascribed to the presence of a drift electric field assisting in the carrier collection while preventing back side recombination.

Hence, these results confirm the possibility of generating back bandgap grading in kesterite solar cells and open the way to a further development of the photovoltaic technology towards higher power conversion efficiencies through tailored bandgap engineering strategies.

iv) [“U-Shaped Graded Bandgap Profile on Kesterite Thin Film Solar Cells”](#).

Jacob Andrade-Arvizu, Z. Jehl, M. Courel, R. Fonoll-Rubio, V. Izquierdo-Roca, Y. Sánchez, M. Guc, D. Sylla, I. Becerril, M. Placidi, A. Pérez-Rodríguez, Osvaldo Vigil-Galán and E. Saucedo. Under preparation.

Also, this chapter assembles together the abovementioned strategies in order to simultaneously generate both anionic and cationic compositional grading profiles inside the same kesterite matrix structure. In this way, providing for the first time a demonstration of the joint synergy between defect passivation and interface energetics-modification, as a result of applying bandgap grading strategies in kesterite structured materials.

This fact leads to significantly improvements in stability and efficiency of thin film based photovoltaic devices. In the case of this Thesis studied kesterite alloyed material (CZTGSSe), the band energy offset can be independently controlled through the sulfur (S) and germanium (Ge) contents, which is explained by a double U-Shaped graded bandgap model.

Finally, the **seventh chapter** summarizes the main results and conclusions developed by this Thesis by suggesting the direct materialistic applications urgency on scrutinizing Nature's complex properties exposed at the far from thermodynamic equilibrium conditions.

Additionally following publications which are co-authored by **MSc Jacob Antonio Andrade Arvizu** contributed in the preparation of this Thesis but are not specifically included in the text:

- (5) “Insights into the role of the intrinsic zinc oxide buffer in chalcogenide photovoltaics”. **J. Andrade-Arvizu**, R. Fonoll-Rubio, I. Becerril, M. Guc, K. Tiwari, D. Sylla, Y. Sanchez, S. Giraldo, V. Izquierdo-Roca, A. Pérez-Tomás, M. Espindola-Rodriguez, L. Calvo-Barrio, Z. Jehl Li-Kao, A. Pérez-Rodríguez, E. Saucedo, M. Placidi. Under Preparation.
- (6) [“High efficiency \$\text{Cu}_2\text{ZnSnS}_4\$ solar cells over FTO substrate and its CZTS/CdS interface passivation via thermal evaporated \$\text{Al}_2\text{O}_3\$ ”](#). Esteban Ojeda-Durán, Karim Monfil-Leyva, **Jacob Andrade-Arvizu**, Ignacio Becerril-Romero, Yudania Sánchez, Robert Fonoll-Rubio, Maxim Guc, Zacharie Jehl Li-Kao, José A. Luna-López, Jesús Carrillo-López, Ana L. Muñoz-Zurita, Victor Izquierdo-Roca, Marcel Placidi, Edgardo Saucedo. **Journal of Materials Chemistry C**, 9, 5356-5361 (2021). DOI: 10.1039/D1TC00880C. Impact factor: **7.059 (Q1)**
- (7) [“Insights on the limiting factors of \$\text{Cu}_2\text{ZnGeSe}_4\$ based solar cells”](#). I. Anefnaf, S. Aazou, Y. Sanchez, P. Vidal-Fuentes, R. Fonoll-Rubio, K. Tiwari, S. Giraldo, Z. J. Li-Kao, **Jacob Andrade-Arvizu**, M. Guc, E. Saucedo, Z. Sekkat. **Solar Energy Materials and Solar Cells**, 227, 111106 (2021). DOI: 10.1016/j.solmat.2021.111106. Impact factor: **6.984 (Q1)**
- (8) [“Insights into interface and bulk defects in a high efficiency kesterite-based device”](#). Robert Fonoll-Rubio, **Jacob Andrade-Arvizu**, Javier Blanco-Portals, Ignacio Becerril-Romero, Maxim Guc, Edgardo Saucedo, Francesca Peiró, Lorenzo Calvo-Barrio, Maurizio Ritzer, Claudia S. Schnohr, Marcel Placidi, Sònia Estradé, Víctor Izquierdo-Roca, Alejandro Pérez-Rodríguez. **Energy and Environmental Science**, (2021), 14, 507-523. DOI: 10.1039/D0EE02004D. Impact factor: **30.289 (Q1)**
- (9) [“Argon vs. air atmosphere in close spaced vapor transport deposited tin sulfide thin films”](#). **Jacob Andrade-Arvizu**, Maykel Courel, M. García-Sánchez, R. González, D. Jiménez, I. Becerril-Romero, A. Ramírez, O. Vigil-Galán. **Solar Energy** 208, 227-235 (2020). DOI: 10.1016/j.solener.2020.07.070. Impact factor: **4.674 (Q1)**

- (10) [“Investigation on limiting factors affecting \$\text{Cu}_2\text{ZnGeSe}_4\$ efficiency: Effect of annealing conditions and surface treatment”](#). Nada Benhaddou, Safae Aazou, Yudania Sánchez, **Jacob Andrade-Arvizu**, Ignacio Becerril-Romero, Maxim Guc, Sergio Giraldo, Víctor Izquierdo-Roca, Edgardo Saucedo, Zouheir Sekkat. **Solar Energy Materials & Solar Cells** 216, 110701 (2020). DOI: 10.1016/j.solmat.2020.110701. Impact factor: **6.984 (Q1)**
- (11) [“Transition-Metal Oxides for Kesterite Solar Cells Developed on Transparent Substrates”](#). Ignacio Becerril-Romero, Diouldé Sylla, Marcel Placidi, Yudania Sánchez, **Jacob Andrade-Arvizu**, Víctor Izquierdo-Roca, Maxim Guc, Alejandro Pérez-Rodríguez, Sigbjørn Grini, Lasse Vines, Benjamín Pusay, Rosa Almache, Joaquim Puigdollers, Paul Pistor, Edgardo Saucedo, Moisés Espíndola-Rodríguez. **ACS Applied Materials & Interfaces** 12 (30), 33656–33669 (2020). DOI: 10.1021/acsami.0c06992. Impact factor: **8.758 (Q1)**
- (12) [“Efficient Se-rich \$\text{Sb}_2\text{Se}_3/\text{CdS}\$ planar-heterojunction solar cells by sequential processing: control and influence of Se content”](#). Pedro Vidal-Fuentes, Marcel Placidi, Yudania Sánchez, Ignacio Becerril-Romero, **Jacob Andrade-Arvizu**, Zacharie Jehl, Alejandro Pérez-Rodríguez, Víctor Izquierdo-Roca, and Edgardo Saucedo. **RRL Solar** 4 (7), 2000141 (2020). DOI: 10.1002/solr.202000141. Impact factor: **7.527 (??)**
- (13) [“CZTS solar cells and the possibility of increasing \$V_{\text{OC}}\$ using evaporated \$\text{Al}_2\text{O}_3\$ at the CZTS/CdS interface”](#). E. Ojeda-Durán, K. Monfil-Leyva, **J. Andrade-Arvizu**, I. Becerril-Romero, Y. Sánchez, R. Fonoll-Rubio, M. Guc, Z. Jehl, J.A. Luna-López, A.L. Muñoz-Zurita, J.A.D. Hernández-de la Luz, V. Izquierdo-Roca, M. Placidi, E. Saucedo. **Solar Energy** 198, 696-703 (2020). DOI: 10.1016/j.solener.2020.02.009. Impact factor: **4.674 (Q1)**
- (14) [“Sputtered ZnSnO Buffer Layers for Kesterite Solar Cells”](#). Louis Grenet, Fabrice Emieux, **Jacob Andrade-Arvizu**, Eric De Vito, Géraldine Lorin, Yudania Sánchez, Edgardo Saucedo, and Frédéric Roux. **ACS Applied Energy Materials** 3(2), 1883–1891 (2020). DOI: 10.1021/acsaem.9b02329. Impact factor: **4.473 (Q1)**

- (15) [“Structural and vibrational properties of \$\alpha\$ - and \$\pi\$ -SnS polymorphs for photovoltaic applications”](#). Maxim Guc, **Jacob Andrade-Arvizu**, Ibbi Y. Ahmet, Florian Oliva, Marcel Placidi, Xavier Alcobé, Edgardo Saucedo, Alejandro Pérez-Rodríguez, Andrew L. Johnson, Victor Izquierdo-Roca. **Acta Materialia** 183, 1-10 (2020). DOI: 10.1016/j.actamat.2019.11.016. Impact factor: **7.656 (Q1)**
- (16) [“Study and optimization of alternative MBE-deposited metallic precursors for highly efficient kesterite CZTSe:Ge solar cells”](#). Sergio Giraldo, Shinho Kim, **Jacob Antonio Andrade-Arvizu**, Xavier Alcobé, Claudia Malerba, Matteo Valentini, Hitoshi Tampo, Hajime Shibata, Victor Izquierdo-Roca, Alejandro Pérez-Rodríguez, Edgardo Saucedo. **Progress in Photovoltaics** 27(9), 779-788 (2019). DOI: 10.1002/pip.3147. Impact factor: **7.690 (Q1)**
- (17) [“An innovative alkali doping strategy for \$\text{Cu}_2\text{ZnSnSe}_4\$ through the CdS buffer layer”](#). Y. Sánchez, S. Giraldo, **J. A. Andrade-Arvizu**, M. Neuschitzer, L. Calvo-Barrio, V. Izquierdo-Roca, A. Pérez-Rodríguez, E. Saucedo. **2018 IEEE 7th World Conference on Photovoltaic Energy Conversion (WCPEC)**. DOI: 10.1109/PVSC.2018.8547417. Impact factor: **3.557**
- (18) [“Influence of Ge content on \$\text{Cu}_2\text{Zn}\(\text{SnGe}\)\text{Se}_4\$ physical properties deposited by sequential thermal evaporation technique”](#). J. R. González-Castillo, F. A. Pulgarín-Agudelo, Eugenio Rodríguez-González, O. Vigil-Galán, Maykel Courel-Piedrahita, **J. A. Andrade-Arvizu**. **Materials Science in Semiconductor Processing** 83, 96-101 (2018). DOI: 10.1016/j.mssp.2018.04.024. Impact factor: **3.085 (Q1)**
- (19) [“Cu content dependence of \$\text{Cu}_2\text{Zn}\(\text{SnGe}\)\text{Se}_4\$ solar cells prepared by using sequential thermal evaporation technique of Cu/Sn/Cu/Zn/Ge stacked layers”](#). F. A. Pulgarín-Agudelo, O. Vigil-Galán, **Jacob A. Andrade-Arvizu**, J. R. González-Castillo, Eugenio Rodríguez-González, Maykel Courel, Y. Sánchez, E. Saucedo. **Journal of Materials Science: Materials in Electronics** 29, 18, 15363-15368 (2018). DOI: 10.1007/s10854-018-8915-5. Impact factor: **2.195**

- (20) [“Preparation and characterization of \$\text{Cu}_2\text{ZnSnSe}_4\$ and \$\text{Cu}_2\text{ZnSn}\(\text{S,Se}\)_4\$ powders by ball milling process for solar cells application”](#). Fabian Andres Pulgarín-Agudelo, Osvaldo Vigil-Galán, M. M. Nicolás-Marín, Maykel Courel, R. González, Héctor Mendoza-Leon, S. Velumani, M. Rohini, **Jacob A. Andrade-Arvizu**, F. Oliva, Victor Izquierdo-Roca. **Materials Research Express** 4, 12 (2017). DOI: 10.1088/2053-1591/aa9a8d. Impact factor: **1.929**
- (21) [“Study of CBD-CdS/CZTGSe solar cells using different Cd sources: behavior of devices as a MIS structure”](#). O. Vigil-Galán, **J. A. Andrade-Arvizu**, Maykel Courel-Piedrahita, C. Mejía-García, E. Valencia-Resendíz, Y. Sánchez-González, M. Espíndola-Rodríguez, E. Saucedo-Silva, R. González-Castillo, E. Rodríguez-González, D. Seuret-Jiménez, D. Jiménez-Olarte. **Journal of Materials Science: Materials in Electronics** 28, 24, 18706-18714 (2017). DOI: 10.1007/s10854-017-7820-7. Impact factor: **2.220**
- (22) [“Processing pathways of \$\text{Cu}_2\text{Zn}\(\text{SnGe}\)\text{Se}_4\$ based solar cells: The role of CdS buffer layer”](#). O. Vigil-Galán, Maykel Courel, **J. A. Andrade-Arvizu**, Y. Sánchez, M. Espíndola-Rodríguez, E. Saucedo, D. Seuret-Jiménez, R. González. **Materials Science in Semiconductor Processing** 67, 14-19 (2017). DOI: 10.1016/j.mssp.2017.05.003. Impact factor: **3.085 (Q1)**

***All impact factor values were gathered on 20210420**

To create and to annihilate material substance, cause it to aggregate in forms according to his desire, would be the supreme manifestation of the power of Man's mind, his most complete triumph over the physical world.



To see a world in a grain of sand, and a heaven in a wild flower,

Hold infinity in the palm of your hand and eternity in an hour.

-William Blake

Chapter I

Introduction

1.1 General Introduction

As specie conformed by living organisms, humanity is doomed to look after survival. Regarding the complexity of the human development, we have whimsically adapted to thrive. Unfortunately, and despite the enormous scientific and technological advances in human history, the same economic and sociopolitical development of the systems that have led our civilization to the endless quest for prosperity and growth; has been so far fundamentally based on the selfish idea of Universe's resources and materials ownership. Long time ago, we have understood that in order to properly and effectively observe a function on a system -or a machine-, energy must be somehow involved. Without energy, there is no action therefore any work to be produced. Therefore, energy is inherently important in all physical processes ¹⁻⁵. In words of Harold Morowitz: "The flow of energy through a system acts to organize that system". ⁶Light, chemical reactions, electricity, mechanical work, heat, and life itself could all be described in terms of energetic activity. ⁷⁻⁹ Thus, we conceptualized energy as measurement of the capacity to change our environment.

Along with this understanding, we have translated the utilization, possession and management of energy into "goods for surviving" -amongst other things-.

As our energy consumption grows exponentially, so did the abilities of our civilization. Between 1800 and 2015, the worldwide population size has been seven-folded, while humanity was consuming twenty five times more energy by that time.

Unfortunately, it is likely that this process and tendencies will continue this behavior in the far future. ^{10,11}

Furthermore, it is natural to think that a sustained population growth will demand a proportional continuous energy input. In the contemporary world, progress is intrinsically linked to the energy demand.

In line with the last International Energy Outlook (IEO) report (2019) ¹², the world energy consumption is projected to raise around 800 BTU in 2040 and might reach 900 BTU by 2050 as it is shown in Figure 1.1.

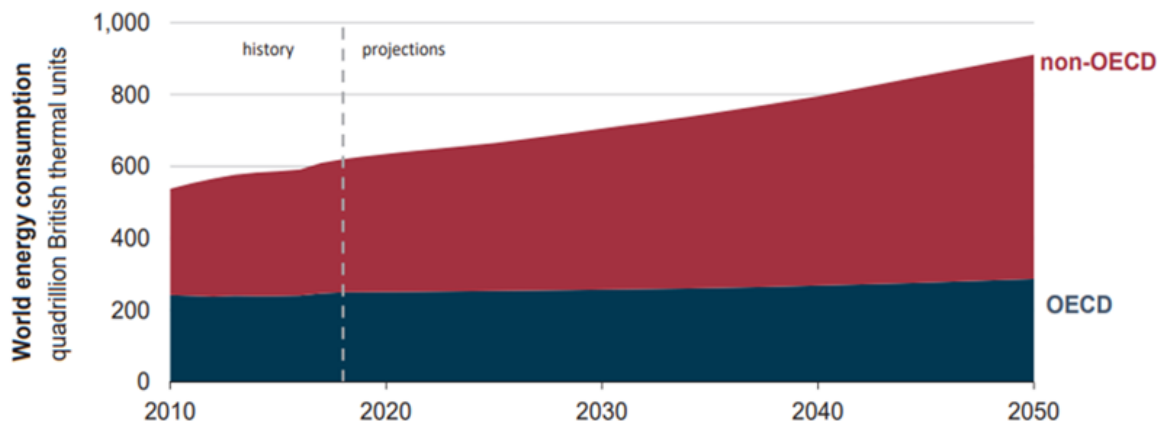


Figure 1.1- World energy consumption rises nearly 50% between 2018 and 2050 in the reference case. ¹² British Thermal Units (1 BTU = 1055.6 J).

Also, according to the 2019 IEO, amongst the actual distinct primary energy sources, the principal current consumptions for both members and non-members countries of the Organisation for Economic Co-operation and Development (OECD) are the utilization of natural gas, coal, petroleum and derivatives as it is shown in Figure 1.2. ³

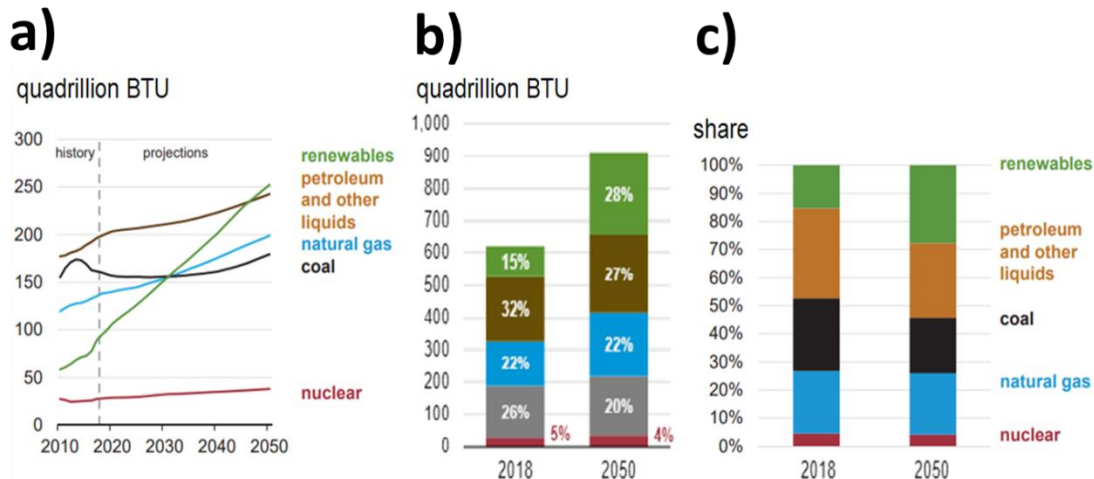


Figure 1.2- Worldwide primary energy consumption (2010-2050) by **a)** energy source and **b)** consumption percentage and **c)** market share projections for 2050. ¹²

In this way, renewable energy becomes the leading source of primary energy consumption by 2050 in the reference case. ¹²

It is also noteworthy to note that by year 2018; only a 15% of consumption has been associated to the use of renewables energies which include hydro, thermal, wind, solar, etc. ¹³ However, fossil fuel account for more than 80% of the worldwide energy consumption.

Additionally to the 30% renewable global market share projection in Figure 1.2c, nuclear energy is predicated to suffer a 1-2% share decrease by year 2050. Also, it is well known that the excessive and fast burning of the fossil fuels such as crude oil and coal has already surpassed the oil's tipping point. ^{14,15}

Therefore, due to the scarcity of the resources and by the economic law of supply and demand ¹⁶, the price of fossil fuels is projected to experience preposterous fluctuations and eventually, an exponentially increase.

Since the consumerist capital economy is mainly based on the manufacturing and production of process and/or services, which at the time are directly energy-dependent, unbridled energy goods price increments may lead to an absolute economic collapse. ¹⁷

Influence of all major human-produced greenhouse gases (1979-2018)

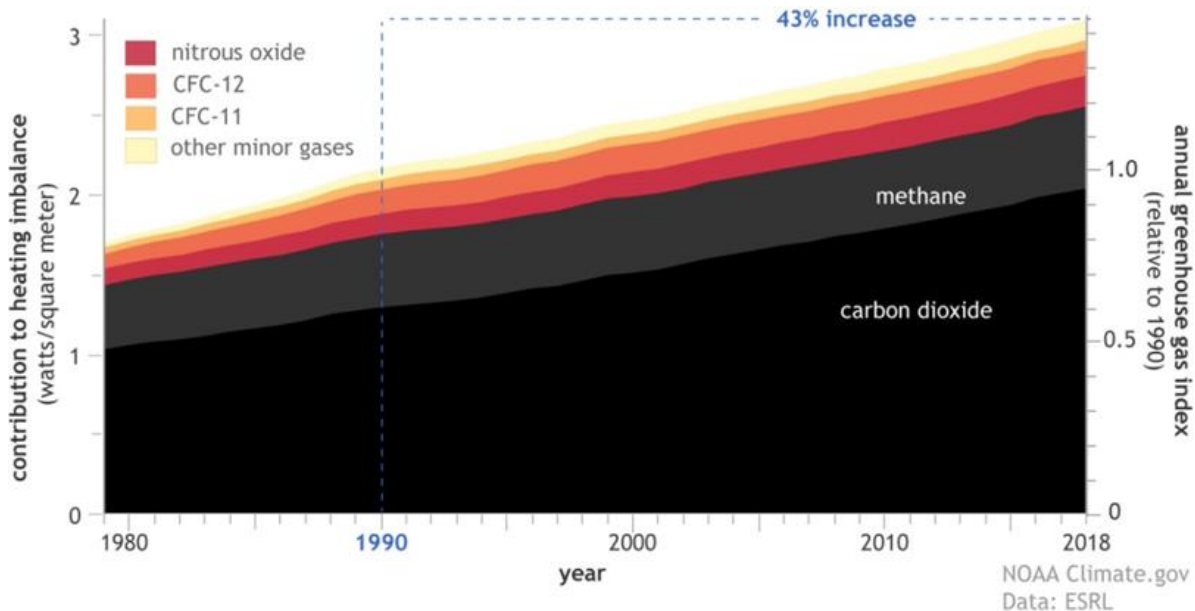


Figure 1.3- Heating imbalance [$W.m^{-2}$] (relative to year 1750) caused by all major human-produced GHG such as carbon dioxide (CO_2), methane, nitrous oxide, chlorofluorocarbons 11 and 12, along with 15 other minor contributors. According to NOAA's Annual Greenhouse Gas Index (AGGI, right axis) the combined heating influence of all major GHG has increased by 43% relative to 1990.¹⁷

Besides the abovementioned fatalist scenario, even more critical is to immediately stop the actual ludicrously emission of the so-called greenhouse gases (GHG) produced by the combustion of organic fuels and responsible for global warming.^{18,19}

Figure 1.3 shows the actual increase in the annual greenhouse gas index along with the contribution to earth's heating imbalance with respect during the last 40 years.

The 43% increase during the past 30 years along with the atmospheric carbon dioxide abrupt increase (See Figure 1.4) are an alarming warning that in the case that this trending continues the consequences and impact of a global warming will be irreversible for the planet.

Therefore, it is urgent to produce sustainable and clean energy as well as reduce the actual global GHG emission, which is necessary to further research and explore renewable energy technologies.

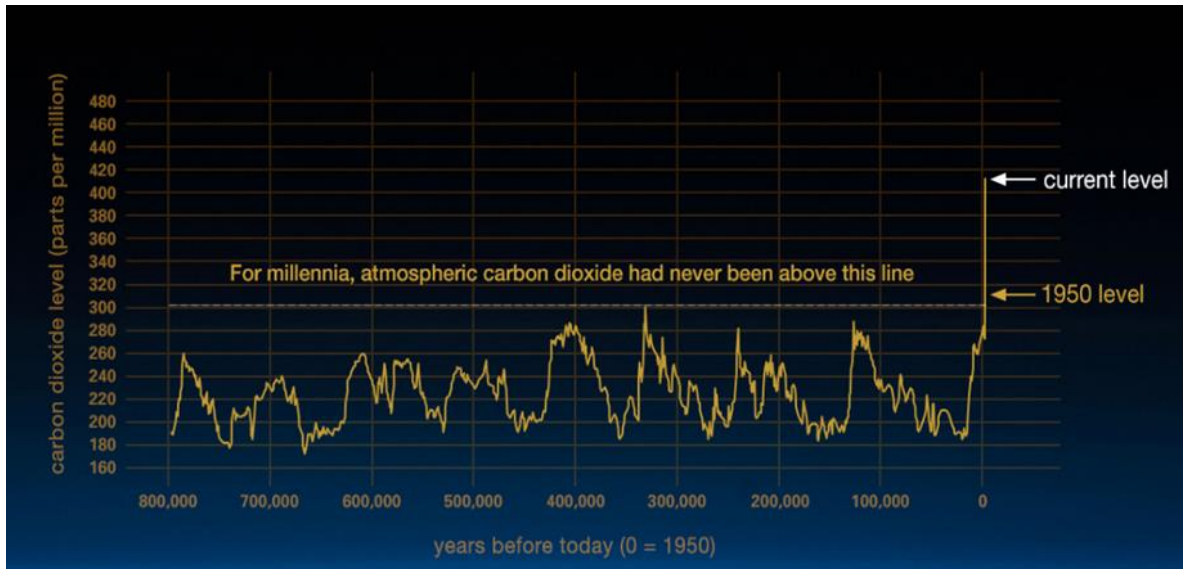


Figure 1.4- Atmospheric carbon dioxide (CO₂) level. ^{20–24}

According to the Special Report on Emissions Scenarios (SRES) and the 5th Assessment Report of the Intergovernmental Panel on Climate Change (IPCC), the warming of the Earth's climate system is unequivocal, and most of the observed increase in global average temperatures since the mid-20th century is very likely due to the observed increase in anthropogenic GHG concentrations. ²⁵

In this regards, the Special Report on Renewable Energy sources and climate change mitigation (SRREN), also from the IPCC assesses the existing literature on renewable energy commercialization for the mitigation of climate change.

However, during the conclusion of COP 21 (the 21st meeting of the Conference of the Parties), it was adopted by consensus by all of the 195 United Nations Framework Convention on Climate Change (UNFCCC) and all the 28 European Union members ²⁶ to reduce emissions as part of the method for reducing GHG emissions.

In this agreement ²⁷ the members promised to reduce, as soon as possible, their carbon output and to do their best to keep global warming to well below 2 °C.

On the other hand, for the first time in history, the International Energy Agency's (IEA) World Energy Outlook 2020 ²⁸ includes a detailed modeling of a 1.5 °C pathway that reaches global net-zero CO₂ emissions by 2050.

Since two thirds of total CO₂ emissions from fossil fuels are associated with electricity generation, heating, and transportation ²⁸, and the actual viral pandemic crisis (COVID-19) that is actually haunting humankind, by restricting our possibilities to meet and interact, has provoked a dramatic decline in global energy demand, in which fossil fuels take the biggest of the economical negative impacts.

At the same time, it is crystal clear, that in order reduce emissions while providing the actual and future energy services necessary to accommodate global economic growth.

Thus, the ratio of CO₂ emissions to global energy use ought to be substantially reduced. In this regard, an urgent implementation of eco-friendly and renewable sources of energy must take place with more urgency than ever.

Solar energy importance ultimately derives from the profound long-term threat posed by global climate change. CO₂ emissions from the combustion of fossil fuels account for by far the largest share of GHG that are causing climate change. Since fossil fuels are finite and will be exhausted in the future, sustainable and renewable energy production methods such as solar energy, wind power, and biomass power generation are required.

By taking into account that the IEA finds that for solar energy, the capital cost of is at its lowest values, around 2.6 - 5.0% in the European Union and the United States of America, 4.4 - 5.5% in China and 8.8 - 10.0% in India, largely as a result of policies designed to reduce the risk of renewable investments. Therefore, solar energy has the potential to play a major role in achieving this goal.

Furthermore, by observing the shares of the OECD countries generating capacity for renewables energies of the last 30 years, Solar Photovoltaics (PV) possesses the highest average annual growth rate (> 33%) of the electricity production market (See Figure 1.5).

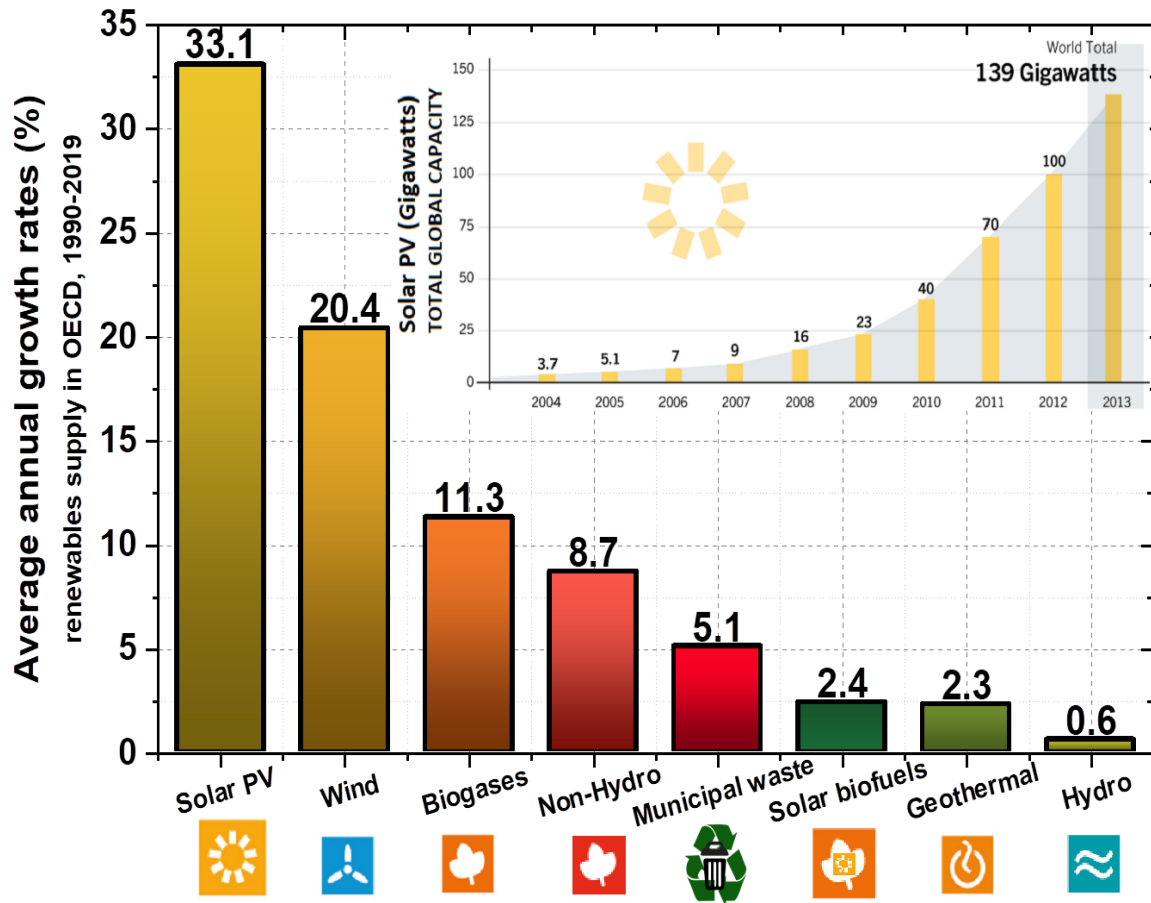


Figure 1.5- Average annual growth rates of electricity production in the OECD countries, 1990-2019.^{29,30}

Figure 1.5 shows that, solar photovoltaics (PV) are the fastest growing member in the renewable energies team. This is merely a reflection and it's intrinsically linked to the academic and industrial research interest into the topic.

However, humanity actually utilizes less than 0.1% of the received solar energy, and this might change if solar panels become more affordable and efficient by the development of solar cell advances.

1.2 Solar Photovoltaic (PV) Technology

Fueled by crude raw light and with no moving parts (except in solar tracking systems), Solar PV can operate near room/ambient temperature, enabling power generation at any scale. Figure 1.6 shows the main PV classifications as either wafer-based or thin film technologies. Thin film solar cells consist of layers of semiconducting material deposited onto an inert substrate, such as glass, flexible plastic, or metallic foils. Further, the thin film PV category is divided into commercial and emerging thin film technologies.

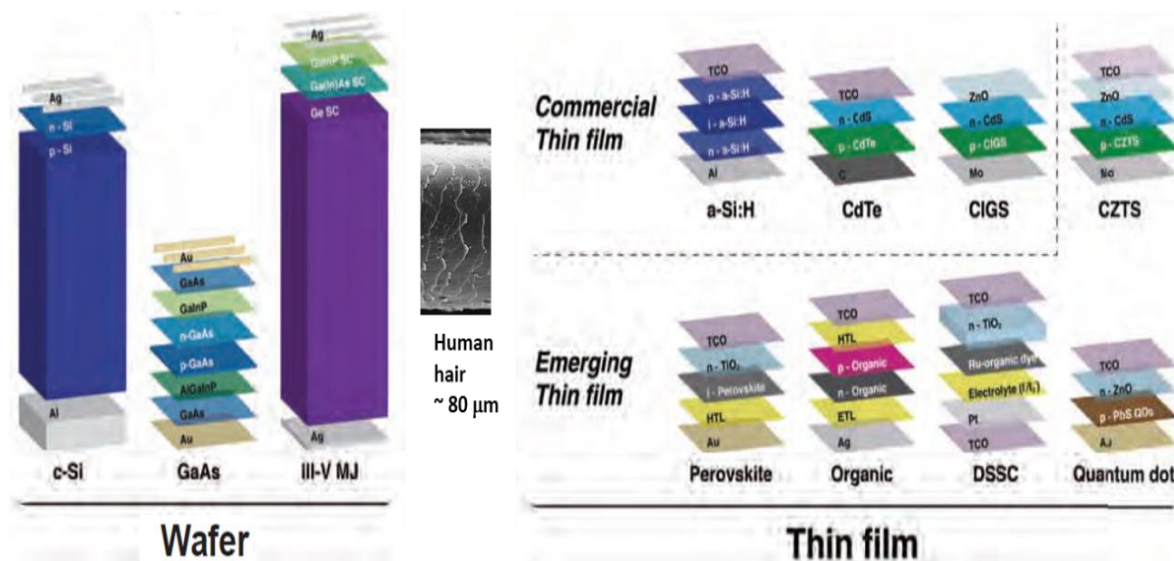


Figure 1.6- Current Solar PV device structures. ³¹

Nowadays, the majority of commercial PV module production is based in silicon technologies. The poor ability to absorb light that exhibit crystalline silicon (c-Si) translates in high capital costs, low power-to-weight ratios, and constraints on module flexibility and design, because thick Si wafers are required (100-300 μm). Therefore, alternative technologies may be able to achieve lower costs in the long run.

Thin film solar cells are made by additive in-line fabrication processes, which may reduce material usage, manufacturing capital outlays, and lifecycle of GHG emissions ^{17,32,33}.

Thin film based solar cells extends from commercial technologies based on conventional inorganic semiconductors to emerging technologies based on nanostructured materials (Figure 1.6). In this sense, the world record laboratory scale solar cell power conversion efficiencies for all the actual PV technologies is provided by the National Renewable Energy Laboratory (NREL) chart as it is shown in Figure 1.7.²⁵

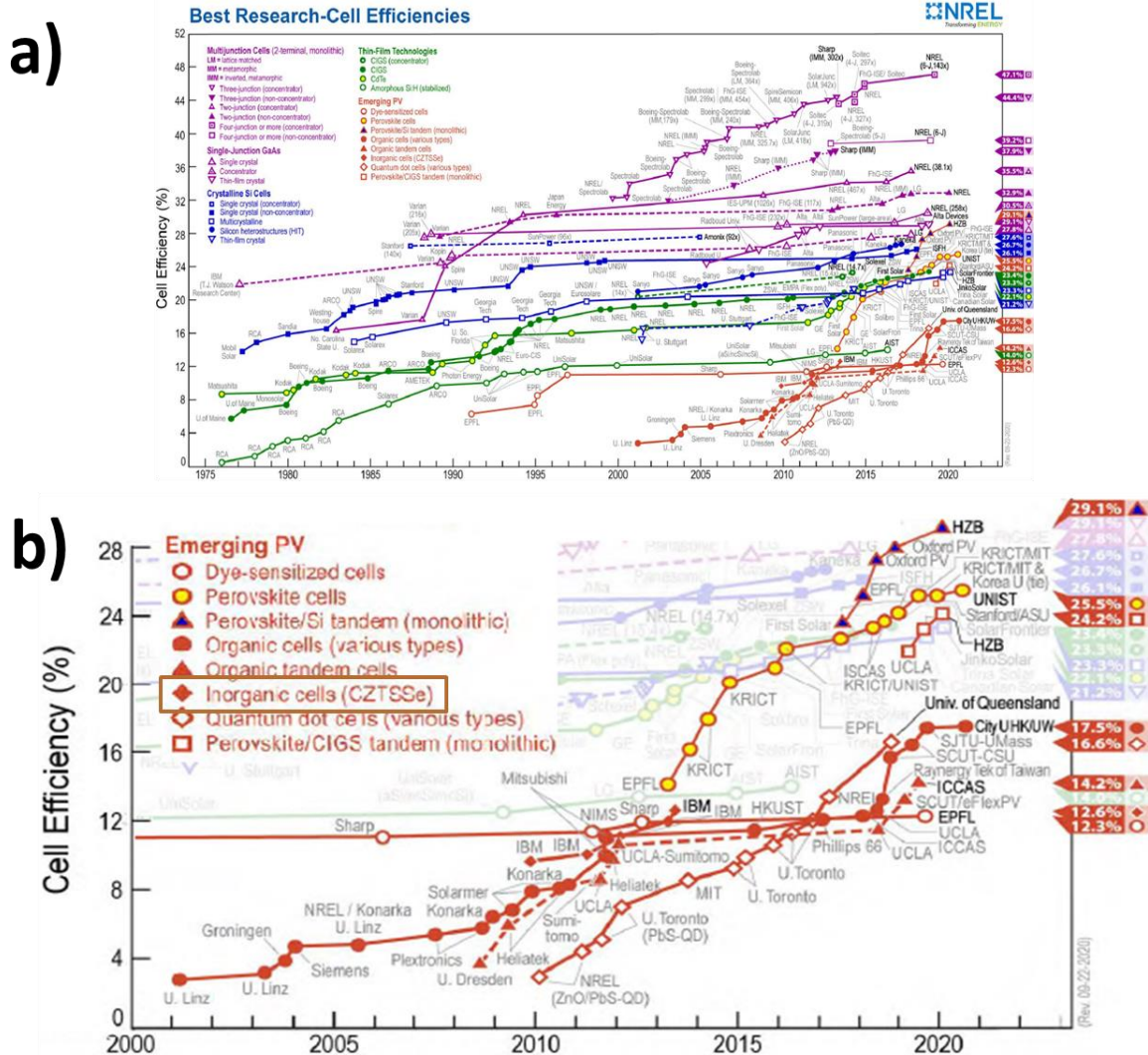


Figure 1.7.- a) NREL trends in record lab-scale solar cell power conversion efficiencies. **b)** Last 20 years development of emerging PV technologies.³⁴

Actual commercial thin film PV technologies are mainly represented by hydrogenated amorphous silicon (a-Si:H), cadmium telluride (CdTe), and copper indium gallium diselenide (CIGS).

These materials can absorb light up to 100 times more efficiently than c-Si, allowing the use of films with just a few microns (μm) thick layered materials. In this regard, the low use of raw materials is thus a key advantage of these technologies.

Additionally, advanced industrial factories can produce thin film photovoltaic (TFPV) modules in a highly streamlined and automated way, reducing this way the price per-watt of the module.

The main disadvantage of today's commercial thin film modules is their comparatively lower average efficiency, typically in the range of 12%-15%. Most of the actual thin film materials show a polycrystalline nature, thus containing considerable higher defect densities than c-Si.

Also, compound semiconductors, such as CIGS show complex stoichiometry, performing high-yield, uniform, large-area deposition a difficult engineering task. Additionally, recycling of toxic-controlled elements (Cd) and dependency on rare elements (Te and In) would likely to reduce the capability for large-scale deployment.

Therefore, there are open current innovation opportunities in thin film technology which include improving power conversion efficiencies, also improving reliability with the introduction of hefty materials and solar cell architectures by decreasing the dependence on scarce elements by developing new materials with similar ease of processing.

In recent years, several new thin film PV technologies have emerged as a result of intense research and development efforts in materials discovery and device optoelectronic engineering.

1.3 Solar PV Technology Classification by Material Complexity

Solar PV technologies can be classified by wafer-based, thin film based, and new emerging concepts that basically delineate three distinct generations.³⁵ However, an alternative classification approach based on material complexity might result of high interest for emerging thin film PV technologies.

Material complexity is usually associated with the degree of disorder in a material. For example, amorphous materials might be qualitatively classified as generally more complex than their crystalline counterparts. In this sense, all PV technologies fall on a spectrum from elemental (lowest) to nanomaterial (highest) complexity, as it is shown in Figure 1.8.

In this regards, material complexity classification starts from the “relatively simple” building block technologies of silicon to more complex materials thin film deposited based technologies, ranging from polycrystalline thin films, such as cadmium telluride (CdTe), copper indium gallium sulfo/selenide (CIGS), and kesterite (CZTS) to complex nanomaterials such as organic, dye-sensitized (DSSC) and quantum dots solar cells (QDs).

On the left hand, it is noteworthy to say, that material complexity is not equivalent to processing complexity. Moreover, there could be a trade-off between them. But on the right hand, increased material complexity allows several disruptive, novel and potentially valuable technological attributes such as a defect tolerance, possibility of flexible substrates utilization, the possibility of visible transparency for building integrated photovoltaics (BIPV) applications as well as automotive integrated ones (AIPV), the use for powering new concepts such as agrovoltatics or energetic portability like the Internet of Things (IoT), unmanned aircraft systems³⁶, aesthetics, and durability of wearable power supply devices.

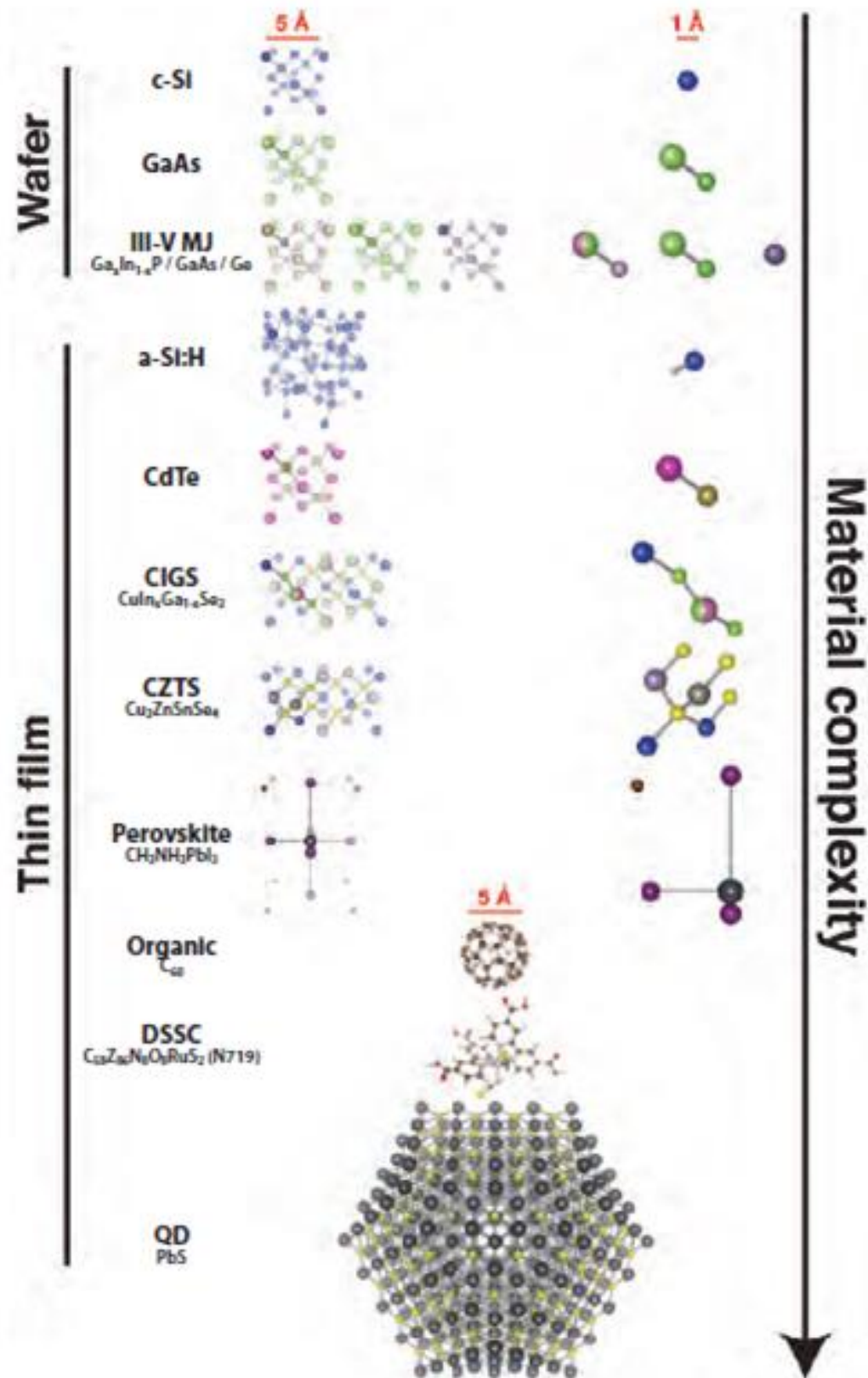


Figure 1.8.- Alternative photovoltaic (PV) technology classification scheme based on material complexity.³¹

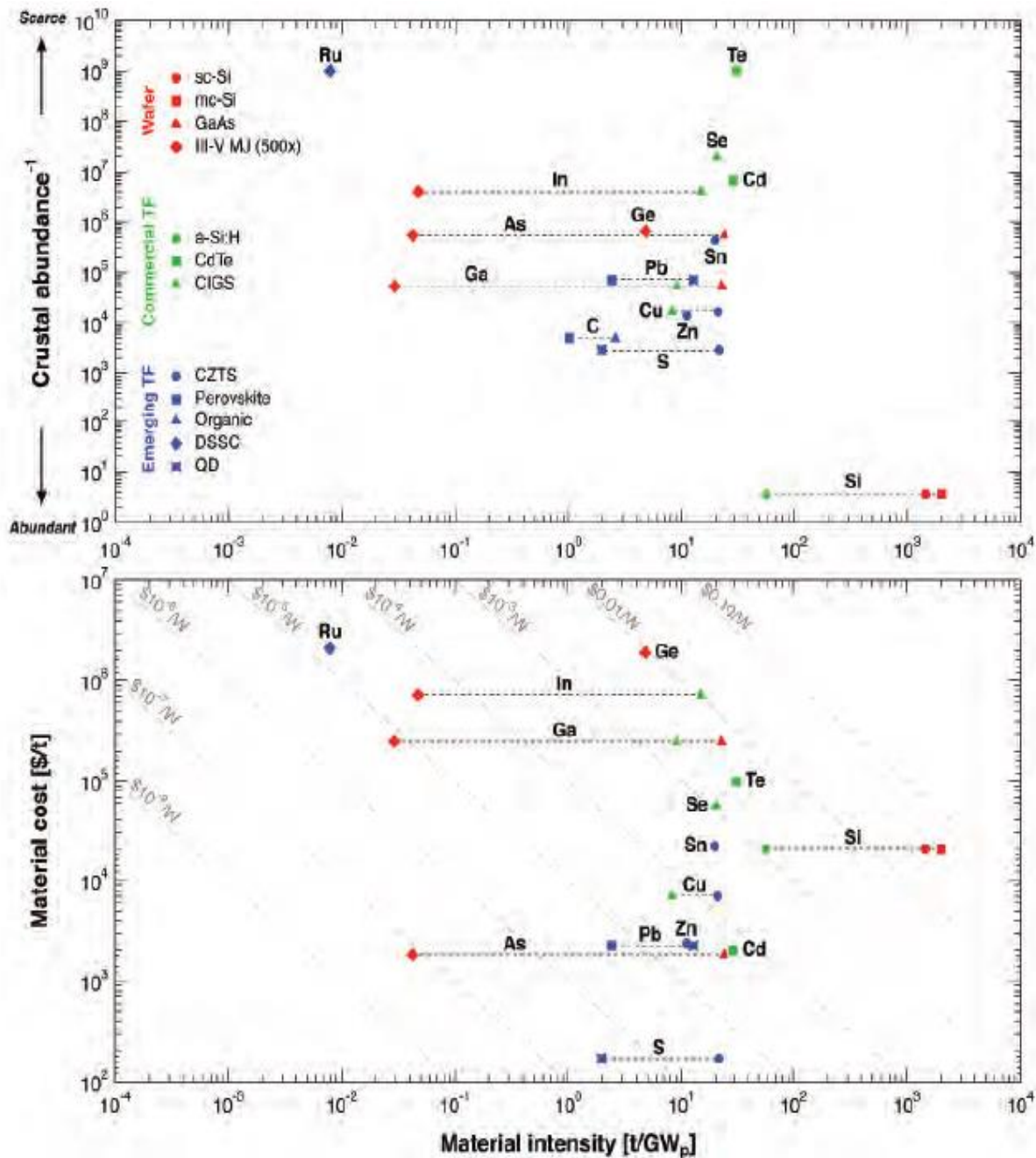


Figure 1.9.- Materials usage, crustal abundance, and cost vs. material intensity plots for key (strategic) elements utilized in commercial and emerging PV technologies.³¹

Hence, PV devices will be a key element in harvesting environmental energy. It is expected to move toward lower materials usage for all technologies in the next years. Additionally, thinner glass, frames, and active layers could reduce material consumption and in general costs.

Also, PV technologies that require scarce elements may be unable to achieve terawatt-scale deployment. Material cost, usage, and the crustal elemental abundance as function of the material intensity for different solar cell technologies are shown in Figure 1.9.

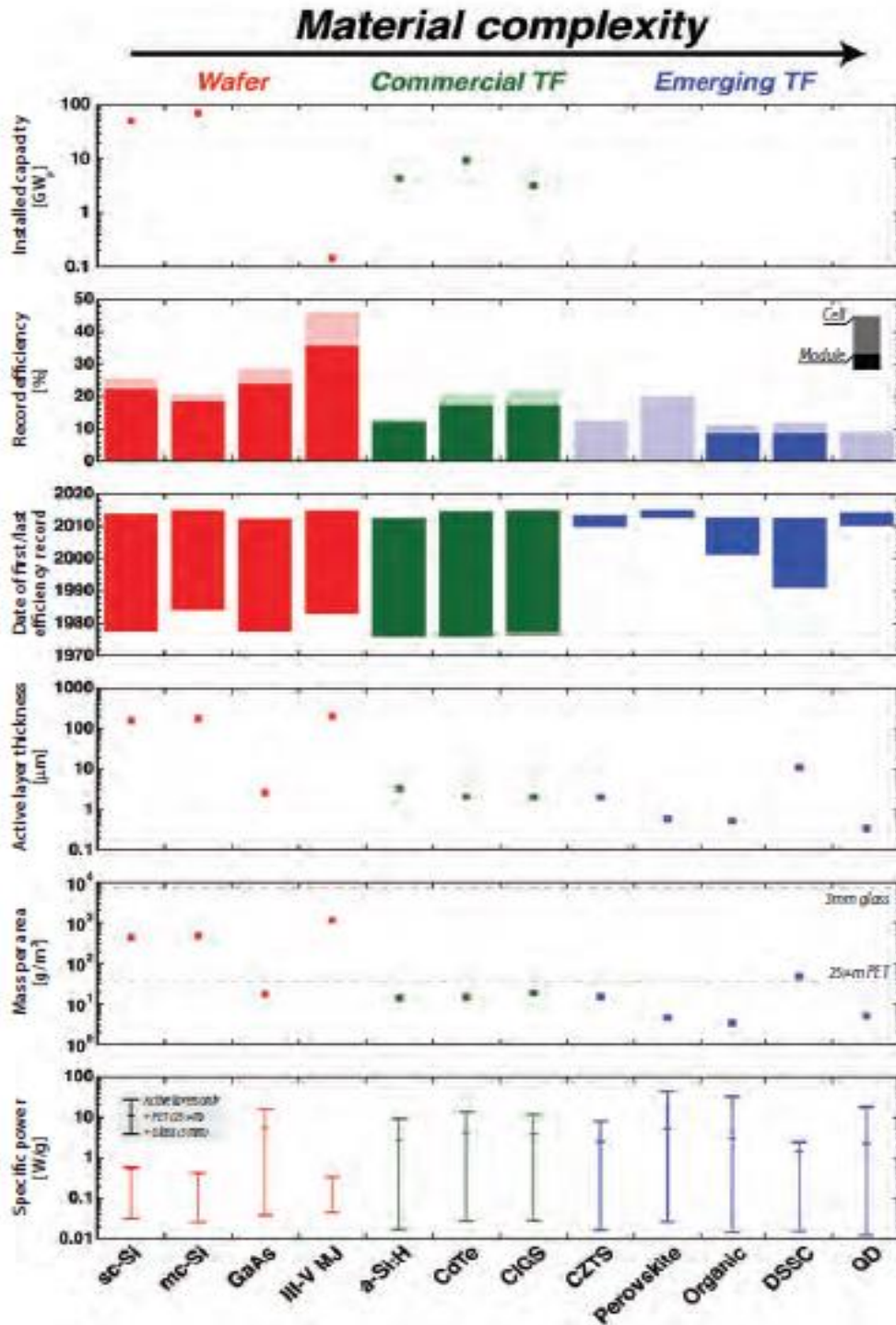


Figure 1.10.- Key metrics for photovoltaic technologies ordered by material complexity. ³¹

Thin film PV production currently uses three raw materials (In, Te and Ga) which are listed as Critical Raw Materials (CRM) in the European Commission Review's list of critical raw materials for the European Union (COM-2014/297).^{37,38} Thus, for the consolidation of independent and secure European PV technology, and to meet the actual greenhouse gases emission and energy supply commitments, it is essential to overcome the photovoltaic technology CRM constraint.^{39,40}

Finally, Figure 1.10 compares the technological maturity (installed capacity, last-time record), power conversion efficiency, materials usage, and specific power of actual solar PV technologies. Also, from Figure 1.10, it could be noted that the only actual established solar PV technologies stands for silicon and thin films.

Since thin films could use up to 1000 times less material than c-Si, thin film technologies are able to increase the power output per unit weight. Moreover, all the actual PV technologies have been under a research and development stage for at least the last 30 years.

Naturally, as technological and processing pathways have been exponentially developed, actual emerging PV technologies are improving far faster than actual commercial solar PV technologies improved in their early stages (See Figure 1.7).

Therefore, novel active materials may reach cost and performance targets by device fundamental engineering that are inaccessible using the actual developed solar PV technologies.

An Earth-abundant alternative to CIGS, with similar processing strategies and challenges are the so-called **kesterite structure** based compounds like: $\text{Cu}_2\text{ZnSnS}_4$ (CZTS), $\text{Cu}_2\text{ZnSnSe}_4$ (CZTSe), $\text{Cu}_2\text{ZnGeSe}_4$ (CZGSe) and the anionic and cationic derivative combinations such as $\text{Cu}_2\text{ZnSn}(\text{S,Se})_4$ (CZTSSe), $\text{Cu}_2\text{Zn}(\text{Sn,Ge})\text{Se}_4$ (CZ(T,G)Se), respectively.

In view of the high relevance that emerging photovoltaic technologies based in earth-abundant elements have for the future deployment of solar energy, in the following Chapter the most relevant characteristics and state of the art of the "so-called" kesterite absorbers will be presented, together with the main objectives of this Doctoral Thesis.

1.4 Chapter References

1. Boltzmann, L. (1886). The Second Law of Thermodynamics. In B. McGinness, ed., *Ludwig Boltzmann: Theoretical physics and philosophical problems: Selected writings*. Dordrecht, Netherlands: D. Reidel, 1974.
2. Lotka, A. J. Natural Selection as a Physical Principle. *Proc. Natl. Acad. Sci.* 8, 151–154 (1922).
3. Lotka, A.J. (1922) Contribution to the Energetics of Evolution, *Proceedings of the National Academy of Sciences* 8 (6): 147–151.
4. Schrödinger, E. (1944). *What is Life? The Physical Aspect of the Living Cell*. Cambridge: Cambridge University Press.
5. Heisenberg, W. (1958). *Physics and Philosophy: The Revolution in Modern Science*. New York: Harper & Brothers Publishers.
6. Morowitz, H. (1979). *Energy Flow in Biology*. Woodbridge: Conn.: Ox Bow Press.
7. Chaisson, E. J. (2001). *Cosmic Evolution: The Rise of Complexity in Nature*. Cambridge, MA: Harvard University Press.
8. Morowitz, H., and Smith, E. (2007). Energy flow and the organization of life. *Complexity*. 13, 51–59.
9. Smil, V. (2008). *Energy in Nature and Society: General Energetics of Complex Systems*. Cambridge, MA: MIT Press.
10. Based on data published by Gapminder, HYDE (2016) and United Nations Population Division (2019). in.
11. Based on Vaclav Smil, 2017. *Energy Transitions: Global and National Perspectives*. & BP Statistical Review of World Energy. in.
12. *International Energy Outlook*, U.S. Energy Information Administration, 2019. <https://www.eia.gov/outlooks/ieo/pdf/ieo2019.pdf>(accessed September 15, 2020). in.
13. *Renewable Capacity Statistics 2019*. ISBN: 978-92-9260-123-2. <https://www.irena.org/publications/2019/Mar/Renewable-Capacity-Statistics-2019>. in.
14. Hirsch, R. L., Bezdek, R. & Wendling, R. *Peaking of World Oil Production: Impacts, Mitigation, & Risk Management* (US Department of Energy, 2005). in.
15. Murray, J. & King, D. Oil's tipping point has passed. *Nature* 481, 433–435 (2012).
16. Fleetwood, S. Do labour supply and demand curves exist? *Camb. J. Econ.* 38, 1087–1113 (2014).
17. Butler, J. and Montzka, S. (2019). The NOAA Annual Greenhouse Gas Index (AGGI). Earth System Research Laboratory, Global Monitoring Division Website. Accessed August 14, 2020. in.
18. Bolin, B, and Doos, B R. Greenhouse effect. United States: N. p., 1989. Web.
19. A.D. Barnosky, et al., Approaching a state shift in Earth's biosphere. *Nature*, 2012 486 (7401) 52-58. <https://www.nature.com/articles/nature11018>.
20. Lüthi, D. et al. High-resolution carbon dioxide concentration record 650,000–800,000 years before present. *Nature* 453, 379–382 (2008).
21. Yeung, L. Y. et al. Isotopic constraint on the twentieth-century increase in tropospheric ozone. *Nature* 570, 224–227 (2019).
22. Yan, Y. et al. Two-million-year-old snapshots of atmospheric gases from Antarctic ice. *Nature* 574, 663–666 (2019).
23. Bereiter, B., Shackleton, S., Baggenstos, D., Kawamura, K. & Severinghaus, J. Mean global ocean temperatures during the last glacial transition. *Nature* 553, 39–44 (2018).
24. Brook, E. J. & Buizert, C. Antarctic and global climate history viewed from ice cores. *Nature* 558, 200–208 (2018).

25. Riahi, K. The Shared Socioeconomic Pathways and their energy, land use, and greenhouse gas emissions implications: An overview. 16.
26. Sutter, John D.; Berlinger, Joshua (12 December 2015). 'Final draft of climate deal formally accepted in Paris'. CNN. Cable News Network, Turner Broadcasting System, Inc. Archived from the original on 12 December 2015. Retrieved 12 December 2015. in.
27. 'Framework Convention on Climate Change'. United Nations FCCC Int. United Nations. 12 December 2015. Archived from the original on 12 December 2015. <https://unfccc.int/resource/docs/2015/cop21/eng/l09.pdf>. in.
28. World Energy Outlook 2020. ISBN PDF: 978-92-64-44923-7.
29. Renewables Information: Overview. Comprehensive historical review and current market trends in renewable energy. Statistics report — July 2020. <https://www.iea.org/reports/renewables-information-overview>.
30. REN21. 2014. Renewables 2014 Global Status Report (Paris: REN21 Secretariat). in.
31. Reja Amaty et al. The future of solar energy. An interdisciplinary MIT study.
32. Hsu, D. D. et al. Life Cycle Greenhouse Gas Emissions of Crystalline Silicon Photovoltaic Electricity Generation: Systematic Review and Harmonization. *J. Ind. Ecol.* 16, S122–S135 (2012).
33. Khattak, Y. H. et al. Effect of CZTSe BSF and minority carrier life time on the efficiency enhancement of CZTS kesterite solar cell. *Curr. Appl. Phys.* 18, 633–641 (2018).
34. Best Research-Cell Efficiencies. National Renewable Energy Laboratory (NREL), National Center for Photovoltaics (rev. 22-09-2020). <https://www.nrel.gov/pv/assets/pdfs/best-research-cell-efficiencies.20200925.pdf>.
35. Green, M. A. Third generation photovoltaics: Ultra-high conversion efficiency at low cost. *Prog. Photovolt. Res. Appl.* 9, 123–135 (2001).
36. AFRL Incorporates Solar Cell Technology into Small Unmanned, <https://www.suasnews.com/2012/11/afri-incorporates-solar-cell-technology-into-small-unmanned-aircraft-systems/> (accessed: November 2017).
37. "Communication from the Commission to the European Parliament, the Council, the European Economic and Social Committee and the Committee of the Regions on the 2017 list of Critical Raw Materials for the EU," <http://eur-lex.europa.eu/legal-content/EN/ALL/?uri=COM:2017:0490:FIN> (accessed: July 2018).
38. Fthenakis, V. Sustainability of photovoltaics: The case for thin-film solar cells. *Renew. Sustain. Energy Rev.* 13, 2746–2750 (2009).
39. Zuser, A. & Rechberger, H. Considerations of resource availability in technology development strategies: The case study of photovoltaics. *Resour. Conserv. Recycl.* 56, 56–65 (2011).
40. Wadia, C., Alivisatos, A. P. & Kammen, D. M. Materials Availability Expands the Opportunity for Large-Scale Photovoltaics Deployment. *Environ. Sci. Technol.* 43, 2072–2077 (2009).

Science walks forward on two feet, namely theory and experiment,

...**B**ut continuous progress is only made by the use of both.

-Robert **A. Millikan**

Chapter II

Kesterite: State of the Art and Thesis Objectives

Chapter II presents a brief introduction to kesterite as a complex structured material. Hence, by debunking the most relevant defects in an extensive and critical literature review; thus, the identification of the open circuit voltage (V_{OC}) deficit, therefore the corresponding technological resolute discussion is provided.

Thus, several anionic and cationic graded bandgap profiling strategies are explored and advertised as this **Thesis objectives** as a plausible strategy to overcome the actual power energy conversion efficiency limitations for kesterite based thin film solar cells.

2.1 Kesterite: Main Properties of a Complex Material

In Nature, kesterite appears as a sulfide mineral with a chemical formula $Cu_2(Zn,Fe)SnS_4$. The synthetic forms of kesterite are usually abbreviated as CZTS (Cu_2ZnSnS_4), CZTSe ($Cu_2ZnSnSe_4$), CZTSSe, CZTGSSe, and so on. Kesterite is a greenish-black textbook-folded shaped mineral; it was first plucked in 1958 from the Ynnakh (Ыннах), also known as Mother Mountain in Russia.^{1,2}

Moreover, combinations of rare kesterite (Figure 2.1) species with mushistonite (a Cu-Zn-Fe-Sn hydroxide) varieties have been found in the tungsten (W) mines on the mountain of Xuebaoding (雪宝顶; lit.: snowy treasure peak), in China by the year 1990.

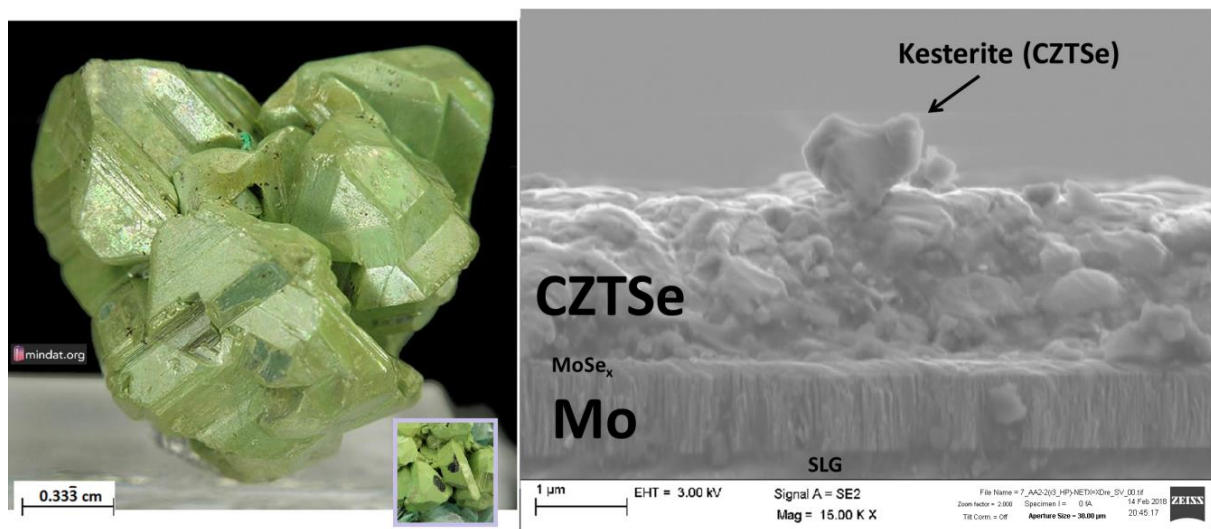


Figure 2.1.- Left: The underlain Natural Kesterite is actually black metallic color (purple inset), in this photography picture, Kesterite is fully coated with an elegant layer of green Mushistonite. Mountain Xuebaoding, Pingwu County, Mianyang Prefecture, Sichuan Province in China.³ **Right:** Scanning Electron Micrograph (SEM) of an artificially synthesized Kesterite (CZTSe) absorber thin film layer deposited over a molybdenum (Mo) coated soda lime glass (SLG) support substrate, IREC laboratories, Sant Adrià de Besòs, Barcelona, España.

Structurally (and in a very roughly way), kesterite shows a tetragonal crystalline structured matrix in which the metallic ions are situated at very specific, yet easy interchangeable locations (Figure 2.1 and Figure 2.2).

Atomic positioning swaps and absence or vacancies, during material's natural or synthetic formation can disrupt up to 30% of the sites in the lattice, generating a preposterous number of crystalline defects.⁴

When utilizing kesterite-like structured materials in pn junctions for thin film PV, defects can ruin the power generating processes by introducing additional levels between the two main energy bands (*VB* and *CB*) of the system.

Some defects can “sit” close to the edges of the bands, which may effectively reduce the gap in between like silt narrowing a river. Others are smack in the mid closer states, providing a way station where charge carriers can recombine.

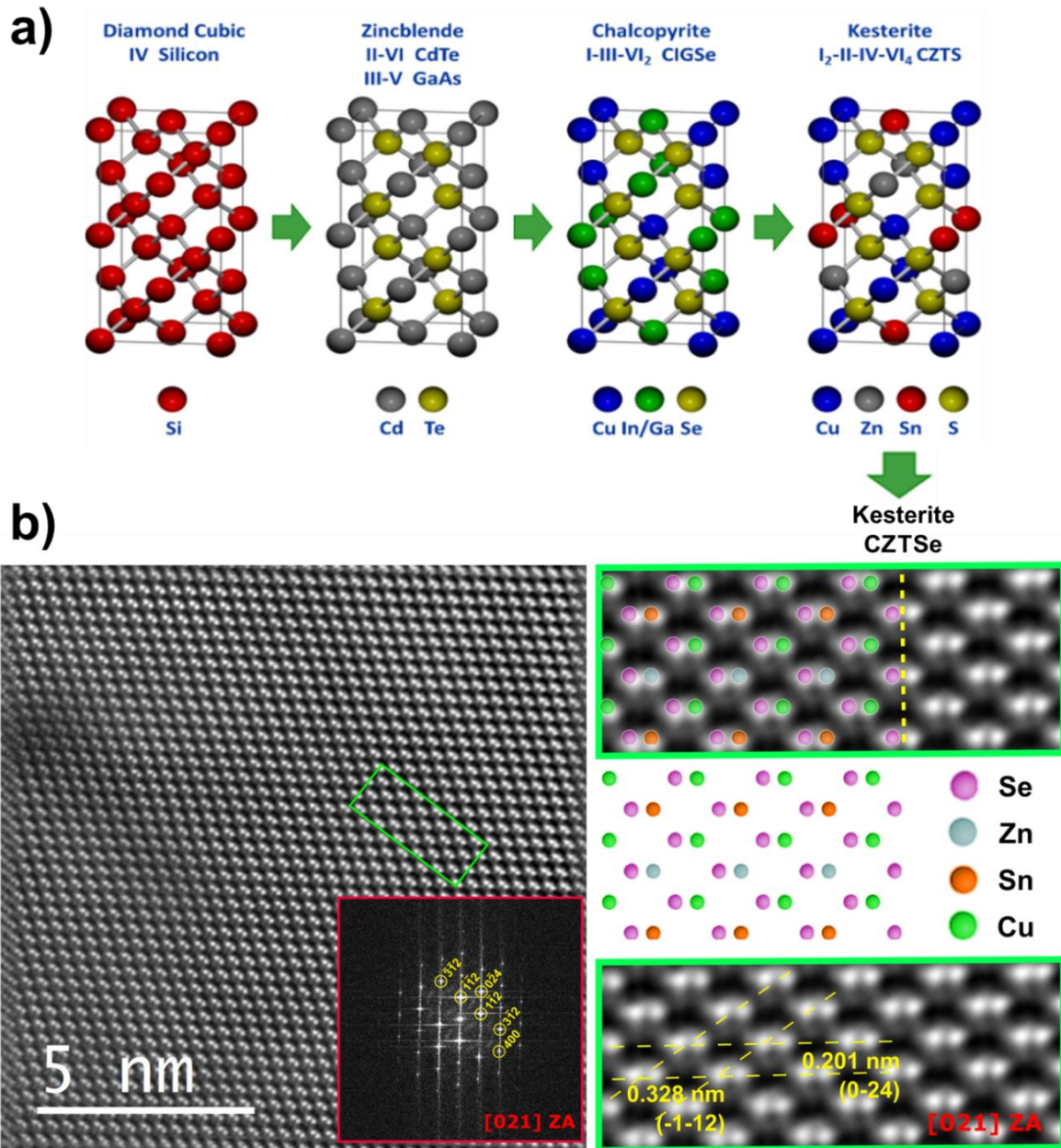


Figure 2.2.- a) Simplified crystal structure of thin film PV semiconductor materials.⁵
b) Left: Inverse Fast Fourier Transformation (FFT) of a High-Angle Angular Dark Field (HAADF) filtered image of a CZTSe grain. Red inset: FFT of the whole area of the image. The area in green is zoomed on the right, where an overlay of the atomic structure and the HAADF image is shown at the top with some of the atomic planes resolved in yellow. In the right-bottom image, the atomic structure of the kesterite in [021] Zone Axis (ZA) is also displayed.⁶

For chalcopyrite structure case, the replacement of the group III element with one Zn(II) atom and one Sn(IV) and/or Ge(IV) atom leads to a quaternary compound which exists in both the kesterite and stannite structure (See Figure 2.2). However, high energy neutron diffraction scattering studies have demonstrated that the former one is more energetically favourable.

The main difference between the two structures is the distribution of the Cu-Zn and Cu-Sn atoms in the crystallographic z-planes. In the stannite structure, some planes alternate the position of Zn-Sn atoms, while the rest of the z-planes remain electrostatically occupied by Cu atoms.

Conversely, for the kesterite structure case, the alternation in z-planes is between Cu-Sn atoms, while planes $z = \frac{1}{4}$ and $\frac{3}{4}$ alternate between Cu-Zn atoms in 2c and 2d positions in Figure 2.3.

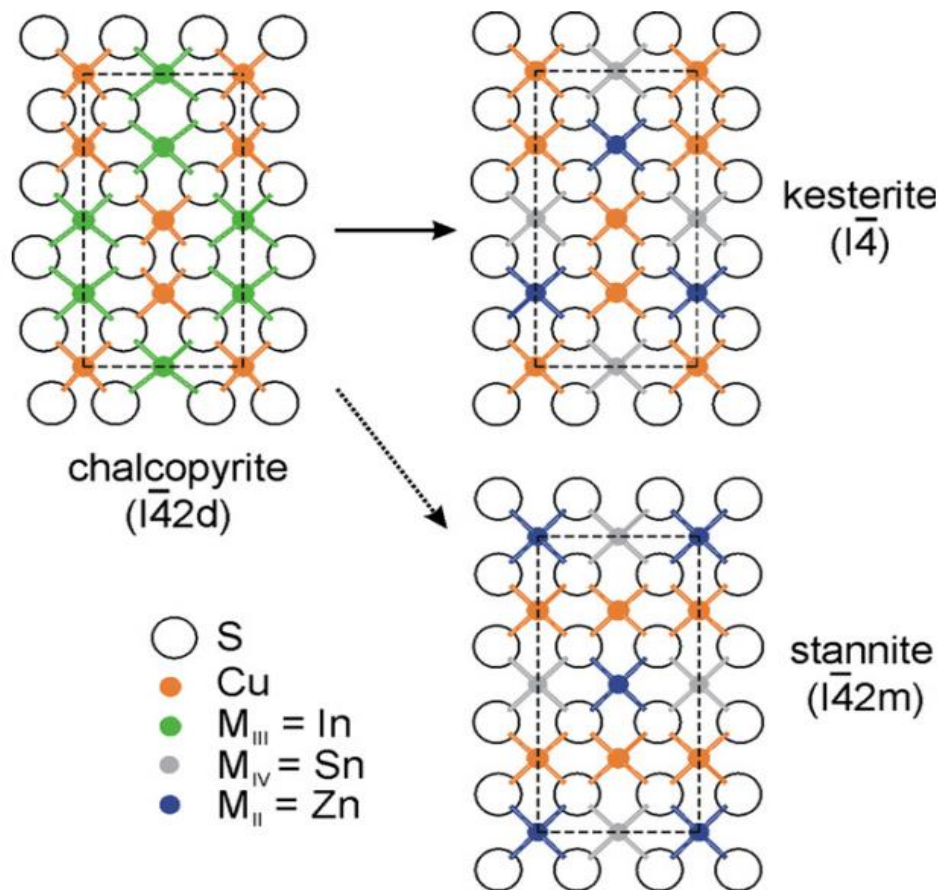


Figure 2.3.- Schematic representation of the chalcopyrite structure, and kesterite and stannite structures. The unit cell boundaries are denoted with dashed lines and is also denoted the space group for each structural type.⁹

These positions can be practically indistinguishably occupied because of the similar size of Cu and Zn cations leading to the so-called Cu/Zn order-disorder the sublattice.^{7,8} It follows that the sublattice disorder indicates the inevitable presence of Cu_{Zn} and Zn_{Cu} point defects, and therefore lattice disorder leads to band edge fluctuations.

Alternatively, for relative comparisons among samples, it is possible to assess the amount of disorder by measuring the ratio $c/2a$, where 'c' and 'a' are the lattice parameter of the kesterite crystal structure.

The degree of crystalline disorder in kesterite mostly depends on the $\text{Cu}/(\text{Zn}+\text{Sn})$ and Zn/Sn metal ratios content and the post- and during- synthesis thermal records of the absorber layer.¹⁰⁻¹²

Recently, it has been demonstrated the existence of single crystal kesterite for several different types of off-stoichiometric compositions (around 12), and identified the relative intrinsic point defects through neutron diffraction studies.¹²

On the other hand, it is experimentally well known amongst kesterite thin film PV-community that the highest device performance is usually obtained for Cu-poor and Zn-rich compositions compared to the stoichiometric compound ($\text{Cu}/(\text{Zn}+\text{Sn}) = 0.8$ and $\text{Zn}/\text{Sn} = 1.2$).¹³

For this particular metallic ratios combination, pure single crystal kesterite could be synthesized.

However, the better performance of kesterite solar cells with such composition is mostly due to the type of defects and detrimental secondary phases that could be formed during compound formation and/or synthesis process.

2.2 Defects

For Cu-poor Zn-rich composition, Cu is substituted in the kesterite lattice by the formation of Cu vacancies (V_{Cu}) and Zn_{Cu} antisite defects. Additionally, a Zn enriched composition would not favour the formation of the Cu_2SnSe_3 phase; at the same time that the $[2Cu_{Zn}+Sn_{Zn}]$ defect clusters are avoided.

On the other hand, a low Cu content allows the decrement of the Cu-Zn order/disorder, bulk defects, and guarantee the p-type semiconductor conductivity.¹⁴ The main reason for the enhanced solar cell performance of Cu-poor and Zn-rich kesterite absorber may be due the intrinsic defect structure of the material. In this sense, a detailed analysis of the $Cu_2X-ZnX-SnX_2$ pseudo-ternary system (where X could be S or Se) was performed by Olekseyuk et. al.¹⁵, in which it is presented a phase diagram for this system at 400 °C (See Figure 2.4).

It is important to note that Cu_2ZnSnX_4 as a single phase is present only within a rather narrow range of compositions. In all other regions of the phase diagram there are up to two additional secondary phases present, always alongside $CZTX_4$.

As a result, regardless the method used for kesterite thin film deposition, one of the greatest challenges of this technology is to obtain single-phase kesterite layers. However, the type of secondary phases strongly depends on precursor concentrations as presented in Figure 2.4.

The complexity of kesterite-structured materials implies that even in the most favourable cases, intrinsic detrimental defects are expected due to compositional or processing issues.

Therefore, these defects could be compensated, for example, through an adequate design of extrinsic doping or by grading the material bandgap (E_G), but it remains a challenging task considering that very little is known about deep defects in these materials.¹⁶

Table 2.1.- Summary of the most probable defects expected in kesterite, depending on the compositional regime and the synthesis conditions. Deep defects are bold marked due to their potential to act as recombination centers, significantly affecting the V_{OC} of the solar cell devices.¹⁶

Condition	Defects	Comments
Cu-poor Zn-rich Sn-stoichiometric	V_{Cu} and Zn_{Cu}	Both defects are predicted as shallow centers. (PV most benign and recommended composition)
Cu-poor Zn-rich Sn-poor	Zn_{Cu} and Zn_{Sn}	Zn_{Sn} as a relatively deep defect
Cu-poor Zn-stoichiometric Sn-stoichiometric	Zn_{Cu} , Sn_{Cu} , and V_{Cu}	Sn_{Cu} as a deep defect. (Not recommended composition for PV applications)
Zn-poor condition	Sn_{Zn} and Sn^{+2}	Sn_{Zn} and reduced Sn species can be very detrimental. Formation possible due to intrinsic nature of kesterite
Low chalcogen availability	V_X and Sn^{+3}	Depending on chalcogen availability, there is a possibility to form chalcogenide vacancies, which although being benign, can induce the formation of Sn reduced species that introduce deep defects
Sn-loss	V_{Sn} , Zn_{Sn} , and Cu_{Sn}	Due to the intrinsic volatility of Sn-chalcogenides, during slow cool-down processes Sn can be lost at least at the very surface, forming V_{Sn} , Zn_{Sn} , and Cu_{Sn} deep defects

Taking into account that secondary phase electrical and optical properties change from one type to another and are different from the host kesterite semiconductor one, an important impact on kesterite solar cell performance should be expected.

Several studies on this subject have been reported in literature using different calculation methods: the common point is that, single phase CZTS and CZTSe exist only in a very small region of the phase diagram.¹⁵

Figure 2.4 b) shows, in the case of pure CZTS, a slice (in black) in a given Cu-rich plane, for which the CZTS is stable: outside this area there will be the simultaneous existence of CZTS with one of the other phases like ZnS, CuS, SnS, Cu_2SnS_3 (CTS)¹⁷; which is also true for pure selenide ZnSe, CuSe, SnSe, Cu_2SnSe_3 (CTSe)¹⁸

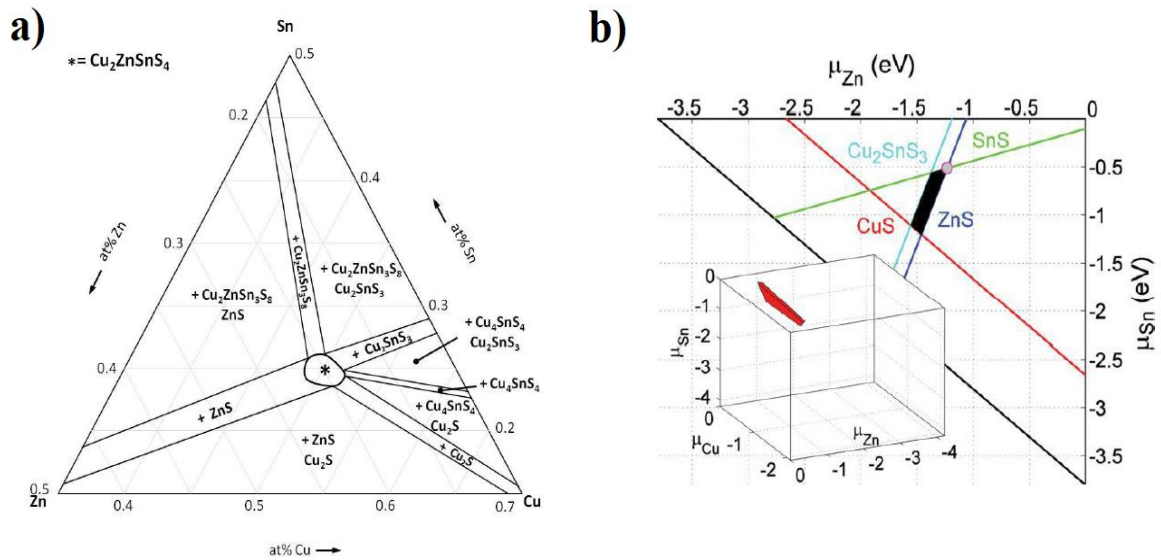


Figure 2.4.- a) Ternary phase diagram taken from reference,¹⁵ showing the expected secondary phases at 400 °C. b) Calculated chemical-potential stability diagram of pure CZTS.¹⁹

Since the best performing CZTS_{Se} solar cells are made with an absorber which is Zn-rich, the control over the Zn-content in CZTS_{Se} alloys is very important: Zn-poor samples lead to CT(S,Se) formation, instead Zn-rich samples lead to Zn(S,Se)²⁰, fact which is congruent with the narrow line in the Zn-region in Figure 2.4.

From Figure 2.5, it could be noted that intrinsic defects with the lowest formation energy are Zn_{Sn} and V_{Cu} , which resemble p-type conductivity. Moreover, the population of isolated defects with deep donor levels is diminished, such as Sn_{Zn}^{2+} and acts as a recombination centre.

In this way, the inclusion of Ge is also suggested to minimize the Sn^{+2} formation of deep defects due to associated with high open-circuit voltage (V_{OC}) deficit values.

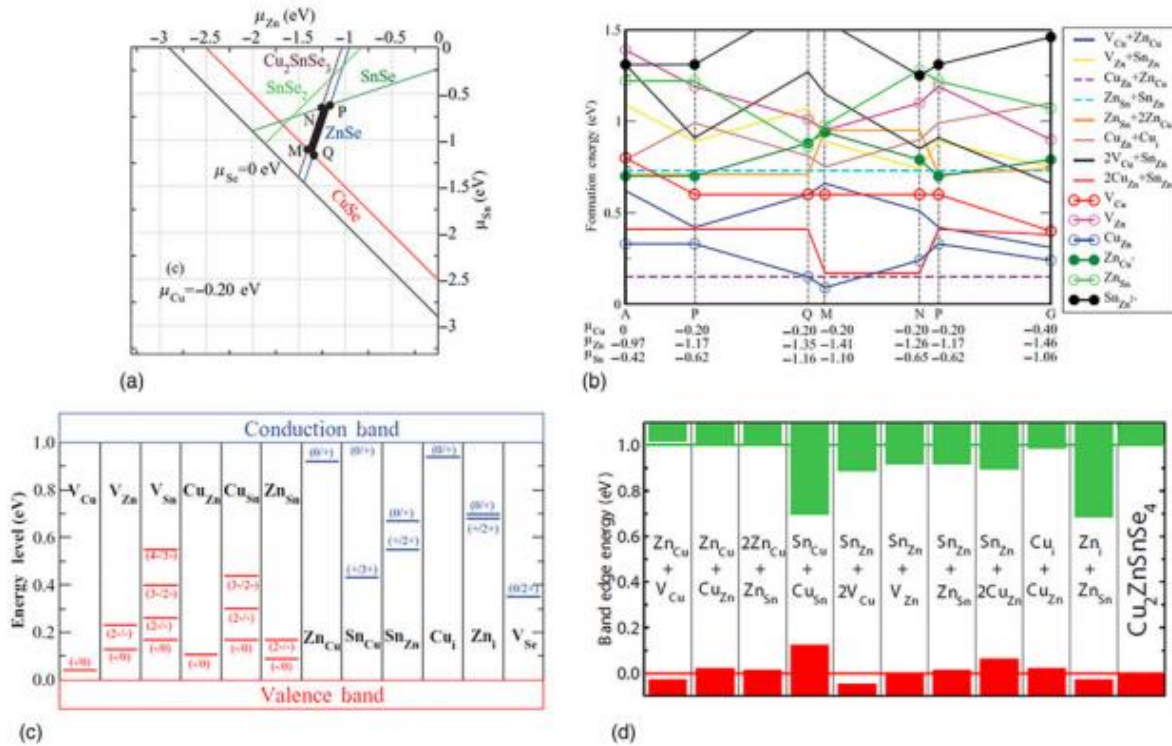


Figure 2.5.- (a) The calculated stable region of the phase diagram for CZTSe as a function of zinc and tin chemical potentials (fixed copper chemical potential). (b) The calculated formation energies of various point defects and defect complexes in CZTSe as a function of chemical potential (specified in (a), p-type conditions were assumed). (c) The ionization energies of various point defects in the band gap of CZTSe, where red lines represent acceptors, blue lines represent donors, and the initial and final charge states are indicated in parentheses. (d) Calculated band gap shifts induced by various defect clusters in CZTSe, where red and green lines indicate the valence and conduction bands, respectively.²¹

Meanwhile, the partial substitution of Sn by Ge tends to accumulate toward bottom absorber and forms back band gradient due to the natural up-diffusion of Cu, Zn and Sn atomic species during the selenization process.²² In practice it was believed that both S/Se and Ge/Sn engineering could only achieve a single gradient within kesterite devices.²³ However, the here presented Thesis findings demonstrate its actual and real feasibility.

On account of to its structural similarities with chalcopyrite (CIGSSe)²⁴, kesterite-structured materials (See Figure 2.2) exhibit remarkable properties as an absorber in next generation of emerging thin film PV technologies, which are basically based on the following requirements:

*Earth abundant, non-toxic (Eco-friendly) in the form of low cost materials. ²⁵⁻²⁷

*High weatherability (stability against environmental effects). ^{28,29}

*Adequate material optoelectronic properties:

-P-type semiconductor (n-type conductivity also achievable by doping). ³⁰⁻³³

-Tunable band offsets and profiles with direct bandgap around 1 to 1.5 eV, leading to high absorption coefficient ($>10^4 \text{ cm}^{-1}$); hence small absorption thickness requirements for the terrestrial incident solar radiation applications. ^{30,34-38}

-High dielectric constant to generate excitation with weak binding energy, thus readily generating free charge carriers. ^{39,40}

-Sufficiently large charge carrier mobility and diffusion lengths in order to collect all the photogenerated electron-hole pairs. ^{30,41}

*Suitable “in-device” optoelectronic properties:

-Easy-building of homo- and/or hetero-junctions with the highest contact difference of potential to maximize the open circuit voltage (V_{OC}). ^{39,42}

-Ohmic metallic contact reliability. ⁴³

Historically, kesterite thin films were first synthesized and properly studied in 1988 as an alternative candidate to CuInSe_2 solar cells. ⁴⁴ To such an extent that the first kesterite-based solar cells (showing a power conversion efficiency of a barely 0.66%) were fabricated in the CIGS-like configuration: SLG/Mo/CZTS/CdS/ZnO/Al by Katagiri et al. by 1997. ⁴⁵ This group rapidly optimized and increased by a whole order of magnitude the efficiency of their devices to around 6.8% in 2008 by a sulfurization annealing method of metallic compound RF sputtered layers. ⁴⁶

This resulted in sufficient technological progress with this material to arouse the interest of large technology and semiconductor developer companies such as IBM (International Business Machines Corporation). By that time, this American multinational technology and consulting company was researching (amongst many other things) on solution deposition processes as a possible route to reduce the cost of high vacuum-based CIGS manufacturing.

In 2010, David Mitzi et al. applied a novel CIGS solution-based process to CZTSSe material and achieved a remarkable 9.6% efficiency device.⁴⁷ Further optimization of a hydrazine process led IBM in 2013 to the current certified record efficiency of 12.6%.^{48–50} By this means, the progress made in the past years established kesterite as the most relevant and promising CRM-free fully inorganic thin film candidate for large scale PV deployment.^{49,51}

Most recently, in 2019, several uncertified and yet unpublished results of a 13.8% efficiency kesterite solar cell from a South Korean group (DGIST) have been presented during well-known by the community congresses and PV meetings.^{52,53}

Nevertheless, as the efficiency of kesterite solar cells has plateaued around 12–13% for as much as 7 years, and since there is a required threshold of 20% efficiency in order to become commercially interesting; a readily frustration in the kesterite community has grown.

However, by reviewing the historical evolution of NREL best research-cell efficiency tables (Figure 1.7), it is possible to note that such a temporary stagnation is not rare at all at the early stages of development of well-known PV technologies (CdTe⁵⁴ and CIGS⁵⁵). Inevitably, these periods are prone to legitimate questioning about the ultimate potential of a given material under scrutiny.⁵⁶

Hence, a natural questioning arises:

What is actually limiting the efficiency of kesterite solar cells?

Aiming to answer this question, several review articles have been published trying to explain the main efficiency limitations of kesterite solar cells.^{27,42,57,58} On one side, authors mostly agree that since the voltage currently stands at a dismal 60% of its theoretical maximum value, it represents a tremendous V_{OC} deficit. On the other hand, around 80-85% of the maximum theoretical Shockley–Queisser limit for the J_{SC} and FF values has been achieved.^{48,59,60} In this sense, these values feature the role of secondary hurdles to boost in kesterite solar cells. Despite the improvements achieved so far in several of the optoelectronic parameters, the V_{OC} deficit is the fine and key point to achieve higher energy conversion efficiency in kesterite devices.^{48,61,62}

2.3 V_{OC} deficit in Kesterite Thin Film Solar Cells

Ideally, the open circuit voltage (V_{OC}) of the solar cell must be equal to the bandgap of the active (absorber) material which means high voltage deficit reflects much lower V_{OC} than the bandgap. In this sense, extensive literature research has revealed following features influencing V_{OC} in kesterite based solar cells: ⁶³

1. Compositional/Structural disorder: The presence of secondary phases like $ZnS(e)$, $Cu_2S(e)$, $Cu_2SnS(e)_3$, $SnS(e)_2$, etc. along with pure CZTSSe phase during growth process which are detrimental for the device performance. ^{32,64,65}
2. Order-disorder phenomena: The potential impact of the Cu/Zn disorder. ⁵⁶
3. Point defects: Antisite defects (Cu_{Zn} , Cu_{Sn} , Sn_{Zn} , etc.), vacancies (V_{Zn} , V_{Sn} , V_{Cu} , etc.), defect complexes ($V_{Cu} + Zn_{Cu}$, $V_{Zn} + Sn_{Zn}$, $Zn_{Sn} + 2Zn_{Cu}$, etc.) along with defects states associated with secondary phases leads to band tailing in the material causing non-radiative recombination. ^{14,39,66,67}
4. Band alignment/tailing: The undesirable energy level alignment at the charge separating interfaces, especially at CZTSSe/CdS heterojunctions contributes in trap-assisted recombination, moreover inappropriate interface chemistry leads to high density of interface defects. This V_{OC} deficit arises due to interface recombination and/or band tailing due to electrostatic fluctuations, which eventually results in lower minority carrier lifetime. ^{63,66,68,69}
5. Back contact: The formation of thick $MoSe_2$ at the rear interface hindering the flow of majority charge carriers (holes) from the kesterite absorber thin film towards the back interface. ^{70,71}
6. Deep level defects: Last, but not least, the Sn_{Zn} deep-level donor defect forms a recombination center, which also increases the V_{OC} deficit. The incorporation of Ge has been recently reported to reduce the formation of the Sn_{Zn} defect. Additionally, the presence of Ge inhibits the formation of the oxidation state Sn^{+2} of Sn, which occupies the Zn site, therefore improving the crystal quality. ⁷²⁻⁷⁴

Despite it is possible to enlist several of the most well-known limitations; nowadays, there is a lot of debate about the origins of high V_{OC} deficit since it usually stems from either bulk or surface charge carrier transport limitations.^{32,38,56}

The prime suspects are the natural defects within the kesterite film bulk, along with the low formation energies of abundant and largely distributed Cu_{Zn} and Zn_{Cu} antisite points or cluster defects (cationic disordering).^{19,65,75}

The Cu_{Zn} antisite defect induces relatively deep acceptor levels inside the band gap (recombination centers), which can cause Fermi-level pinning when a large concentration of these defects is present. In turn, this deteriorates the device performance by diminishing the short minority carrier lifetimes.^{38,39,57,76–78}

Besides, structural disorder manifests itself as a band tail and deep trap states introduced by the potential fluctuations. Therefore, it would further reduce the effective band gap of the kesterite absorber and thus decrease the V_{OC} of kesterite solar cells, raising the V_{OC} deficit.^{17,24,48,62,79–83}

Noteworthy is to say that these states are found to show the highest potential risk, due to the current difficulty to identify and prevent them, along with the formation of deep “killer defects” within the band gap.^{72,84–86}

On the other hand, and in a very interestingly manner, it has been recently observed that the incorporation of Ge diminishes the formation of the deep-level donor Sn_{Zn} defects that act as recombination centers.^{14,73,74,87}

Figure 2.6 shows the open circuit voltage-deficit values published for several CZTSe, CZTSSe, CZTGSe, and CZTS solar cells. Figure 2.6, it could be observed that the V_{OC} deficit of CZTGSe increased along with its bandgap, indicating that the band tailing caused by compositional disorder may seem increased with the Ge content.

Although the band tailing increases with the Ge content, CZTGSe exhibit a reduced band tailing in comparison with CZTSSe. A possible reason for the reduced band tailing upon Ge incorporation is related to stable growth conditions as a result of cation incorporation into the kesterite structure matrix.^{73,88}

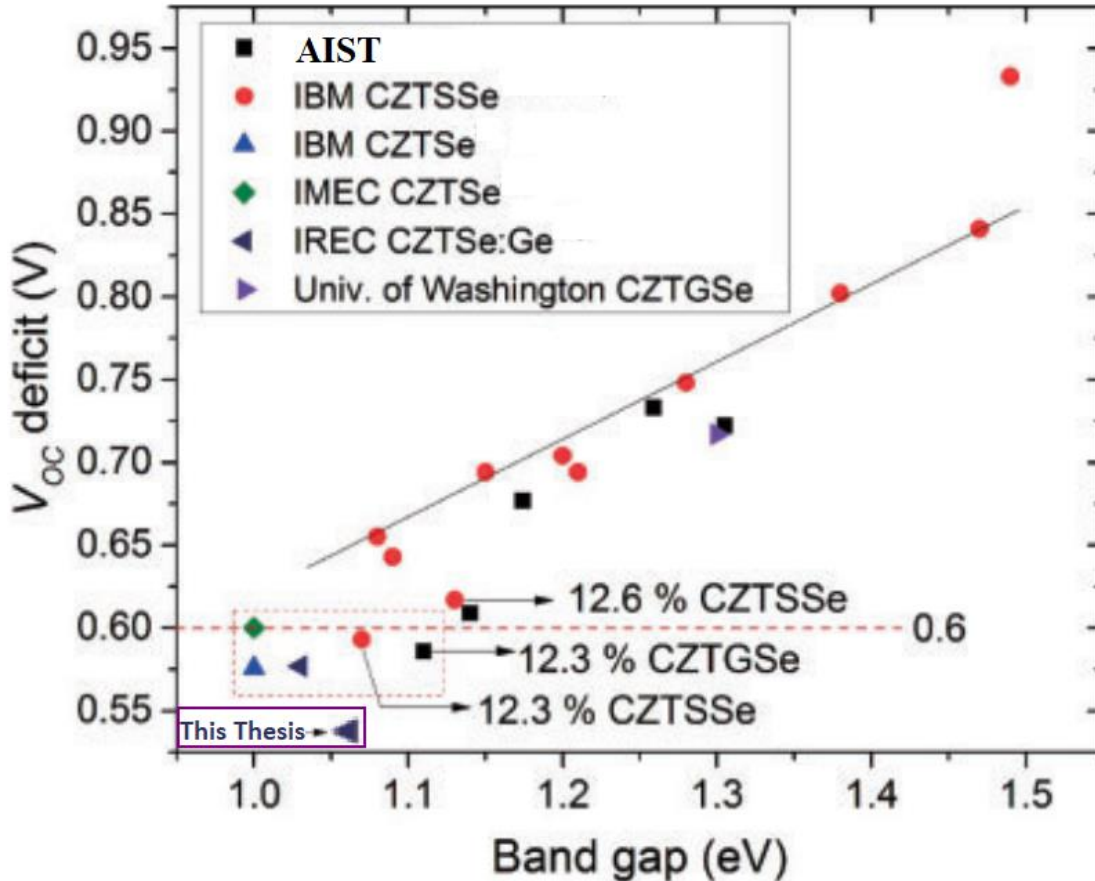


Figure 2.6.- V_{OC} deficit values published for CZTSe, CZTSSe, CZTGSe, and CZTS solar cell devices.⁸⁸

Other beneficial effects of Ge have been reported, including the interaction with Na, which explains the impact of this doping element on the carrier's concentration, the modification of the formation pathways that minimize the risk of Sn loss and secondary phases formation, and the passivation of detrimental grain boundary related recombination.¹⁶

Finally, there exists a general consensus for an optimal composition to high efficiency kesterite devices, an increasing number of studies have identified compositional fluctuations (inhomogeneities) at the micro- and nanoscale levels, a possible culprit for electric field and band gap fluctuations in the material, as well as 'unpassivated' junction interfaces and undesirable conduction band offset (CBO)^{48,89-91}; such observation could partly explain the voltage deficit observed in the material.^{16,76,92-95}

2.4 Possible Technological Solutions of Kesterite Thin Film Solar Cells V_{OC} deficit

A general mapping of the fundamental failures in kesterite solar cells has been drawn by L. Grenet et al.⁹⁶ as shown in Figure 2.7. Additionally, a list of the failure modes specially related to the V_{OC} deficit in kesterite devices is summarized in Table i.2. When statistical data from production lines are not available to quantify a Risk Priority Number (RPN) for each failure mode, they need to be subjectively determined from knowledge and experience of the experts. As this Thesis has been carried out within the framework of the H2020-NMBP-03-2016-720907 European Project STARCELL; it has been requested to both members of the national (IREC, AYESA and WIREC) and international consortium (NREL, UDUKE AIST, MIDS, IMRA, HZB, UU, CEA, EMPA, and ICL) to evaluate the three (FOM) figures of merit (Severity, Occurrence and Non-Detectability) for several failure modes through the participation in a survey. This evaluation has been based on our own samples and characterization/observations derived, and are not extracted from any literature review.⁹⁶

$$RPN = (\text{severity of effect}) \times (\text{likelihood of occurrence}) \times (\text{likelihood of non - detection})$$

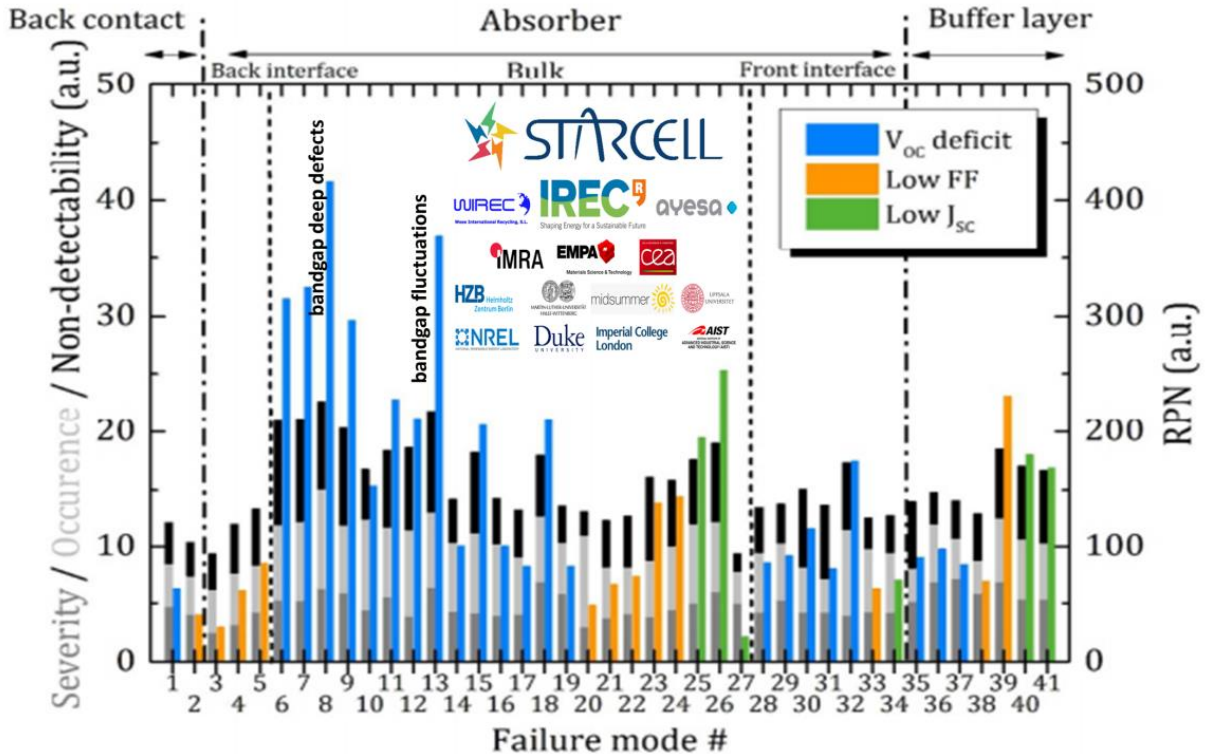


Figure 2.7.- Mean values obtained for each FOM is shown in grey a scale (left). Mean value of the RPN (right) is shown in color bars.⁹⁶ See Table i.1 in Thesis Appendix: Additional and Supporting Information.

From Figure 2.7, it could be noticed that the main of the failure mode on kesterite solar cell technologies stand on the self-absorber material, particularly, and amongst the enlisted FOM's for each failure mode (See Table i.1 in Thesis Appendix: Additional and Supporting Information), the bandgap deep defects and fluctutations are the most critical issues. This way, bandgap grading engeieering emerges as a suitable and plausible technological solution.

2.5 Graded Bandgap in Kesterite

2.5.1 Front Graded Bandgap Through Anion Replacement

In the search for technological solutions in order to reduce the V_{oc} deficit, important insights may be gathered from the evolution of CIGSSe, in which one of the most relevant improvements in this regard are commonly related to the introduction of Ga in the alloy.⁹⁷ Introduction of Ga has been decisive in the development of advanced graded band gap concepts, increasing the band gap at the surface for boosting the open circuit voltage (V_{oc}), as well as at the back region for creating an electron reflector, boosting the short circuit current intensity (I_{sc}) and fill factor (FF).⁹⁸

In the case of this material (CIGSSe), the implementation of complex graded compositional profiles to selectively increase the band gap (E_G) at the surface and back interfaces was proved to be a key point in order to achieve high efficiency devices.^{16,98}

By increasing the $Ga/(In+Ga)$ ⁹⁹ or the $S/(S+Se)$ ¹⁰⁰ ratios towards the interfaces, it is possible to tune the band gap at those regions and, thus, optimize band-alignment, reducing interface recombination, or even creating selective carrier reflectors.^{101,102}

These band gap engineering concepts are nowadays present in every high efficiency CIGSSe solar cell with the compositional gradients being commonly achieved by an increased Ga content at the back and at the front,^{99,103} or an increased Ga content at the back and an increased S content at the front.¹⁰⁰ These strategies have contributed to push the efficiency of CIGS devices above 20%.¹⁰⁴ In fact, CIGS devices with flat band gap profiles rarely exceed ~15% efficiency,¹⁰⁵ i. e., their efficiency is comparable to that of planar band gap kesterite devices (~13%). As a matter of fact and learning from CIGSSe developed technologies, significant improvements are expected by the implementation of bandgap engineering using compositional grading.

This could be achieved by controlling the anionic distribution in $\text{Cu}_2\text{ZnSnS}_4$ ($E_G = 1.5$ eV) and $\text{Cu}_2\text{ZnSnSe}_4$ ($E_G = 1.0$ eV) structural matrices along the absorber material (as this Thesis reports)⁸⁹, or by creating cationic substitutional gradients (e.g. Ge and Sn,^{22,106} as it is tackled in this work, or Cu by Ag),^{107,108} also by regulating a Na doping profile.¹⁰⁹ In fact, this Thesis proposed numerical modeling and simulations suggest that band gap grading could boost the efficiency of CZTSSe-based solar cells towards values greater than 17% as it will be shown in Chapter 4.^{110,111}

In this regard, some attempts of implementing band gap engineering by adjusting the S/(S+Se) compositional ratio along the bulk material have already been reported in the literature. Kato et al.¹¹² implemented a “linearly graded band gap profile” with a low S content at the front and a high S content at the back of the absorbers. In which they have observed the formation of ZnS at the back S-rich region which may lead to an increased series resistance in the devices.

By controlling such ZnS back segregation through the adjustment of the precursor and of the selenization/sulphurization process, they reported a sub-module record efficiency of 11%, opening interesting perspectives for S/(S+Se) grading in kesterite solar cells. Another S/(S+Se) grading approach was reported by Woo et al.¹¹³ This group has prepared CZTS films by multiple spin coating of ethanol slurries and annealed them first under hydrogen sulfide (H_2S) and then under Se atmosphere in a graphite box.

Furthermore, by employing grazing incidence X-ray diffraction (GIXRD), they observed a gradual and quasi linear S/(S+Se) gradient profile, going from an almost Se-pure surface to a very S-rich back interface. However, no influence of the S/(S+Se) ratio on the V_{OC} value was found, and a 7.1% record efficiency device was reported. In another publication, Yang et al.¹¹⁴ reported a 12.3% efficiency front-graded CZTSSe device.

This was achieved by employing SeS_2/Se mixtures during the kesterite annealing process, which resulted in a S-rich surface with a S/(S+Se) ratio of 0.20 that decreased down to 0.08 in the bulk. This gradient was confined to the first 300 nm of the absorber and an improvement (i.e. reduction) in the V_{OC} deficit was demonstrated. Similarly, Hwang et al.¹¹⁵ developed a single-step sulpho-selenization process for front bandgap grading.

For this purpose, Se/Cu-ZnSe-Sn precursor materials were co-evaporated and annealed in a mixed S-containing atmosphere (Ar 90%, H₂S 10%) using a rapid thermal process (RTP) specialized furnace. They have observed a gradual decrease of the S content from the surface (E_G of 1.161 eV) towards the back/rear (E_G of 1.029 eV) along the first micron of the absorber thickness. This S/(S+Se) grading led to a +80 mV V_{OC} enhancement and to an energy conversion efficiency boost from 7.2% up to 10.3%. In a slightly different approach, Cai et al.¹¹⁶ introduced a graded band gap on CZTSSe absorbers synthesized from sputtered precursors by flowing H₂S/Ar gas during the cooling down process. They have observed a relatively sharp S gradient in the first 50 nm of the absorber, with the S/(S+Se) ratio decreasing from 0.15 to 0.10. As a result, they reported improvements in the V_{OC} and the FF of the CZTSSe devices with a maximum efficiency of 7.1%.

Neuwirth et al.¹¹⁷ investigated the feasibility of inducing a graded band gap in an already pre-synthesized Se-rich CZTSSe absorber by employing an additional annealing step with sulphur at different temperatures and times. With this approach, they observed a compositional gradient with most of the effects occurring at the back region, although in some cases there is no correlation of the S/(S+Se) profiles with the performance of the devices. Furthermore, they noticed an increase in the V_{OC} but not in the efficiency. Therefore it is not clear if the higher voltage was arising from the grading profile or just from the increased overall S content in the absorber. As a summary, Table 2.2 gathers together the most relevant information extracted from these selected papers. From all these studies, it is clear that front S/(S+Se) grading is a very interesting approach for band gap engineering in kesterite-based solar cells.

In particular, a sharp S gradient at the front interface appears as the most promising option to enhance the V_{OC} and FF of the devices without deteriorating the J_{SC} values.^{35,114,116,118}

Nevertheless, the creation of a very sharp S/(S+Se) compositional gradient at the very top surface of the CZTSSe (it should be ideally confined to the space charge region, i.e., to the first few hundred of nanometers absorber) is revealed as very complex in contrast to the relatively easily achievable Ga/In gradients in CIGSSe.^{115,119–121}

A simple thermodynamic comparison between the kesterite and CIGSSe systems illustrates this difference. Table 2.3 summarizes the enthalpy of formation of Cu₂ZnSnS₄, Cu₂ZnSnSe₄, CuInS₂, CuInSe₂, and CuGaSe₂.^{122–125}

For CIGSSe, the large difference between the enthalpy of formation of CuInSe_2 and CuGaSe_2 ($112 \text{ kJ}\cdot\text{mol}^{-1}$) indicates that phase separation in the $\text{CuIn}_{1-x}\text{Ga}_x\text{Se}_2$ system could be rather easy to achieve. In fact, CuGaSe_2 tends to segregate naturally from the CIGSe matrix and accumulate at the back contact in sequential fabrication processes.^{126,127}

On the contrary, the low difference between the enthalpy of formation of CuInSe_2 and CuInS_2 ($18 \text{ kJ}\cdot\text{mol}^{-1}$) implies that the separation of sulphur and selenium phases becomes much more difficult (although possible employing surface selective alloying).¹⁰⁰

Finally, in the case of kesterite, a challenging implementation of compositional S/(S+Se) grading profiles (i.e. phase separation) can be anticipated from the small predicted differences in the enthalpy of formation of $\text{Cu}_2\text{ZnSnS}_4$ and $\text{Cu}_2\text{ZnSnSe}_4$ of $\sim 24.7 \text{ kJ}\cdot\text{mol}^{-1}$.

In view of the importance that band gap engineering may have for the development of the kesterite photovoltaic technology, this Thesis¹²⁸ presents a methodology to implement S/(S+Se) gradient profiles in CZTSSe absorbers based in an in-situ sulphurization-after-selenization process.

Therefore in this part of Thesis work, it has been experimentally corroborated the predicted easy mix between the sulfide and selenide kesterite compounds, showing that the only way to achieve sharp front gradient profiles is by incorporating sulphur in out-of-equilibrium conditions using highly reactive sulphur sources.

As a result, it is reported a successful generation of sharp S/(S+Se) compositional gradients at the surface of the CZTSSe absorbers novel and disruptive methodology.

Working devices are fabricated with such graded absorbers and a clear improvement of the V_{OC} deficit of the corresponding solar cell devices is observed reaching a maximum efficiency of 9.2%.

Table 2.2.- Summary of relevant information of selected articles reporting (anionic) S/(S+Se) graded band gap in kesterite thin film PV. ¹²⁸

Ref.	Methodology	Gradient description	Impact on solar cell devices
Kato, et al. ¹²⁹	Annealing of metallic stacks (no further details available)	Back grading. Higher S content at the back (rear) contact (non-quantified)	Sub-module (14 cm ²). Slight improvement on V _{OC} (+14 mV) and PCE (+0.2%)
Woo, et al. ¹³⁰	Slurries spin coating. Annealing: 1) Under H ₂ S/N ₂ atmosphere, 530 °C, 30 min; 2) Under Se, graphite box, 500 °C, 20 min	Back grading. Se-rich front (E _G = 1.04 eV) and S-rich back (E _G = 1.40 eV). Quasi linear gradient	J _{SC} (+5.69 mA/cm ²) with respect to the S-pure absorber
Yang, et al. ¹³¹	Sputtering and RTP annealing: 2-step process using SeS ₂ /Se mixtures (1st step: 300 °C, 25 min; 2nd step: 510 °C, 18 min 20 s)	Front grading, from S/(S+Se) ~ 0.22 at the surface, and ~ 0.08 in the bulk (at 300 nm approximately from the surface)	Large improvement of V _{OC} (521 mV), PCE up to 12.3%
Hwang, et al. ¹³²	Co-evaporation of Cu/ZnSe/Sn precursor. RTP annealing under Ar (90%) + H ₂ S (10%) atmosphere (500 °C, 3 min)	Front grading, with E _G = 1.161 eV at the front and 1.029 eV at the bulk (900 nm from the surface)	Large improvement in V _{OC} (+81 mV), in FF (+12.7%) and PCE (+3.1%)
Cai, et al. ¹³³	Sputtering of ZnS/SnS ₂ /Cu precursor. Selenization with Se in a graphite box (550 °C, 60 min). H ₂ S introduced during the cooling down process	Front grading, with S/(S+Se) ~ 0.15 at the surface and ~ 0.10 at 50 nm from the surface	Large improvement in V _{OC} (+82 mV), in FF (+7.5%) and PCE (+2.65%)
Neuwirth et al. ¹³⁴	Doctor blade dimethylsulphoxide solutions and further annealing in a Se atmosphere (540 °C, 10 min). Final sulphurization at different temperatures (470-600 °C)	Back grading, with markedly more sulphur at the back (no quantification available)	V _{OC} improvement (~ +200 mV), but efficiency deterioration (~ -4%)

Table 2.3.- Enthalpy of formation (H_F) of relevant kesterite and chalcopyrite compounds. ¹²⁸

Material	Enthalpy of Formation H _F (kJ.mol ⁻¹)	Comments ^[Reference]
CuInSe ₂	-204	Experimental ^{124,135,136}
CuGaSe ₂	-316	Experimental ^{124,135}
CuInS ₂	-222	Experimental ¹³⁶
Cu ₂ ZnSnSe ₄	-312.2	Theoretical (First principles calculations) ¹³⁷
Cu ₂ ZnSnS ₄	-336.9	Theoretical (First principles calculations) ¹³⁷

In this fashion, the majority of the work so far reported in the literature relies on the implementation of back and/or front anionic gradients using S and Se^{111,128,138,139}, since anionic substitution has its main influence on the position of the VB¹⁴⁰. Several groups have reported proof-of-concept devices with anionic (S-Se) front band gap grading leading to efficiencies up to 12.3%^{114,118,120,128}. It is also noteworthy to mention that the current kesterite record efficiency (12.6%) was obtained using $\text{Cu}_2\text{ZnSn}(\text{S}_x\text{Se}_{1-x})_4$ solid state solution giving proof of the importance of combining S and Se anions.^{48,87,141}

2.5.2 Rear Graded Bandgap Through Cationic Substitution

First-principle calculations demonstrate that the conduction band minimum of CZTSSe is related to the antibonding Sn s and anion p hybrid orbitals, while the valence band maximum is mainly influenced by hybridization of Cu d and anion p orbitals.^{107,142,143} Hence, substitution of Sn (IV) by Ge (IV), and Cu (I) by Ag (I) can be used to adjust the conduction band and valence band edges, respectively.^{144–147} As follows, cationic substitution allows for a specific tuning of the conduction band, creating an electric field that can assist the transport of photoelectrons. Furthermore, the combination of cationic substitution (including Cu by Ag, Zn by Cd, Mg or Mn, or Sn by Ge)^{73,87,107,148}, with anionic substitution between S and Se¹²⁸ represents a particularly interesting strategy to follow that could eventually lead to be a breakthrough in the near future.

Nevertheless, the use of efficient cationic grading in kesterite is still a pending issue. On the other hand, regarding rear/back band gap grading (in which mostly the second part of this Thesis is focused), previous works by Qi et al. have offered one of the first demonstrations of cationic-based grading via Cu by Ag substitution in multi-layered kesterite precursor stacks.¹⁴⁹

By investigating several back and front Ag concentrations, improved power energy conversion efficiencies were obtained for 30% of Ag content both at front and back, and 5% in the bulk of the $(\text{Cu,Ag})_2\text{ZnSn}(\text{S,Se})_4$ absorber layers. However, the incorporation of Ag was found to alter the crystalline structure of the material transitioning from kesterite to a stannite structure, with less favorable optoelectronic properties.

This way a promising strategy for cationic band gap engineering lies in the partial substitution of Sn by Ge in the $\text{Cu}_2\text{ZnSn}_x\text{Ge}_{1-x}(\text{S},\text{Se})_4$ (CZTGSe) lattice, which does not modify the kesterite structure. Germanium alloying can potentially promote grain growth and suppress the formation of Sn-related defects.^{68,78,145,150–152}

In addition, Ge is similar to the isoelectronic Sn atom but with a lower atomic number, hence making it possible to tune the electronic band profile through modifications of the IV-VI anti-bonding sp-orbital of the conduction band edge.^{148,153}

Moreover, deep Sn-related defects which are responsible for electron trapping in kesterite are mainly related to Sn^{+2} and Sn^{+4} multivalence, and the possibility to form intermediate Sn^{+3} oxidation state, that has been proposed at the origin of killer defects on kesterite.⁸⁶

In this sense, the formation of deep defects related to multivalence can be in principle reduced by substituting Sn with Ge, because it is well known that +4 state is more likely to occur with Ge than with Sn,¹⁵⁴ reducing the probability to form detrimental lower oxidation states.

As it is above mentioned, this bandgap variation is expected to occur mainly by changes in the energy position of the conduction band minimum (CBM). In fact, Nagai et al.¹⁵⁵ have recently demonstrated that the electron affinity of CZTGSe linearly decrease with increasing Ge content, whereas the ionization potential remains unaltered.

This implies that the position of the CBM can be controlled by tuning Ge composition along the depth of the absorber. Ge incorporation on Sn site in CZTSe can also be productively utilized due to its good miscibility without altering the kesterite structure.¹⁵⁶

Therefore, the incorporation pathways of Ge into the Sn-containing kesterite were previously studied by using advanced synchrotron techniques.²²

Besides band gap grading, the incorporation of Ge in CZTSe absorbers has been widely demonstrated to enhance device performance, making the substitution of Sn by Ge a truly attractive strategy to push forward the efficiency of kesterite devices.^{41,131,157–159}

2.5.3 Rear Ge-Sn Graded Bandgap as a BSF in Kesterites

In this context, the investigation reported (in the upcoming part) of the present Thesis, experimentally tackles the band engineering by implementing a steep cationic mixing substitution (Sn by Ge) strategy during the formation of precursor layers in order to achieve a rear grading band gap effect on CZTGSe absorber layers. Ge has been revealed to naturally accumulate at the back region of the CZTGSe absorber with a demonstrated increased band gap, in a similar fashion to Ga in CIGS.¹⁶⁰

The accumulation of Ge at the back interface of kesterite films has previously been reported¹⁵² and while promising steps, no solar cell improvement attributable to the presence of the Back Surface Field (BSF) effect was reported for the first time. Also, this Thesis work demonstrates for the first time that deliberate band engineering can lead to improved photovoltaic performances. Particularly, this work deals also with the engineering of deliberate rear bandgap profiles in kesterite.

Herein, it is presented a deep study of the influence of Ge content on material properties in graded CZTGSe and the evolution of the Sn/Ge gradient as a function of selenization temperature.

Moreover, the positive impact on the photovoltaic performance of the Sn-Ge alloyed kesterite solar cells is also presented and discussed in this Thesis by deliberately generating several graded bandgap profiles by modifying absorber annealing synthesis conditions for the first time.¹⁶⁰

Hence, highlighting the remarkable improvement in the conversion efficiency with respect to the non-graded reference, this is attributed to the BSF effect.

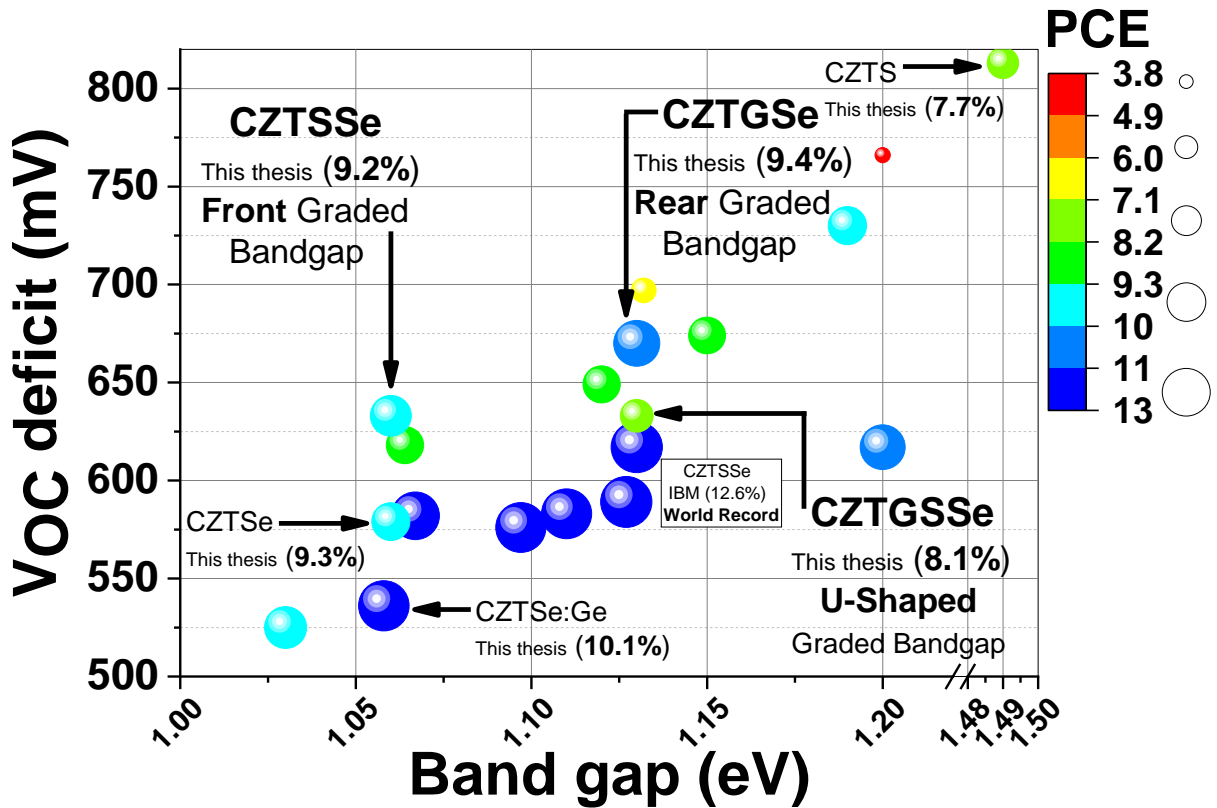


Figure 2.8.- Kesterite solar cell devices efficiency as a function of the band gap. See Chapter VII: Thesis Conclusions, Closing Remarks and Outlook and Thesis Appendix: Additional and Supporting Information.

Figure 2.8 shows that the V_{OC} deficit increases linearly as a function of the band gap, while it is markedly reduced for lower than 1.3 eV band gap values, highlighting the V_{OC} deficit problem largely discussed among the kesterite community.

Finally, the Table 2.4 condensates several V_{OC} deficit beating grading profiling strategies in kesterite absorber materials:

Table 2.4.- Most relevant V_{oc} deficit beating grading profiling strategies in kesterite absorber materials.

	Band gap profiling and driven strategy			V_{oc}		PCE (η) (%)	Institute	Year	Ref.
	Target profile	Grading strategy	Value (eV)	(mV)	deficit (mV)				
CZTSse	Front graded band gap	$S/(S + Se)$ > 0.25 (<i>front</i>) < 0.10 (<i>back</i>)	1.030	505	525	10.3	DGIST	2016	115
	U-shaped graded band gap	-	1.058	522	536	12.4	CHON	2020	161
	Frontal semi-U graded band gap	$S/(S + Se)$ = 0.22 (<i>front</i>) = 0.08 (<i>back</i>)	1.097	521	576	12.3	DGIST	2016	114
	?	$S/(S + Se)$ > 0.90	1.067	485	582	11.8	CHON	2018	162
	Rear graded band gap	$[S]_{Rear}$ > $[S]_{Front}$	1.127	541	589	12.6	DGIST	2019	163
	Front graded band gap	$S/(S + Se)$ > 0.40 (<i>front</i>) < 0.20 (<i>back</i>)	1.130	513	617	12.6*	IBM	2013	48
	Frontal semi-U graded band gap	$S/(S + Se)$ = 0.50 (<i>front</i>) = 0.20 (<i>back</i>)	1.064	444	620	9.2	IREC	2019	^{35*} This Thesis
?	$[S]_{Rear}$ < $[S]_{Front}$	1.130	460	670	11.3	IBM	2013	80	
CZTGeSe	Reduced band tailing/ Suppression of non-radiative recombination	$Ge/(Ge + Sn)$ = 0.39	1.110	527	583	12.3	AIST	2016	34,88
	Rear semi-U graded band gap	$Ge/(Ge + Sn)$ = 0.05 (<i>front</i>) = 0.23 (<i>back</i>)	1.120	470	650	9.4	IREC	2020	^{160*} This Thesis
	Rear semi-U graded band gap	$Ge/(Ge + Sn)$ = 0.40	1.150	476	674	9.1	IBM	2012	157
	?	$Ge/(Ge + Sn)$ = 0.09	1.132	435	697	6.1	INU	2016	164
CZTGSse	U-shaped graded band gap	$Ge/(Ge + Sn)$ = 0.25 (<i>front</i>)	1.200	583	617	11.0	UW	2016	151
	U-shaped graded band gap	-	1.130	456	633	8.1	IREC	2021	^{in progress} This Thesis
	U-shaped graded band gap	$Ge/(Ge + Sn)$ = 0.30 (<i>front</i>) = 0.14 (<i>back</i>)	1.190	460	730	9.4	PRUD	2015	87
	Rear semi-U graded band gap	$Ge/(Ge + Sn)$ = 0.12 $S/(S + Se) =$ 0.46	1.200	434	766	3.8	CHON	2017	165

2.6 Thesis Objectives*

The Main Objective of this Thesis is the development of an advanced technological process aiming the dexterously engineering of a U-Shaped bandgap profile in thin film kesterite-based photovoltaic devices, by increasing the charge carrier collection and reducing the V_{OC} deficit resulting in improved energy conversion efficiency.

In order to fulfil its main objective, this Thesis proposes the following specific objectives:

i) Front graded band gap: Optimizing the pn junction band alignment by engineering a semi-U graded bandgap profile; from a disruptive chalcogenide superficial substitution in the frontal part of the CZTSSe thin film layers, i.e., from high abruptly towards lower bandgap values along the material thickness.
→Developing and optimizing the **CZTSSe/CdS** front interface to achieve high efficiency surface graded bandgap thin film solar cells.

ii) Rear graded band gap: Minimize the effect of deep defect formation and impose an additional drift (back surface) field within quasi-neutral region. Additionally, to improve the crystallization quality by generating metallic Ge liquid phase fluxes. On top of that, the diffused Ge ions into bulk absorber would passivate the detrimental Cu_{Zn} and Cu_{Sn} deep level defects.
→Optimizing the **MoSe_x/CZTGSe** back interface to achieve high efficiency graded bandgap solar cells.

iii) U-Shaped graded band gap: Therefore, by combining both strategies, a dual gradient profile absorber architecture to enhance the device performance involving the downshift of absorber VBM at front contact and upshift of absorber CBM at back contact. Thus, reducing the interface defects and enhancing the junction band bending in kesterite (CZTGSSe) solar cells.
→Validating the **MoSSe_x/CZTGSSe/CdS** structure to achieve high efficiency double graded bandgap profiles in kesterite solar cells.

In summary, the aim of this Thesis work is to develop advanced synthesis and characterization techniques in order to experimentally demonstrate and overcome the V_{OC} deficit limit of kesterite based thin film solar cells by both anionic and cationic substitution and to further shed light into several emerging prospective strategies.

2.7 Chapter References

1. Uwe Rau; Daniel Abou-Ras; Thomas Kirchartz (2011). Advanced Characterization Techniques for Thin Film Solar Cells. John Wiley & Sons. p. 351. ISBN 978-3-527-63629-7.
2. Ingrid Repins, Nirav Vora, Carolyn Beall, Su-Huai Wei, Yanfa Yan, Manuel Romero, Glenn Teeter, Hui Du, Bobby To, Matt Young, and Rommel Noufi. 'Kesterites and Chalcopyrites: A Comparison of Close Cousins' Presented at the 2011 Materials Research Society Spring Meeting San Francisco, California, April 25–29, 2011 NREL Preprint. in.
3. Copyright CC-BY-SA-3.0 © Rob Lavinsky, iRocks.com.
Mindat.org relies on the contributions of thousands of members and supporters. Mindat.org does not offer minerals for sale.
4. Dhawale, D. S., Ali, A. & Lokhande, A. C. Impact of various dopant elements on the properties of kesterite compounds for solar cell applications: a status review. *Sustain. Energy Fuels* 3, 1365–1383 (2019).
5. Courtesy of Dr. Bryce Walker. <https://www.pveducation.org/es/fotovoltaica/czts>.
6. Robert Fonoll-Rubio et al. Insights into interface and bulk defects in a high efficiency kesterite-based device. *Energy Environ. Sci.* 14, 507–523 (2020).
7. Choubrac, L. et al. Multinuclear (⁶⁷Zn, ¹¹⁹Sn and ⁶⁵Cu) NMR spectroscopy – an ideal technique to probe the cationic ordering in Cu₂ZnSnS₄ photovoltaic materials. *Phys. Chem. Chem. Phys.* 15, 10722 (2013).
8. Schorr, S. The crystal structure of kesterite type compounds: A neutron and X-ray diffraction study. *Sol. Energy Mater. Sol. Cells* 95, 1482–1488 (2011).
9. Mitzi, D. B., Gunawan, O., Todorov, T. K., Wang, K. & Guha, S. The path towards a high-performance solution-processed kesterite solar cell. *Sol. Energy Mater. Sol. Cells* 95, 1421–1436 (2011).
10. Krämmer, C. et al. Reversible order-disorder related band gap changes in Cu₂ZnSn(S,Se)₄ via post-annealing of solar cells measured by electroreflectance. *Appl. Phys. Lett.* 105, 262104 (2014).
11. Vigil-Galán, O. et al. Secondary phases dependence on composition ratio in sprayed Cu₂ZnSnS₄ thin films and its impact on the high power conversion efficiency. *Sol. Energy Mater. Sol. Cells* 117, 246–250 (2013).
12. Gurieva, G., Valle Rios, L. E., Franz, A., Whitfield, P. & Schorr, S. Intrinsic point defects in off-stoichiometric Cu₂ZnSnSe₄: A neutron diffraction study. *J. Appl. Phys.* 123, 161519 (2018).
13. Fairbrother, A. et al. Compositional paradigms in multinary compound systems for photovoltaic applications: a case study of kesterites. *J. Mater. Chem. A* 3, 9451–9455 (2015).
14. Chen, S., Walsh, A., Gong, X.-G. & Wei, S.-H. Classification of Lattice Defects in the Kesterite Cu₂ZnSnS₄ and Cu₂ZnSnSe₄ Earth-Abundant Solar Cell Absorbers. *Adv. Mater.* 25, 1522–1539 (2013).
15. Olekseyuk, I. D., Dudchak, I. V. & Piskach, L. V. Phase equilibria in the Cu₂S–ZnS–SnS₂ system. *J. Alloys Compd.* 368, 135–143 (2004).
16. Giraldo, S. et al. Progress and Perspectives of Thin Film Kesterite Photovoltaic Technology: A Critical Review. *Adv. Mater.* 31, 1806692 (2019).
17. Scragg, J. J. S., Choubrac, L., Lafond, A., Ericson, T. & Platzer-Björkman, C. A low-temperature order-disorder transition in Cu₂ZnSnS₄ thin films. *Appl. Phys. Lett.* 104, 041911 (2014).
18. Altamura, G. et al. Cu₂ZnSn(S_{1-x}Se_x)₄ thin films for photovoltaic applications: Influence of the precursor stacking order on the selenization process. *J. Alloys Compd.* 588, 310–315 (2014).
19. Chen, S., Wang, L.-W., Walsh, A., Gong, X. G. & Wei, S.-H. Abundance of Cu_{zn} + Sn_{zn} and 2Cu_{zn} + Sn_{zn} defect clusters in kesterite solar cells. *Appl. Phys. Lett.* 101, 223901 (2012).
20. Mousel, M. et al. HCl and Br₂-MeOH etching of Cu₂ZnSnSe₄ polycrystalline absorbers. *Thin Solid Films* 535, 83–87 (2013).
21. Gershon, T. et al. Understanding the relationship between Cu₂ZnSn(S,Se)₄ material properties and device performance. *MRS Commun.* 4, 159–170 (2014).
22. Márquez, J. et al. Chemistry and Dynamics of Ge in Kesterite: Toward Band-Gap-Graded Absorbers. *Chem. Mater.* 29, 9399–9406 (2017).
23. Seo, S. W. et al. Compositional and Interfacial Modification of Cu₂ZnSn(S,Se)₄ Thin-Film Solar Cells Prepared by Electrochemical Deposition. *ChemSusChem* 9, 439–444 (2016).

24. Tai, K. F., Gershon, T., Gunawan, O. & Huan, C. H. A. Examination of electronic structure differences between CIGS_{Se} and CZTS_{Se} by photoluminescence study. *J. Appl. Phys.* 117, 235701 (2015).
25. Katagiri, H. et al. Development of CZTS-based thin film solar cells. *Thin Solid Films* 517, 2455–2460 (2009).
26. Taylor, S. R. Abundance of chemical elements in the continental crust: a new table. *Geochim. Cosmochim. Acta* 28, 1273–1285 (1964).
27. Vigil-Galán, O. et al. Route towards low cost-high efficiency second generation solar cells: current status and perspectives. *J. Mater. Sci. Mater. Electron.* 26, 5562–5573 (2015).
28. Larramona, G. et al. Stability, reliability, upscaling and possible technological applications of kesterite solar cells. *J. Phys. Energy* 2, 024009 (2020).
29. Lai, F.-I., Yang, J.-F., Chen, W.-C., Hsu, Y.-C. & Kuo, S.-Y. Weatherability of Cu₂ZnSnSe₄ thin film solar cells on diverse substrates. *Sol. Energy* 195, 626–635 (2020).
30. Grossberg, M. et al. The electrical and optical properties of kesterites. *J. Phys. Energy* 1, 044002 (2019).
31. Sai Gautam, G., Senftle, T. P. & Carter, E. A. Understanding the Effects of Cd and Ag Doping in Cu₂ZnSnS₄ Solar Cells. *Chem. Mater.* 30, 4543–4555 (2018).
32. Siebentritt, S. & Schorr, S. Kesterites-a challenging material for solar cells: Kesterites-a challenging material for solar cells. *Prog. Photovolt. Res. Appl.* 20, 512–519 (2012).
33. Gershon, T. et al. Photovoltaic Materials and Devices Based on the Alloyed Kesterite Absorber (Ag_xCu_{1-x})₂ZnSnSe₄. *Adv. Energy Mater.* 6, 1502468 (2016).
34. Kim, S. et al. Ge-incorporated Cu₂ZnSnSe₄ thin-film solar cells with efficiency greater than 10%. *Sol. Energy Mater. Sol. Cells* 144, 488–492 (2016).
35. Andrade-Arvizu, J. et al. Is It Possible To Develop Complex S–Se Graded Band Gap Profiles in Kesterite-Based Solar Cells? *ACS Appl. Mater. Interfaces* 11, 32945–32956 (2019).
36. Chen, S., Gong, X.-G., Walsh, A. & Wei, S.-H. Structural, Electronic and Defect Properties of Cu₂ZnSn(S,Se)₄ Alloys. *MRS Proc.* 1370, mrs11-1370-yy0-06 (2011).
37. Seol, J., Lee, S., Lee, J., Nam, H. & Kim, K. Electrical and optical properties of CuZnSnS thin films prepared by rf magnetron sputtering process. *Sol. Energy Mater. Sol. Cells* 75, 155–162 (2003).
38. Hages, C. J. et al. Identifying the Real Minority Carrier Lifetime in Nonideal Semiconductors: A Case Study of Kesterite Materials. *Adv. Energy Mater.* 7, 1700167 (2017).
39. Gokmen, T., Gunawan, O., Todorov, T. K. & Mitzi, D. B. Band tailing and efficiency limitation in kesterite solar cells. *Appl. Phys. Lett.* 103, 103506 (2013).
40. Brammertz, G. et al. Characterization of defects in 9.7% efficient Cu₂ZnSnSe₄-CdS-ZnO solar cells. *Appl. Phys. Lett.* 103, 163904 (2013).
41. Choubrac, L. et al. Sn Substitution by Ge: Strategies to Overcome the Open-Circuit Voltage Deficit of Kesterite Solar Cells. *ACS Appl. Energy Mater.* 3, 5830–5839 (2020).
42. Siebentritt, S. Why are kesterite solar cells not 20% efficient? *Thin Solid Films* 535, 1–4 (2013).
43. Platzer-Björkman, C. et al. Back and front contacts in kesterite solar cells: state-of-the-art and open questions. *J. Phys. Energy* 1, 044005 (2019).
44. Ito, K. & Nakazawa, T. Electrical and Optical Properties of Stannite-Type Quaternary Semiconductor Thin Films. *Jpn. J. Appl. Phys.* 27, 2094–2097 (1988).
45. Katagiri, H. et al. Preparation and evaluation of Cu₂ZnSnS₄ thin films by sulfurization of E₂B evaporated precursors. *Sol. Energy Mater. Sol. Cells* 49, 407–414 (1997).
46. Katagiri, H. et al. Enhanced Conversion Efficiencies of Cu₂ZnSnS₄-Based Thin Film Solar Cells by Using Preferential Etching Technique. *Appl. Phys. Express* 1, 041201 (2008).
47. Todorov, T. K., Reuter, K. B. & Mitzi, D. B. High-Efficiency Solar Cell with Earth-Abundant Liquid-Processed Absorber. *Adv. Mater.* 22, E156–E159 (2010).
48. Wang, W. et al. Device Characteristics of CZTS_{Se} Thin-Film Solar Cells with 12.6% Efficiency. *Adv. Energy Mater.* 4, 1301465 (2014).
49. Green, M. A. et al. Solar cell efficiency tables (version 54). *Prog. Photovolt. Res. Appl.* 27, 565–575 (2019).
50. Yan, C. et al. Cu₂ZnSnS₄ solar cells with over 10% power conversion efficiency enabled by heterojunction heat treatment. *Nat. Energy* 3, 764–772 (2018).

51. Best Research-Cell Efficiencies. National Renewable Energy Laboratory (NREL), National Center for Photovoltaics (rev. 22-09-2020). <https://www.nrel.gov/pv/assets/pdfs/best-research-cell-efficiencies.20200925.pdf>.
52. Reported at PVSEC-36 by a research team led at DGIST in South Korea. A 0.181 cm² solar cell was certified at 13.80% by KIER. in.
53. D.-H. Son, S.-Y. Kim, S.-H. Kim, Y.-I. Kim, S.-N. Park, D.-H. Jeon, D.-K. Hwang, K.-J. Yang, J.-K. Kang, D.-H. Kim, in 9th European Kesterite Workshop, Ghent, Belgium 2018. in.
54. Bosio, A., Pasini, S. & Romeo, N. The History of Photovoltaics with Emphasis on CdTe Solar Cells and Modules. *Coatings* 10, 344 (2020).
55. Reinhard, P. & Tiwari, A. N. Review of Progress Toward 20% Efficiency Flexible CIGS Solar Cells and Manufacturing Issues of Solar Modules. *IEEE J. Photovolt.* 9.
56. Bourdais, S. et al. Is the Cu/Zn Disorder the Main Culprit for the Voltage Deficit in Kesterite Solar Cells? *Adv. Energy Mater.* 6, 1502276 (2016).
57. Liu, X. et al. The current status and future prospects of kesterite solar cells: a brief review: Kesterite solar cells. *Prog. Photovolt. Res. Appl.* 24, 879–898 (2016).
58. Polizzotti, A., Repins, I. L., Noufi, R., Wei, S.-H. & Mitzi, D. B. The state and future prospects of kesterite photovoltaics. *Energy Environ. Sci.* 6, 3171 (2013).
59. Shockley, W. & Queisser, H. J. Detailed Balance Limit of Efficiency of p-n Junction Solar Cells. 11.
60. Sun, R. et al. Efficient Cu₂ZnSn(S_xSe_{4-x})₄ solar cells with 79% fill factor using two-step annealing. *Sol. Energy Mater. Sol. Cells* 215, 110682 (2020).
61. Lee, Y. S. et al. Cu₂ZnSnSe₄ Thin-Film Solar Cells by Thermal Co-evaporation with 11.6% Efficiency and Improved Minority Carrier Diffusion Length. *Adv. Energy Mater.* 5, 1401372 (2015).
62. Kim, J. et al. High Efficiency Cu₂ZnSn(S,Se)₄ Solar Cells by Applying a Double In₂S₃/CdS Emitter. *Adv. Mater.* 26, 7427–7431 (2014).
63. Kaur, K. & Kumar, M. Progress and Prospective of CZTSSe/CdS interface engineering to combat high open-circuit voltage deficit of kesterite photovoltaics: A critical review. 73.
64. Babichuk, I. S. Control of secondary phases and disorder degree in Cu₂ZnSnS₄ films by sulfurization at varied subatmospheric pressures. *Sol. Energy Mater. Sol. Cells* 9 (2019) doi:10/gjp3r9.
65. Kumar, M., Dubey, A., Adhikari, N., Venkatesan, S. & Qiao, Q. Strategic review of secondary phases, defects and defect-complexes in kesterite CZTS–Se solar cells. *Energy Environ. Sci.* 8, 3134–3159 (2015).
66. Liu, F., Wu, S., Zhang, Y., Hao, X. & Ding, L. Advances in kesterite Cu₂ZnSn(S, Se)₄ solar cells. *Sci. Bull.* 65, 698–701 (2020).
67. Chen, S., Yang, J.-H., Gong, X. G., Walsh, A. & Wei, S.-H. Intrinsic point defects and complexes in the quaternary kesterite semiconductor Cu₂ZnSnS₄. *Phys. Rev. B* 81, 245204 (2010).
68. Courel, M., Andrade-Arvizu, J. A. & Vigil-Galán, O. The role of buffer/kesterite interface recombination and minority carrier lifetime on kesterite thin film solar cells. *Mater. Res. Express* 3, 095501 (2016).
69. Rondiya, S. et al. CZTS/CdS: interface properties and band alignment study towards photovoltaic applications. *J. Mater. Sci. Mater. Electron.* 29, 4201–4210 (2018).
70. Kim, J. et al. Effects of Mo back-contact annealing on surface potential and carrier transport in Cu₂ZnSnS₄ thin film solar cells. *RSC Adv.* 6, 103337–103345 (2016).
71. Scragg, J. J. et al. Effects of Back Contact Instability on Cu₂ZnSnS₄ Devices and Processes. *Chem. Mater.* 25, 3162–3171 (2013).
72. Gunawan, O. et al. Electronic properties of the Cu₂ZnSn(S_xSe_{4-x})₄ absorber layer in solar cells as revealed by admittance spectroscopy and related methods. *Appl. Phys. Lett.* 100, 253905 (2012).
73. Giraldo, S. et al. Large Efficiency Improvement in Cu₂ZnSnSe₄ Solar Cells by Introducing a Superficial Ge Nanolayer. *Adv. Energy Mater.* 5, 1501070 (2015).
74. Biswas, K., Lany, S. & Zunger, A. The electronic consequences of multivalent elements in inorganic solar absorbers: Multivalency of Sn in Cu₂ZnSnS₄. *Appl. Phys. Lett.* 96, 201902 (2010).

75. Shin, D., Saporov, B. & Mitzi, D. B. Defect Engineering in Multinary Earth-Abundant Chalcogenide Photovoltaic Materials. *Adv. Energy Mater.* 7, 1602366 (2017).
76. Hages, C. J., Carter, N. J., Agrawal, R. & Unold, T. Generalized current-voltage analysis and efficiency limitations in non-ideal solar cells: Case of $\text{Cu}_2\text{ZnSn}(\text{S}_x\text{Se}_{1-x})_4$ and $\text{Cu}_2\text{Zn}(\text{Sn}_y\text{Ge}_{1-y})(\text{S}_x\text{Se}_{1-x})_4$. *J. Appl. Phys.* 115, 234504 (2014).
77. Gunawan, O., Gokmen, T. & Mitzi, D. B. Suns- V_{OC} characteristics of high performance kesterite solar cells. *J. Appl. Phys.* 116, 084504 (2014).
78. Courel, M., Pulgarín-Agudelo, F. A., Andrade-Arvizu, J. A. & Vigil-Galán, O. Open-circuit voltage enhancement in CdS/Cu₂ZnSnSe₄-based thin film solar cells: A metal-insulator-semiconductor (MIS) performance. *Sol. Energy Mater. Sol. Cells* 149, 204–212 (2016).
79. Yin, L. et al. Limitation factors for the performance of kesterite $\text{Cu}_2\text{ZnSnS}_4$ thin film solar cells studied by defect characterization. *RSC Adv.* 5, 40369–40374 (2015).
80. Todorov, T. K. et al. Beyond 11% Efficiency: Characteristics of State-of-the-Art $\text{Cu}_2\text{ZnSn}(\text{S},\text{Se})_4$ Solar Cells. *Adv. Energy Mater.* 3, 34–38 (2013).
81. Romero, M. J., Du, H., Teeter, G., Yan, Y. & Al-Jassim, M. M. Comparative study of the luminescence and intrinsic point defects in the kesterite $\text{Cu}_2\text{ZnSnS}_4$ and chalcopyrite $\text{Cu}(\text{In},\text{Ga})\text{Se}_2$ thin films used in photovoltaic applications. *Phys. Rev. B* 84, 165324 (2011).
82. Zawadzki, P., Zakutayev, A. & Lany, S. Entropy-Driven Clustering in Tetrahedrally Bonded Multinary Materials. *Phys. Rev. Appl.* 3, 034007 (2015).
83. Rey, G. et al. The band gap of $\text{Cu}_2\text{ZnSnSe}_4$: Effect of order-disorder. *Appl. Phys. Lett.* 105, 112106 (2014).
84. Aninat, R., Quesada-Rubio, L.-E., Sanchez-Cortezon, E. & Delgado-Sanchez, J.-M. Mapping and comparison of the shortcomings of kesterite absorber layers, and how they could affect industrial scalability. *Thin Solid Films* 633, 146–150 (2017).
85. Ratz, T. et al. Physical routes for the synthesis of kesterite. *J. Phys. Energy* 1, 042003 (2019).
86. Kim, S., Park, J.-S. & Walsh, A. Identification of Killer Defects in Kesterite Thin-Film Solar Cells. *ACS Energy Lett.* 3, 496–500 (2018).
87. Hages, C. J. et al. Improved performance of Ge-alloyed CZTGeSSe thin-film solar cells through control of elemental losses: Improved performance of CZTGeSSe solar cells. *Prog. Photovolt. Res. Appl.* 23, 376–384 (2015).
88. Kim, S., Kim, K. M., Tampo, H., Shibata, H. & Niki, S. Improvement of voltage deficit of Ge-incorporated kesterite solar cell with 12.3% conversion efficiency. *Appl. Phys. Express* 9, 102301 (2016).
89. Walsh, A., Chen, S., Wei, S.-H. & Gong, X.-G. Kesterite Thin-Film Solar Cells: Advances in Materials Modelling of $\text{Cu}_2\text{ZnSnS}_4$. *Adv. Energy Mater.* 2, 400–409 (2012).
90. Courel, M., Andrade-Arvizu, J. A. & Vigil-Galán, O. Towards a CdS/ $\text{Cu}_2\text{ZnSnS}_4$ solar cell efficiency improvement: A theoretical approach. *Appl. Phys. Lett.* 105, 233501 (2014).
91. Courel, M., Andrade-Arvizu, J. A. & Vigil-Galán, O. Loss mechanisms influence on $\text{Cu}_2\text{ZnSnS}_4$ /CdS-based thin film solar cell performance. *Solid-State Electron.* 111, 243–250 (2015).
92. Rey, G. et al. On the origin of band-tails in kesterite. *Sol. Energy Mater. Sol. Cells* 179, 142–151 (2018).
93. Schöppe, P. et al. Discrepancy between integral and local composition in off-stoichiometric $\text{Cu}_2\text{ZnSnSe}_4$ kesterites: A pitfall for classification. *Appl. Phys. Lett.* 110, 043901 (2017).
94. Aguiar, J. A. et al. Cation ratio fluctuations in $\text{Cu}_2\text{ZnSnS}_4$ at the 20 nm length scale investigated by analytical electron microscopy: Cation ratio fluctuations in $\text{Cu}_2\text{ZnSnS}_4$. *Phys. Status Solidi A* 213, 2392–2399 (2016).
95. Collord, A. D., Xin, H. & Hillhouse, H. W. Combinatorial Exploration of the Effects of Intrinsic and Extrinsic Defects in $\text{Cu}_2\text{ZnSn}(\text{S},\text{Se})_4$. *IEEE J. Photovolt.* 5, 288–298 (2015).
96. Grenet, L., Suzon, M. A. A., Emieux, F. & Roux, F. Analysis of Failure Modes in Kesterite Solar Cells. *ACS Appl. Energy Mater.* 1, 2103–2113 (2018).
97. Devaney, W. E., Stewart, J. M. & Mickelsen, R. A. Structure and Properties of High Efficiency ZnO/CdZnS/CuInGaSe₂ Solar Cells. 6.
98. Nakada, T., Hirabayashi, Y., Tokado, T., Ohmori, D. & Mise, T. Novel device structure for $\text{Cu}(\text{In},\text{Ga})\text{Se}_2$ thin film solar cells using transparent conducting oxide back and front contacts. *Sol. Energy* 77, 739–747 (2004).

99. Sun, Y. Review on Alkali Element Doping in Cu(In,Ga)Se₂ Thin Films and Solar Cells. 8 (2017).
100. Tai, K. F., Kamada, R., Yagioka, T., Kato, T. & Sugimoto, H. From 20.9 to 22.3% Cu(In,Ga)(S,Se)₂ solar cell: Reduced recombination rate at the heterojunction and the depletion region due to K-treatment. *Jpn. J. Appl. Phys.* 56, 08MC03 (2017).
101. Sohn, S. H. et al. Band gap grading and photovoltaic performance of solution-processed Cu(In,Ga)S₂ thin-film solar cells. *Phys Chem Chem Phys* 16, 27112–27118 (2014).
102. Izquierdo-Roca, V. et al. Electrochemical synthesis of CuIn(S,Se)₂ alloys with graded composition for high efficiency solar cells. *Appl. Phys. Lett.* 94, 061915 (2009).
103. Caballero, R., Guillen, C., Gutierrez, M. T. & Kaufmann, C. A. CuIn_{1-x}Ga_xSe₂-Based Thin-Film Solar Cells by the Selenization of Sequentially Evaporated Metallic Layers. 9 (2005).
104. Kato, T. Recent Research Progress of High-efficiency CIGS Solar Cell in *Solar Frontier*. 21.
105. Amin, N., Chelvanathan, P., Hossain, M. I. & Sopian, K. Numerical Modelling of Ultra Thin Cu(In,Ga)Se₂ Solar Cells. *Energy Procedia* 15, 291–298 (2012).
106. Giraldo, S. et al. Study and optimization of alternative MBE-deposited metallic precursors for highly efficient kesterite CZTSe:Ge solar cells. *Prog. Photovolt. Res. Appl.* 27, 779–788 (2019).
107. Li, J., Wang, D., Li, X., Zeng, Y. & Zhang, Y. Cation Substitution in Earth-Abundant Kesterite Photovoltaic Materials. *Adv. Sci.* 5, 1700744 (2018).
108. Qi, Y. et al. Elemental precursor solution processed (Cu_{1-x}Ag_x)₂ZnSn(S,Se)₄ Photovoltaic Devices with over 10% Efficiency. 24.
109. Sutter-Fella, C. M. et al. Sodium Assisted Sintering of Chalcogenides and Its Application to Solution Processed Cu₂ZnSn(S,Se)₄ Thin Film Solar Cells. *Chem. Mater.* 26, 1420–1425 (2014).
110. Hironiwa, D., Murata, M., Ashida, N., Tang, Z. & Minemoto, T. Simulation of optimum band-gap grading profile of Cu₂ZnSn(S,Se)₄ solar cells with different optical and defect properties. *Jpn. J. Appl. Phys.* 53, 071201 (2014).
111. Mohammadnejad, S. & Baghban Parashkouh, A. CZTSSe solar cell efficiency improvement using a new band-gap grading model in absorber layer. *Appl. Phys. A* 123, 758 (2017).
112. Kato, T., Sakai, N. & Sugimoto, H. Efficiency improvement of Cu₂ZnSn(S,Se)₄ submodule with graded bandgap and reduced backside ZnS segregation. in 2014 IEEE 40th Photovoltaic Specialist Conference (PVSC) 0844–0846 (IEEE, 2014). doi:10.1109/PVSC.2014.6925047.
113. Woo, K. et al. Band-gap-graded Cu₂ZnSn(S_{1-x}Se_x)₄ Solar Cells Fabricated by an Ethanol-based, Particulate Precursor Ink Route. *Sci. Rep.* 3, 3069 (2013).
114. Yang, K.-J. et al. A band-gap-graded CZTSSe solar cell with 12.3% efficiency. *J. Mater. Chem. A* 4, 10151–10158 (2016).
115. Hwang, D.-K. et al. Single-step sulfo-selenization method for achieving low open circuit voltage deficit with band gap front-graded Cu₂ZnSn(S,Se)₄ thin films. *Sol. Energy Mater. Sol. Cells* 161, 162–169 (2017).
116. Cai, C.-H. et al. Efficiency enhancement of Cu₂ZnSn(S,Se)₄ solar cells by S-modified surface layer. *Sol. Energy Mater. Sol. Cells* 162, 21–29 (2017).
117. Neuwirth, M. et al. Band-gap tuning of Cu₂ZnSn(S,Se)₄ solar cell absorbers via defined incorporation of sulphur based on a post-sulphurization process. *Sol. Energy Mater. Sol. Cells* 182, 158–165 (2018).
118. Hwang, D.-K. et al. Single-step sulfo-selenization method for achieving low open circuit voltage deficit with band gap front-graded Cu₂ZnSn(S,Se)₄ thin films. *Sol. Energy Mater. Sol. Cells* 161, 162–169 (2017).
119. Englund, S., Saini, N. & Platzer-Björkman, C. Cu₂ZnSn(S,Se)₄ from annealing of compound co-sputtered precursors – Recent results and open questions. *Sol. Energy* 175, 84–93 (2018).
120. Cai, C.-H. et al. Efficiency enhancement of Cu₂ZnSn(S,Se)₄ solar cells by S-modified surface layer. *Sol. Energy Mater. Sol. Cells* 162, 21–29 (2017).
121. Grini, S., Ross, N., Persson, C., Platzer-Björkman, C. & Vines, L. Low temperature incorporation of selenium in Cu₂ZnSnS₄: Diffusion and nucleation. *Thin Solid Films* 665, 159–163 (2018).
122. Hergert, F., Jost, S., Hock, R., Purwins, M. & Palm, J. A thermodynamical approach to the formation reactions of sodium-doped Cu(In,Ga)Se₂. *Thin Solid Films* 511–512, 147–152 (2006).

123. Shigemi, A. & Wada, T. First-principles studies on the interface between light-absorbing layer and Mo back electrode in $\text{Cu}(\text{In,Ga})\text{Se}_2$, $\text{Cu}_2\text{ZnSn}(\text{S,Se})_4$, and Cu_2SnS_3 solar cells. *Jpn. J. Appl. Phys.* 57, 08RC17 (2018).
124. Cahen, D. & Noufi, R. Free energies and enthalpies of possible gas phase and surface reactions for preparation of. *J. Phys. Chem. Solids* 53, 991–1005 (1992).
125. Maeda, T., Nakamura, S. & Wada, T. First Principles Calculations of Defect Formation in In-Free Photovoltaic Semiconductors $\text{Cu}_2\text{ZnSnS}_4$ and $\text{Cu}_2\text{ZnSnSe}_4$. *Jpn. J. Appl. Phys.* 50, 04DP07 (2011).
126. Li, G. et al. The influence of cracked selenium flux on CIGS thin film growth and device performance prepared by two-step selenization processes. *Sol. Energy Mater. Sol. Cells* 139, 108–114 (2015).
127. Noikaew, B., Sukaiem, S., Namnuan, B. & Chatraphorn, S. CIGS thin film solar cells with graded-band gap fabricated by CIS/CGS bilayer and CGS/CIS/CGS trilayer systems. *J. Phys. Conf. Ser.* 1144, 012069 (2018).
128. Andrade-Arvizu, J. et al. Is It Possible To Develop Complex S–Se Graded Band Gap Profiles in Kesterite-Based Solar Cells? *ACS Appl. Mater. Interfaces* 11, 32945–32956 (2019).
129. Kato, T., Sakai, N. & Sugimoto, H. Efficiency improvement of $\text{Cu}_2\text{ZnSn}(\text{S,Se})_4$ submodule with graded bandgap and reduced backside ZnS segregation. in 2014 IEEE 40th Photovoltaic Specialist Conference (PVSC) 0844–0846 (IEEE, 2014). doi:10.1109/PVSC.2014.6925047.
130. Woo, K. et al. Band-gap-graded $\text{Cu}_2\text{ZnSn}(\text{S}_{1-x}\text{Se}_x)_4$ Solar Cells Fabricated by an Ethanol-based, Particulate Precursor Ink Route. *Sci. Rep.* 3, 3069 (2013).
131. Yang, K.-J. et al. A band-gap-graded CZTSSe solar cell with 12.3% efficiency. *J. Mater. Chem. A* 4, 10151–10158 (2016).
132. Hwang, D.-K. et al. Single-step sulfo-selenization method for achieving low open circuit voltage deficit with band gap front-graded $\text{Cu}_2\text{ZnSn}(\text{S,Se})_4$ thin films. *Sol. Energy Mater. Sol. Cells* 161, 162–169 (2017).
133. Cai, C.-H. et al. Efficiency enhancement of $\text{Cu}_2\text{ZnSn}(\text{S,Se})_4$ solar cells by S-modified surface layer. *Sol. Energy Mater. Sol. Cells* 162, 21–29 (2017).
134. Neuwirth, M. et al. Band-gap tuning of $\text{Cu}_2\text{ZnSn}(\text{S,Se})_4$ solar cell absorbers via defined incorporation of sulphur based on a post-sulphurization process. *Sol. Energy Mater. Sol. Cells* 182, 158–165 (2018).
135. Hergert, F., Jost, S., Hock, R., Purwins, M. & Palm, J. A thermodynamical approach to the formation reactions of sodium-doped $\text{Cu}(\text{In,Ga})\text{Se}_2$. *Thin Solid Films* 511–512, 147–152 (2006).
136. Shigemi, A. & Wada, T. First-principles studies on the interface between light-absorbing layer and Mo back electrode in $\text{Cu}(\text{In,Ga})\text{Se}_2$, $\text{Cu}_2\text{ZnSn}(\text{S,Se})_4$, and Cu_2SnS_3 solar cells. *Jpn. J. Appl. Phys.* 57, 08RC17 (2018).
137. Maeda, T., Nakamura, S. & Wada, T. First Principles Calculations of Defect Formation in In-Free Photovoltaic Semiconductors $\text{Cu}_2\text{ZnSnS}_4$ and $\text{Cu}_2\text{ZnSnSe}_4$. *Jpn. J. Appl. Phys.* 50, 04DP07 (2011).
138. Liu, F. et al. Kesterite $\text{Cu}_2\text{ZnSn}(\text{S,Se})_4$ Solar Cells with beyond 8% Efficiency by a Sol–Gel and Selenization Process. *ACS Appl. Mater. Interfaces* 7, 14376–14383 (2015).
139. Wei, H. et al. Tunable band gap $\text{Cu}_2\text{ZnSnS}_4\text{Se}_4(1-x)$ nanocrystals: experimental and first-principles calculations. *CrystEngComm* 13, 2222 (2011).
140. Duan, H.-S. et al. The Role of Sulfur in Solution-Processed $\text{Cu}_2\text{ZnSn}(\text{S,Se})_4$ and its Effect on Defect Properties. *Adv. Funct. Mater.* 23, 1466–1471 (2013).
141. Pulgarín-Agudelo, F. A. et al. Preparation and characterization of $\text{Cu}_2\text{ZnSnSe}_4$ and $\text{Cu}_2\text{ZnSn}(\text{S,Se})_4$ powders by ball milling process for solar cells application. *Mater. Res. Express* 4, 125501 (2017).
142. Chen, S., Gong, X. G., Walsh, A. & Wei, S.-H. Electronic structure and stability of quaternary chalcogenide semiconductors derived from cation cross-substitution of II-VI and I-III-VI 2 compounds. *Phys. Rev. B* 79, 165211 (2009).
143. Chen, S., Gong, X. G., Walsh, A. & Wei, S.-H. Crystal and electronic band structure of $\text{Cu}_2\text{ZnSnX}_4$ (X=S and Se) photovoltaic absorbers: First-principles insights. *Appl. Phys. Lett.* 94, 041903 (2009).

144. Yuan, Z.-K. et al. Engineering Solar Cell Absorbers by Exploring the Band Alignment and Defect Disparity: The Case of Cu- and Ag-Based Kesterite Compounds. *Adv. Funct. Mater.* 25, 6733–6743 (2015).
145. Vigil-Galán, O. et al. Processing pathways of $\text{Cu}_2\text{Zn}(\text{SnGe})\text{Se}_4$ based solar cells: The role of CdS buffer layer. *Mater. Sci. Semicond. Process.* 67, 14–19 (2017).
146. Pulgarín-Agudelo, F. A. et al. Cu content dependence of $\text{Cu}_2\text{Zn}(\text{SnGe})\text{Se}_4$ solar cells prepared by using sequential thermal evaporation technique of Cu/Sn/Cu/Zn/Ge stacked layers. *J. Mater. Sci. Mater. Electron.* 29, 15363–15368 (2018).
147. González-Castillo, J. R. et al. Influence of Ge content on $\text{Cu}_2\text{Zn}(\text{SnGe})\text{Se}_4$ physical properties deposited by sequential thermal evaporation technique. *Mater. Sci. Semicond. Process.* 83, 96–101 (2018).
148. Chen, G. et al. Bandgap engineering of $\text{Cu}_2\text{ZnSn}_{1-x}\text{Ge}_x\text{S}(\text{e})_4$ by adjusting Sn-Ge ratios for almost full solar spectrum absorption. *J. Alloys Compd.* 718, 236–245 (2017).
149. Ya-Fang, Q. et al. Engineering of Interface Band Bending and Defects Elimination via Ag-graded active layer for efficient (Cu,Ag)₂ZnSn(S,Se)₄ Solar Cells. *Energy Environ. Sci.* 10, 2401–2410 (2017).
150. Saini, N. Germanium Incorporation in $\text{Cu}_2\text{ZnSnS}_4$ and Formation of a Sn–Ge Gradient. *Phys Status Solidi A* 12 (2019).
151. Collord, A. D. & Hillhouse, H. W. Germanium Alloyed Kesterite Solar Cells with Low Voltage Deficits. *Chem. Mater.* 28, 2067–2073 (2016).
152. Andres, C., Cabas-Vidani, A., Tiwari, A. N. & Romanyuk, Y. E. From sputtered metal precursors towards $\text{Cu}_2\text{Zn}(\text{Sn}_{1-x}\text{Ge}_x)\text{Se}_4$ thin film solar cells with shallow back grading. *Thin Solid Films* 665, 168–172 (2018).
153. Benhaddou, N. et al. Investigation on limiting factors affecting $\text{Cu}_2\text{ZnGeSe}_4$ efficiency: Effect of annealing conditions and surface treatment. *Sol. Energy Mater. Sol. Cells* 216, 110701 (2020).
154. Romanyuk, Y. E. et al. Doping and alloying of kesterites. *J. Phys. Energy* 1, 044004 (2019).
155. Nagai, T. et al. Characterization of Surface and Heterointerface of $\text{Cu}_2\text{ZnSn}_{1-x}\text{Ge}_x\text{Se}_4$ for Solar Cell Applications. *Phys. Status Solidi RRL – Rapid Res. Lett.* 1900708 (2020) doi:10.1002/pssr.201900708.
156. Shu, Q. et al. $\text{Cu}_2\text{Zn}(\text{Sn,Ge})\text{Se}_4$ and $\text{Cu}_2\text{Zn}(\text{Sn,Si})\text{Se}_4$ alloys as photovoltaic materials: Structural and electronic properties. *Phys. Rev. B* 87, 115208 (2013).
157. Bag, S., Gunawan, O., Gokmen, T., Zhu, Y. & Mitzi, D. B. Hydrazine-Processed Ge-Substituted CZTSe Solar Cells. *Chem. Mater.* 24, 4588–4593 (2012).
158. Neuschitzer, M. et al. V_{oc} Boosting and Grain Growth Enhancing Ge-Doping Strategy for $\text{Cu}_2\text{ZnSnSe}_4$ Photovoltaic Absorbers. *J. Phys. Chem. C* 120, 9661–9670 (2016).
159. Khadka, D. B., Kim, S. & Kim, J. Effects of Ge Alloying on Device Characteristics of Kesterite-Based CZTSSe Thin Film Solar Cells. *J. Phys. Chem. C* 120, 4251–4258 (2016).
160. Andrade-Arvizu, J. et al. Rear Band gap Grading Strategies on Sn–Ge-Alloyed Kesterite Solar Cells. *ACS Appl. Energy Mater.* acsaem.0c01146 (2020) doi:10.1021/acsaem.0c01146.
161. Gong, Y. et al. Sn⁴⁺ precursor enables 12.4% efficient kesterite solar cell from DMSO solution with open circuit voltage deficit below 0.30 V. 9 (2020).
162. Gang, M. G. et al. Band Tail Engineering in Kesterite $\text{Cu}_2\text{ZnSn}(\text{S,Se})_4$ Thin-Film Solar Cells with 11.8% Efficiency. *J. Phys. Chem. Lett.* 9, 4555–4561 (2018).
163. Son, D.-H. et al. Effect of solid- H_2S gas reactions on CZTSSe thin film growth and photovoltaic properties of a 12.62% efficiency device. *J. Mater. Chem. A* 7, 25279–25289 (2019).
164. Khadka, D. B., Kim, S. & Kim, J. Effects of Ge Alloying on Device Characteristics of Kesterite-Based CZTSSe Thin Film Solar Cells. *J. Phys. Chem. C* 120, 4251–4258 (2016).
165. Lokhande, A. C. Fabrication of pulsed laser deposited Ge doped CZTSSe thin film based solar cells_ Influence of selenization treatment. *Sol. Energy Mater.* 13 (2017).

But you got to stop and think about it, to really get the pleasure

About the complexity and inconceivable nature of Nature.

-Richard Feynman

Chapter III

Experimental Procedures and Theoretical Studies on Kesterite Based Thin Film Solar Cells: From Glass to Alloyed Brass

In Chapter III, a road trip from the experimental very beginning, i.e., from the very bare cleaning of the substrate (glass), passing through the back contact deposition (Mo), to the sputtering of the metallic precursor layers (CZT), up to the synthesis of the graded bandgap kesterite structured alloyed compounds. Also, its adequation and surface cleaning preparation for the completion of the solar deceive structure (buffer and front contact layers) are commented and outlined. Just after this, a general overview on the thin film material and system characterization is summarized. Finally, it is provided a brief compilation on theoretical solar PV physics from the semiconductor materials and the PN junction to several of the optoelectronic characterization techniques utilized in this Thesis. In this way, it may be easily and logically followed the fact that a remarkable substrate surface cleaning ought to be a good (if not the best) starting point whenever developing thin film solar cells is the goal. During the development of the following results, three millimeter thick Soda Lime Glass (**SLG**) substrates were typically utilized.

3.1 Soda Lime Glass Substrate Cleaning and Preparation

There is a “non-written” almost mandatory command regarding the utilization of nitrile gloves during glass substrate cleaning.

Ideally, the employed gloves should be firstly cleaned by employing water and dishwashing soap before handling a (10 x 10) cm² SLG substrate.

i. Identifying the back side of the SLG (i.e. the side of the SLG that will not be utilized for thin film deposition, and that was normally in contact with the Sn during the floating preparation process).

ii. Thus, by cleaning (rubbing) the SLG surface with tap water and basic pH, 'dishwashing' soaps employing a clean and a sponge.

iii. Rinse in distilled water and, subsequently, in de-ionized water.

iv. Firstly drying the front side of the SLG by employing a N₂ or Ar gas guns.

v. Repeat (ii), by gently sweeping (softly rubbing) the SLG surface, rinsing with deionized (18 MΩ) water and 'Liquinox (ALCONOX ®)' critical-cleaning liquid detergent employing a specialized clean and soft non-abrasive sponge.

vi. Rinse in distilled water and, subsequently in de-ionized water.

vii. Dry the glass employing a N₂ or Ar gun. Dry the front side of the SLG first.

viii. Submit the SLG to an ultrasonic bath in acetone at 56 °C during 10 minutes.

ix. Dry the SLG employing a N₂ or Ar gun. Dry the front side of the SLG first.

x. Submit the SLG to an ultrasonic bath in de-ionized water at 56 °C during 2 min.

xi. Dry the SLG employing a N₂ or Ar gun. Dry the front side of the SLG first.

xii. Submit the SLG to an ultrasonic bath in isopropanol at 56 °C during 10 min.

xiii. Dry the SLG employing a N₂ or Ar gun. Dry the front side of the SLG first.

xiv. Submit the SLG to an ultrasonic bath in de-ionized water at 56 °C during 10 min.

xv. Finally, drying the SLG by employing a N₂ or Ar gun.

Therefore, extremely carefully (avoiding any residues) drying the front side of the glass first. Finally repeating steps (xi and xii) but a shorter ultrasonic bath time (2 - 5 min) should conclude the process (See Figure 3.1).

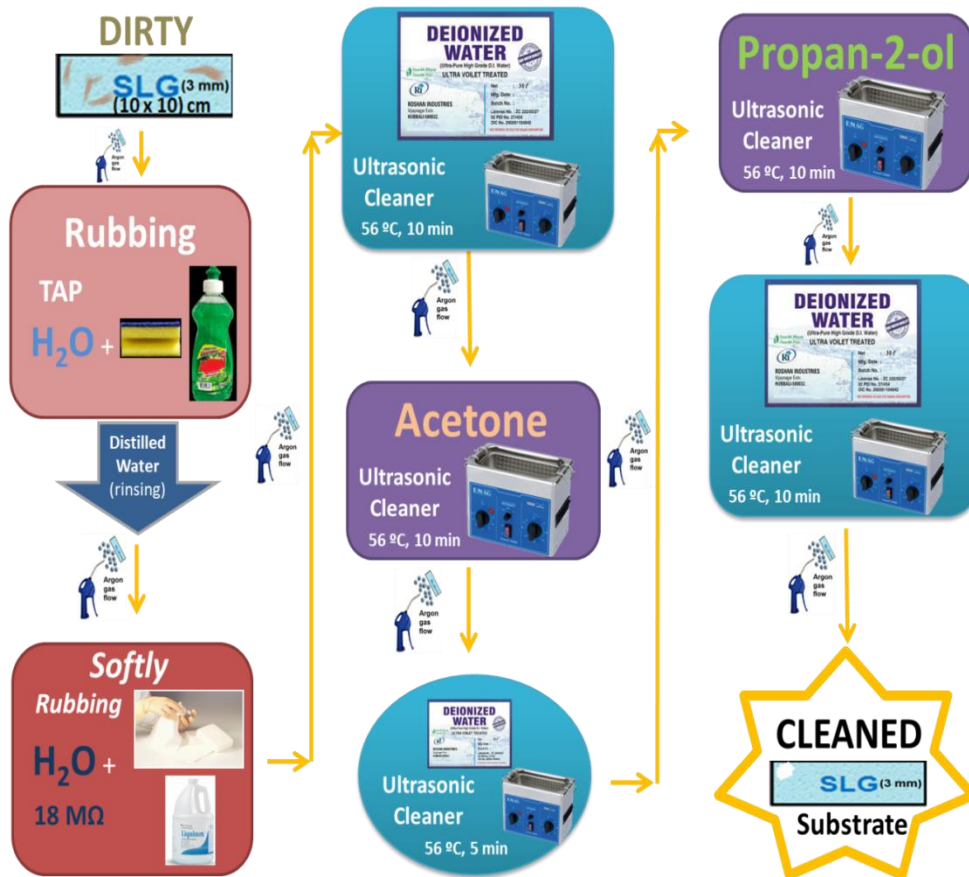


Figure 3.1.- Sketched flow chart for the SLG substrate cleaning process.

Just after the cleaning process, it is strongly recommended to reduce as much as possible the elapsed time between the SLG cleaning and the (next step) Mo deposition in order to avoid dust over the surface.

3.2 Molybdenum (Mo) Back Contact Sputtering Deposition

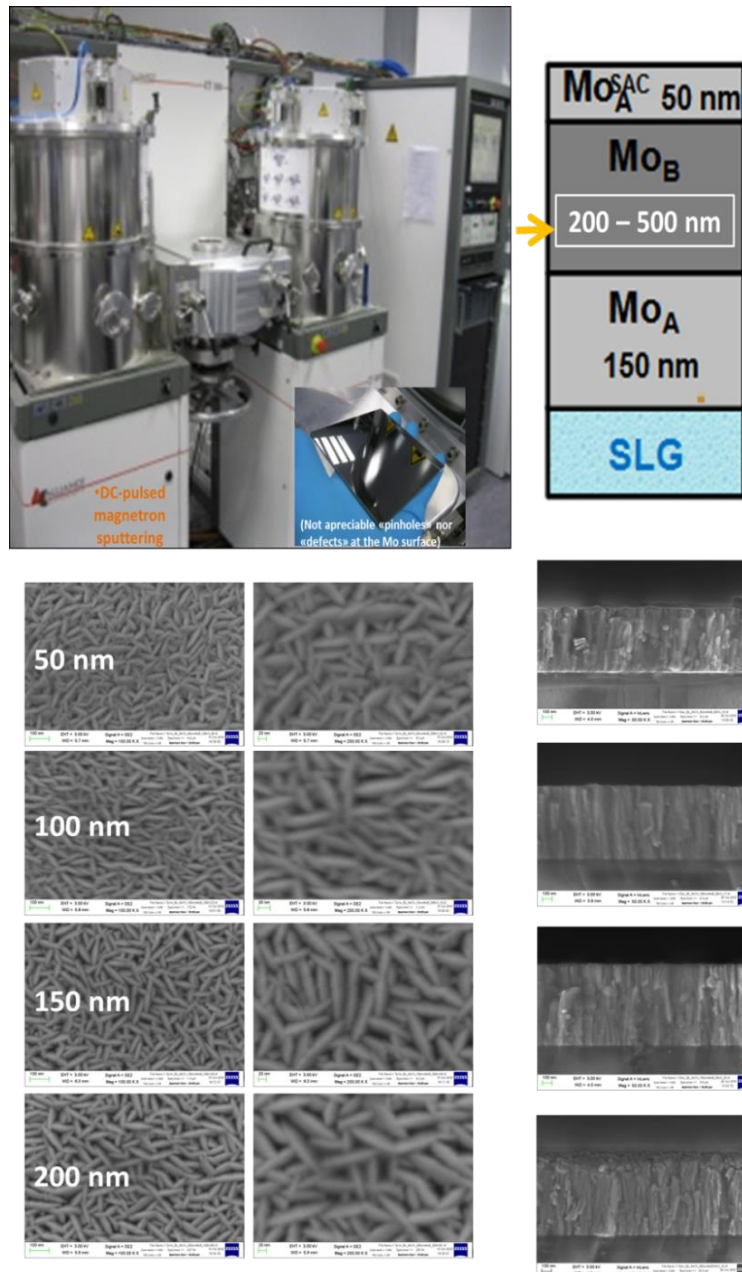


Figure 3.2.- Molybdenum (Mo) tri-layer back contact deposition by DC-sputtering.

The typical standard thin film back contact in the Solar Energy Material and Systems (**SEMS**) Group at the Catalonia Institute for Energy Research (**IREC**) consists on a DC-pulsed magnetron sputtering deposition of a tri-layered thin film molybdenum (Mo) structure as follows: SLG/ Mo_A / Mo_B / Mo_A - Mo_A^{SAC} with thicknesses: 500/150/50 nm, respectively (See Figure 3.2).

With a base vacuum pressure of 6×10^{-6} mbar The DC-Sputtering deposition parameters are:

Mo_A: 330W 15 sccm Ar (34% A.V., $P \sim 1.5 \times 10^{-3}$ mbar), typically rates @ $20 \text{ nm} \cdot \text{min}^{-1}$ (i.e. 25 - 30 min deposition).

Mo_B: 220W 15 sccm Ar (16.5% A.V., $P \sim 5 \times 10^{-3}$ mbar), typically rates @ $15 \text{ nm} \cdot \text{min}^{-1}$ (i.e. 8 - 10 min deposition).

Mo_{A-Sacrificial layer}: 330W 15 sccm Ar (34% A.V., $P \sim 1.5 \times 10^{-3}$ mbar), typically rates @ $20 \text{ nm} \cdot \text{min}^{-1}$ (i.e. 2 - 3 min deposition).

An XRF measurement measured thickness should be around 690 - 730 nm and the (four-point probe) sheet resistance around $0.3 - 0.4 \Omega/\square$. After this step, it would be strongly recommended to vacuum storage the Mo deposited structure during one week to endurance the metallic behavior performance.

3.3 Kesterite Precursor Metallic Layer Sputtering Deposition

With a base vacuum pressure of 7×10^{-6} mbar, the DC-Sputtering deposition parameters are as follow:

Cu_{Under-layer} (~20 nm): 100 W (~400 V, 0.25 A) @ 30 sccm Ar (25% A.V., $P \sim 3.3 \times 10^{-3}$ mbar), during 20 seconds.

Sn (290 nm): 50 W (~420 V, 0.12 A) @ 30 sccm Ar (25% A.V., $P \sim 3.3 \times 10^{-3}$ mbar), at typically deposition rates of $9.5 \text{ nm} \cdot \text{min}^{-1}$ (i.e. around 30 - 31 minutes as deposition time).

Cu (190 nm): 100 W (~400 V, 0.25 A) @ 30 sccm Ar (25% A.V., $P \sim 3.3 \times 10^{-3}$ mbar), at typically deposition rates of $13.3 \text{ nm} \cdot \text{min}^{-1}$ (i.e. around 14 -15 minutes deposition).

Zn (175 nm): 100 W (~500 V, 0.20 A) @ 30 sccm Ar (25% A.V., $P \sim 3.3 \times 10^{-3}$ mbar), at typically deposition rates of $23 \text{ nm} \cdot \text{min}^{-1}$ (i.e. around 7 - 8 minutes deposition).

Aiming as precursor XRF-measured compositional ratios:

$$\text{Cu}/(\text{Zn}+\text{Sn}) = 0.63 - 0.73$$

$$\text{Zn}/\text{Sn} = 1.03 - 1.13$$

$$\text{Cu}/\text{Zn} = 1.35 - 1.45$$

$$\text{Cu}/\text{Sn} = 1.40 - 1.50$$

Experimental procedure →



Figure 3.3.- Collage sketch for the general overview of the experimental solar cell device line processing steps followed during this Thesis.

As it is sketched in Figure 3.3, the typical standard sequential processed SEMS-IREC kesterite-based solar cell begins with the deposition of the CZT precursor material layers that has been performed by a joined sequential metallic layer deposition process in the SLG/Mo/Cu/Sn/Cu/Zn configuration.

In this way, a metallic precursor stacking was deposited by DC-magnetron sputtering (Alliance Concept Ac450) over Mo (≈ 700 nm, $0.3 \Omega \cdot \text{sq}^{-1}$) coated 3 mm SLG substrates. Therefore, the film composition was adjusted near the range of those reported as optimal for high-efficiency CZTSe solar cell devices ¹⁻³, i.e., the so-called Cu-poor-Zn-rich regime.

3.4 Absorber Synthesis and Device Fabrication

3.4.1 Absorber Material Development

The absorber layer formation experimental procedure is mainly divided in two stages (See Figure 5.8 and Figure 5.9 in Chapter V).

Formerly, at the 1st stage of the process, the synthesis and crystallization of the CZTSe absorber material is implemented as the first thermal reactive annealing (See Figure 3.3, selenization stage). Thus, a novelty second stage (sulfurization) for this process is introduced as an in-situ superficial chalcogenide reactive insertion.

3.4.2 Front Graded Bandgap on Kesterite

$\text{Cu}_2\text{ZnSn}(\text{S},\text{Se})_4$ thin-film absorbers were fabricated by modifying the standard sequential SEMS-IREC process, based on a reactive thermal annealing “chalcogenization” process of sputtered Cu/Sn/Cu/Zn metallic layered precursor ($\text{C}/\text{ZT}= 0.70$, $\text{Z}/\text{T}= 1.04$, $\text{C}/\text{Z}= 1.37$, $\text{C}/\text{T}=1.43$) thin films resulting in absorber materials with compositions around ($\text{C}/\text{ZT}= 0.71$, $\text{Z}/\text{T}= 1.09$, $\text{C}/\text{Z}= 1.37$, $\text{C}/\text{T}=1.49$) which are detailed and reported elsewhere.^{2,4,5}

This process optimization relays on a special setup was designed based on a multi-zoned tubular furnace with a double semi-open graphite box system interconnected by a quartz tube as it is later discussed and demonstrated in Chapter V.

3.5 Absorber Surface Cleaning and Passivation: Chemical Etchings

The as-synthesized kesterite absorber materials were typically subjected to always fresh and new solutions by one or two wet-chemical etchings.

Superficial passivation and removal of spurious secondary phases figured as the main porpoise of this procedure (See Figure i.5 in Thesis Appendix: Additional and Supporting Information):

- Potassium permanganate (KMnO₄ + H₂SO)
- Amonium sulfide ((NH₄)₂S)
- Hydrochloric acid (HCl)
- Potassium cyanide (KCN)

A purely empirical evidenced demonstration on the most adequate superficial cleaning chemical etching for each kesterite thin film solar cell technology fabricated in this Thesis is provided below (See Figure 3.4).

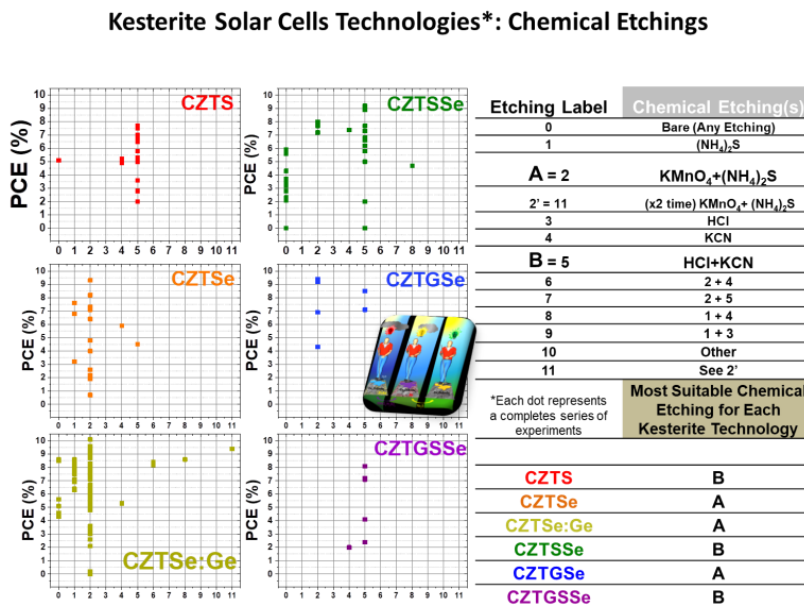


Figure 3.4.- Best chemical etching for each kesterite technology developed during this Thesis. (See Figure i.5 in Thesis Appendix: Additional and Supporting Information):

In this sense, Figure 3.4 schematizes the record PCE obtained for various chemical etchings applied in each kesterite technology developed and optimized in this Thesis.

Immediately after applying any chemical etching(s), the samples were rinsed in deionized water and therefore, perpendicularly positioned with respect to chemical bath deposition (CBD) flow direction, a typical SEMS-IREC CdS (50 nm) buffer layer was deposited by a $[\text{Cd}(\text{NO}_3)_2] = 0.12 \text{ M} + [\text{Thiourea}] = 0.3 \text{ M}$ ($\text{pH} \approx 9.5$, $T \approx 80 \text{ }^\circ\text{C}$) magnetically stirred, and combined solution, during 40 minutes.^{8–10}

The devices were subsequently finished by DC-magnetron sputtering (Alliance Concept CT100) deposition of a $\text{iZnO}(\sim 50 \text{ nm})/\text{In}_2\text{O}_3:\text{SnO}_2$ (ITO: $\sim 250 \text{ nm}$, $200 \text{ }^\circ\text{C}$, $60 \text{ } \Omega/\square$) bilayer. For the optoelectronic characterization, $3 \times 3 \text{ mm}^2$ solar cells were mechanically insulated with a manual microdiamond scribe (MR200 OEG). An example of a typical processed solar cell device is shown in the confocal microscopy images of Figure 3.5.

In this work, neither antireflective coating (ARC) nor metallic grids (fingers) were utilized for the optoelectronic characterization of the solar cell devices.

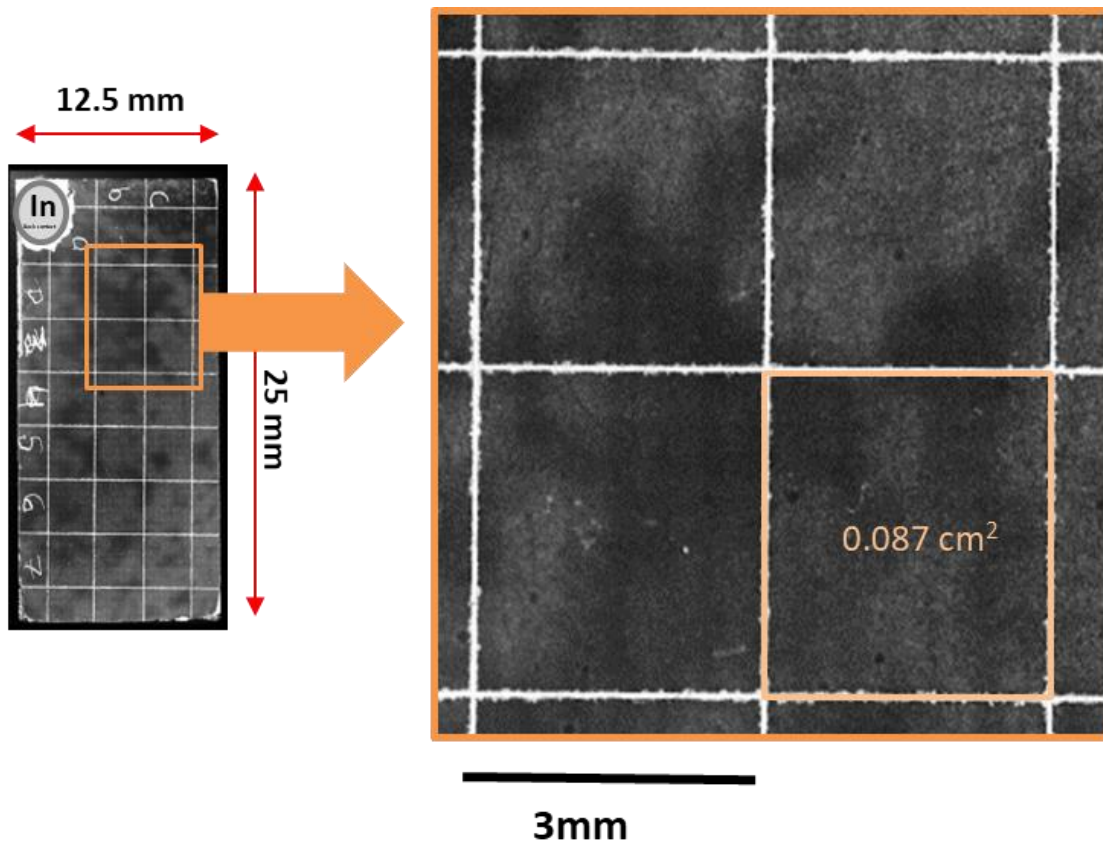


Figure 3.5.- Kesterite solar cell confocal microscopy images. The inhomogeneous contrast inside of the cells is related to surface roughness differences. The indium-shoot welded Mo/In back contact is also schematized.

3.6 Thin Film Material and Systems Characterization

3.6.1 General Overview

Thermal gravimetric analysis (TGA 4000 System, from PerkinElmer) was employed to investigate the Nature and the behavior of the sulfur pulses introduced in the annealing using different chalcogen sources. The TGA curves were acquired in the range of 200 – 600 °C at a heating rate (ramping) of 50 °C.min⁻¹ at 1 bar. Finally, a 20 mL.min⁻¹ N₂ gas flux was utilized during TGA measurements.

The overall composition and thickness of the thin film precursor layers were measured by using X-ray fluorescence (XRF) system (FISCHERSCOPE XDV) previously calibrated by inductively coupled plasma mass spectrometry (ICP-MS). Moreover, the in-depth chemical composition profiles of the thin film layers were investigated by Glow Discharge Optical Emission Spectroscopy (GDOES) using a Horiba Jobin Yvon GD Profiler 2 spectrometer with an anode diameter of 4 mm and Auger electron spectroscopy by using a Phi 670 scanning Auger nanoprobe. XRD measurements were performed using a Bruker D8 Advance system in Bragg Brentano (θ - 2θ) configuration ranging from 10 to 60° with a step size of 0.018°, an integration time of 1 second, and using a one-dimensional detector. Raman spectroscopy was performed with fHR-640 and iHR320 Horiba Jobin Yvon spectrometers coupled to a Raman probe developed at IREC and a CCD detector (cooled to -70 °C). Five different excitation wavelengths (325, 442, 532, 632, and 785 nm) lasers were employed in backscattering configuration, which allowed presenting the material's solid-state solution Raman peaks in the resonant and non-resonant conditions. An excitation power density of ~ 50 W.cm⁻² was utilized to inhibit any thermal effects on the samples. The Raman shift was calibrated using a Si monocrystal reference and imposing the Raman shift for the main Si band at 520 cm⁻¹. This multiwavelength characterization allowed in-depth compositional analysis of the very top surface and subsurface regions of the absorber materials, owing to the different penetrations of each of the excitation sources employed (an approximately 50 nm penetration depth for the 532 nm source, and 150 nm penetration depth for the 785 nm source) and also permitted to investigate the possible presence of secondary phases that could affect the determination of the compositional gradient.

Top view and cross-sectional Field Emission Scanning Electron Microscopy (FESEM) micrographs were obtained with a ZEISS Series Auriga microscope by applying 5 kV as the accelerating voltage and at working distances of (3 – 5 mm) to study the main morphologic and topographical characteristics and details.

On the other hand, Scanning Transmission Electron Microscopy (STEM) analyses were carried out using a Tecnai F30 from FEI (acceleration voltage of 300 kV). The sample was prepared using the focused ion beam in situ lift-out method and thinned to a final thickness of less than 100 nm using a 5 kV Ga⁺ beam.

Room-temperature CV measurements were performed with an impedance analyzer (E4990A from Keysight Technologies) with an AC-voltage of 30 mV at 25 °C to determine the carrier concentration and SCR width of the pn junctions in the devices. The EQE and reflectance (R) curves of the solar cells were measured utilizing a spectral response system (Bentham PVE300) calibrated with Si and Ge photodiodes.

The EQE values were obtained using a lock-in amplifier system operated at a sensitivity $\sim 100 \text{ mV.nA}^{-1}$. The four point probe electrical measurements were employed to measure the sheet resistance of conductive layers such as Mo and TCOs.

An Everbeing SR-4 setup with four equidistant measuring tips connected to a Keithley 2420 power source was employed for this purpose.

Finally, the JV characteristics of the devices were obtained under simulated AM1.5 illumination (1000 W.m^{-2}) employing a pre-calibrated Sun 3000 Class AAA solar simulator from Abet Technologies (uniform illumination area of $15 \times 15 \text{ cm}^2$). These measurements were carried out at 298 K with 20 – 25% relative humidity and after calibrating the system with a Si solar cell reference.

Table 3.1a.- Summary of the characterization techniques utilized in this Thesis along with their common downsides and main limitations.

Characterization Technique	Source	Main Gathered Information	Resolution Limit	Main Constraints
Thermal Gravimetric Analysis (TGA)	Balance and furnace	<u>Physical phenomena:</u> Phase transitions, Absorption, Adsorption and Desorption <u>Chemical phenomena:</u> Chemisorptions, Thermal decomposition, and Solid-gas reactions (e.g., Oxidation or Reduction)	Maximum temperature of 1000 °C	Exact temperature of the sample cannot be detected
X-Ray Fluorescence (XRF)	X-ray	Fast elemental composition analyses	2 - 5 μm	Sample ionization, elements with $Z < 11$, Cannot distinguish ions of the same element in different valence states or variations among isotopes of an element
Glow Discharge Optical Emission Spectroscopy (GDOES)	Low pressure type plasma	Qualitative and quantitative elemental concentration analyses and layer thickness of thin film materials	Spatial ~ 5 nm	Element calibration dependent
Auger Spectroscopy (AES)	Electron beam	Surface-specific morphological and quantitative elemental and chemical state information	Spatial <1 μm Surface: >20 Å	Reproducibility of results can be a challenge
X-Ray Diffraction (XRD)	X-ray	Crystal structure, Crystallite size	~ 10 μm	Unable to differentiate between CZTS(e), CuSnS(e) ₃ and ZnS(e) phases due to similar crystal structure
(Raman) Spectroscopy	Multiwavelength laser	CZ(T,G)(S,Se) phase and bandgap grading confirmation and secondary phase detection	~ 1 μm	Surface damaging due to long lasting laser exposure, small scan area
Field Emission Scanning Electron Microscopy (FESEM)	Electron beam	Morphological and topographical visualization, grain size approximation	1 - 100 nm	Superficial degradation after prolonged exposure to electron beam often during elemental mapping

Table 3.1b.- Summary of the characterization techniques utilized in this Thesis along with their common downsides and main limitations.

Characterization Technique	Source	Main Gathered Information	Resolution Limit	Main Constraints
Scanning Transmission Electron Microscopy (STEM)	Electron beam	Defect studies, distinguish monocrystalline, polycrystalline and amorphous phases, elemental composition, atomic structure of heterointerfaces	2 - 50 Å	Very extensive and tedious sample preparation which can produce potential artifacts to the samples
Current Density-Voltage (JV)	Electrical bias	Solar cell main optoelectronic parameters	Illuminated area: 55 x 55 mm	Uniformity of irradiance ~ 2% and AM 1.5G spectral match: 0.75 – 1.25
External Quantum Efficiency (EQE)	Optoelectronic bias	Direct determination of thin film total reflectance (R) and transmittance (T) curves: EQE/IPCE, IQE, theoretical J _{sc}	0.3 nm (1200 g/mm) 0.6 nm (600 g/mm)	Diode calibration dependent
Four-Point Probe (4PP)	Electrical bias	Sheet resistivity, Doping quality, P/N probing	Z-Resolution ~ 1 µm	Short-ranged measurement, limited to specimen confinement
Capacitance-Voltage (CV)	Electrical bias	PN junction properties like depletion width, electric field, defect density, defect energy level. Measurement parameters: Z , Y , θ, R, X, G, B, L, C, D, Q, Complex Y & Z, V _{AC} , I _{AC} , V _{DC} , I _{DC}	25 – 40 MΩ Impedance accuracy of ±0.08%	Provides limited information about capture cross-section

3.7 Theoretical Solar PV Physics

The main objective of the following sections of Chapter III, is to briefly contextualize the main optoelectronic analysis and studies of this Thesis' solar cells as solid-state devices.

3.7.1 Semiconductor Materials and the PN Junction

Based on the quantum Nature of light and its implications on the physical phenomena that we recognize as the photovoltaic effect, ¹¹ solar photovoltaics (PV) technologies are the only (so far known) direct energy source systems which allow to produce work; Moreover, the most anthropomorphic utilizable type of work: electricity.

In a physical system with two different energy states such as a semiconducting material or a molecule, the generation of electron–hole pairs by the absorption of sunlight resembles as essential for the operation of solar cells.

The photonic excitation of an electron directly from the valence to the conduction band dropping an electron hole behind is called fundamental absorption.

In this sense, if a photon with energy ($E = h\nu$ where h is the Planck's constant and ν the frequency of the light) is equal or higher than the energy bandgap (E_g) between the top of the valence (VB) and the bottom of the conduction (CB) band strikes an electron positioned in the VB , the electric particle can be excited from the VB to the CB by leaving a free charge deficit, also known as hole.

Therefore, the optical bandgap determines which part of the whole received solar spectrum a photovoltaic solar cell device will absorb. However, the electron–hole pairs generated by the absorption phenomena somehow need to be separated and extracted in order to take an advantage and liberate this “free energy” released by an incoming solar photon.

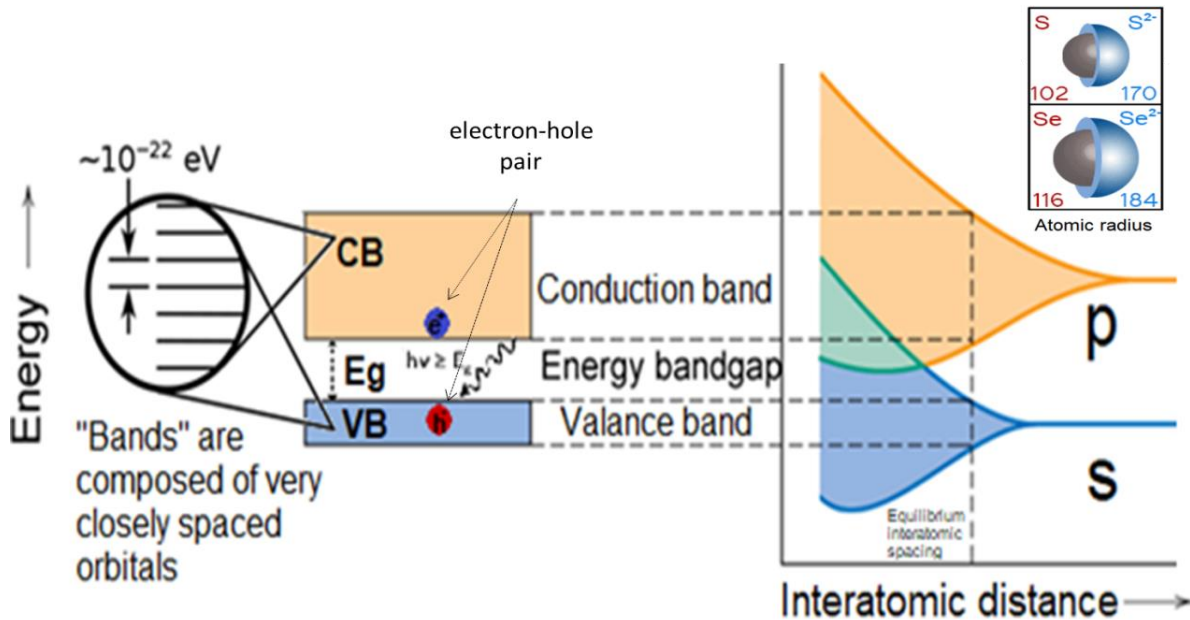


Figure 3.6- Basic band diagram of a semiconductor. *VB* and *CB* stand for valence and conduction band, respectively; E_g is the energy of the forbidden bandgap and $h\nu$ is the energy of an incident photon. The right part plots the energy versus interatomic distance, in which *p* and *s* represent molecular orbital levels. Additionally, it is shown an atomic radius comparison between sulfur (S) and selenium (Se) atoms.

For semiconductor materials, a pn junction diode is capable of generating a built-in electric field, at the same time that it is able to perform a charges separation between electron-holes and electrons to both sides of the junction (Figure 3.6). In this way, the pn junction acts as a double selective contact:

- 1) As selective for the electrons from p to n, and
- 2) As selective for the holes from n to p region.

Due to differences in charge concentrations (Figure 3.7a), once a metallurgic joint of a charge-deficient (p-type) with a charge-excess (n-type) semiconductor materials takes place, the regions nearby the p/n interface get excited and abandon a neutral-charged state due to diffusive and drift processes (Figure 3.7b). Therefore, creating a spatial transition region lacking of mobile electric charge, widely known as depletion or space charge region (**SCR**) at equilibrium.

Thus, the boundary regions of both types of semiconductors experience an electric field force directed from the n to the p side of the junction, which in turn opposes the diffusive processes.

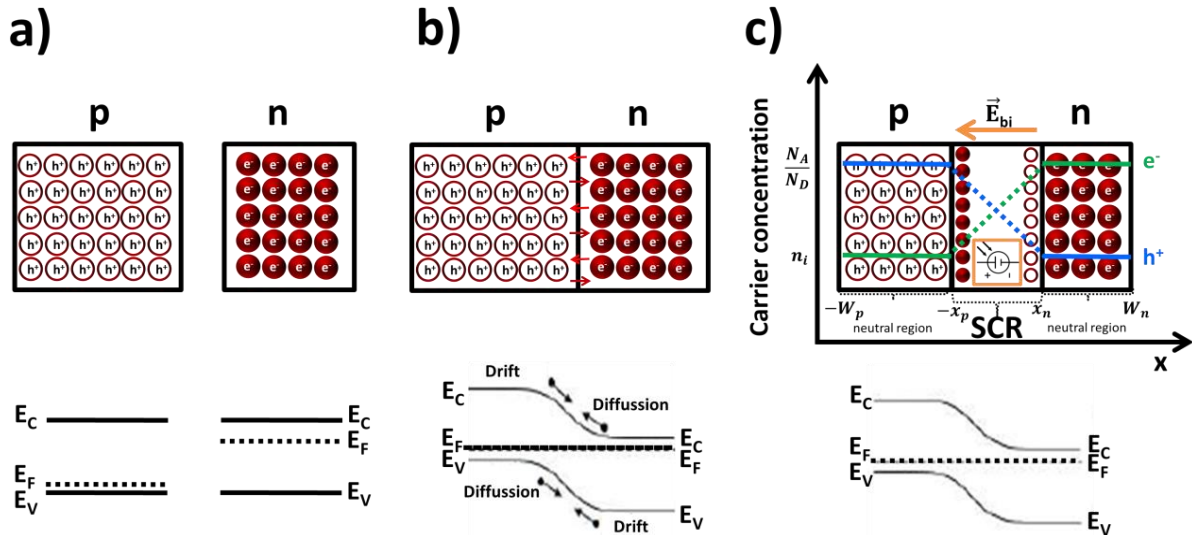


Figure 3.7.- **a)** p- and n-type semiconductors and scheme of energy bands. **b)** pn junction: diffusion (majority carriers) and drift (minority charge carriers) processes after joining the p and n-type semiconductor materials. **c)** Diagram of a pn junction and band alignment at thermodynamic equilibrium. Also, simple solar cell structure used to analyze the operation of a solar cell. Free carriers have diffused across the junction ($x = 0$) leaving a *SCR* practically devoid of any free or mobile charges. The fixed charges in the depletion region are due to ionized donors on the n side and ionized acceptors on the p side.

From Figure 3.7, it is observed that E_C and E_V represent the conduction and valence band energies, respectively, and N_A/N_D represents the acceptor to donor carrier concentration. The intrinsic carrier concentrations ($n_i = n_0 = p_0$) stand for the intrinsic carrier concentration level (same for electrons and holes). In Figure 3.7c, immediately after the drift force exerted on the carriers by the electric field equals the diffusion force, thus an equilibrium state is reached. Then, if the particle-quasiparticle pairs reach the *SCR*, both electrons and electron holes are separated away from each other by the electrostatic potential difference resulting from the junction formation is called the built-in voltage (V_{bi}) that arises from the electric field (\vec{E}_{bi}) created by the exposure of the positive and the negative space charge in the depletion region (Figure 3.7c).

On the other hand, the energy can be radiated, lost in the form of heat, or can be utilized to excite another electron (impact ionization). However, in thermal equilibrium, the diffusion and drift currents for each carrier type exactly balance each other, so there is no net current flow and by definition the Fermi energy (E_F) must be independent of position.

3.7.2 Heterojunction

A heterojunction is an interface that occurs between two layers or regions of dissimilar semiconductors.¹² When the conductivity types differ, the junction is called an anisotype heterojunction. The energy band model of an ideal abrupt heterojunction without interface traps was proposed by Anderson.^{13,14}

Since this model can adequately explain most transport mechanisms, the scientific community often considers this approach to be the most adequate one. The energy band diagram of two isolated semiconductors is shown in Figure 3.8a. These two semiconductors were assumed to have different bandgap (E_{g1} and E_{g2}), permittivity (ϵ_1 and ϵ_2), work function (ϕ_1 and ϕ_2) and electron affinity (χ_1 and χ_2) values.

The energy difference of the conduction and valence band edges for the two different semiconductors -band offsets- are represented by ΔE_C and ΔE_V , respectively. Under Anderson's approach¹³, ΔE_C is considered to be the difference between electron affinity values ($\Delta E_C = \chi_1 - \chi_2$). However, this electron affinity rule may not be a valid assumption; when a junction is formed between these two semiconductors, the energy-band profile at equilibrium strongly depends on affinity, work function and bandgap values of the materials. One example is as shown in Figure 3.8b for a pn anisotype heterojunction.

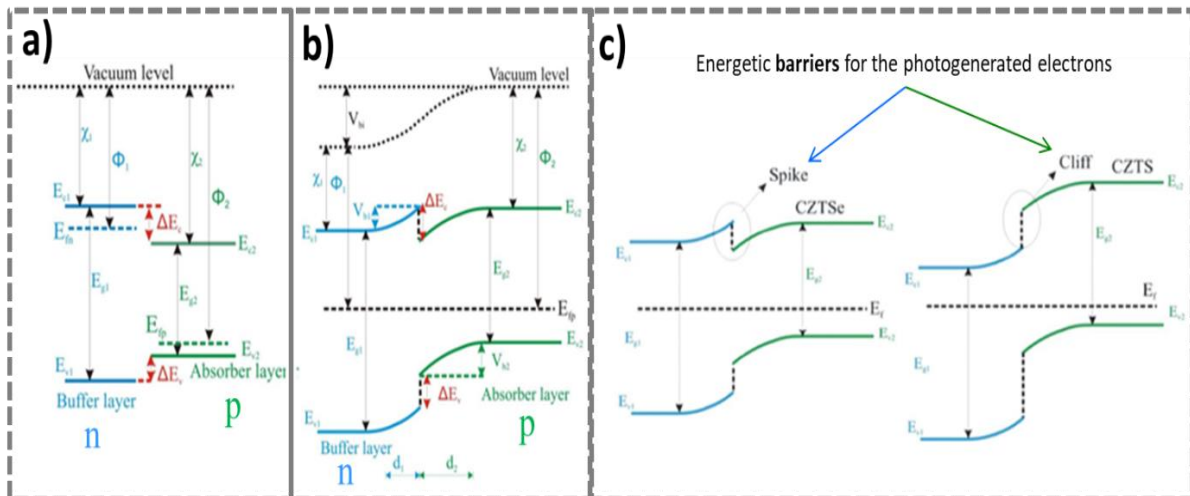


Figure 3.8- **a)** Energy band diagram of two isolated semiconductors with p and n conductivity (buffer and absorber layers). **b)** Equilibrium energy band diagram after the formation of an abrupt p-n heterojunction for CdS/CZTSe. **c)** Band alignment for CZTSe/CdS -spike-like- and CZTS/CdS -cliff-like- heterojunctions.^{15–20}

The energy Fermi level (E_F) of a solid-state body is defined as the thermodynamic work required to add one electron to self's configuration. This level does not necessarily correspond to an actual energy level, nor does it require the existence of a band structure. Nonetheless, the Fermi level is a precisely defined thermodynamic quantity.²¹

On the other hand, a quasi-Fermi level -also called "imref", which is the palindrome for "fermi"- is a term utilized in solid state physics for the Fermi level -chemical potential of electrons- that describes the population of electrons separately in the conduction band (E_{fn}) and valence band (E_{fp}), when their charge carrier populations are displaced from equilibrium.²² Since the Fermi level must coincide on both sides in equilibrium and vacuum levels, it is parallel and continuous at every point of the band edges. The discontinuity in conduction band edges (ΔE_c) and valence band edges (ΔE_v) is invariant with doping (i.e, non-degenerated semiconductors).

Conversely, a depletion layer is formed on either side of the interface. The total built-in potential (V_{bi}) is equal to the sum of the partial built-in voltage ($V_{b1} + V_{b2}$), where V_{b1} and V_{b2} are the electrostatic potentials supported at equilibrium by buffer and absorber semiconductors, respectively. The depletion widths can be obtained by solving Poisson's equation for the step junction on either side of the interface. From Figure 3.7c, and for the sake of simplicity, it is assumed that each side of the pn junction is non-degenerately doped and that the dopants are fully ionized. Within the depletion region, defined by: ($-x_p < x < x_n$), it can also be assumed that p_0 and n_0 are both negligible compared to $|N_A - N_D|$, so that the Poisson equation (3.1) of the electrostatics assuming a single acceptor and a single donor level is:

$$\nabla^2 \varphi = \frac{q}{\varepsilon} (n_0 - p_0 + N_A^- + N_D^+) \quad (3.1)$$

Where φ is the electrostatic potential, q the electron charge, ε is the electric permittivity of the semiconductor, n_0 and p_0 are the equilibrium electron and hole concentrations. N_A^- and N_D^+ are the ionized acceptor and donor concentrations, respectively. Thus, Equation (3.1) may be simplified to (3.2 and 3.3):

$$\nabla^2 \varphi = \frac{q}{\varepsilon} N_D^+ \quad \text{for } (0 < x < x_n) \quad (3.2)$$

$$\nabla^2 \varphi = -\frac{q}{\varepsilon} N_A^- \quad \text{for } (-x_p < x < 0) \quad (3.3)$$

However, outside of the *SCR*, charge neutrality is assumed:

$$\nabla^2 \varphi = 0 \quad \text{for } (x < -x_p \text{ and } x > x_n) \quad (3.4)$$

This is commonly referred to as the depletion approximation. The regions on either side of the depletion regions are the quasi-neutral regions.

By applying as boundary condition the continuity of the electric displacement that is at the interface of the junction:

$$\varepsilon_1 \mathbf{E}_1 = \varepsilon_2 \mathbf{E}_2 \quad \text{for } (x = 0) \quad (3.5)$$

After solving these equations, the expression obtained for the *SCR* depletion widths is as follows:

$$d_1 = \sqrt{\frac{2N_{A2}\varepsilon_1\varepsilon_2(V_{bi}-V)}{qN_{D1}(\varepsilon_1N_{D1}+\varepsilon_2N_{A2})}} \quad (3.6.1)$$

&

$$d_2 = \sqrt{\frac{2N_{D1}\varepsilon_1\varepsilon_2(V_{bi}-V)}{qN_{A2}(\varepsilon_1N_{D1}+\varepsilon_2N_{A2})}} \quad (3.6.2)$$

In general, $N_{D1} \gg N_{A2}$ and since in kesterite thin film systems $V_{bi} \approx 1V$, the depletion width formula greatly simplifies into:

$$d = \sqrt{\frac{2\varepsilon_1\varepsilon_2}{qN_A}} \quad (3.6.3)$$

Up to date, there has not been proposed any model capable to even nearly explain the physical phenomena and energy band coupling of heterojunctions. Even though, particularly for kesterite compounds, two types of alignments have been observed²³⁻²⁵ as it is shown in Figure 3.8.

In before, from Figure 3.7c, once the non-recombined electron-hole pairs, whose diffusion length allows them to be effectively separated by the *SCR*, reach a steady-state equilibrium condition, an “open circuit voltage” (V_{OC}) across the pn junction is settled-up. Thus, the imref level splitting (E_{fn} and E_{fp}) drives the maximum value of the solar cell V_{OC} .

Whereas electronic charges cannot effectively flow through the device, there is no current and no power can be extracted from the cell. If the electronic circuit constituted by the pn junction holds to short circuit current (J_{SC}) conditions -through an external ideal non-resistive wire for example-, charges can freely escape the solar cell.

Since there is no external load and/or resistive elements, a maximum of photogenerated and intrinsic charge carriers can flow freely towards the opposite side of the circuit through the wire and recombine there. As there is no voltage, no power can be extracted from the pn diode. In this sense, J_{SC} is defined as the current delivered by the cell at no bias, when the diode is directly polarized -forward bias-.

Furthermore, aiming to effectively extract power from the solar cell -pn diode-, an external load is connected to the device, the photogenerated and intrinsic charge carriers can accumulate inside both sides of the pn junction up to a certain point in which the voltage between them is high enough to leave the cell generating an electrical current and, this way producing electrical work at the load. In this regard, kesterite thin film solar cells are two-electrode -cathode and anode- metallized pn diodes, which constitutive layers are optimized for converting the incident solar radiation into electrical energy. As a way of understanding how the light reaches the devices and how the charges are extracted from the cells, it is necessary to look at the internal structure of a solar cell. Figure 3.9a shows the basic structure of a pn diode solar cell, which consists of:

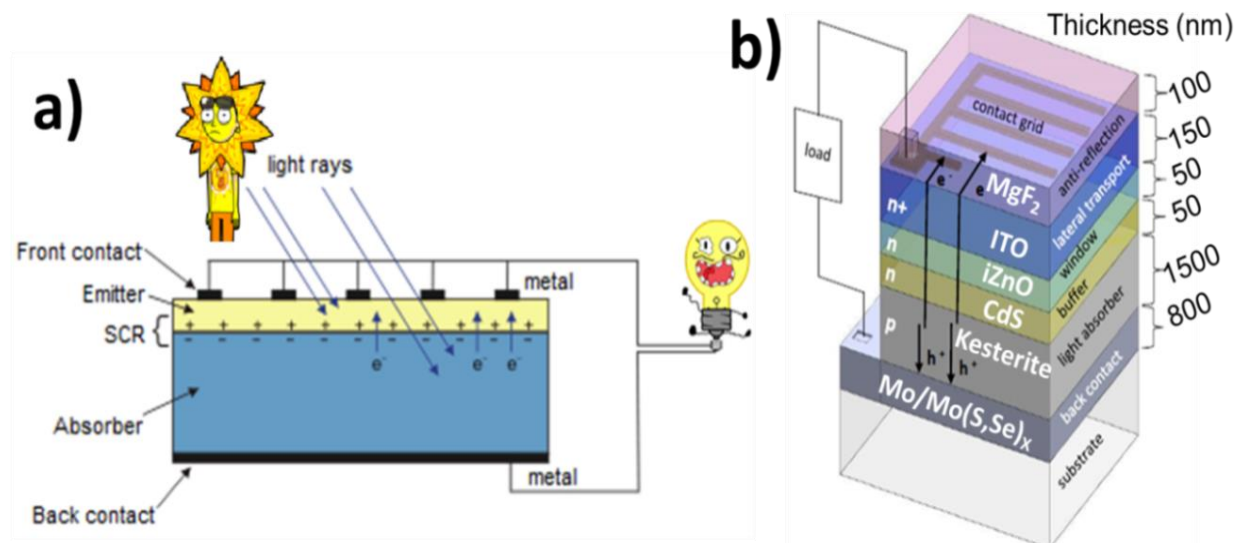


Figure 3.9- a) Basic structure of a pn diode solar cell. b) Typical structure of a kesterite based thin film solar cell.

-Absorber: (Kesterite layer in Figure 3.9b); in this material, most of the light is absorbed and most of the free charge carriers are generated in this layer. Accordingly to the detailed balance (Shockley Queisser Efficiency Limit, later discussed in this Chapter), its bandgap should be around $1.1 - 1.4 \text{ eV}$, for the purpose of most efficiently absorbing sunlight in terms the radiative efficiency limit.²⁶

-Emitter (buffer layer): (CdS/iZnO in Figure 3.9b); this material must be as transparent as possible to sunlight, so it can reach the absorber. In pn junction cells, the buffer layer must possess the opposite conductive type of semiconductor than that of the absorber.

-Back and a front contact: Mo and Indium tin oxide (ITO), respectively in Figure 3.9b; the contacts capture and conduct the charge carriers allowing them to travel into an external circuit.

Normally, metallic materials are utilized due to their high conductivity and good charge transport properties. However, other materials like graphene, transparent conductive oxides or even organic layers are also commonly employed. Each part of the solar cell is usually constituted by a combination of different layers to optimize its properties for charge generation, separation and/or collection and to avoid any incompatibilities between them that can cause losses. Therefore, each solar PV technology has its own optimized layer structure. Figure 3.9b shows a typical multi-layered structure of a typical kesterite thin film solar cell.

3.7.3 Optoelectronic PV Physics

In a practical way, it might be easier to handle the problem of a biased solar cell by means of a mathematical artifact, in which the current is modeled as the sum of two opposite sign electrical currents. The former stands for the photocurrent (J_{ph}), which is equal to the short circuit current density (J_{SC}), that is constant at any bias voltage and flows from the front contact to the back contact. The second current is the diode current (J_d), -or recombination current-, that flows in the opposite direction and increases with voltage. With this model, the current as a function of the voltage of the solar cell could be expressed as:

$$J(V) = J_{ph} - J_d(V) \quad (3.7)$$

In Equation 3.7, $J(V)$ corresponds to the net current flowing through the solar device. Then, the pn diodes are commonly modeled with a one-dimensional diode equation. In dark conditions, the voltage-dependent recombination current $J_d(V)$ can be expressed as:

$$J_d(V) = J_0 \left[\exp\left(\frac{qV}{k_B T}\right) - 1 \right] \quad (3.8)$$

In Eq. (3.8), J_0 represents the -dark- reverse saturation current, k_B is the Boltzmann's constant and T is the temperature. Normally, under unbiased conditions $J_{SC} > 0$, while $J_d = 0$. The voltage at which $J_{SC} = J_d(V)$ is the open circuit voltage. Thus, if illumination is removed, $J_{SC} = 0$ and the current-voltage behavior of the solar cell becomes that of a pn junction diode:

$$J(V) = -J_d(V) \quad (3.9)$$

On the other hand, under illumination conditions, it is necessary to add to the former equation an extra term in order to include the photocurrent generated by the cell (J_{SC}):

$$J(V) = J_0 \left[\exp\left(\frac{qV}{k_B T}\right) - 1 \right] - J_{SC} \quad (3.10)$$

Therefore, it could be observed that this equation describes the electric behavior of an equivalent to a circuit with a current source and a parallel connected diode. A graphical representation of this dark and illuminated solar cell behavior is later observed in Figure 3.11a. From this figure, it is possible to extract the main parameters that describe the operation of solar cells. As it was previously commented, the maximum possible voltage of a solar cell is the V_{OC} and the maximum current density is the J_{SC} . The product of these last two parameters defines the maximum theoretical -mostly thermodynamic- power of the cell. However, in real operating conditions, the maximum power that can be extracted from a solar cell (P_{max}) is given by the point of the JV curve that maximizes the current-voltage product and is called the maximum power point (MPP). The MPP defines the current density and voltage at maximum power denoted by J_{mp} and V_{mp} respectively. The ratio between P_{max} and P_{theo} is called the Fill Factor (FF):

$$FF = \frac{P_{max}}{P_{theo}} = \frac{J_{mp} V_{mp}}{J_{sc} V_{oc}} \quad (3.11)$$

This parameter measures the behavior similarities of a JV curve of the solar cell with respect to its theoretically idealized diode version, i.e., the more the illuminated JV characteristic of the solar cell approximates to a square, or in other words, the closer the FF is to the unity (1).

Finally, the power conversion efficiency (PCE, η) of a solar cell, i.e. the ratio between the maximum power generated by the device P_{max} and the power reaching the solar cell (P_{in}), is usually expressed as:

$$\eta = \frac{P_{max}}{P_{in}} = \frac{J_{mp} V_{mp}}{P_{in}} = \frac{J_{sc} V_{oc} FF}{P_{in}} = \frac{J_{sc} V_{oc} FF}{\int_0^{\infty} n_{ph}(E) E dE} \quad (3.12)$$

In standard measuring conditions, $P_{in} = \int_0^{\infty} n_{ph}(E) E dE$ corresponds to the power extracted from the integration of the solar spectrum at standard test conditions for a 1.5 Air Mass in which the Sun is about 41° above the horizon (STC-AM1.5g ($\sim 100 \text{ mW}/\text{cm}^2$ or 1 Sun at 1 atm and 25°C).²⁷ Thus, as a way of experimentally measuring the efficiency of a solar cell (See Figure 3.10), it is not enough to measure what voltage (V) and current (I) it produces without load. When measuring the voltage with a voltmeter directly over the solar cell contacts, the V_{oc} is being obtained, which is the voltage of the unloaded circuit. At a higher load, the voltage will drop until the load is infinitely high. The situation reached by infinite load is a short circuit of the system and is precisely the state that is measured when an ammeter is connected to the solar cell for the purpose of accurately measuring the current intensity passing through the solar cell measurement circuit (See Figure 3.10).

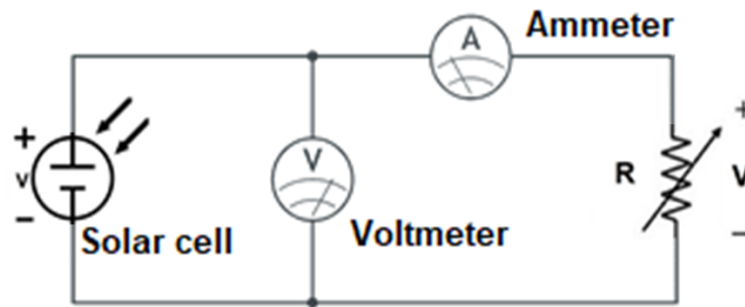


Figure 3.10- Equivalent electronic circuit for experimentally test and obtain the characteristic IV curves for solar cell devices.

Considering the total power (P) is defined as:

$$P = I \times V \quad (3.13)$$

It is possible to find the point where the solar cell produces the maximum power, we therefore need to expose the solar cell to many different loads and measure current and voltage. Then, the maximum power point (MPP) is calculated as the product of power and voltage.

3.7.4 Characteristic JV Curves

The current-voltage curve (IV) or in a more comparative fashion, the current density-voltage (JV) is utilized and shows the possible combinations of voltage dependent pairs the photovoltaic device. Conceptually, the JV curve represents the combinations of current and voltage at which the cell can operate, if the irradiance and cell temperature are kept constant.

The evaluation of the performance of solar cells and the design of photovoltaic systems must be based on the electrical characteristics, that is, in the current-voltage relationships of the cells subjected to various levels of irradiation and temperature. Since solar cells convert light to electricity it might seem odd to measure the photovoltaic cells in the dark. However, dark IV measurements are invaluable in examining the diode properties.

Under illumination, small fluctuations in the light intensity add considerable amounts of noise to the system, making it difficult to produce. Dark IV measurements utilize injected carriers into the circuit with electrical means rather than with light generated carriers.

In this sense, the current paths under illumination and in the dark are the same. In the dark condition case the current flows into the cell and in the illuminated case the current flows out of the cell. The use of Dark IV curves in solar cell analysis relies on the principle of superposition.

That is, in the absence of resistive effects, that the light IV curve is the dark IV curve shifted by the light generated current. Figure 11a shows the characteristic dark and STC-AM1.5g illuminated JV curves of a kesterite (CZTGSe) solar cell represented by Equations (3.10) and (3.15).

Furthermore, since the solar cell is a power source, Figure 3.11b depicts the power-voltage (PV), also known as “output power curve”. The horizontal axis represents the working cell bias voltage (V) and the vertical axis the current density ($J = [mA \cdot cm^{-2}]$) for Figure 3.11a and ($P = [mW \cdot cm^{-2}]$) for Figure 3.11b.

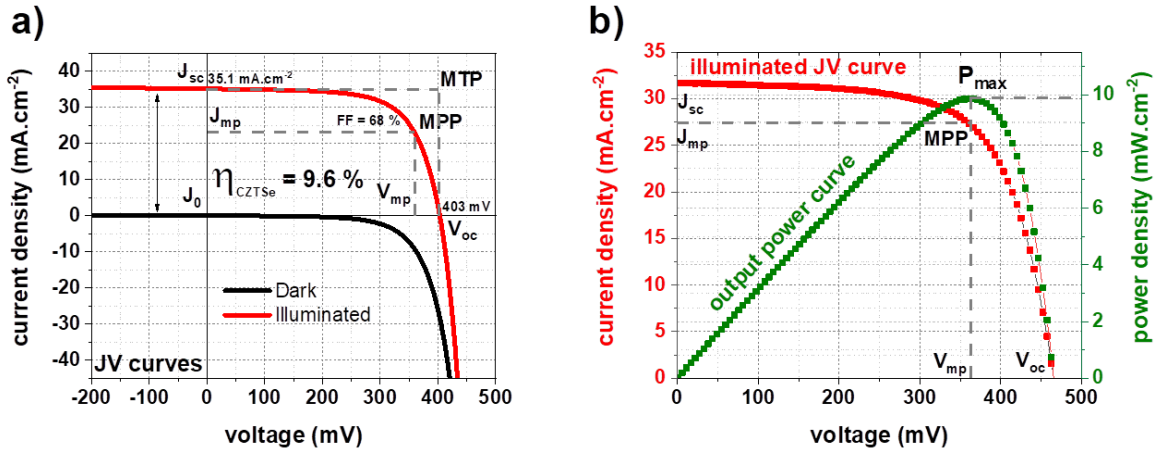


Figure 3.11- **a)** Characteristic dark and illuminated JV curves of a kesterite (CZTSe:Ge) solar cell represented by Equations (11) and (16). **b)** Illuminated JV and output power curves. The main parameters used for its description are also depicted. MTP stands for maximum theoretical power point.

The output power curve shows the energy produced by the solar cell at a point, called “operating point”, in any part of the PV curve. The solar cell will produce the maximum intensity when the resistance between the terminals of the output circuit is minimal; this is when there is short circuit.

In before (See Chapter I and Chapter II), a more realistic approach of a solar cell is subjected to several losses. Some of these can be enclosed in the parameters: series (R_S) and shunt resistance (R_{SH}). The series resistance includes all the resistive losses along the device -different layers and the contact resistance between them at the interfaces- (See Figure 3.9) while R_{SH} accounts for losses caused by alternative current paths – shunts-. Therefore, these parameters can be included in Equation (3.14) as follows:

$$J(V) = J_0 \left[\exp\left(\frac{qV - qJR_S}{k_B T}\right) - 1 \right] + \frac{V - JR_S}{R_{SH}} - J_{ph} \quad (3.14)$$

The electric circuit represented by this equation can be observed in Figure 3.12. Equation (3.14) accurately describes an ideal solar cell behavior, in which the main recombination losses occur by radiative processes taking place in the neutral region, diffusion and thermionic emission. However, in the case of non-ideal solar cells, there are important losses due to recombination inside the SCR . This recombination can have both radiative and non-radiative components.

Inside the non-radiative, the main recombination mechanisms are kesterite/buffer interface recombination, Shockley-Read-Hall (*SRH*) bulk, trap-assisted tunneling, and Auger recombination.

All of these losses can be included in Equation (3.14) by means of an extra term known as the diode quality factor, n .

$$J(V) = J_0 \left[\exp\left(\frac{qV - qJR_s}{nk_B T}\right) - 1 \right] + \frac{V - JR_s}{R_{SH}} - J_{ph} \quad (3.15)$$

Therefore, the equivalent electronic circuit may be represented as it is shown in Figure 3.12:

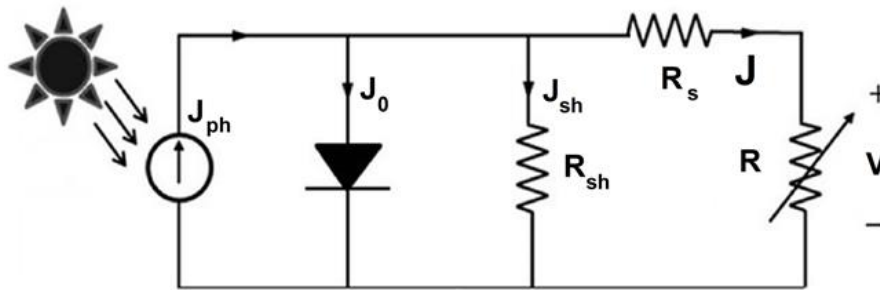


Figure 3.12- Solar cell with resistive and shunt losses equivalent circuit. J_{ph} corresponds to the photogenerated current and J_{SH} stands for the shunt current density.

The diode parameter (n) relates the voltage dependence of the main recombination path between short circuit conditions and the open circuit voltage point. In this sense, the higher its value, the more gradually the recombination current increases between zero bias and the open circuit voltage. In principle, the value of n is fixed by the type of recombination that is dominant.

For example, in an ideal solar cell with pure band-to-band recombination $n = 1$; in a solar cell with *SRH*-recombination domination in the depletion region through defective states near the absorber material's midgap $\left(\frac{E_g}{2}\right)$, $n = 2$.²⁸

Further, in order to gather additional information regarding device behavior and possible recombination losses due to charge carrier recombination or shunt and series resistance, it is necessary to deeply analyze the JV measurements in an extended manner.

Non-trivially, but commonly practiced in thin film solar cells JV analysis, is the application of the single diode fitting model with the purpose of obtaining parameters such as diode quality factor (n), series (R_S), and shunt (R_{SH}) resistances, and saturation current density (J_0) parameters.²⁹

$$J(V) = J_0 \left[\exp\left(\frac{qV - qJR_S}{nk_B T}\right) - 1 \right] + \frac{V - JR_S}{R_{SH}} - J_{SC} \quad (3.16)$$

In this regards, a methodology mainly based on linear fitting of dV/dJ vs. $(J + J_{SC}) - 1$ with a correction factor for shunting resistance is proposed in literature³⁰. In this procedure, starting from the equation standing for the single diode model for a solar cell equation:

$$J(V) = J_0 \left[\exp\left(\frac{q(V - JR_S)}{nk_B T}\right) \right] + \frac{V}{R_{SH}} - J_{SC} \quad (3.17)$$

From Equation (3.17), the derivation dJ/dV yields to:

$$\frac{dJ}{dV} = \frac{1}{R_{SH}} + J_0 \left[\exp\left(\frac{q(V - JR_S)}{nk_B T}\right) \right] \frac{q}{nk_B T} \quad (3.18)$$

Therefore, in reverse bias conditions:

$$dJ/dV = 1/R_{SH} = G_{SH} \quad (3.19)$$

Also known as shunt conductance (G_{SH}).

On the other hand, the derivative dV/dJ of Equation (3.17) yields to:

$$\frac{dV}{dJ} = \frac{nKT}{q} \left(\frac{1 - \frac{1}{R_{SH}} \frac{dV}{dJ}}{J + J_{SC} - \frac{1}{R_{SH}} V} \right) + R_S \quad (3.20)$$

Thus, the linear fitting of: $\frac{dV}{dJ}$ vs. $\left(\frac{1 - \frac{1}{R_{SH}} \frac{dV}{dJ}}{J + J_{SC} - \frac{1}{R_{SH}} V}\right)$, the parameter R_S can be obtained from the intercept and A (also known as n) from the slope of the fit.

Utilizing the extracted R_{SH} and R_S to correct density voltage plot $\left(J + J_{SC} - \frac{1}{R_{SH}} V\right)$ vs. $(V - JR_S)$, it is possible to obtain the J_0 and n parameters by fitting $y = J_0 \exp \frac{q}{nk_B T} x$ as it is shown in Figure 3.13.

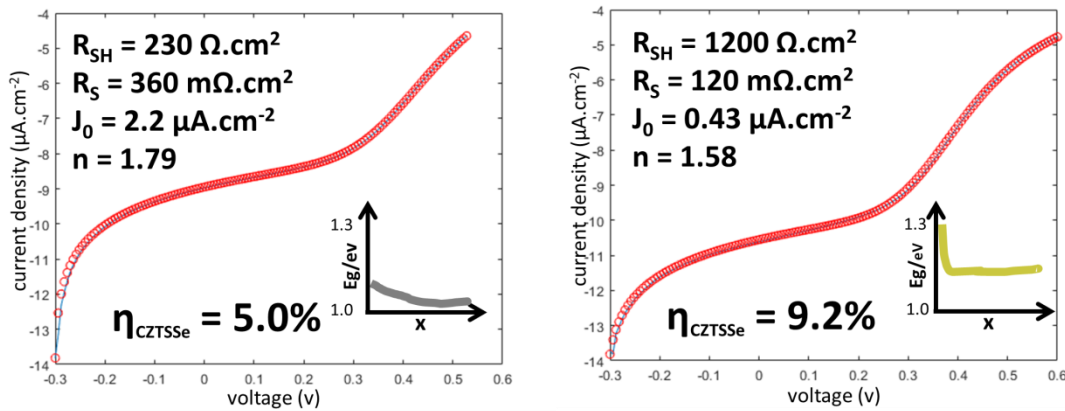


Figure 3.13- Examples for different logarithmic scale JV fittings for kesterite solar cells.

The main importance of calculating these parameters when processing thin film solar cells is described below:

- Series resistance (R_S): related to any parameter hindering the movement of minority carriers toward the extraction point. Mostly affects the FF and P_{max} but not J_{SC} -unless R_S is huge-.
- Shunt resistance (R_{SH}): demonstrates the existence of a short-circuit within the system bypassing -shunt paths- the diode. It is related to fabrication issues rather than intrinsically linked to the design of the heterostructure. It affects most of the cell parameters, which can specially impact the FF .

In this sense, good devices require low R_S and high R_{SH} and ultimately high FF values.

-Reverse saturation current (J_0): leakage current through the diode in reverse bias - opposes the photocurrent-. It is, therefore, specific to each diode in a two diode model (not discussed in this Thesis). This current is related to carrier recombination, often within the SCR -on either sides of the pn junction-. It will mostly affect the V_{OC} of the cells.

-Ideality factor (n): it quantifies the difference between an ideal diode and the real device, where second order effects -specifically recombination bulk and interface- can affect the JV characteristic curves.

The ideality factor of a well behaved thin film solar cell is typically in the range 1.3 – 2. If the recombination processes occur in the neutral region, $n = 1$. If recombinations in the space charge region dominate, $n = 2$. It will mostly affect the FF of the cell.

Finally, $n > 2$ indicates the junction is incorporating additional tunneling recombination.

Several factors may limit the solar cell efficiency; the most important ones are shunt resistance arising from leakage of current through the cell, series resistance coming from each layer composing the solar cell and the interfaces between the layers, and carrier recombination that may occur in the layer stacking (See Figure 3.9b).

3.7.5 Shockley–Queisser Efficiency Limit and the $JV - E_g$ Dependence

The limiting values for the main solar cell optoelectronic parameters: J_{SC} , V_{OC} , and FF can also be calculated as a function of the bandgap (E_g). As it was previously commented, the limiting J_{SC} is calculated by assuming unity quantum efficiency for all energies above E_g . Limiting V_{OC} , is calculated by assuming the solar cell to be a perfect black body, with any non-radiative recombination. Limiting FF is calculated by optimizing the JV curves.

The equations for these calculations were shown in ³¹ and the results are shown in Figure 3.14 for STC-AM1.5g. ²⁷ From Figure 3.14, it can be seen how these parameters follow a trend along with the E_g values. The limiting J_{SC} value is largest at low E_g values, while V_{OC} and FF are largest at higher E_g values. Since this calculation is not done at absolute zero, the ideal FF is less than 100%, and the ideal V_{OC} is below the E_g value.

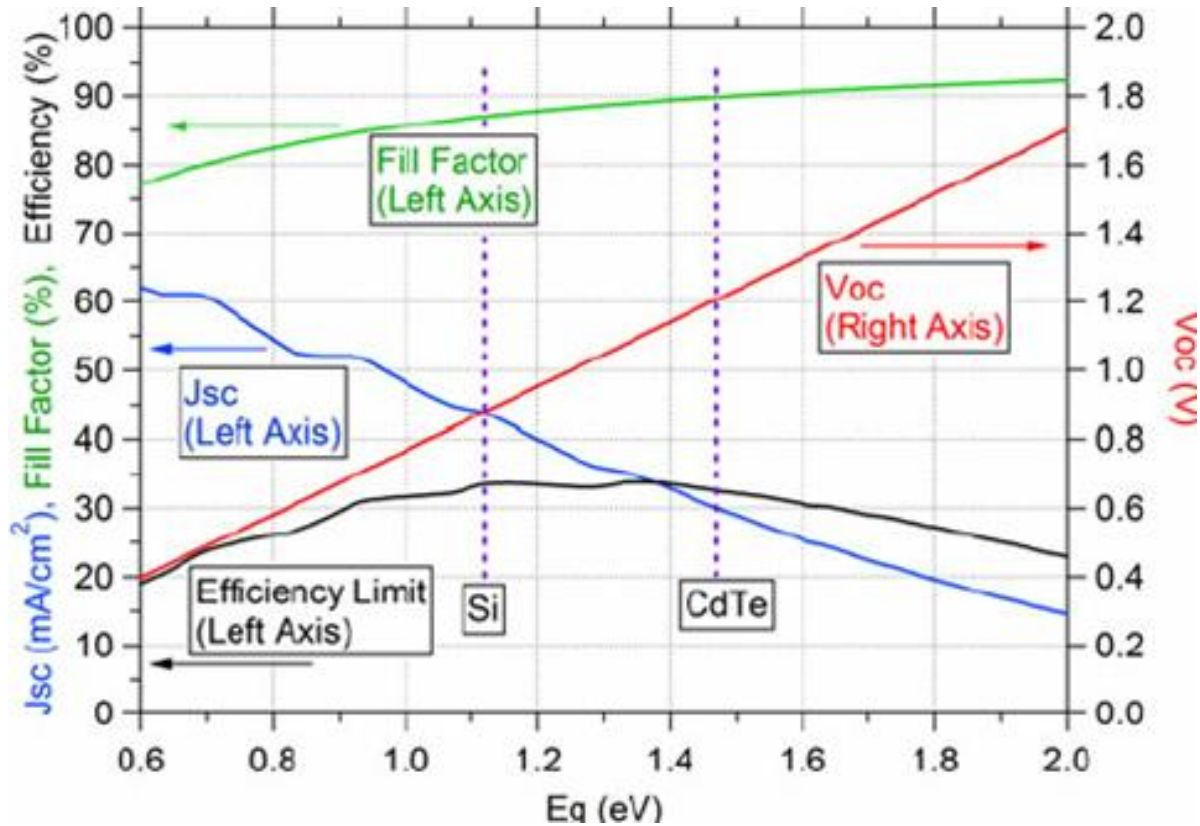


Figure 3.14- Ideal values for J_{sc} , V_{oc} , FF and η with changes in E_g values (under STC-AM1.5g). The room temperature E_g values of Si and CdTe are plot-marked as reference.³⁴

3.7.6 Spectral Response and Quantum Efficiency

As it was previously commented, the dark and illuminated JV measurements are powerful characterization tools for solar cell's general output and electrical behavior. However, a detailed spectral analysis of the optoelectronic characteristics of the solar cell devices is found in the Quantum Efficiency (QE) measurements.

The QE determines the number of electron-hole pairs generated and effectively collected by the solar cell compared to the number of spectrally incident photons on the device, while the spectral response is the ratio of the current generated by the solar cell to the power incident on the solar cell.

The Spectral Response (SR) and the QE are both utilized in solar cell analysis and the choice depends on the application.

The SR uses the power of the light at each wavelength (λ) whereas the quantum efficiency uses the photon flux. Naturally, it is possible to convert the QE into SR -, which is done with the following formula:

$$SR(\lambda) = \frac{q\lambda}{hc} QE(\lambda) \quad (3.21)$$

Experimentally, in order to obtain one or the other of these parameters - QE or SR -, a calibration photodiode -for example Si or Ge depending on the wavelength range- detector responsivity is normally measured.

Therefore, this spectrum is utilized as a reference and posteriorly matched with solar cell response to spectral excitation (See Figure 3.15).

However, it is important to note that the External Quantum Efficiency (EQE) is recorded without considering losses due to reflection or absorption in the window layers. By measuring the reflectance (R) of the solar cell device, the internal quantum efficiency (IQE) is calculated as follows:

$$IQE(\lambda) = \frac{EQE(\lambda)}{(1-R(\lambda))} \quad (3.22)$$

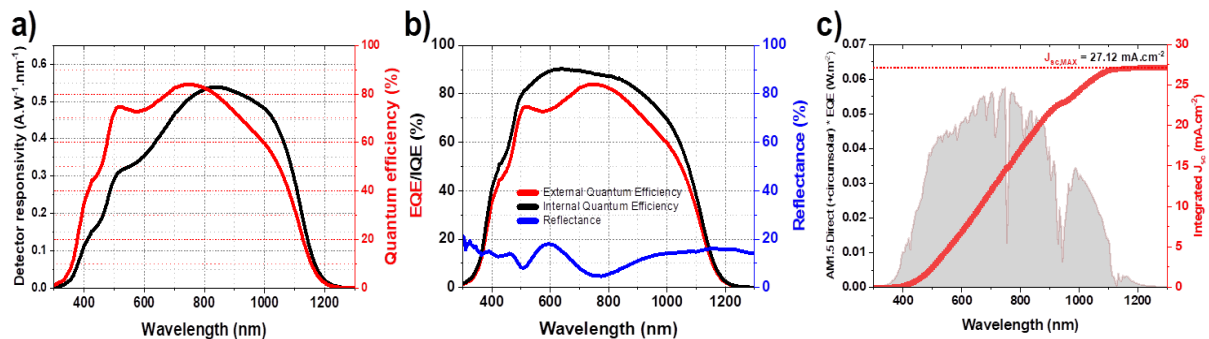


Figure 3.15.- a) Detector responsivity/Spectral Response (SR), Quantum Efficiency (QE), **b)** External Quantum Efficiency (EQE), Internal Quantum Efficiency (IQE) and Reflectance (R) curves. **c)** Plots the convolution of the irradiation spectra with the EQE for a kesterite solar cell. By integrating this spectra, a maximum theoretical value is obtained for J_{SC} .

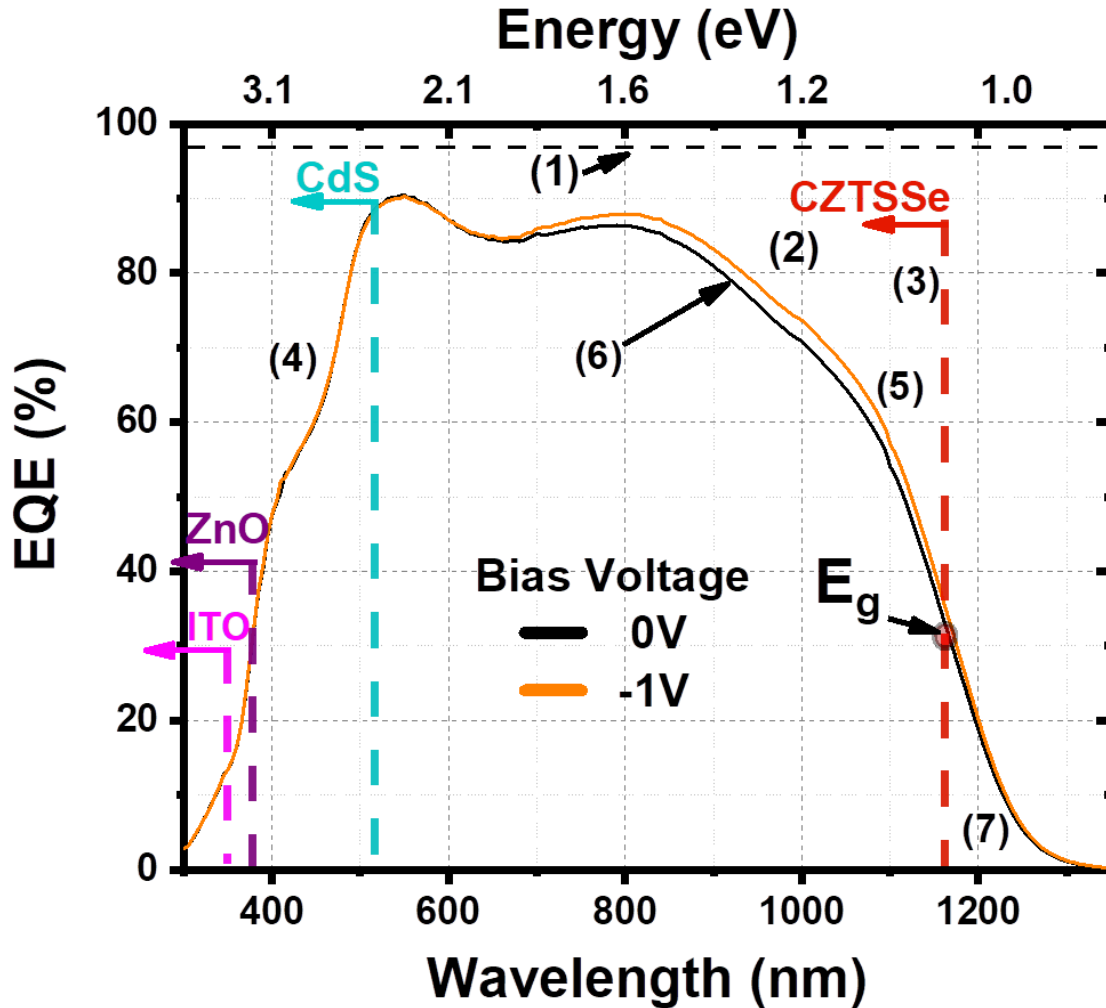


Figure 3.16- Overview of main layer spectral charge carrier generation-collection and losses. Also it is shown how these can be affected in a voltage-biased *EQE* curve for a kesterite (CZTSSe) solar cell. An ideal theorized *EQE* for this solar cell would be the perfect rectangle comprised between a 100% *EQE* and 1170 nm.

In Figure 3.16, losses (1) represents shading from the front grid of the solar cell while (2) corresponds with the loss due to reflection of light from the kesterite device structure (See Figure 3.9b). In this figure, Zones (3) and (4) are losses caused by the light absorption in the intrinsic zinc oxide (iZnO or i-ZnO) window and CdS layers, respectively.

On the first side, the loss due to incomplete generation in the CZTSSe layer is indicated by (5) while the difference (6) between *EQE*(0V) and *EQE*(-1V) curves, corresponds to the loss due to voltage dependent current collection. And, on the other side (7) stands for the absorber's band tailing absorption losses.

Additionally, it is possible to calculate the maximum theoretical short circuit density photo-current ($J_{SC,MAX}$) by integrating over the incident illumination spectra (photon flux: Φ):

$$J_{SC,MAX} = q \int_{\lambda_1}^{\lambda_2} \Phi(\lambda) EQE(\lambda) d\lambda \quad (3.23)$$

Where, λ_1 and λ_2 are the limits of the taken solar spectrum.

However, the absorption coefficient (α) is proportional to the bandgap (E_g) of the absorber material by the relation ^{32,33}:

$$\alpha(h\nu) \propto \sqrt{h\nu - E_g} \quad (3.24)$$

Where h is the Planck constant and ν represents the frequency.

As a first approach, the bandgap could be approximated by the linear extrapolation in the EQE curve for the low energy range:

Furthermore, it is possible to estimate (E_g) by a Gaussian fitting of $\frac{dEQE(\lambda)}{d(\lambda)}$ vs. $h\nu$ ³⁴:

However, this method slightly overestimates the bandgap if there are tail states present. More appropriately, it is possible to calculate the bandgap (E_g) of the absorber material by plotting and intercepting the x – axis at the low energy regime linear fitting of the following equation (Figure 3.17) ³⁵:

$$((h\nu) * EQE(\lambda))^2 \text{ vs. } h\nu = (E * EQE(\lambda))^2 \text{ vs. } E$$

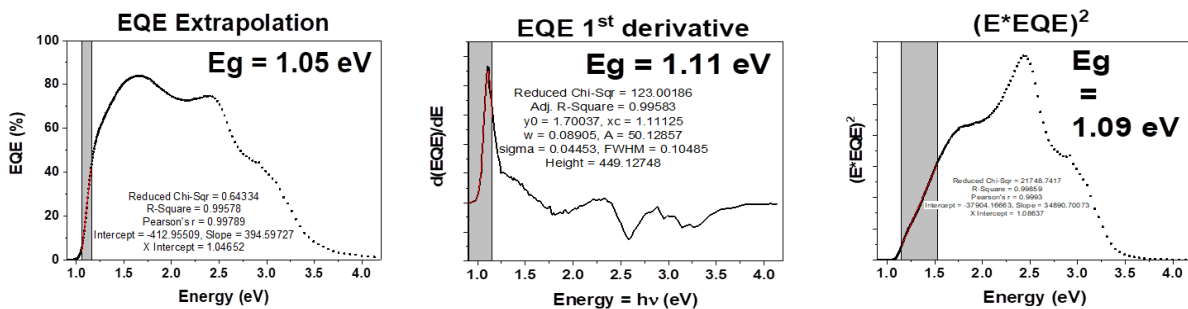


Figure 3.17- Numerical bandgap calculation from a kesterite EQE by different methodologies.

Accordingly to Hegedus et al.³⁶, the Internal Quantum Efficiency (*IQE*) could be approximated by Equation (3.25):

$$IQE(\lambda) \cong 1 - \frac{\exp(-\alpha(\lambda) * W(V))}{(\alpha(\lambda) * L) + 1} \quad (3.25)$$

In which $\alpha(\lambda)$ corresponds to the absorption coefficient, $W(V)$ to the voltage dependent space charge region, and L to the minority carrier diffusion lengths. In this sense, when carrier collection just occurs in the space charge region -low diffusion length values-: $(\alpha(\lambda) * L) \ll 1$. Equation (3.25) reduces to the well-known Gartner equation³⁷:

$$IQE(\lambda) \cong 1 - \exp(-\alpha(\lambda) * W(V)) \quad (3.26)$$

From these last two equations, it could be observed that the *IQE* depends on the space charge region width $W(V)$. Therefore, not collecting charge carriers that are generated beyond $(W(V) + L)$ represents a significant loss in the photogenerated current. By applying a bias voltage (See Figure 3.18) to the solar cell during *EQE* measurement, it is possible to modify $W(V)$, thus by comparing biased with unbiased *QE* measurements, it is possible to gather information regarding the completeness of the current collection and possible loss mechanisms in the device.

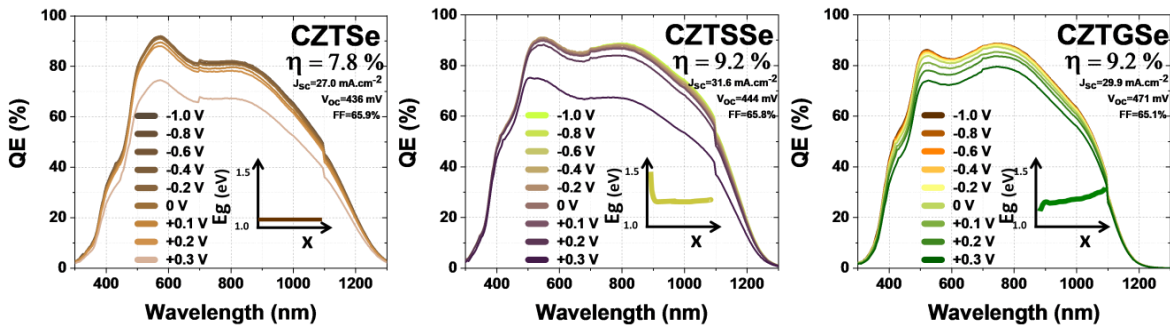


Figure 3.18- Voltage biased ($-1V$ to $+0.3V$) *EQE* curves for distinct kesterites with bandgap profiles.

3.7.7 Capacitive-Voltage Profiling

The capacitive measurements are commonly utilized to test pn diode devices like solar cells.³⁸ The capacitance (C) of the pn junction is highly sensitive to charge changes due to capture and emission of charge carriers from trap states. Name (dQ) to the charge response due to a small applied voltage (dV), then $C = dQ/dV$.

Capacitive analysis are performed by applying an oscillating AC voltage with a frequency (f), then the component of linear current response is measured in phase with the voltage and the perpendicular component.³⁸

These measurements are carried out by a LCR meter. Therefore, from the complex admittance of the whole junction and by employing an equivalent circuit model, in which, the simplistic model is a parallel capacitance with a parallel resistor (See Figure 3.19b), it is possible to derive relevant electrical parameters of the solar cell device. One of the most prominent experimental techniques using capacitance measurements is capacitance-voltage profiling.

If a highly doped $n^+ - p$ junction is considered, it is possible to assume that the depletion only takes place in the p side. In this depletion approximation, the depletion region (SCR) is precisely defined, ends abruptly and is fully depleted of free carriers.

By applying a reverse bias voltage (V), it is assumed the formation of a depletion layer of a thickness (x) and that the doping density (i. e. electrically active impurities) is $N(x)$.³⁹ If the reverse bias voltage is then increased by an amount dV the increase of electric field (\vec{E}_{bi}) across the junction is:

$$dE = dV/x \quad (3.27)$$

And the charge increment by increasing ($x + dx$) is $qN(x)dx$.

Thus, it is followed:³⁹

$$dE = \frac{dV}{x} = \frac{q}{\epsilon_0 \epsilon} N(x) dx \quad (3.28)$$

Where q the electric is charge and ϵ_0 and ϵ correspond to vacuum and semiconductors' permittivity (a.k.a. dielectric constant).

From a parallel plate capacitor, which corresponds to the pn junction in the depletion approximation the capacitance is given by:

$$C = \frac{\epsilon_0 \epsilon A}{x} \rightarrow dx = -\frac{\epsilon_0 \epsilon A}{C^2} dC \quad (3.29)$$

In which A is the area. Combining the last two equations, it is possible to find a relationship for $N(x)$ such as:³⁸⁻⁴⁰

$$N(x) = -\frac{c^3}{q\epsilon_0\epsilon A^2} \frac{dV}{dC} = -\frac{c^3}{q\epsilon_0\epsilon A^2} \left(\frac{dC}{dV}\right)^{-1} = -\frac{2}{q\epsilon_0\epsilon A^2} \left(\frac{d(c^{-2})}{dV}\right)^{-1} \quad (3.30)$$

Where x corresponds to the profiling position $x = \frac{\epsilon_0\epsilon A}{C}$

On the other hand, w_0 can be found by fitting the peak of the derivative $-dC/dw(w/kT)$ as it is shown in Figure 3.19d.

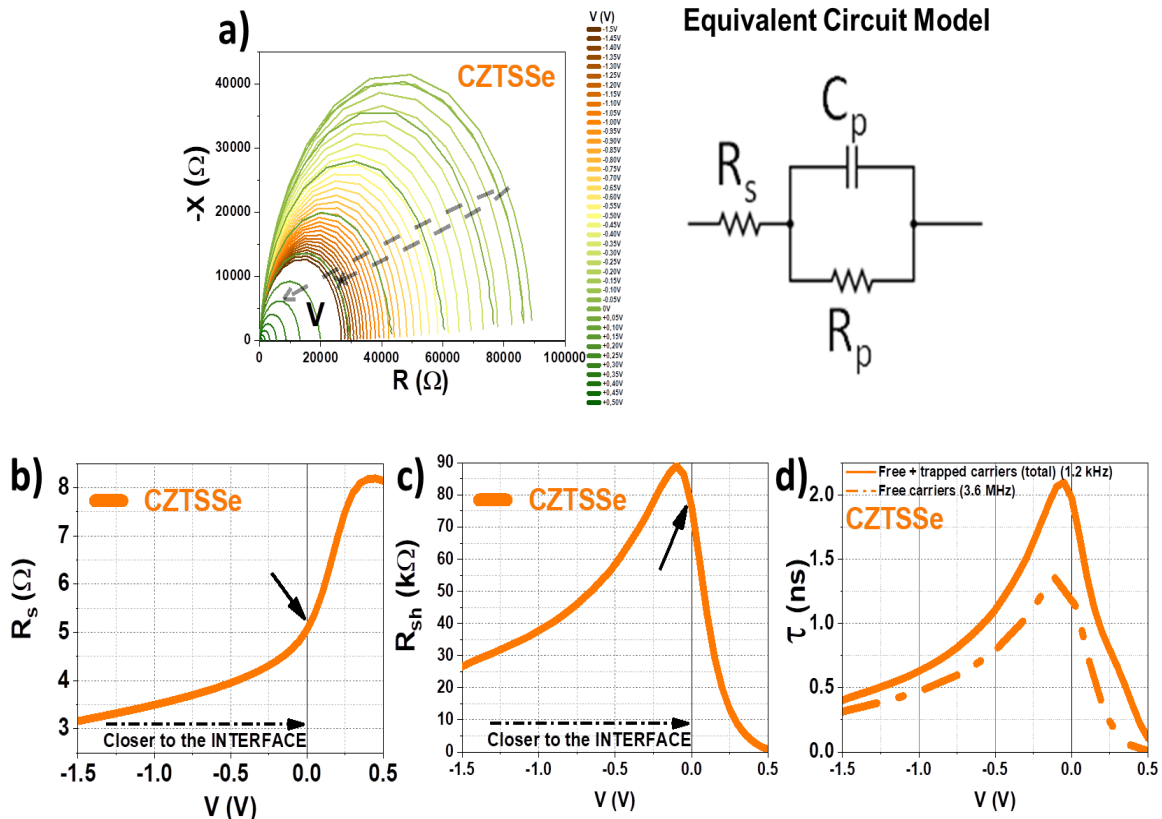


Figure 3.19- a) Impedance curves for a CZTSSe. Its Equivalent circuit model is also represented. b) Series and c) Shunt resistance as a function of a voltage sweep for a CZTSSe solar cell. d) Represents the lifetime calculation.

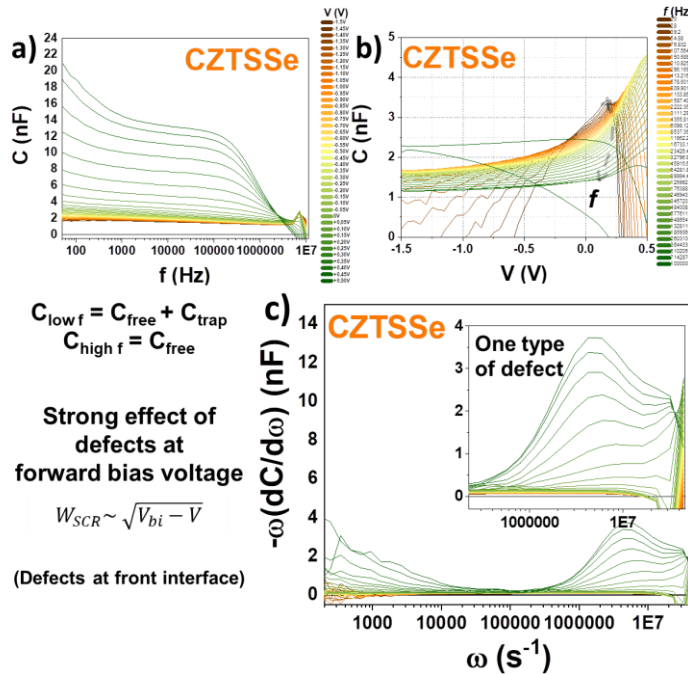


Figure 3.20- a) Frequency swept CV and b) Voltage swept fC and c) ω vs. $-\omega \left(\frac{dC}{d\omega}\right)$ curves for a CZTSSe kesterite solar cell.

Therefore, by measuring the junction capacitance (C), in the dependence of the applied bias voltage (V), it is obtained the so called CV profiling (See Figure 3.20), from which it is possible to derive one dimensional profiles of the doping density $N(x)$ through the thickness of the semiconductor. However, if deep trap states are present in the absorber layer, one has to be careful when interpreting CV data, because these trap states can respond to the AC voltage applied for measuring the capacitance or may adjust their charge state to the DC bias conditions and therefore create artifacts in the CV profiles (See Figure 3.21).^{38,40,41}

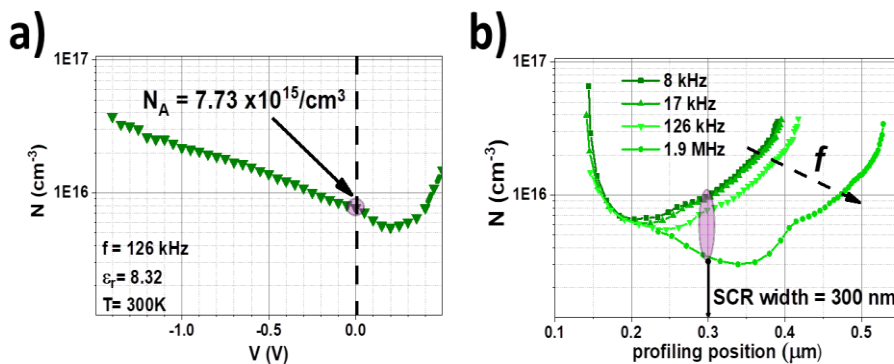


Figure 3.21- Available free charge transport carriers versus a) Voltage (V), b) Profiling position on a kesterite thin film solar cell.

3.8 Chapter References

1. Fairbrother, A. et al. On the formation mechanisms of Zn-rich Cu₂ZnSnS₄ films prepared by sulfurization of metallic stacks. *Sol. Energy Mater. Sol. Cells* 112, 97–105 (2013).
2. Giraldo, S. et al. Study and optimization of alternative MBE-deposited metallic precursors for highly efficient kesterite CZTSe:Ge solar cells. *Prog. Photovolt. Res. Appl.* 27, 779–788 (2019).
3. Giraldo, S. et al. How small amounts of Ge modify the formation pathways and crystallization of kesterites. *Energy Environ. Sci.* 11, 582–593 (2018).
4. Xie, H. et al. Impact of Sn(S,Se) Secondary Phases in Cu₂ZnSn(S,Se)₄ Solar Cells: a Chemical Route for Their Selective Removal and Absorber Surface Passivation. *ACS Appl. Mater. Interfaces* 6, 12744–12751 (2014).
5. Fairbrother, A. et al. Single-Step Sulfo-Selenization Method to Synthesize Cu₂ZnSn(S_ySe_{1-y})₄ Absorbers from Metallic Stack Precursors. *ChemPhysChem* 14, 1836–1843 (2013).
6. López-Marino, S. et al. ZnSe Etching of Zn-Rich Cu₂ZnSnSe₄: An Oxidation Route for Improved Solar-Cell Efficiency. *Chem. - Eur. J.* 19, 14814–14822 (2013).
7. Fairbrother, A. et al. Development of a Selective Chemical Etch To Improve the Conversion Efficiency of Zn-Rich Cu₂ZnSnS₄ Solar Cells. *J. Am. Chem. Soc.* 134, 8018–8021 (2012).
8. Neuschitzer, M. et al. Optimization of CdS buffer layer for high-performance Cu₂ZnSnSe₄ solar cells and the effects of light soaking: elimination of crossover and red kink: CdS and effects of light soaking: elimination of crossover and red kink. *Prog. Photovolt. Res. Appl.* 23, 1660–1667 (2015).
9. Sanchez, Y. et al. An innovative alkali doping strategy for Cu₂ZnSnSe₄ through the CdS buffer layer. in 2018 IEEE 7th World Conference on Photovoltaic Energy Conversion (WCPEC) (A Joint Conference of 45th IEEE PVSC, 28th PVSEC & 34th EU PVSEC) 1645–1647 (IEEE, 2018). doi:10.1109/PVSC.2018.8547417.
10. Grenet, L. et al. Sputtered ZnSnO Buffer Layers for Kesterite Solar Cells. *ACS Appl. Energy Mater.* 3, 1883–1891 (2020).
11. E. Becquerel, Mémoire sur les effets électriques produits sous l'influence des rayons solaires, *C. R. Acad. Sci. Paris* 9 (1839) 561. in.
12. Tsu, R. & Zypman, F. New insights in the physics of resonant tunneling. *Surf. Sci.* 228, 418–421 (1990).
13. R.L. Anderson, *IBM J. Res. Dev.* 4, 283 (1960).
14. R.L. Anderson, *Solid State Electronics* 5, 341 (1962).
15. Courel, M., Andrade-Arvizu, J. A. & Vigil-Galán, O. Loss mechanisms influence on Cu₂ZnSnS₄/CdS-based thin film solar cell performance. *Solid-State Electron.* 111, 243–250 (2015).
16. Courel, M., Valencia-Resendiz, E., Andrade-Arvizu, J. A., Saucedo, E. & Vigil-Galán, O. Towards understanding poor performances in spray-deposited Cu₂ZnSnS₄ thin film solar cells. *Sol. Energy Mater. Sol. Cells* 159, 151–158 (2017).
17. Courel, M., Andrade-Arvizu, J. A. & Vigil-Galán, O. The role of buffer/kesterite interface recombination and minority carrier lifetime on kesterite thin film solar cells. *Mater. Res. Express* 3, 095501 (2016).
18. Courel, M., Andrade-Arvizu, J. A. & Vigil-Galán, O. Towards a CdS/Cu₂ZnSnS₄ solar cell efficiency improvement: A theoretical approach. *Appl. Phys. Lett.* 105, 233501 (2014).
19. Courel, M. et al. Optimization of physical properties of spray-deposited Cu₂ZnSnS₄ thin films for solar cell applications. *Mater. Des.* 114, 515–520 (2017).
20. Courel, M., Pulgarín-Agudelo, F. A., Andrade-Arvizu, J. A. & Vigil-Galán, O. Open-circuit voltage enhancement in CdS/Cu₂ZnSnSe₄-based thin film solar cells: A metal-insulator-semiconductor (MIS) performance. *Sol. Energy Mater. Sol. Cells* 149, 204–212 (2016).
21. Kittel, Charles. *Introduction to Solid State Physics*, 7th Edition. Wiley.
22. Nelson, Jenny (2003-01-01). *The Physics of Solar Cells*. Imperial College Press. ISBN 9781860943492. https://books.google.fr/books/about/The_Physics_of_Solar_Cells.html?id=s5NN34HLWO8C&redir_esc=y.
23. W. Bao and M. Ichimura. *Japanese Journal of Applied Physics* 51 (2012) 10NC31.

24. R. Haight, A. Barkhouse, O. Gunawan, B. Shin, M. Copel, M. Hopstaken, and D. B. Mitzi. *Applied Physics Letters* 98, 253502 (2011).
25. C. Yan, F. Liu, N. Song, B. K. Ng, J. A. Stride, A. Tadich, and X. Hao. *Applied Physics Letters* 104, 173901 (2014).
26. Shockley, W. & Queisser, H. J. Detailed Balance Limit of Efficiency of p-n Junction Solar Cells. 11.
27. Standard Tables for Reference Solar Spectral Irradiances: Direct Normal and Hemispherical on 37° Tilted Surface, ASTM G173-03, (2020).
28. SAHt, C.-T., NOYCEt, R. N. & SHOCKLEYt, W. Junctions and P-N Junction Characteristics. *Proc. IRE* 16 (1957).
29. Clifford W. Hansen, Parameter Estimation for Single Diode Models of Photovoltaic Modules. SANDIA REPORT SAND2015-2065 Unlimited Release Printed March 2015. <https://prod-ng.sandia.gov/techlib-noauth/access-control.cgi/2015/152065.pdf>.
30. Sites, J. R. & Mauk, P. H. Diode quality factor determination for thin-film solar cells. *Sol. Cells* 27, 411–417 (1989).
31. Geisthardt, R. M., Topic, M. & Sites, J. R. Status and Potential of CdTe Solar-Cell Efficiency. *IEEE J. Photovolt.* 5, 1217–1221 (2015).
32. Razeghi, M. Optical Properties of Semiconductors. in *Fundamentals of Solid State Engineering* 365–407 (Springer International Publishing, 2019). doi:10.1007/978-3-319-75708-7_10.
33. Pankove, J. I *Optical Processes in Semiconductors*, Unbridged republication, with slight corr.; Dover Mineola, [NY], 1975.
34. Hages, C. J., Carter, N. J. & Agrawal, R. Generalized quantum efficiency analysis for non-ideal solar cells: Case of $\text{Cu}_2\text{ZnSnSe}_4$. *J. Appl. Phys.* 119, 014505 (2016).
35. Carron, R. et al. Bandgap of thin film solar cell absorbers: A comparison of various determination methods. *Thin Solid Films* 669, 482–486 (2019).
36. Hegedus, S. S. & Shafarman, W. N. Thin-film solar cells: device measurements and analysis. *Prog. Photovolt. Res. Appl.* 12, 155–176 (2004).
37. Gärtner, W. W. Depletion-Layer Photoeffects in Semiconductors. *Phys. Rev.* 116, 84–87 (1959).
38. Abou-Ras D.; Kirchartz T.; Rau, U., *Advanced Characterization Techniques for Thin Film Solar Cells*; Wiley-VCH: Weinheim, Germany, 2011. ISBN: 9783527410033. DOI: 10.1002/9783527636280.
39. Miller, G. L., A Feedback Method for Investigating Carrier Distribution in Thin Semiconductors. *Electron Devices IEEE Trans. On* 1972, 19(10), 1103-1108. in.
40. Roland Scheer, Hans-Werner Schock, *Chalcogenide Photovoltaics: Physics, Technologies, and Thin Film Devices*, 2011. ISBN: 978-3-527-31459-1.
41. Heath, J. T., Cohen, J. D. & Shafarman, W. N. Bulk and metastable defects in $\text{CuIn}_{1-x}\text{Ga}_x\text{Se}_2$ thin films using drive-level capacitance profiling. *J Appl Phys* 95, 12 (2004).

All models are wrong,

But some are useful.

-George Edward Pelham Box

Chapter IV

Results Part I: Kesterite Graded Bandgap - Theoretical Numerical Modeling Simulations (SCAPS-1D)

4.0 Introduction and Chapter Presentation

For the following (Chapter IV) development, the standard SEMS-IREC's baseline pure selenium kesterite solar cell is first modeled using material parameters from the Solar Energy Materials and Solar Systems (SEMS) group device knowledge (mainly based on SCAPS-1D numerical modelling simulation) ¹ along with the current state of the art kesterite device modelling literature. ²

In this way, the first part of this Chapter tackles the first bandgap profile modeled grading attempts, in which factors such as the influence of sulfurization in kesterite (CZTSSe) solar cell devices and the impact of the contact ohmicity due rear sulfur segregations are provided as a comparative between linear and front surface bandgap profiles.

Hence, a discussion on the sulfur content and positioning on the band diagram implications is provided for several sulfurization scenarios.

Finally, the effect of the front sulfurization of CZTSe solar cell with an experimental (realistic) compositional profile is analyzed and discussed.

4.1 First Bandgap Grading Attempts

4.1.1 Influence of Sulfurization in CZTSSe Solar Cells

From this baseline CZTSe solar cell, it was studied the influence of an increasing amount of S on a thickness of 200 nm at the back interface in a sulfur segregation layer (See Figure 4.1) was studied. This way, three distinct representative cases are considered:

$$\frac{S}{(S + Se)} = \text{i) } 0 \text{ (reference), } \quad \text{ii) } 0.2, \quad \text{iii) } 0.4$$

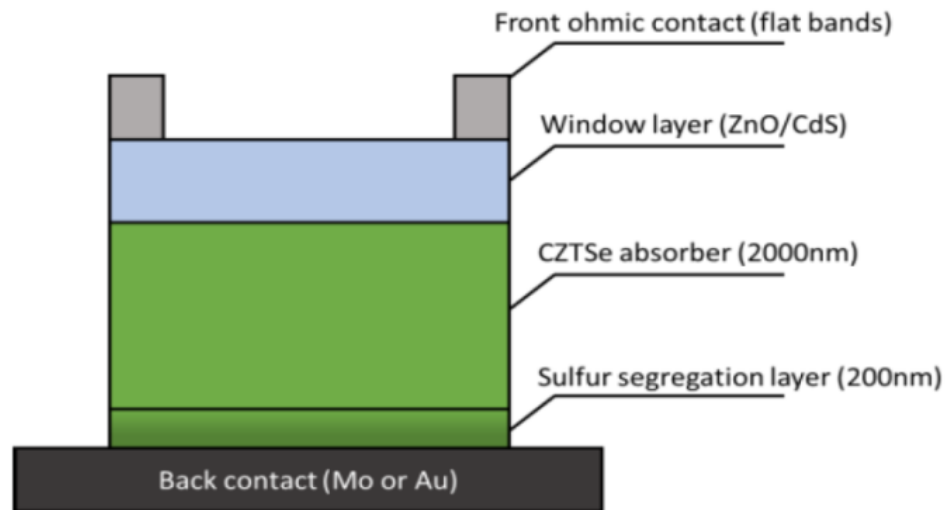


Figure 4.1.- Basic first modeled CZTSe device.

As the Nature of the back contact will strongly influence the behavior of the back interface within the absorber (built in potential screening), for each case, two types of back contacts are investigated:

a) Mo back contact (no MoSe_2) with a work function $W_{\text{Mo}} = 4.6$ eV. This contact is (a priori) not perfectly ohmic.

b) Au back contact with a work function $W_{\text{Au}} = 5.1$ eV. This contact is perfectly ohmic.

At this step of the numerical modeling simulation, no MoSe₂ layer is considered, though this case is probably closer to what is observed for a gold (Au) back contact (ohmic behavior). Several figures of merit (FOM) are calculated or derived solving Poisson's equation: diode current, recombination current, occupation probability, energy band, chemical potential inside the cell, etc.

This part is mainly focused on the current voltage analysis (*JV*) curve and on the back interface recombination current for the absorber material minority carriers (electrons).

The consequent *JV* curves and back side recombination curves (minority carriers, i.e. electrons) are shown in Figure 4.2. For the case of a non-ohmic back contact, the increased sulfur content at the back interface detrimentally impacts the solar cell performances with a strong degradation of the voltage, followed as expected by a deterioration of the diode properties (Fill Factor decreasing).

The analysis of the recombination current at the back interface shows a clear shift in the onset of the recombination process, from about 0.4 V when no sulfur is present at the back interface, to about 0.2 V in the case of a $S/(S+Se) = 0.4$ sulfur ratio.

This recombination process, occurring at a much lower voltage with S, is directly connected to the degradation of the voltage of the solar cell.

As a result, the efficiency plummets from 12.1% (no S) down to 5.9% (0.4 Sulfur).

On one hand, such effect is attributed to the unfavorable band bending on the valence band near the back contact, which reduces the transmission of holes and therefore may favor their segregation and subsequent recombination.

And on the other hand, the case of a purely ohmic Au back contact shows a remarkable resilience to the presence of sulfur at the back interface. The *JV* curves remains perfectly overlapping up to a high sulfur content of $S/(S+Se) = 0.8$.

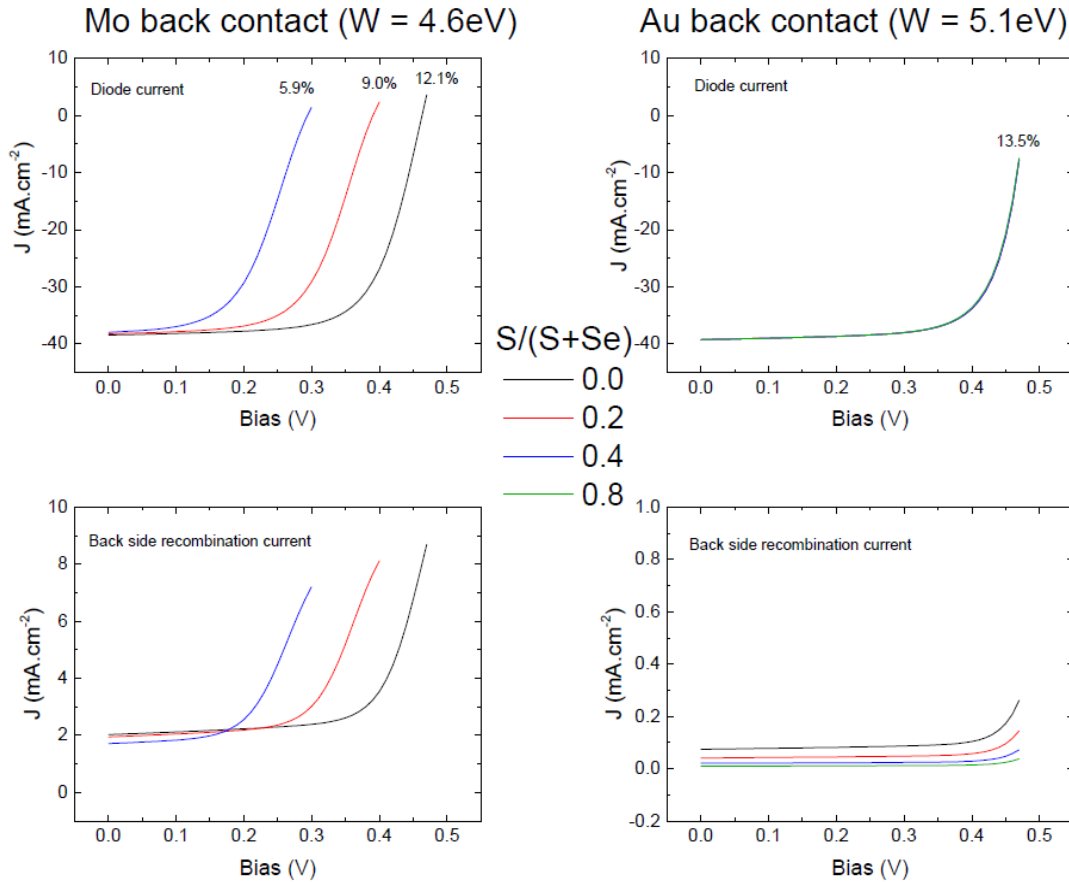


Figure 4.2.- First basic modeled CZTSe device.

In this case, the recombination current shows virtually no onset up to values close to 0.45 V and remains much more limited than for the case of a Mo back contact. By observing the band diagram (not shown here), it is possible to see that the ohmic contact induces a built-in potential in the valence band of the absorber at the vicinity of the back contact; this built in potential counters the barrier resulting from the sulfur at the back interface, and thus promotes the holes transmission through the contact, hence maintaining a perfect ohmicity. Therefore, and as a summary of this subsection (4.1.1), when no S is present at the back interface, our modeling shows that both the Au and Mo back contacts exhibit acceptable photovoltaic properties. However, when some sulfur is segregated at the back interface, the perfectly ohmic contact allows a screening of the band bending and thus remains very resilient; conversely the non-perfectly ohmic back contact (Mo) is strongly degraded due to a reduced hole transport through the contact, hence resulting in an increased recombination. In the real case of Mo contacts, with MoSe_2 providing a good ohmicity, the presence of PV properties of the solar cells is calculated.³

4.1.2 Impact of the Contact's Ohmicity with Rear Sulfur Segregation

In this part, it is tackled the resilience of CZTSSe solar cell to the segregation of sulfur at the back interface depending on the Nature of the contact. Thus, two distinct absorber cases are considered: one without sulfur segregation (pure CZTSe absorber) and one with a $S/(S+Se) = 0.4$ linear S segregation at the back interface, on 200 nm width.

The back contact's work function is being varied from 4.6 eV (pure Mo, poor ohmicity) up to 5.3 eV (showing an excellent ohmicity, $W_{Au} = 5.1$ eV).

At the same time, this part of the analysis is mainly focused on the diode's parameters, as the degradation mechanism has been described in Part I (high recombination current at the back interface).

Figure 4.3 compares the JV curves as a function of the back contact work function for absorbers with segregated sulfur at the back side (top) and without sulfur (bottom).

The conclusions are straightforward; if sulfur is segregated at the back interface, a good ohmicity ($W \geq 4.9$ eV) is absolutely needed to preserve the efficiency of the solar cell.

For work function values above 5 eV, the efficiency of pure CZTSe is fully recovered. The complete set of FOM is shown in Figure 4.4.

As expected from an interface recombination based degradation (See Section 4.1.1), the limiting parameters are the V_{OC} and the FF, while the J_{SC} remains roughly unaffected.

(SCAPS-1D)

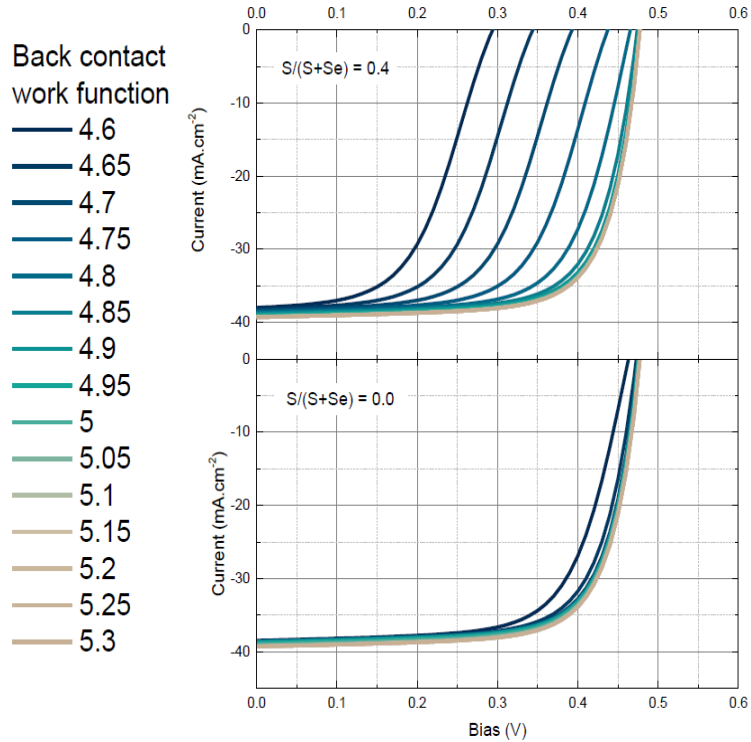


Figure 4.3.- Top) JV curves for a sulfur segregated absorber with different back contact work function values; **Bottom)** similar curves for pure CZTSe.

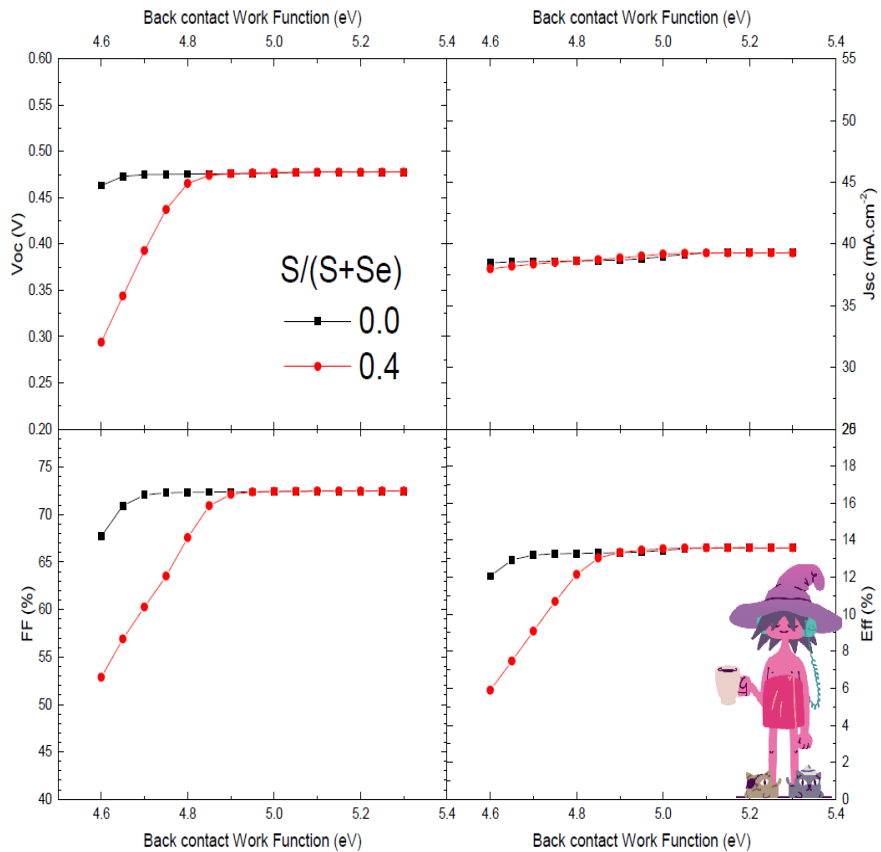


Figure 4.4.- Figures of merit (FOM) for the curves shown in Figure 4.3.

Thus, the resilience of good ohmic back contacts to sulfur segregation at the back side of the absorber has been confirmed. In realistic cells, MoSe₂ plays the role of an efficient hole filter, guaranteeing a near perfect ohmicity, so sulfur segregation may not be a problem from a band diagram point of view (once again, the possible variation of defect density is ignored in this model).

Hence, if alternative back contacts are used in combination to absorber sulfurization processes, one should pay attention to the quality of contact, which could be a source of significant degradation of the performances.

4.1.3 Linear Bandgap Profiles in CZTSSe

While the preliminary concerns (See subsections 4.1.1 and 4.1.2) were mostly related to the influence of the sulfur segregation at the back contact, the next interesting fact relied on the bandgap profile of the bulk material using realistic composition profiles. From experimental directly structural and indirectly compositional characterization techniques analysis such as X-ray diffraction (XRD) and Raman spectroscopy information (See next Chapter V), the bandgap profiles analyzed are modeled as an approximated linear gradients as it is shown in Figure 4.5b.

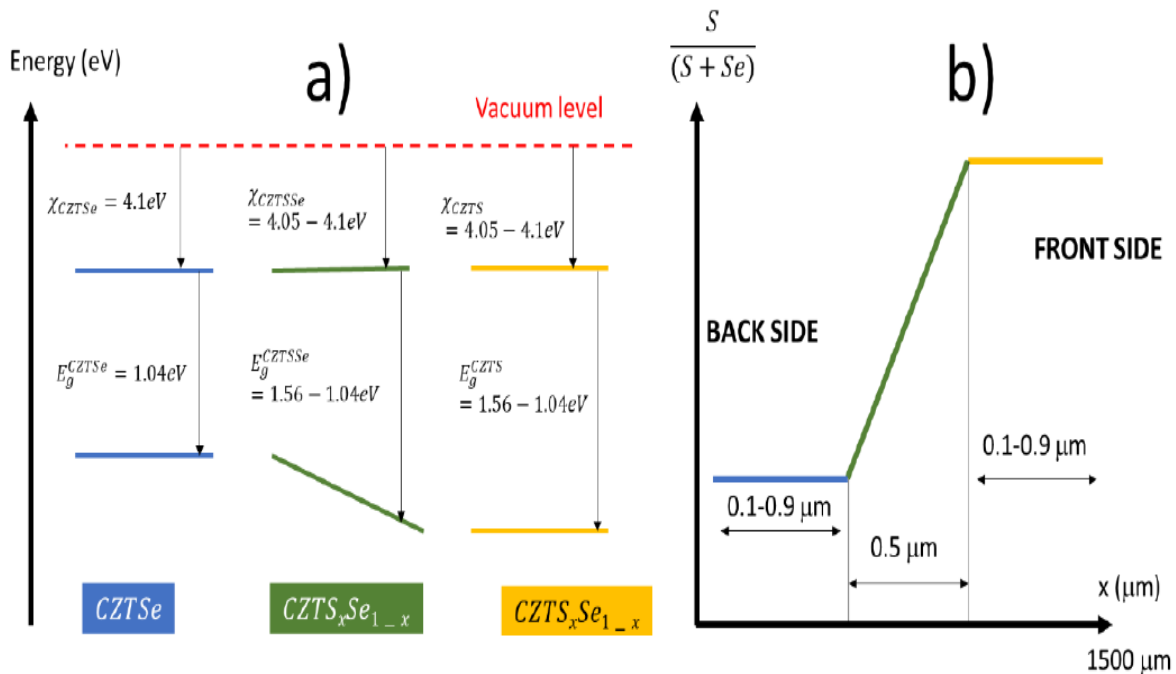


Figure 4.5.- a) Energetic levels of distinct layers composing the absorber material (with respect to vacuum level). **b)** Sulfur compositional profile.

Particularly, a special attention is given to the electric field in the bulk absorber, which should affect the holes more than electrons as sulfur incorporation is supposed to lower the VB. However, this is not as straightforward as intuition could dictate (Later tackled in Subsection 4.2.1. In this way, the S content is approximated with linear variations as shown Figure 4.5b. Conversely, in Figure 4.5a there are shown the different layers composing the absorber, isolated, with their band parameters with respect to the vacuum level. The maximum S content is $S/(S+Se) = 0.5$. A batch modeling with almost 40 different conditions is performed and both the band diagram in open circuit conditions and the PV performances are analyzed (See Figure 4.6). While the total thickness of the absorber remains fixed at 1500 nm, and the width of the grading layer is fixed at 500 nm, the front CZT(S_xSe_{1-x}) and back CZTSe widths are simultaneously varied from values ranging from 0 nm to 900 nm by 100 nm steps, therefore 10 steps in total.

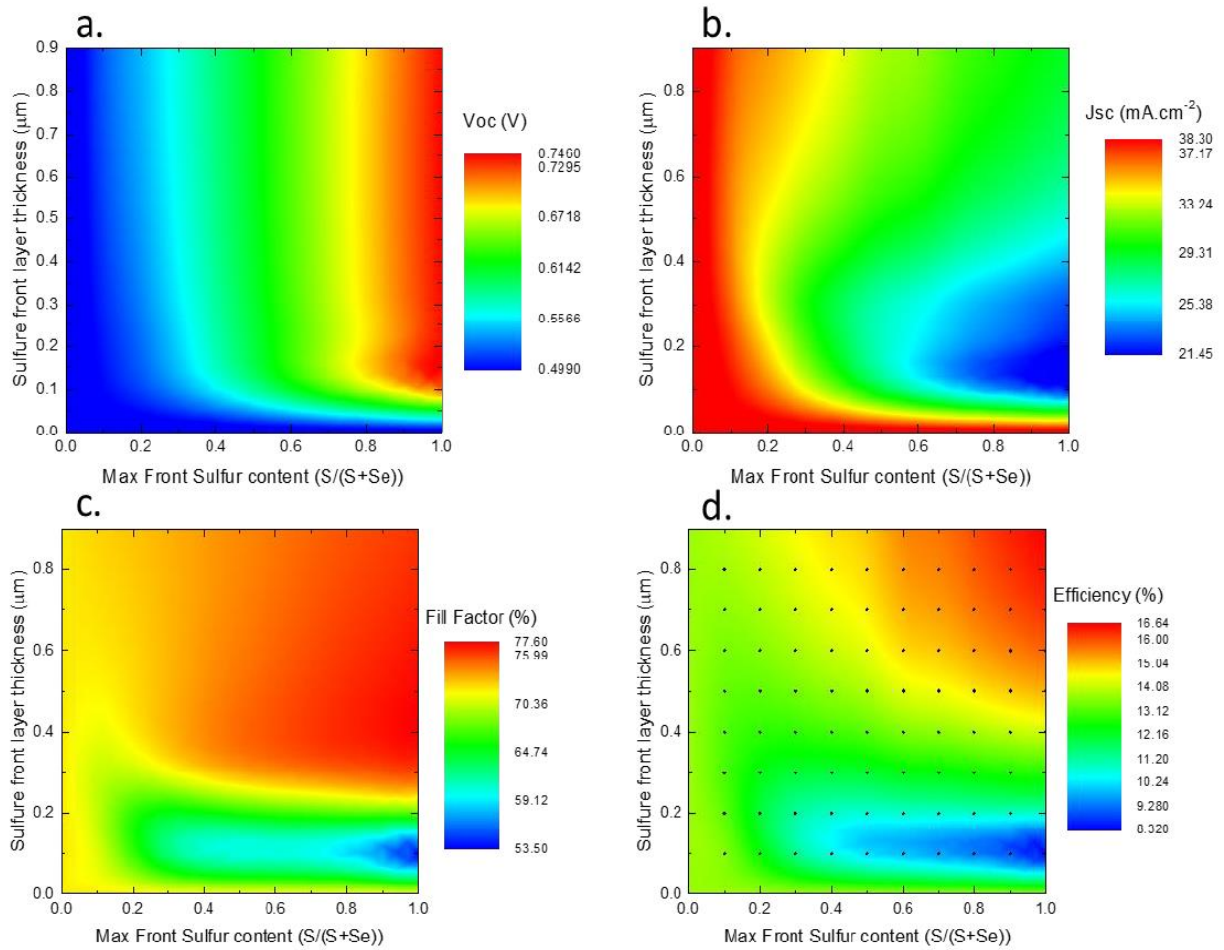


Figure 4.6.- PV parameters modeled as a function of the front S content and front sulfurized layer thickness.

The maximum S composition at the front side of the absorber is varied by steps of 0.1 with values ranging from $S/(S+Se) = 0$ to $S/(S+Se) = 1$, therefore 11 steps in total. The total number of steps is $10 \times 11 = 110$ steps. This approach is similar to what was previously utilized in a successful manner for studying CIGSe solar cell devices.⁴

Figure 4.6 shows the evolution of the figure of merits depending on the bulk Sulfur composition depth and maximum sulfur composition at the front side. Both voltage and current values evolve with the expected trend when the average bandgap of the absorber is increased by S incorporation.

A significant improvement of the FF is observed for high S content cells (thick layer and high front S). This is an expected result as the absorber evolves from a CZTSe layer ($E_G = 1.04$ eV, low Shockley-Queisser limitation efficiency) to a CZTS layer ($E_G = 1.56$ eV, closer to optimum SQ efficiency).

However, it is well known that realistic devices do not behave like this due to an increased Shockley-Read-Hall recombination (SRH), also called trap-assisted recombination when more S is incorporated, further damaging the V_{OC} deficit and hindering the FF (increased n and J_0).

This effect is not observed in the current model, as it does not account for the variation in defect density when S is incorporated; therefore, the cells modeled here follow the predictions of a SQ theoretical solar cell.

Surprisingly, the efficiency Figure 4.6d shows degradation for thin front surface sulfur layers. In this figure, the mesh used for the modeling is also shown (each black point corresponds to a modeled condition). The basic hypothesis implied in here involves a 500 nm thick $CZTS_xSe_{1-x}$ graded layer; therefore, it is obvious from the mesh shown in Figure 4.6d that the case of thin sulfurized surface layers (less than 300 nm) is ignored.

Therefore, a degradation of the photovoltaic performances is observed here when the front layer (uniform) is around 100 - 300 nm but should not be taken as an argument to reject the use of thin front sulfur layers as a way to enhance the efficiency.

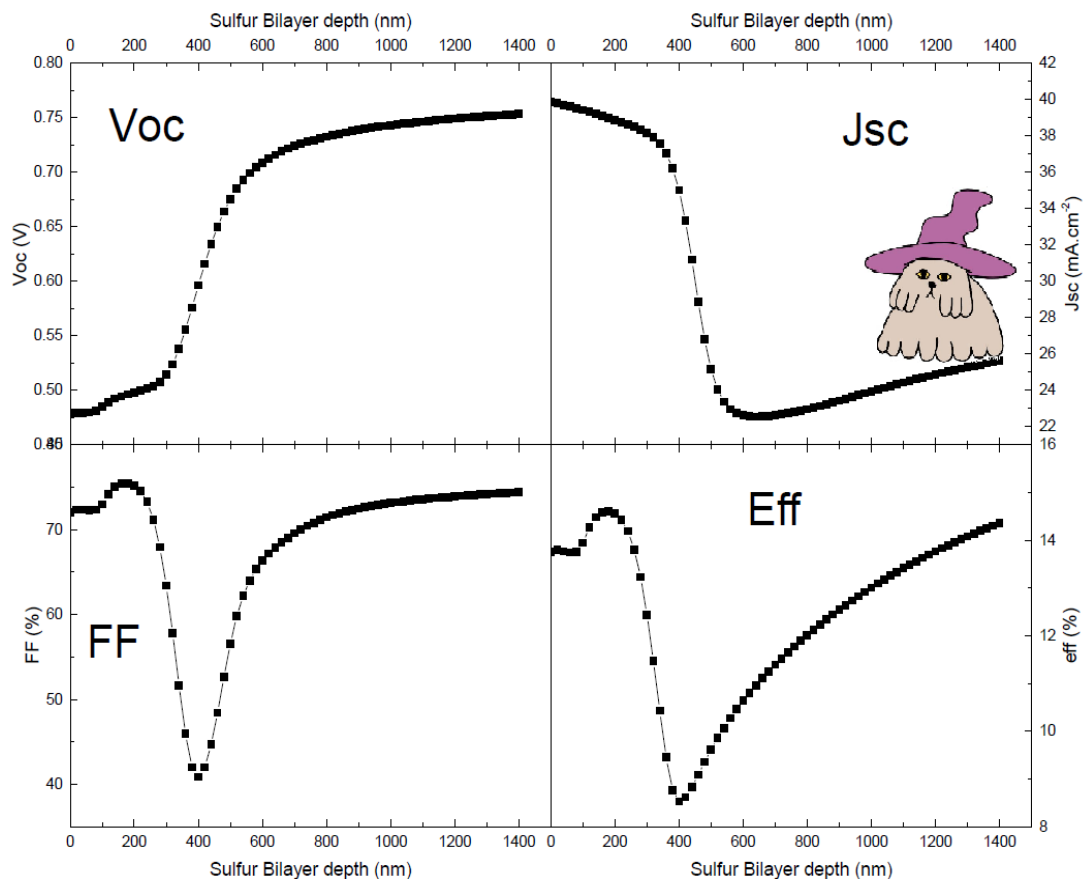


Figure 4.7.- PV optoelectronic parameters modeled for a fixed front S composition with a fine mesh on the thickness of the sulfurized bilayer.

To support and strengthen the idealization of the use of a very thin front S layer, we focus now in a specific fixed front S composition $S/(S+Se) = 0.6$ and investigate the effect of the front layer thickness with a much finer mesh; here, the thickness variation steps are 20 nm for the sulfurized bilayer (uniform $CZTS_xSe_{1-x}$ and graded $CZTS_xSe_{1-x}$). The photovoltaic parameters are shown in Figure 4.7. Very thin sulfur bilayers markedly improve the efficiency of the cells for values around 200 nm, from 14% to 15%; after 300 nm, a steep drop in the performances is observed down to 8.5%.

This substantial PCE drop will be addressed in the later discussion (See subsection 4.1.4). After 400 nm, the efficiency starts rising again which corresponds, as mentioned earlier, to the transition toward a pure CZTS compound. In the following part, we focus on the front sulfurization only and investigate on the optimal conditions for performance (Eff.) improvements.

4.1.4 Front Surface Sulfurization Profiles in CZTSSe

Front sulfurization is a well-known pathway to improve CIGSe cells efficiency, particularly used by Solar Frontier for their world record cells. In our previous part, it was demonstrated that for a fixed front S composition, an efficiency increase of the performances of kesterite solar cells was possible in the case of very thin layers. In this following, this matter, along with studying the variations on the S composition and depth of the sulfurized layer will be addressed (See Figure 4.8). Therefore, it is possible to notify the existence of 3 cases:

- * A thin layer (less than 300 nm) of sulfur can potentially improve the efficiency of the cell.
- * A thicker layer ($300 \text{ nm} < d < 800 \text{ nm}$) will strongly degrade the photovoltaic properties.
- * A very thick sulfur layer behaves like a high sulfur content absorber and thus improves the efficiency here, because the defect density variation is not taken into account; this latter point is out of the scope of this Thesis. Thus, a possible interpretation of these observations will be discussed in the latter paragraphs.

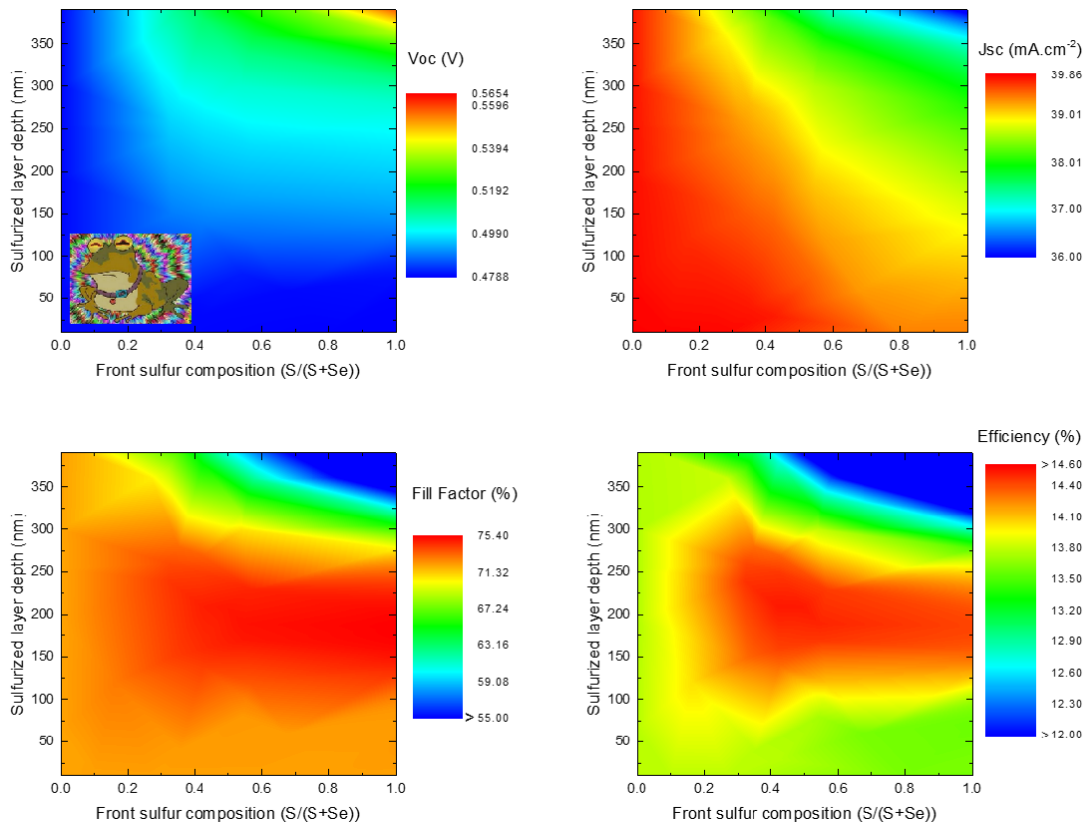


Figure 4.8.- Fine mesh analysis of the sulfur profile at the front side of the absorber.

4.2 Discussion on the Sulfur Content and Band Diagram Implications

4.2.1 CZTSSe: Front Sulfurization with a Layer ($d < 300$ nm)

The interpretation of the beneficial effect of the front sulfurization is quite straightforward. By lowering the valence band near the PN interface, the holes are repelled from the space charge region, thus reducing the recombination pathways for the electrons through the interface defects. This effect is discussed in detail for CIGS somewhere else.⁵ Figure 4.9 illustrates this effect for a 200 nm graded sulfurized layer, with a front (S/(S+Se)) composition of 0.6 and compared to the band diagram of a pure CZTSe absorber solar cell. Both are taken at the maximum power point (0.41 V). The lowering of the valence band in the space charge region is evident. The effect on the increased efficiency is maximized for a sulfurized layer thickness equal to the width of the space charge region.

In realistic devices, one should also pay attention to the increased defects introduced by S, which could in return damage the performances. Particularly, for CIGSe the best results were obtained for superficial S layers of about 25 – 75 nm.⁵

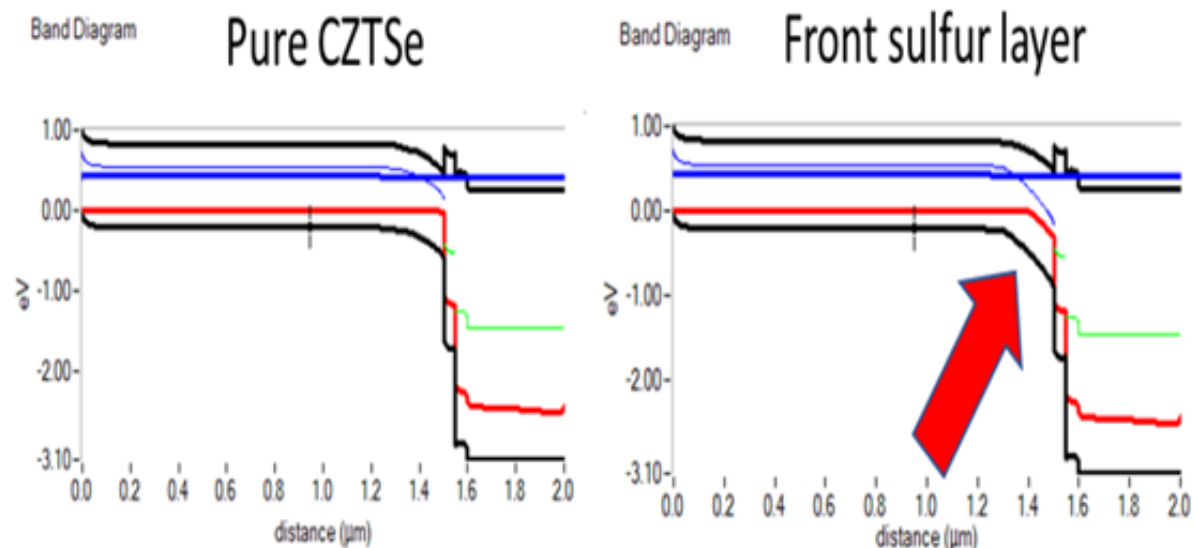


Figure 4.9.- Compared band diagram between a pure CZTSe cell and a CZTSSe cell with a 200 nm front sulfurization layer.

4.2.2 CZTSSe: Front Sulfurization with a Layer ($300 \text{ nm} < d < 800 \text{ nm}$)

In this case, the sulfurized thickness is larger than the space charge region. As it was previously demonstrated (See Figure 4.5a), the valence band (VB) is normally lowered by the incorporation of sulfur in the material. However, in the complete solar cell heterostructure, the p-doped material aligns the hole quasi-Fermi level with the work function of the metal (5.1 eV in here). Therefore, as the hole quasi-Fermi level is fixed, the conduction band is pushed upward. This built-in potential in the absorber leads to the formation of a barrier for the electrons at the PN interface as it is shown in Figure 4.10.

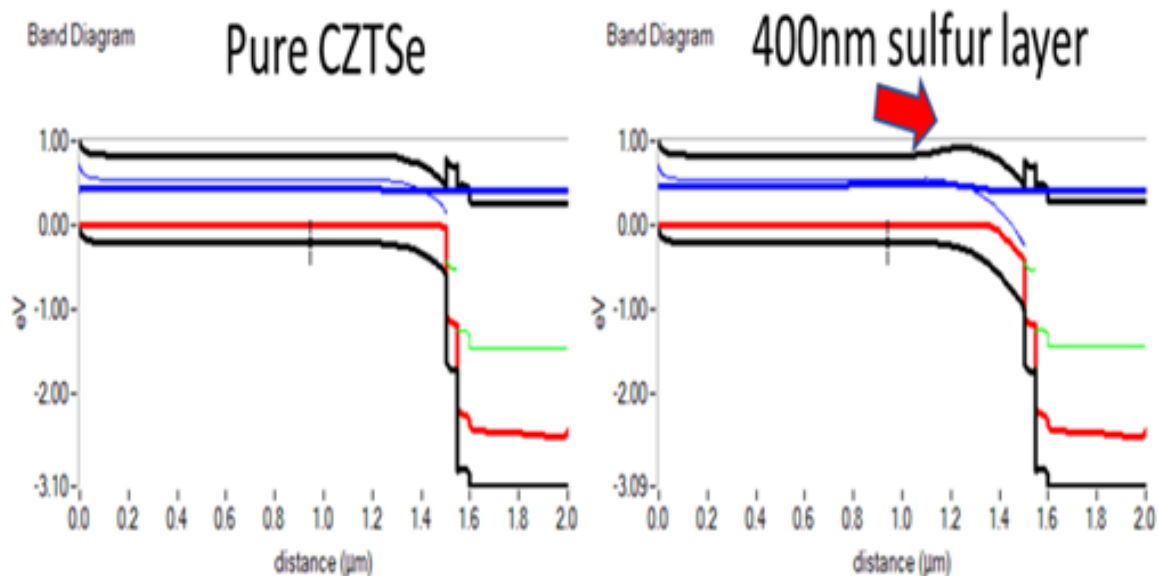


Figure 4.10.- Compared band diagram between a pure CZTSe cell and a CZTSSe cell with a 400 nm front sulfurization layer.

The drift current opposes the photovoltaic effect which is based on the diffusion of carriers toward the PN junction and thus significantly increases the series resistance.⁶ As a result, the FF is severely reduced while the voltage remains unaffected; the latter point supports the fact that this is a resistive effect rather than a recombination effect (in case of a recombination effect, both V_{OC} and FF would be degraded). Finally, Figure 4.10 summarizes this idea, using as an example a 400 nm sulfurized layer with a maximum $S/(S+Se) = 0.8$ composition taken at the maximum power point (0.42 V).

4.2.3 CZTSSe: Deep Bulk Sulfurization ($d > 800$ nm)

In this last case (See Subsection 4.2.1), the absorber behaves like a uniform sulfur compound absorber, as we get closer to the photons' maximum penetration depth in the material (around 1 μm). The modeled efficiency is increased because if no variation of the defect density is considered, a larger bandgap puts the cell closer to the optimal Shockley-Queisser (SQ) efficiency. Such case is however unrealistic, as the increased V_{OC} deficit for large bandgap materials is a well-established phenomenon.

By introducing a variable defect density linear with the S content, it could be possible, in a future model, to account for this effect and demonstrate the inherent limitations of sulfur incorporation. However, more experimental data are needed for that. As a take home message from this modeling part, we could notice that the segregation of sulfur at the back is only problematic when the back contact is not perfectly ohmic; ohmic contacts are yet very resilient to the sulfur content. Front sulfurization should be finely tuned to remain below the thickness of the space charge region.

Deeper sulfurization will create an electron barrier near the PN interface and reduce the performances of the device. It is therefore important that the variation of the defect density with the sulfur content should be also considered, which is finally discussed in the subsequent sections.

4.3 Frontal Graded Bandgap Profile in CZTSSe

4.3.1 Variations of the Defect Density with the Sulfur Content

In the next part of this CZTSSe solar cell modeling Chapter, it will be introduced a certain variation of the defect density with the introduction of sulfur in the (originally CZTSe) crystalline matrix. This variation participates is related to the V_{OC} deficit observed in such cell. The defects are single acceptor with a capture cross section of $\sim 10^{-13} \text{ cm}^2$, and energy position of 0.75 eV with respect to the valence band, and uniform distribution over a 0.5 eV width, and a peak density of $\sim 1 \times 10^{14} \text{ cm}^{-3}$ for pure CZTSe. Conversely, for pure CZTS absorber material, the defect density is $\sim 1 \times 10^{15} \text{ cm}^{-3}$. Variations between the two pure compounds are considered to show linear behaviour.

Needless is to say, that this might be a very rough and probably inaccurate approximation, which was just deduced from adjusting the PV parameters of pure CZTSe and CZTS to typical record values in the literature. It may be somehow accurate, but it could be also (completely) wrong and only admittance spectroscopy can give us a clear idea of the real defect distribution in the absorber; specifically, the activation energy remains a guess (in this thesis particular modeled case, it is approximately in the midgap), but this stands out of the scope of this Thesis.

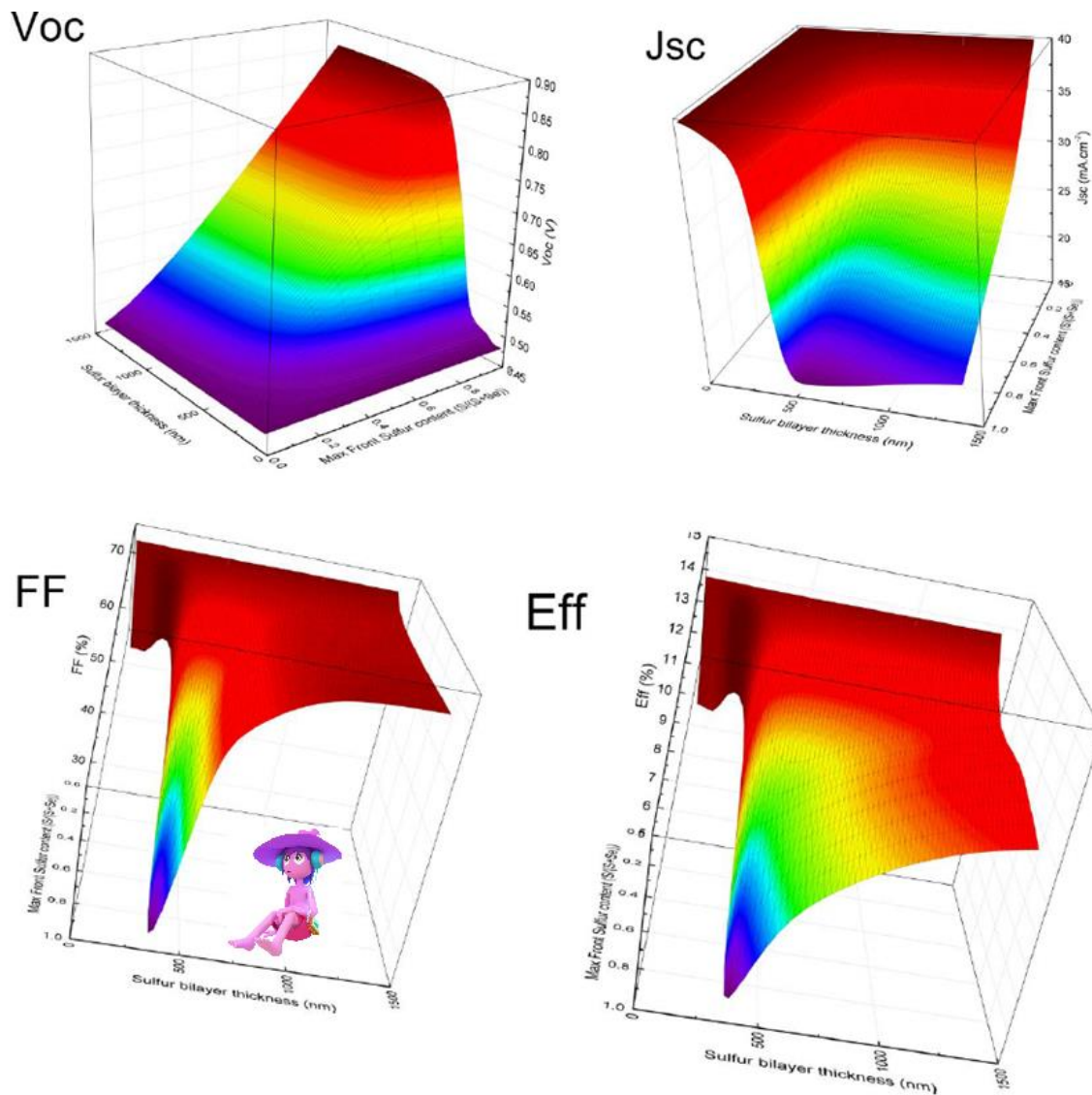


Figure 4.11.- Surf plots for each FOM of the PV optoelectronic parameters on front anionic graded CZTSSe solar cells.

Figure 4.11 shows the surf plots for every figure of merit. We could observe that in this case, the efficiency of high S content cells becomes much more limited, as expected from the experimental results reported so far. **However the front side sulfurization is still beneficial which is a very good sign.** The optimum conditions remains roughly unchanged as compared to Figure 4.8; this is a good indication that in spite of a slight defect density increase at the surface, the beneficial effect of front sulfurization is quite resilient. More discussions are needed on that specific part.

Also, interface defects passivation is not addressed in those simulations. It has been found to play a major role in CIGSSe. Now, it would be firstly necessary to see if it is still in effect even without an order vacancy compound (OVC).^{7,8}

In this way, sulfurization is only beneficial at the front interface within the space charge region depth.

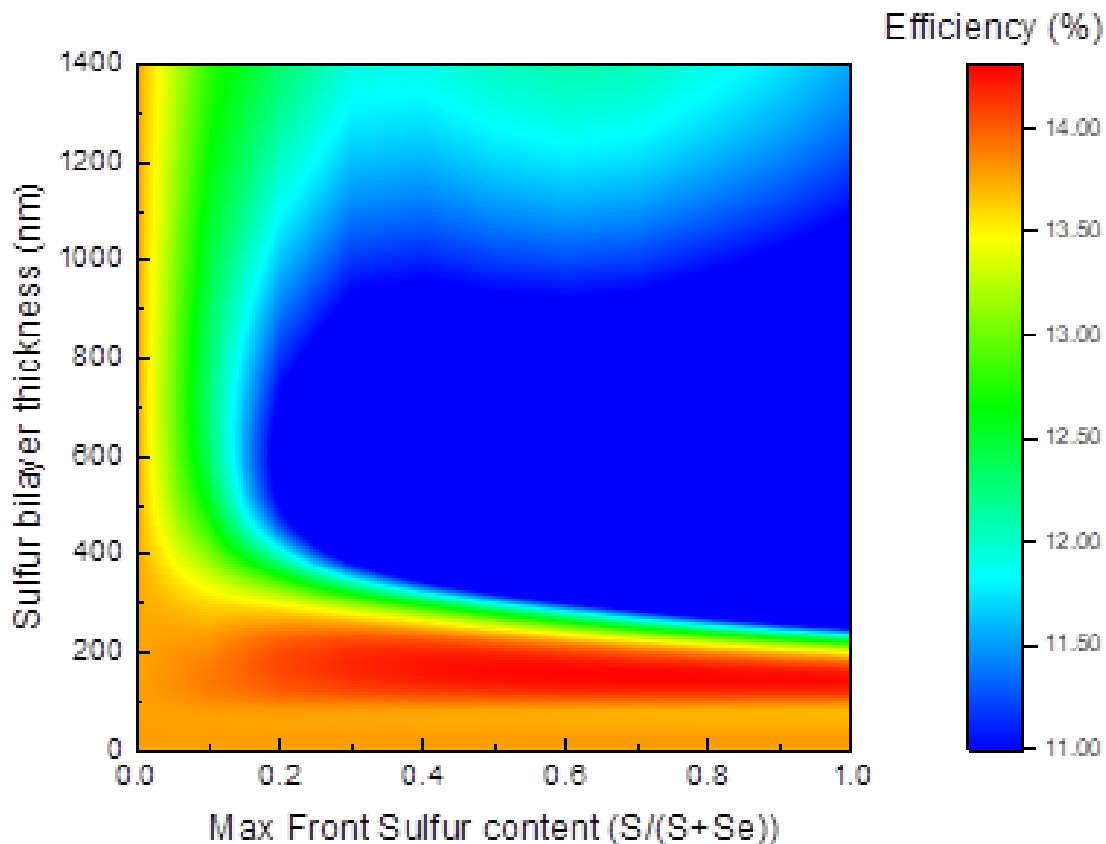


Figure 4.12.- Fine mesh analysis for the maximum sulfur amount profile at the front side of the absorber vs. the thickness of the modeled bilayer.

On the left hand, Figure 4.12 shows the mere result that allows concluding that sulfur affects both the CB, but more importantly the VB. Holes repelled from the p-n interface: **Back Surface Field effect passivation (BSF)**. On the right hand, Figure 4.13 schematizes the enhancement effects resembled in both the JV curves and band diagrams.

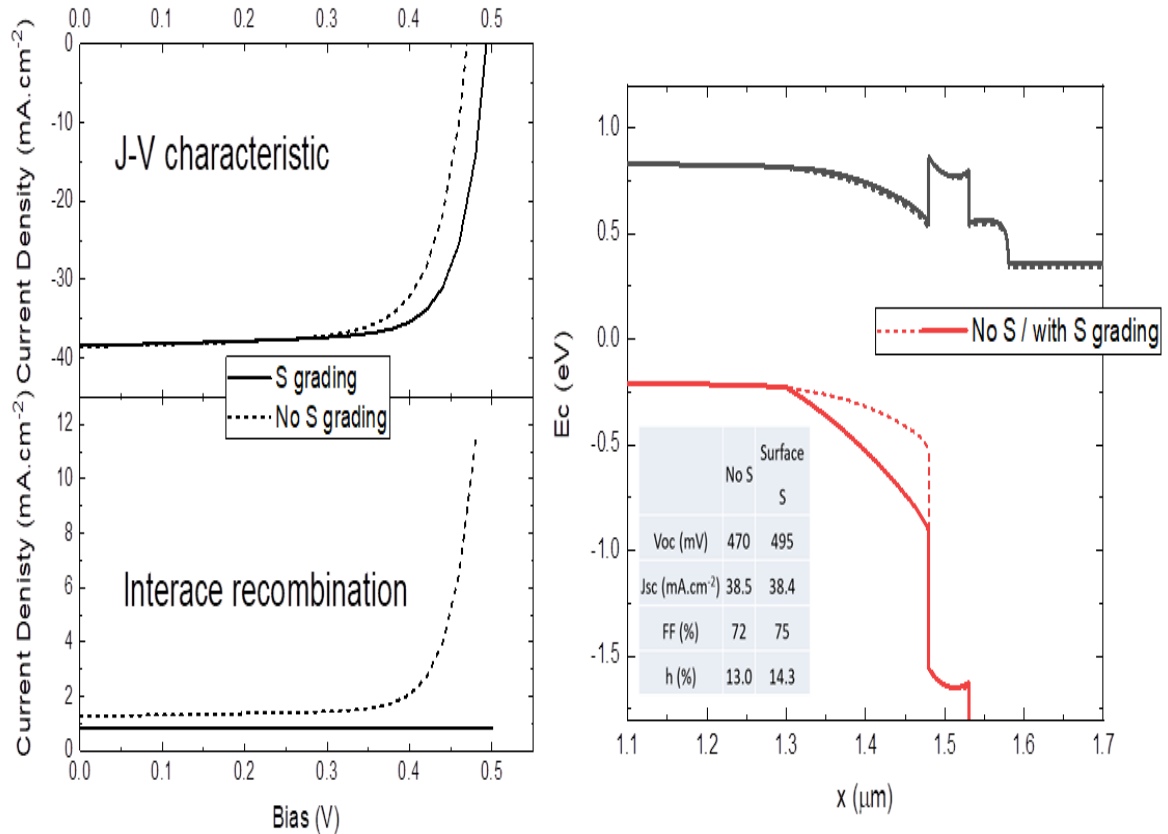


Figure 4.13.- a) JV curves and energy band positioning for a superficial sulfurized (CZTSSe) vs. a non-graded (CZTSe) solar cell modeled device. **b)** Corresponding energy band diagrams.

Therefore, a superficial chalcogenization (S) of kesterite (CZTSe) devices imply:

- Interface recombination almost suppressed.
- Improves both **the voltage and fill factor**.
- Similar effect as in CIGSe (Solar Frontier)*. ⁹

4.4 Effect of the Front Sulfurization of a CZTSSe Solar Cell with a Realistic (Experimental) Compositional Profile

Finally, it was utilized an experimental recorded “real” compositional profile (reconstructed by several characterization techniques) as input in the solar cell model; it was possible in order to perform comparisons. The variations are made with a flat sulfur composition profile, as well as a pure CZTSe solar cell. The case where the defect density increases by a whole order of magnitude between pure CZTSe and pure CZTS will be investigated for comparison purpose.

The following cases were investigated:

Pure CZTSe.

CZTSSe: Flat $S/(S+Se) = 0.2$ composition profile. The real $S/(S+Se)$ composition profile as determined by Raman spectroscopy and presented in Figure 4.14. In this case, the front composition is $S/(S+Se) = 0.5$, the graded composition is 100 nm thick with a linear evolution toward a flat $S/(S+Se) = 0.2$ composition profile for the rest of the absorber.

Pure CZTS.

This way, two types of solar cells are investigated. Firstly, it will be assumed that the defect density is not affected by the presence of S in the compound and remains stable at $\sim 5 \times 10^{14} \text{ cm}^{-3}$. This is normally not the case for real devices, as the incorporation of S often leads to an increased defect density depending on the quality of the process (high quality processes probably do not add much defects as the world record is made with S incorporation).

Secondly, we assume that the defect density increases linearly when introducing S. The defect density becomes $\sim 5 \times 10^{15} \text{ cm}^{-3}$ for the pure sulfur compound CZTS (this value is found by adjusting the performances of the pure CZTS cell to those of a realistic device but has not strong basis beyond that).

The JV curves corresponding to each case are shown in Figure 4.15, while Table 4.1 summarizes the calculated photovoltaic parameters. When the introduction of S does not change the defect density, the band diagram purely determines the performances.

Therefore, the solar cell optoelectronic parameters enhancement benefits from the introduction of S as it brings the bandgap closer to the SQ optimum value (~ 1.45 eV). Also, it could be observed that front sulfur enrichment greatly enhances the FF, because of the previously discussed (See Subsection 4.2.2) lowering of the valence band. Overall, the best solar cell here is the pure CZTS, since its bandgap sits very close to the SQ optimum.

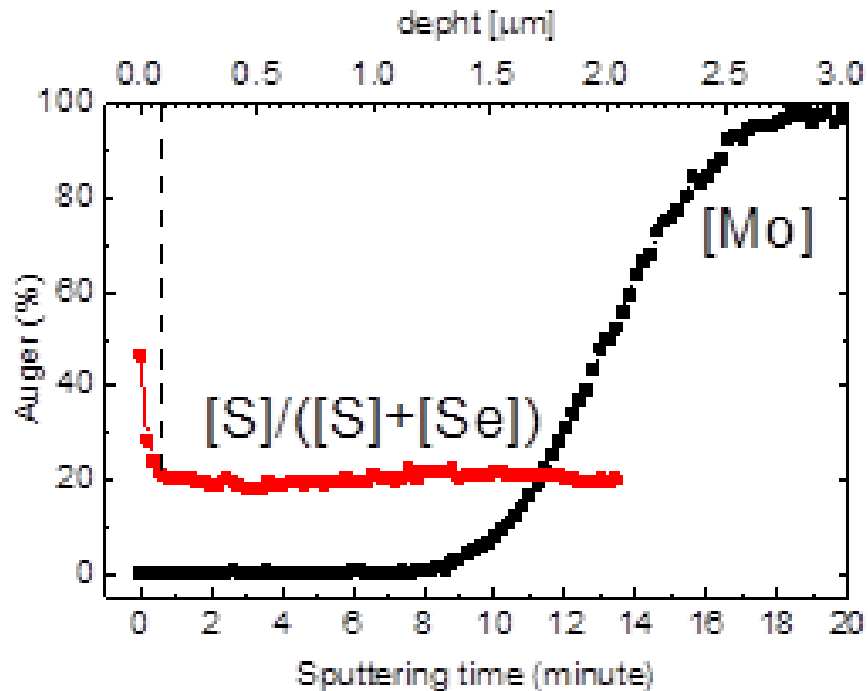


Figure 4.14.- Experimental composition profile determined by Auger, later corroborated by Raman and GDOES.

When the defect variation with S incorporation is considered, the efficiency of the pure CZTS cell becomes the worst of the batch with an efficiency reaching about 12% and every figures of merit decrease significantly.

The pure CZTSe cell has the highest efficiency, as its defect density remains very low.

The comparison between the flat S composition and the front graded one is however interesting. Whenever a front grading is present, a gain in the FF is observed as well as in the voltage, resulting in a moderate efficiency increase compared to the case of a flat S composition, and despite the higher total sulfur content (See Table 4.1).

Both of the previously investigated cases show a net advantage to the front graded cell over the flat graded one. While not huge, the expected improvement is of about 0.5%, which is still substantial enough to be considered. Also, it is probable that better results would be obtained if the composition in the bulk was lowered below $S/(S+Se) < 0.2$ (See Figure 4.15).

Table 4.1.- Optoelectronic parameters extracted from the modeled JV curves.

No defect variation with S content				
	V_{OC} (V)	J_{SC} (mA.cm ⁻²)	FF (%)	Eff. (%)
Front S grading	0.59	35.0	75.4	15.4
Flat S content (0.2)	0.57	35.5	73.4	14.8
Pure Se	0.50	39.8	72.0	13.7
Pure S	0.96	21.6	77.6	16.1
Defect variation with S content				
Front S grading	0.56	33.6	71.0	13.3
Flat S content (0.2)	0.54	34.3	69.9	12.9
Pure Se	0.50	39.8	72.0	13.7
Pure S	0.87	19.6	70.9	12.0

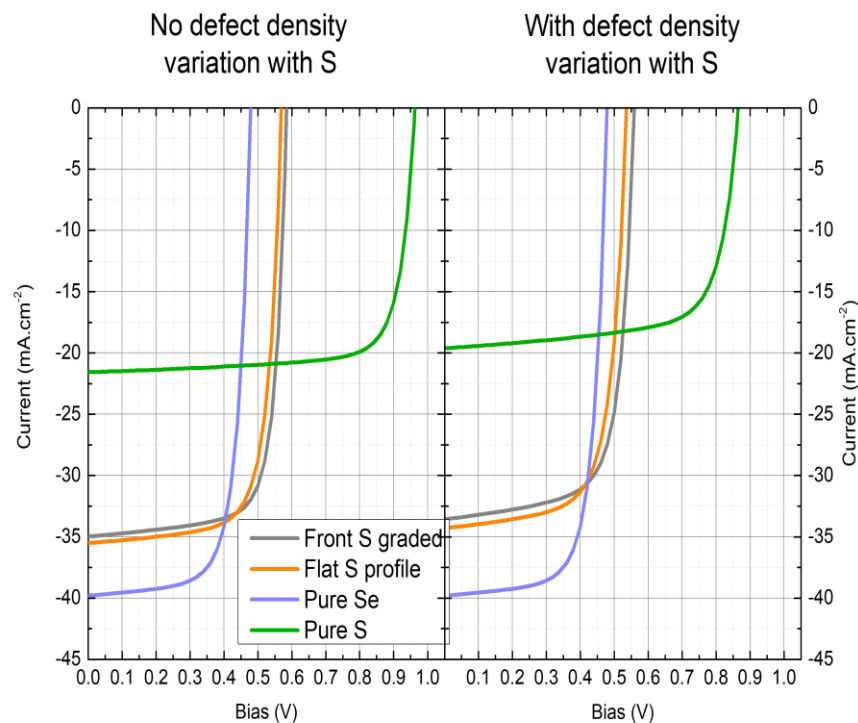


Figure 4.15.- Modeled JV characteristic curves for different anionic bandgap profiling in CZTSSe thin film solar cells.

4.5 Chapter References

1. Burgelman, M., Nollet, P. & Degraeve, S. Modelling polycrystalline semiconductor solar cells. *Thin Solid Films* 361–362, 527–532 (2000).
2. Saha, U. Proposition and computational analysis of a kesterite/kesterite tandem solar cell with enhanced efficiency. *RSC Adv.* 9 (2017).
3. Furlan, K. P., de Mello, J. D. B. & Klein, A. N. Self-lubricating composites containing MoS₂: A review. *Tribol. Int.* 120, 280–298 (2018).
4. Jehl Li Kao, Z., Kobayashi, T. & Nakada, T. Modeling of the surface sulfurization of CIGSe-based solar cells. *Sol. Energy* 110, 50–55 (2014).
5. Kobayashi, T. et al. Impacts of surface sulfurization on Cu(In_{1-x},Ga_x)Se₂ thin-film solar cells: Impacts of surface sulfurization on CIGS solar cells. *Prog. Photovolt. Res. Appl.* 23, 1367–1374 (2015).
6. Conversion of Chemical Energy into Electrical Energy. in *Physics of Solar Cells* (ed. Wurfel, P.) 93–107 (Wiley-VCH Verlag GmbH, 2005). doi:10.1002/9783527618545.ch5.
7. Theelen, M. & Daume, F. Stability of Cu(In,Ga)Se₂ solar cells: A literature review. *Sol. Energy* 133, 586–627 (2016).
8. Bär, M. et al. Determination of the band gap depth profile of the pentenary Cu(In(1-X)GaX)(SYSe(1-Y))₂ chalcopyrite from its composition gradient. *J. Appl. Phys.* 96, 3857–3860 (2004).
9. Kato, T. Recent Research Progress of High-efficiency CIGS Solar Cell in *Solar Frontier*. 21.

Experimentation is the least arrogant method of gaining knowledge

The experimenter humbly asks a question of Nature

-Issac Asimov

Chapter V

Results Part II:

Experimental Front Graded Bandgap on CZTSSe

5.1 Introduction and Chapter Presentation

In before, and as a summary of Chapter IV (Kesterite Graded Bandgap: Theoretical Numerical Modeling Simulations), a natural question may then arise:

Is it experimentally possible to develop complex anionic graded bandgap profiles in kesterite-based solar cells?

In order to give an adequate answer to this natural questioning, the second part of this Thesis results (Chapter V), demonstrates the development of a novel and disruptive chalcogenization process for the fabrication of $\text{Cu}_2\text{ZnSn}(\text{S},\text{Se})_4$ (CZTSSe) solar cells that enable the generation of superficial complex sharp graded anionic compositional profiles. Particularly focused in generating high S contents at the very top or front surface of the absorber, abruptly diminishing (as much as possible) to the rear side inside the same kesterite crystalline structured grains in a thin film (See Chapter IV).

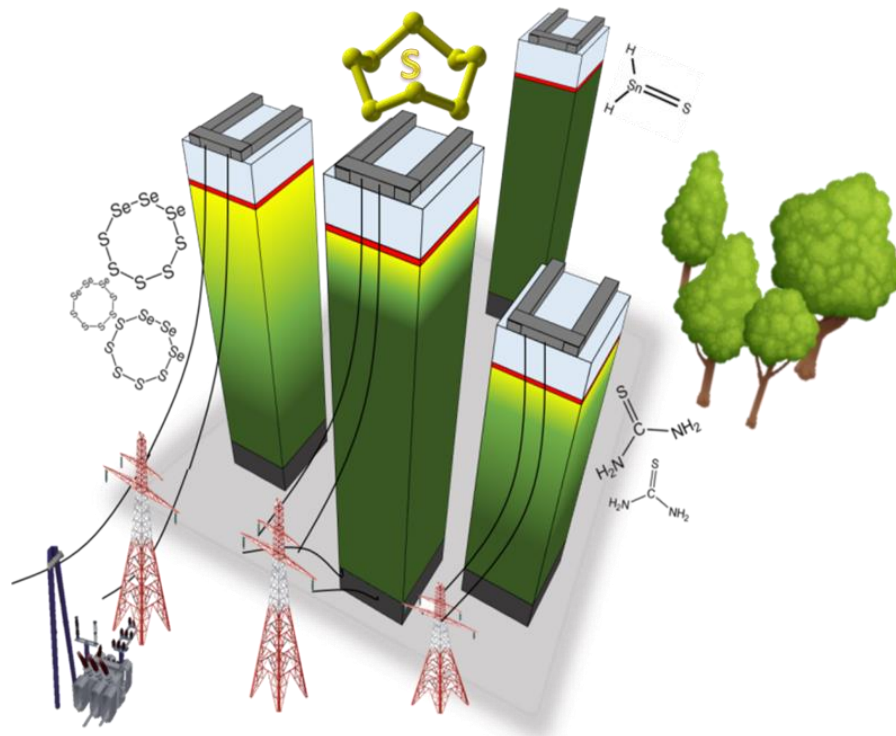
This is achieved through the optimization of the annealing (chalcogenization) parameters including the study of several sulfur sources with different predicted reactivities (elemental S, thiourea, SnS, and SeS_2).

As a result, depending on the sulfur source employed, devices with superficially localized maximum sulfur content between 50 and 20% within the charge depletion zone and between 10% and 30% toward the bulk material are obtained.

This complex graded structure is confirmed and characterized by combining multiwavelength depth-resolved Raman spectroscopy measurements together with in-depth Auger electron spectroscopy and X-ray fluorescence (XRF).

Additionally, the devices fabricated with such graded bandgap absorbers are shown to be fully functional with energy power conversion efficiencies (PCE) of almost 10% with no device optical, nor collection enhancement (such as metallic grids or an antireflective coating (ARC)).

In this way, it is possible to experimentally demonstrate the S-Se anionic profile hypothesized and modeled V_{OC} deficit values reduction and correlating it with the presence of a superficial gradient. These results represent one step forward toward anionic bandgap grading in kesterite solar cells.



5.2 Sulfur Pulse (Shoot) Analysis by Thermo-Gravimetric Analysis

To begin this journey, it is valuable to first analyze the most basic behavior of the chalcogenide thermodynamics, i.e., the later introduced S-shoots introduced during the annealing for the creation of (S)/(S+Se) surface gradients in CZTSSe thin films. For this purpose, thermo-gravimetric analysis (TGA) measurements were carried out. Figure 5.1a shows the TGA curves of the different elements such as Sn, S and Se. For the sulfur (S) case, subtle changes such a “finer evaporation” are observed when utilizing grinded or pulverized version of this element. More importantly, these curves reveal the “break temperatures” and the “happening/occurring times” at which the elements start to blow up when being heated.

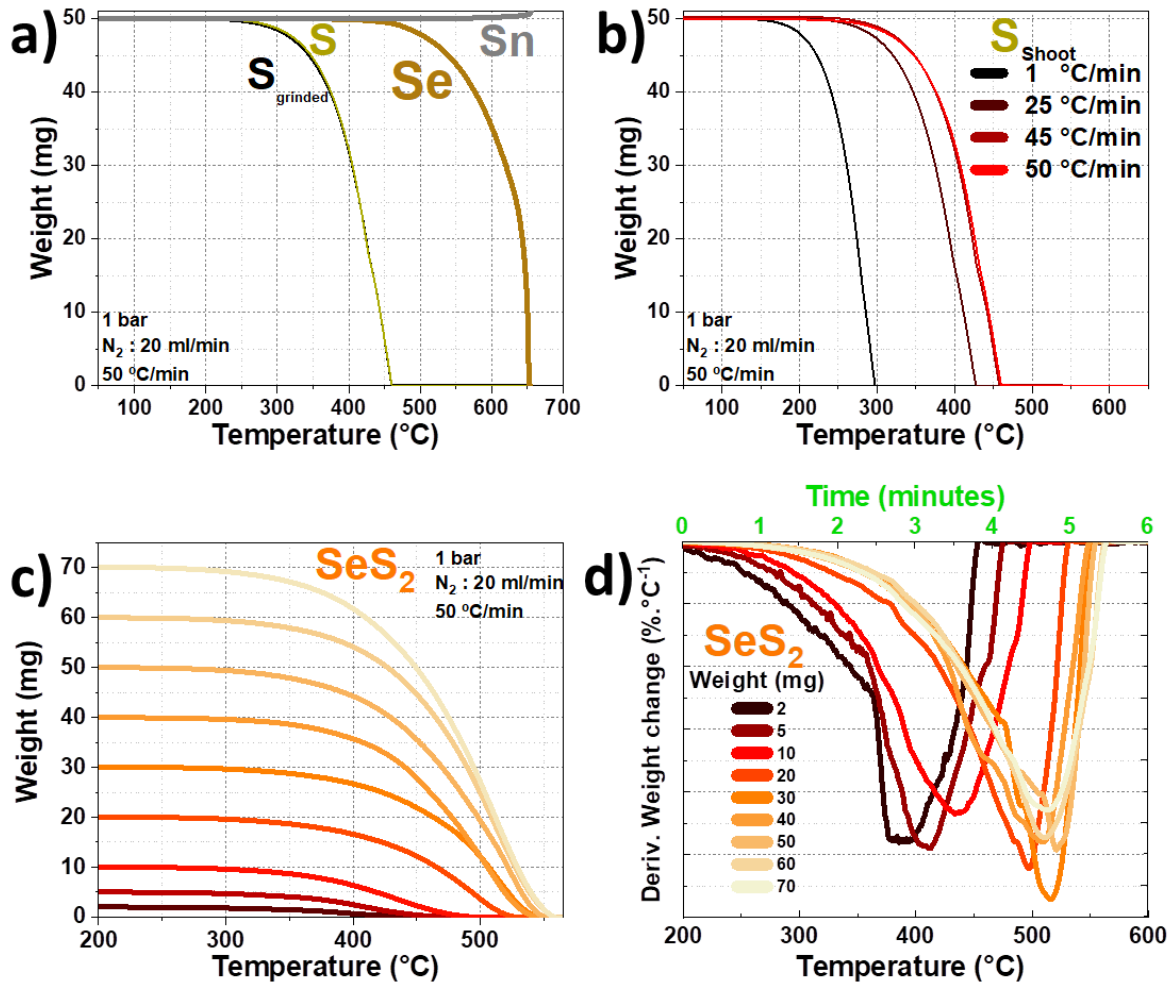


Figure 5.1.- TGA curves for **a)** Metallic tin (Sn) and chalcogenide (S and Se) powders, **b)** Distinct heating velocities (“rampings”) for elemental S pieces. **c)** TGA and **d)** DTA for several powder mass of selenium disulphide (SeS₂).

These results would help to justify the later proposed thermal routines (See Figure 5.5) for the CZTSSe absorber material synthesis and chalcogenide (S) pulse/shoot selected parameters. On one hand, Figure 5.1b reproduces the Sulfurization Type 2 TGA curves for several ramping values revealing the logarithmic Nature of the “volatilization” process for grinded elemental S. On the other hand, Figure 5.1c represents the SeS₂ TGA curves for heating at a constant ramp (50 °C.min⁻¹) for distinct compound mass values, while Figure 5.1d shows the corresponding differential thermal analysis (DTA) curves.

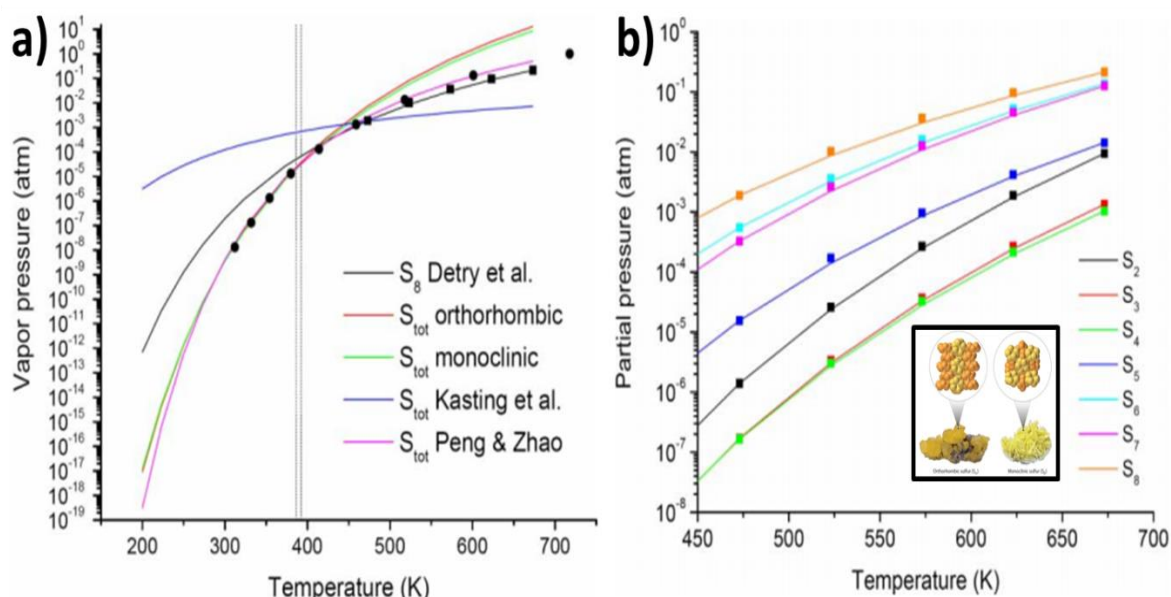


Figure 5.2.- a) Shows several vapor pressure curves for liquid and solid sulfur. The orthorhombic and monoclinic structure curves are applicable at temperatures below the sulfur melting point. The vapor pressure of S₈ over liquid sulfur (S_{liq}) is also shown. **b)** Mathematical fittings to experimental equilibrium vapor pressure curves for sulfur allotropes over liquid sulfur.¹

Figure 5.2 depicts several published measurements and fits for total sulfur vapor pressure versus temperature. Measured values for total sulfur vapor pressure are shown as filled circles. Important is to note that the measured values for S₈ (filled squares) and the (black) fit curve correspond to for liquid sulfur (S_{liq}).

The orthorhombic (red) and monoclinic (green) curves are valid below the appropriate sulfur phase melting point. The vertical dotted lines indicate the melting points of pure monoclinic (392 K) and orthorhombic (386 K) sulfur.¹

Moreover, Figure 5.3a shows the TGA curves of the different S sources (elemental S, SeS_2 , $\text{CH}_4\text{N}_2\text{S}$, and SnS) recorded in the 200–600 °C temperature range (with a ramping of 50 °C.min⁻¹ ramping).

It could be clearly observed that each of the S sources studied exhibits a markedly different volatility ($\text{CH}_4\text{N}_2\text{S} > \text{S} > \text{SeS}_2 \gg \text{SnS}$). In contrast, the differential thermal analysis (DTA) curves are shown in Figure 5.3b for the distinct S source pulse. Thiourea exhibits a high volatility with ~ 80% of its weight being vaporized in just 90 seconds (s) at 300 °C. After this, its evaporation rate stabilizes and remains constant during the rest of the analysis.

On one side, the estimated duration of the resulting sulfur pulse is around 30 s. And on the other hand, it takes around 200 – 240 s and 400 – 450 °C to obtain a sulfur pulse from elemental S. In addition, the duration of this pulse is the shortest with an estimated duration of approximately 23 s. The double peak observed in the curve suggests that the vaporization of this material results in two different S species, in good agreement with the expected vapor phase composition where $\text{S}_{2(g)}$ and a mix of different $\text{Sn}_{(g)}$ ($n = 3 - 8$) molecules are predicted under the equivalent conditions to this experiment.² In the case of SeS_2 , it takes around 270 seconds and a temperature higher than 550 °C to obtain a sulfur pulse, which lasts for roughly 50 seconds.

Finally, SnS does not vaporize at the pressure and temperature conditions employed in the TGA and, as such, it may be possible that it does not generate a sulfur pulse but rather acts as a constant S supply source.

As summary, it is possible to confirm that the setup and annealing routine developed in this work enable the introduction of S into the system in the form of short pulses (most of the chalcogenide supply takes place in less than 50 s, with the exception of SnS). This strongly suggests that for elemental S, thiourea, and SeS_2 , sulfur might be rapidly accumulated at the surface once the chalcogen shot arrives there, creating a very S-rich superficial region. Then, sulfur starts to diffuse from the surface toward the back during the final part of the cooling down process in a pure diffusive process, which is characterized by an exponential decay of the concentration of the in-diffusing element.

As a result, this exponential decay explains the formation of a sharp sulfur in-depth gradient profile.

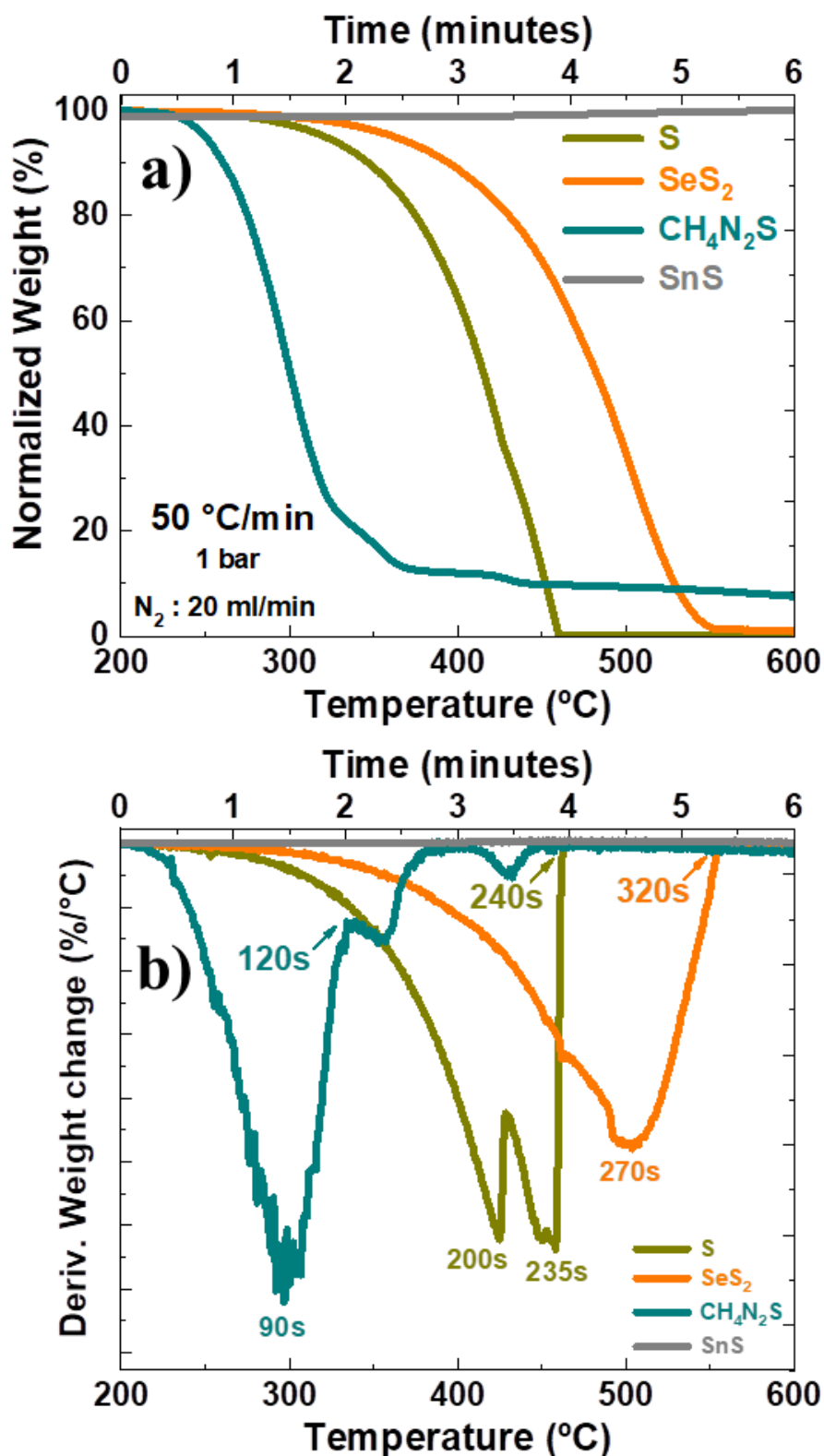


Figure 5.3.- a) Thermal gravimetric analysis (TGA) curves of the chalcogenides (S, SeS₂, CH₄N₂S, and SnS) materials recorded in the range of (200 - 600) °C at a heating rate of 50 °C.min⁻¹. **b)** Corresponding DTA curves.

5.3 CZTSSe structures: Raman Methodology and System Calibration

The assessment of sharp surface S/(S + Se) gradients in complex materials such as kesterite is a nontrivial task because the possible presence of secondary phases can mask the real compositional profile. For this reason, we ought first to develop a reliable methodology based on multi-excitation Raman spectroscopy,^{3,4} which combined with Auger compositional profile measurements can unambiguously quantify the S/(S + Se) gradients in the kesterite (CZTSSe) absorber layers. This Raman methodology is based on the use of macro spots (50–100 μm) and different excitation wavelengths with different in-depth penetrations. The potential of this methodology has been successfully implemented for the evaluation of abrupt S/(S + Se) surface gradients in CIGSSe.⁵ In order to utilize this approach, though, it is first necessary to perform a calibration that allows to estimate the S/(S + Se) ratio of kesterite absorbers from the Raman spectra.

As it was reported by Dimitrievska et al.,⁴ the ratio of the area of the peaks corresponding to the Se–Se (150–260 cm^{-1}) and S–S (270–380 cm^{-1}) vibrations in CZTSSe films correlates with their S/(S + Se) composition. Therefore, it is possible to carry out the aforementioned calibration of the Raman system by measuring reference CZTSSe samples with known compositions and calculated such peak area ratios. Figure 5.4a and Figure 5.4b show the spectra of the calibration samples for excitation wavelengths of 532 nm and 785 nm, respectively. The resulting calibration curves are shown in Figure 5.4c. A second-order parabolic fitting has been applied (Equations 5.1 and 5.2), and quantification errors of the S/(S + Se) ratio below 2 - 3% have been estimated for the 532 and 785 nm excitation wavelengths, respectively.

In the following Figure 5.4, these two calibration curves are extensively used to calculate the anionic ratio at the interfaces of the different CZTSSe samples from Raman measurements. These will be complemented with Auger spectroscopy compositional profiles to corroborate the negligible impact of secondary phases on the S/(S + Se) ratio determination.

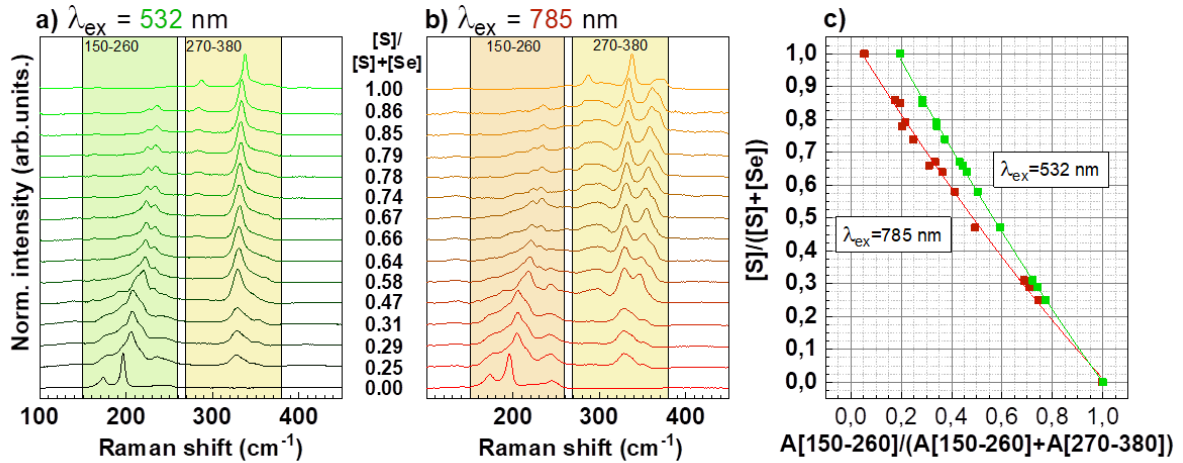


Figure 5.4.- Raman spectra of reference samples under **a)** 532 nm and **b)** 785 nm excitation wavelengths. **c)** Empiric al fitting for the S/(S+Se) compositional ratio and Raman areas calibration using a parabolic model.⁴

$$\left(\frac{[S]}{[S]+[Se]}\right)_{532} = 1.264 - 1.467A + 0.204A^2; r^2 = 0.9994; \varepsilon_{\left(\frac{[S]}{[S]+[Se]}\right),532} < \pm 0.03 \quad (\text{Eq. 5.1})$$

$$\left(\frac{[S]}{[S]+[Se]}\right)_{785} = 1.054 - 1.239A + 0.196A^2; r^2 = 0.9960; \varepsilon_{\left(\frac{[S]}{[S]+[Se]}\right),785} < \pm 0.02 \quad (\text{Eq. 5.2})$$

5.4 First Insights on the Experimental Superficial Chalcogenization of CZTSSe*

Once those facts have been declared, a completely novel and disruptive, originally designed experimental setup for the reactive thermal annealing is proposed for the following experiments (See Figure 5.5). For this part of Thesis absorber material development, in the first zone of the furnace (zone 1, see Figure 5.5a), the sputtered metallic precursor is introduced in one of the graphite boxes together with graphite crucibles containing elemental Se (100 mg, Alfa Aesar, metal basis 5N, 200 mesh) and Sn (5 mg Alfa Aesar, metal basis, 99.995%, 100 mesh).

Therefore, this box is connected through a quartz tube with the second graphite box, which contains a S source and is located in the second zone (zone 2) of the furnace. S pieces (Alfa Aesar, Puratronic, metal basis, 5N purity, $m_S = 50$ mg) were utilized.

First, furnace zone's 1 is energized, in which a graphite box containing the Cu/Sn/Cu/Zn precursor and the Se + Sn elemental powders are placed. In this stage, the precursor is selenized at 400 °C forming $\text{Cu}_2\text{ZnSnSe}_4$ (CZTSe), followed by a crystallization step at 550 °C.^{6,7} Secondly, zone 2 of the furnace is heated (up to 600-650 °C) rapidly evaporating the S source (See Section 5.2).

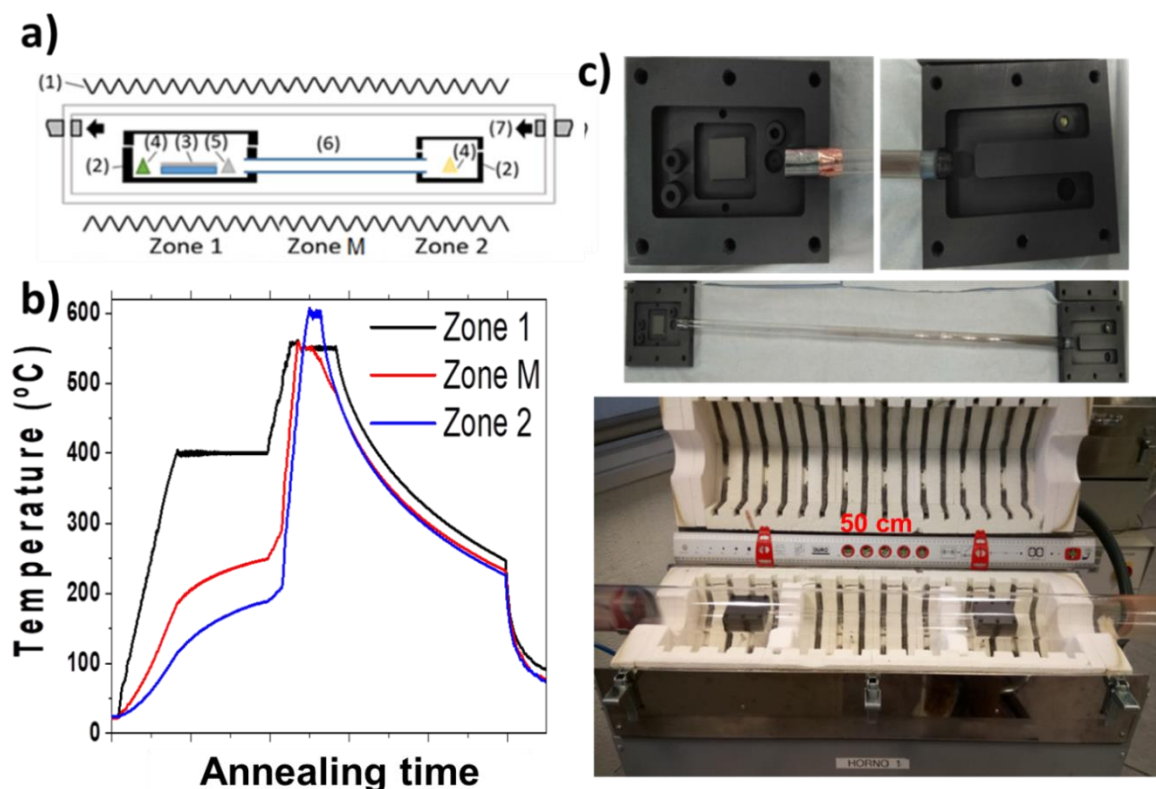


Figure 5.5.- a) Schematic representation of the experimental setup composed by: (1) heating coils, (2) semi-closed graphite boxes, (3) SLG/Mo/CZT precursor, (4) elemental S, (5) Sn, (6) interconnecting quartz tube, (7) carrier gas (Ar) inlet. b) Thermal profiles used for the sulfo-selenization process. c) First experimental approach of the system.

The resulting sulfur vapor is thermally drifted toward zone 1 through the connecting quartz tube and introduced in the system as a “fast sulfur pulse/shoot” assisted by zone’s M + 2 rapidly heating (See Figure 5.5b). In this part, it was investigated the effect of introduce the S shoot during the CZTSe crystallization step (550 °C). Zone M stands for the “medium assisting” heating zone.

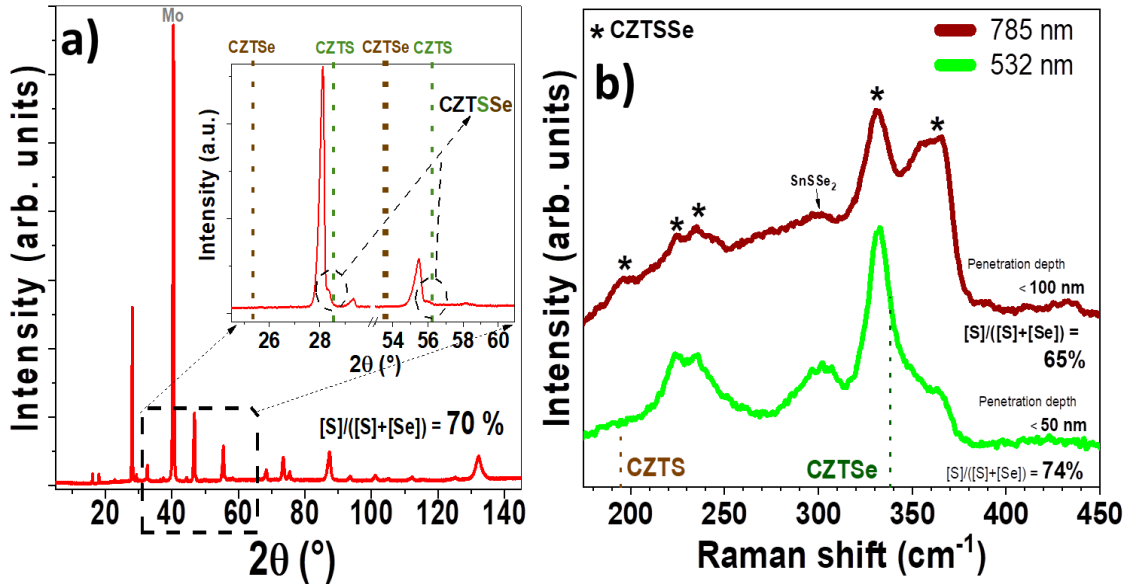


Figure 5.6.- a) XRD and b) Raman spectroscopy of the CZTSSe thin film. ^{3,8,9}

From first experimental structural characterization techniques (XRD and Raman spectroscopy in Figure 5.6) mainly concluded that a CZTSSe structure has been crystallized, but in all study cases (XRD, Raman spectroscopy, XRF, PL and EQE) the final anionic compositional ratio $S/(S + Se) \approx 70\%$ was found to be homogeneously mixed throughout the whole thickness of the absorber.

However, and as it is well known amongst the kesterite community, if it is true that a considerable amount on direct crystallographic information may be gathered from X-ray diffraction, there exists an overlapping of XRD maxima corresponding to the apparition of secondary phases. Furthermore, multiwavelength Raman spectroscopy utterly corroborates the CZTSSe well crystallized phase. Moreover, the difference between the Raman spectra for 785 nm and 532 nm wavelengths indicates the generation of a superficial anionic grading.

Therefore the first intentionally anionic graded SEMS-IREC Mo/MoSSe/CZTSSe/CdS/iZO/ITO solar cell device was performed, which JV and EQE measurements are shown in Figure 5.7.

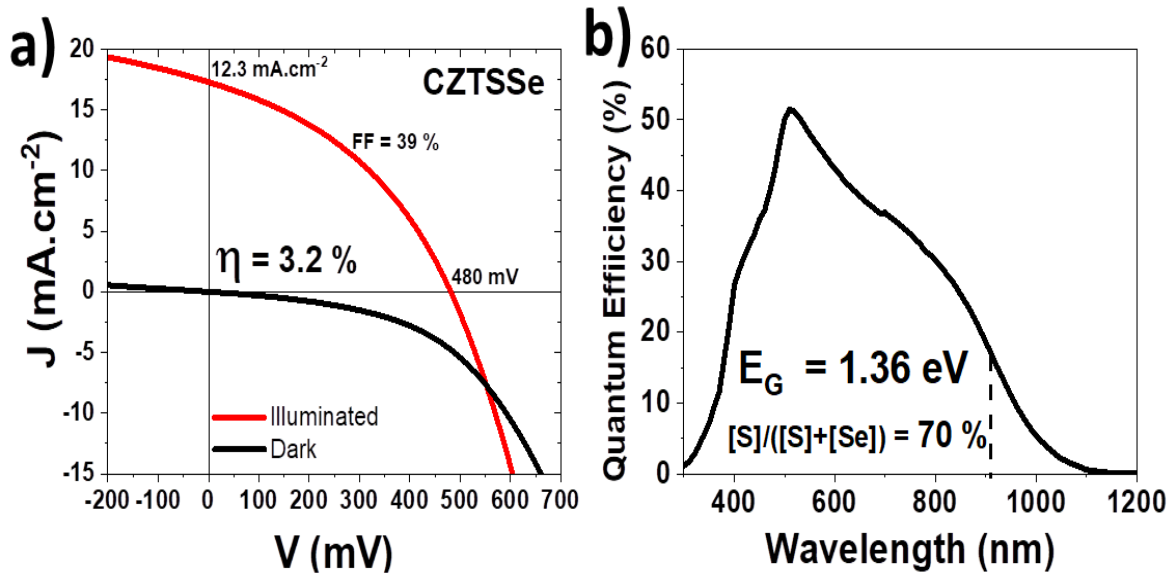


Figure 5.7.- a) JV and b) EQE (inset: photoluminescence spectra) measurements of the first SEMS-IREC anionic graded Mo/MoSSe/CZTSSe/CdS/iZnO/ITO solar cell device. ¹⁰

The optoelectronic parameters derived from the first characterizations of the CZTSSe solar cell device corroborate the high sulfur content present in the device since 12.3 mA.cm⁻² and 480 mV with a 1.36 eV bandgap are most likely CZTS rather than CZTSe device optoelectronic parameters.

These first results strongly encourage the possibility of a successful sulfur introduction into the CZTSe crystalline structure by means of this experimental procedure.

In order to generate the desired (previously commented in the modeling) anionic profiles to further enhance the PCE of the solar cells, thus a fine tuning and optimization of the processing parameters therefore required.

For this purpose, a deeper investigation and understanding on the chalcogenide (S sources) evaporation dynamics had to be performed (See Figure 5.3); but first of all, a deepening into optimization of the experimental arrangement ought to be explored.

5.5 Superficial Chalcogenization: Experimental Setup Optimization

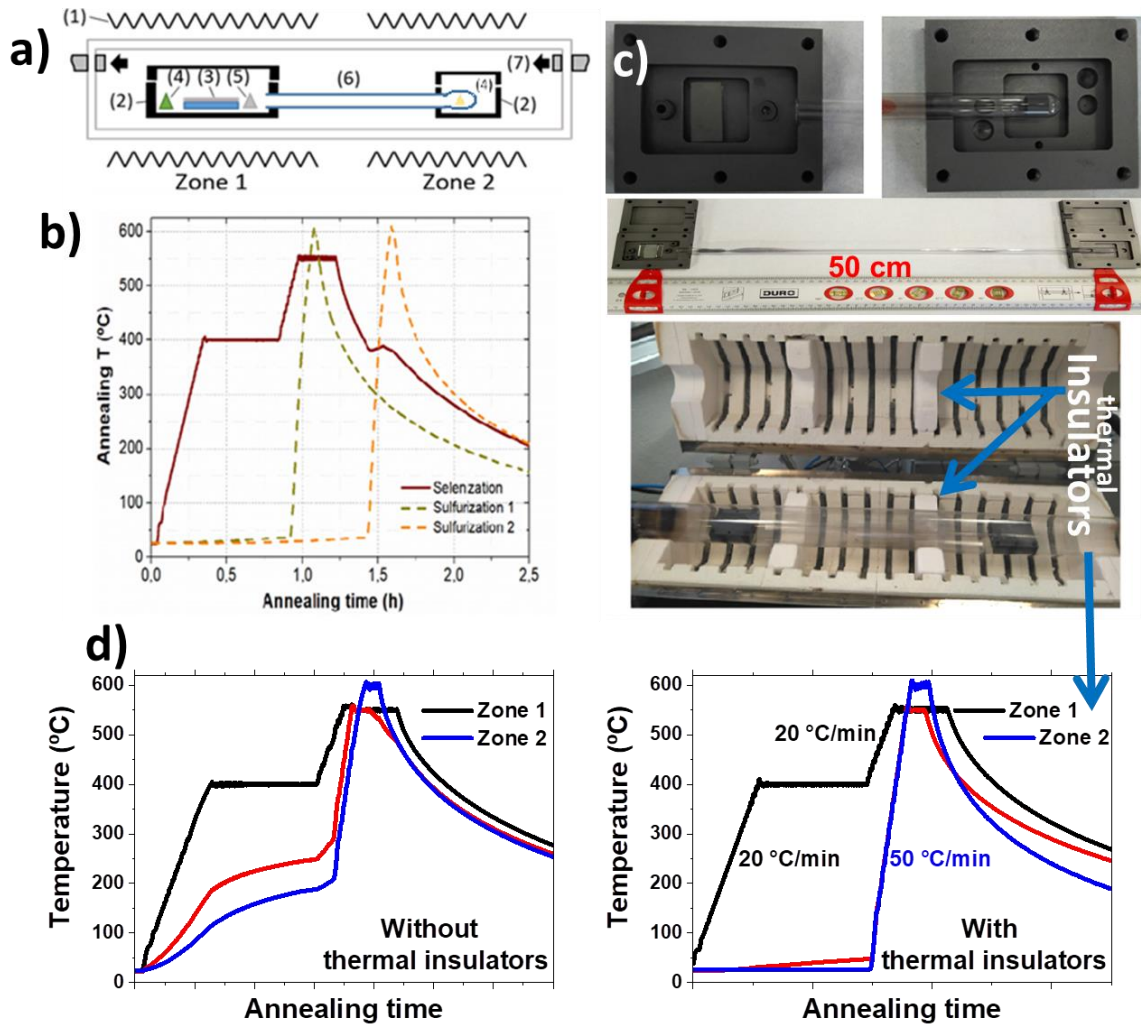


Figure 5.8.- a) Schematic representation of the experimental setup composed by:(1) heating coils, (2) semi-closed graphite boxes, (3) SLG/Mo/CZT precursor, (4) chalcogenide sources, (5) Sn source, (6) interconnecting quartz tube, (7) carrier gas (Ar) inlet. **b)** Distinct thermal profiles utilized (Sulfurization Type 1 and Type 2). **c)** Experimental setup main details. **d)** Comparison of the experimental thermal profiles with and without thermal insulators.

In regards to the optimization of the superficial chalcogenization setup, Figure 5.8a shows a representation of how in the first zone of the furnace (further referenced as zone 1), the sputtered metallic precursor is introduced in one of the graphite boxes together with graphite crucibles containing elemental Se (100 mg, Alfa Aesar, metal basis 5N purity, 200 mesh) and Sn (5 mg Alfa Aesar, metal basis, 99.995%, 100 mesh).

Therefore, this box is connected through a quartz tube with the second graphite box, which contains a S source and is located in the second zone (zone 2) of the furnace. Different S sources with different expected reactivities were investigated: S pieces (Alfa Aesar, Puratronic, metal basis, 5N purity, $m_S = 50$ mg), SeS_2 (Alfa Aesar, 97%, $m_{SeS_2} = 186$ mg), SnS (Alfa Aesar, 99.5%, $m_{SnS} = 422$ mg), and CH_4N_2S (Sigma-Aldrich, $\geq 99\%$, $m_{thiourea} = 188$ mg). The different quantities of the sulfur sources were calculated as a way of ensuring that in all cases there is an equivalent sulfur mass of 50 mg. **For the sake of the separate operation and insulation of the different zones of the furnace, this strategy upgrade enables an independent and improved control of both the selenization and sulfurization processes (Figure 5.8c and Figure 5.8d).**

Figure 5.8b shows the thermal routine employed to create front S/(S + Se) compositional gradients. First, only zone 1 of the furnace, which contains the Cu/Sn/Cu/Zn precursor and the Se + Sn elemental powders, is switched on. In this stage, the precursor is selenized at 400 °C forming $Cu_2ZnSnSe_4$ (CZTSe), followed by a crystallization step at 550 °C.^{6,7} Second, zone 2 of the furnace which contains the chalcogen source is heated up rapidly evaporating the S source. The resulting sulfur vapor is thermally drifted toward zone 1 through the connecting quartz tube and introduced in the system as a “fast sulfur pulse/shoot”.

This work investigated the effect of S-Shoot introduction during the CZTSe re-crystallization step at 550 °C (thermal profile shown as a dark green curve in Figure 5.8b or during equilibrium conditions in the first case, while in the second case it is introduced in experimentally found “sweet spots”, as the order out of a “sandbox of chaos” corresponding

Out from Thermodynamic Equilibria States. 11,12

Additionally, it was tested the introduction of the “sulfur pulse” during the synthesis step at 400 ° and at different stages of the crystallization process at 550 °C and mainly concluded that in all cases the final S/(S + Se) composition is homogeneous throughout the whole thickness of the absorber material.

Additionally, the main details regarding the experimental setup are shown in Figure 5.8c. Finally, a comparison of the experimental thermal profiles with (right side) and without (left side) thermal insulators is represented in Figure 5.8d. Moreover, a finely detailed explanation of the thermal routine of the process is shown in Figure 5.9.

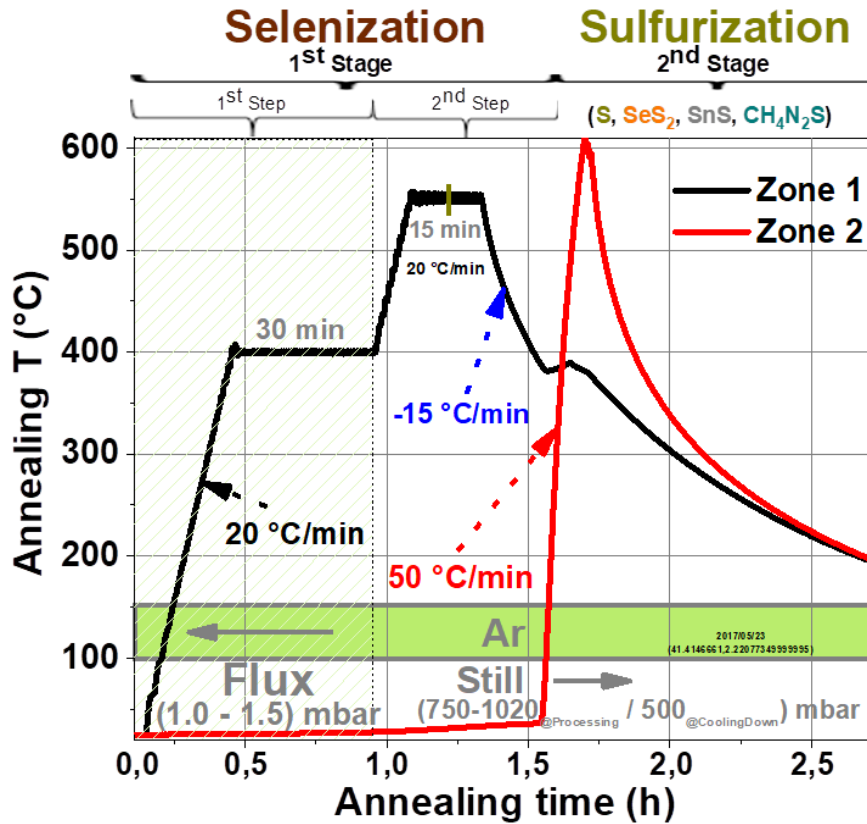


Figure 5.9.- Thermal profiles for the superficial chalcogenization process.

Taking this into account, a graphite box containing the stacked metallic precursor layers in the SLG/Mo/Cu/Sn/Cu/Zn configuration, along with the elemental (Se + Sn) powders are placed inside a multi-zone tubular furnace reactor (zone 1, Figure 5.8). Hence, an analogous graphite box containing the superficial reactive chalcogenide material is placed inside the furnace reactor (zone 2, Figure 5.8). In this sense, the experimental setup consists of a semi-closed system conformed by two graphite boxes (reaction volume of 21 cm³) interconnected by a 50 cm in length quartz tube (See Figure 5.8). As it was previously mentioned, the zone’s 1 first stage (selenization) annealing was conducted in a two-step process. Just after two cleaning evacuation purge cycles (base vacuum of 5×10^{-3} mbar), an inert gas (Ar) flow (Tecfluid 2100 E-08960 gauge valve) was introduced into the furnace system until reaching 1 mbar of dynamic flux (open system) total pressure inside the furnace reactor. In such a way that the thermal routine for this first step (synthesis) consist in heating the furnace’s zone 1 from room temperature to 400 °C with a ramp of 20 °C min⁻¹, during a dwell time of 30 minutes (See Figure 5.9). Immediately upon this second step and, a background argon pressure inside the chamber was raised to 750 mbar, resulting this in a “still” (closed system) pressure state.

In a similar fashion, the thermal routine for the second step (recrystallization) lies again, in heating the furnace's zone 1, from 400 °C to 550 °C with a ramp of 20 °C.min⁻¹, during a dwell time of 15 minutes (See Figure 5.9). Because of the selenium enriched atmosphere, this annealing stage is called selenization. In this way, the selenization annealing process of the CZT precursor material takes about 70 minutes in order to be completed and the CZTSe absorber layer formation takes place. Just right after finishing the 70 minutes selenization (1st stage), the whole experimental setup was cooled to below 400 °C with a naturally occurring cooling ramp of -15 °C.min⁻¹, no dwell time and at almost 1 bar of pressure (See Figure 5.9). Then an additional annealing process after the selenization as a way of introducing sulfur into the already finished absorber takes place as the second stage of the process. Which leads to the exactly moment of the break-off experiment part is performed, by in-situ heating the furnace's zone 2 from ≈ 40 °C up to 650 °C with a ramp of ≈ 50 °C.min⁻¹ (no dwell time), at almost 1 bar of pressure as it is schematized in Figure 5.9. In this instance, because of the S enriched atmosphere, this second annealing stage is called sulfurization. Therefore, a natural cooling down to room temperature occurs. Insertion process time and temperatures are varied to adjust the final S concentration. By these means, the superficial reactive chalcogenide (S, SeS₂, CH₄N₂S, or SnS) introduction as a way of introducing a complex graded anionic composition profile over the SLG/Mo/Mo(S,Se)_x/CZT(S_xSe_(1-x))₄ structure. Approximately, 100 mg of elemental Se powder (Alfa Aesar, metal basis 5N purity, 200 mesh) together with 5 mg of elemental Sn powder (Alfa Aesar, metal basis, 99.995%, 100 mesh) were placed into the zone's 1 graphite box next to the precursor samples. Similarly, 50 mg of S chalcogenide pieces (Alfa Aesar, Puratronic, metal basis, 5N) were placed into the tubular furnace zone's 2 graphite box. The two graphite boxes were then interconnected by a quartz tube (500 mm long, Φ_{ext} = 10 mm) (See Figure 5.9). The sulfo-selenization process of the precursor material (area 2.5 × 2.5 cm²), as well as the novel post-sulfurization thermal annealing were both in-situ performed by conventional thermal process (CTP) using a multi-zone tubular furnace (Hobersal ST1008080SP-37). The temperatures during all the process presented here were measured by a calibrated Type K thermocouple (Eurotherm 3216 controller) located inside the furnace chamber, just below (outside) tube. Finally, the pressure changes during the process presented here were sensed by a calibrated pressure gauge (Oerlikon Leybold vacuum THERMOVAC TM 101) positioned towards the exhaust mechanical pump system.

5.6 Investigations on Chalcogenide Evaporation Dynamics

5.6.1 Case of S and Shoot Introduction Scenario

Since the main objective of this experimental work resides in the generation of a sharp and abrupt superficial anionic grading profile as our modeling previously suggested in Chapter IV.

The before called “Sulfurization Type 1” and related S-shoot/pulse introduction scenarios (Labeled as: **00**, **01**, **1**, **2**, **3** and **4** in Figure 5.10) may be logically counterintuitive since it was already stated that the formation enthalpies for both CZTS and CZTSe are (energetically speaking) so close^{13,14} that the presence of both anionic species (S and Se) during the formation of the CZTSSe compound would tend to homogenize the anionic compositional substitution along thickness of the thin film absorber material.

However the study of this case scenario(s) may shed light on the anionic substitution thermodynamics during the kesterite material formation.

As it is shown in Figure 5.10a, several S-introduction scenarios are studied. Referred to zone 1 (selenization process), during the following:

- (00)** 1st step mid-time (400 °C)
- (01)** Ramping transition between 1st and 2nd step (400 < T <= 550 °C)
- (1)** 2nd step mid-time (550 °C)
- (2)** 2nd step ¾ to-end time (550 °C)
- (3)** End of 2nd step (T <= 550 °C)
- (4)** Cooling down (Zone 2 launched when T_{@Zone 1} = **380 °C**)

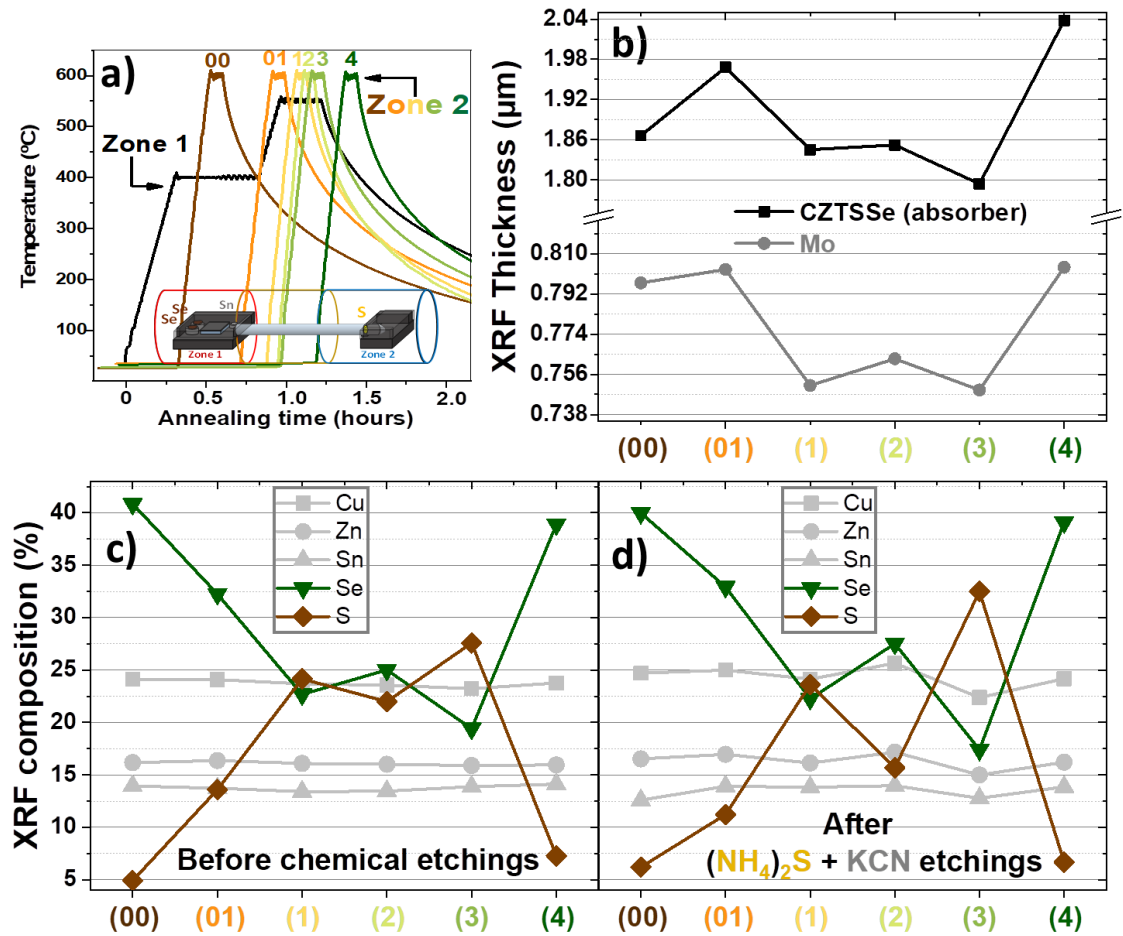


Figure 5.10.- a) Distinct thermal profile scenarios utilized for the superficial chalcogenization process. XRF of the b) Absorber and Mo layer thickness and c) Absorber atomic composition (Cu, Zn, Sn, Se and S) for the absorber material synthesized by the distinct scenarios, before (left) and after (right) applying superficial chemical etchings.

Figure 5.10b shows the absorber and Mo layer X-ray fluorescence (XRF) thickness variations showing a similar behavior for both of them. Suggesting the impact of the thermal profile on the S-Se interplay in both CZTSSe and MoSSe crystalline structure growth processes and how they might be similarly affected.

Furthermore, Figure 5.10c demonstrates how the S-Se composition tends to homogenize when both anionic species are present under a thermal-energy providing active process. However, Figure 5.10d shows that there exist a higher impact on the S- and Se-XRF signals when chemical etchings are applied in these films, also suggesting the appearance of a higher amount of secondary phases at these introduction scenarios.

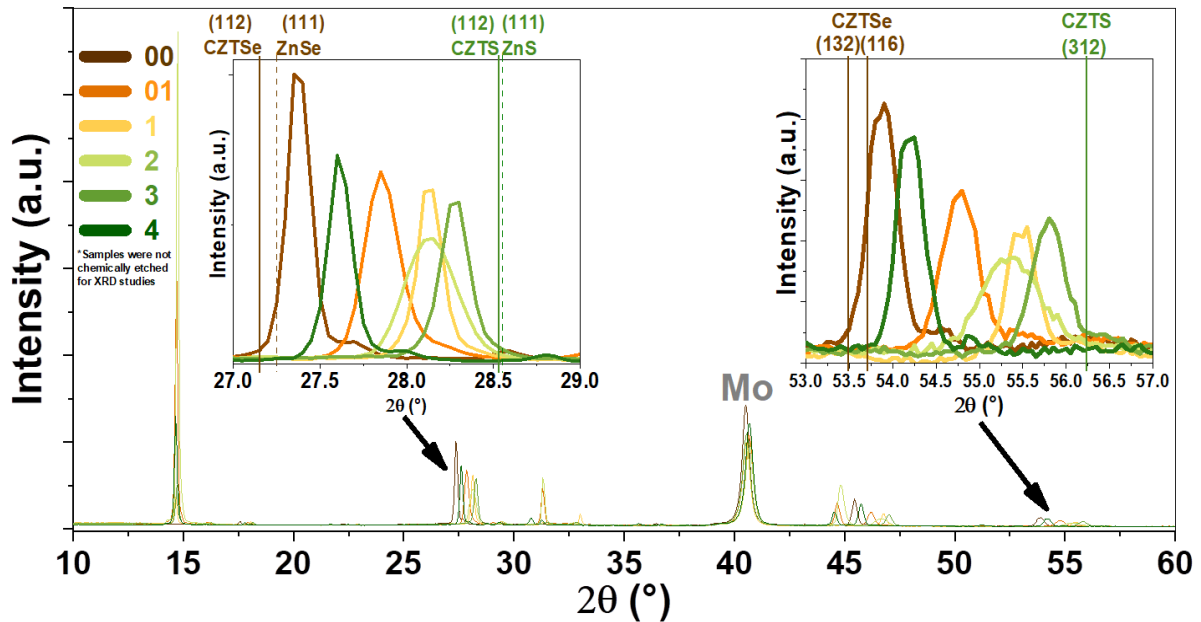


Figure 5.11.- XRD of the kesterite absorber thin films (CZTSSe) for distinct thermal profile scenarios utilized for the superficial chalcogenization process kesterite absorber thin films.

XRD of the kesterite absorber thin films (CZTSSe) for distinct thermal profile scenarios utilized for the superficial chalcogenization process.

On one side, kesterite absorber thin films. Also, back contact (Mo) diffraction signals are observed ($2\theta \approx 41^\circ$).

On the other hand, Figure 5.11 shows the X-ray diffraction (XRD) patterns demonstrating the CZTSSe well crystallized structures.

From Figure 5.11, it could be observed that from scenario (00) up to scenario (3) there exists a linear increase on the sulfur content inside the CZTSSe structures.

And disruptively, while introducing the S-shoot during the cooling down (Scenario 4) there is a subtle S inclusion at the same time that the CZTSSe structure crystalline quality is clearly enhanced.

5.6.2 Accessing the Back (Rear) Interface

As it is a reference procedure for this Thesis, to routinely access to the absorber kesterite/back contact interface, **a far-from-equilibrium thermomechanical lift-off (peeling) process** has been employed and optimized.

Although this lift off method has been successfully applied not only in all types of kesterite/Mo interfaces, but also chalcogenide thin films in general; a deepening on the explanation of this method is beyond the scope of this study.

However demonstrations and practical implications on the results and lift-off performance are shown in Figure 5.12, in which a CZTSe reference sample is demonstrated. Figure 5.12a shows that the CZTSe/back contact interface is characterized by small CZTSe grains, a ~150 nm MoSe_x layer (resulting from the partial selenization of the Mo back contact during annealing) and the presence of voids. A pretty well compact front surface (See Figure 5.12b) with lateral grain size around 2 μm but with several evidenced voids observed at the back interface of the CZTSe absorber once the material is lifted-off as it is shown in Figure 5.12c.

To further corroborate the potentiality of this simple technique and provide a clear example of a fair-enough clean and correct lift-off process, Figure 5.12d shows the top (planar) micrographs of the “Substrate” corresponding to the peeled-off part of the film, which corresponds to the MoSe_x back contact of the film.

Since the SE2 micrographs are a combination of secondary and backscattered detected electrons by secondary emission, while the ESB corresponds to a pure backscattered electron detection, they serve as a Z-contrasted images in all the here exposed cases.

On the other hand, the INLENS stands for a mostly secondary electron detection positioned just above the studied sample. Assisted by three SEM distinct electronic and positional signals (SE2, ESB and INLENS), it could be observed that after an out-of-equilibrium peeling-off process an exposed mostly Mo back contact with some Z-lighter “residues” over absorber’s surface. This pieces may wither correspond to MoSe_x (later confirmed by Raman spectroscopy) or to smaller than bulk’s rear kesterite structures.

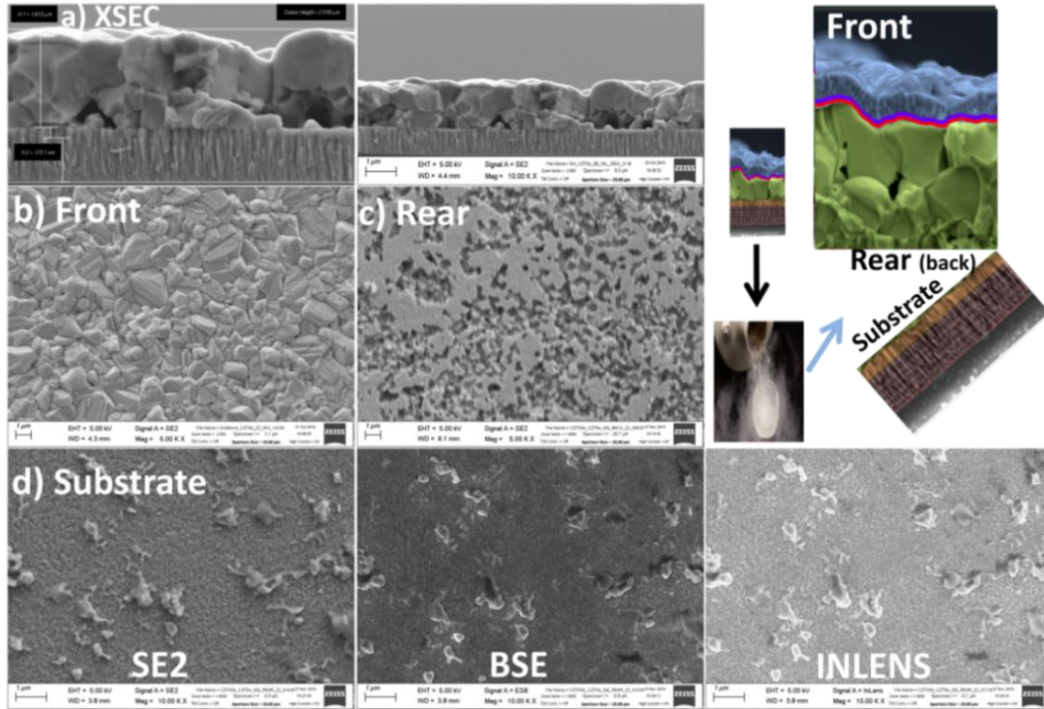


Figure 5.12.- SE2-SEM of **a)** Cross Sectional at 5 kX (left) and 10 kX (right). **b)** Planar-view of the Front surface and **c)** Rear (back) interface after being detached from the **d)** Substrate, in which the secondary (SE2) backscattered (BSE) electron signals and, the sample zenithal positioned detector (INLENS) signal.

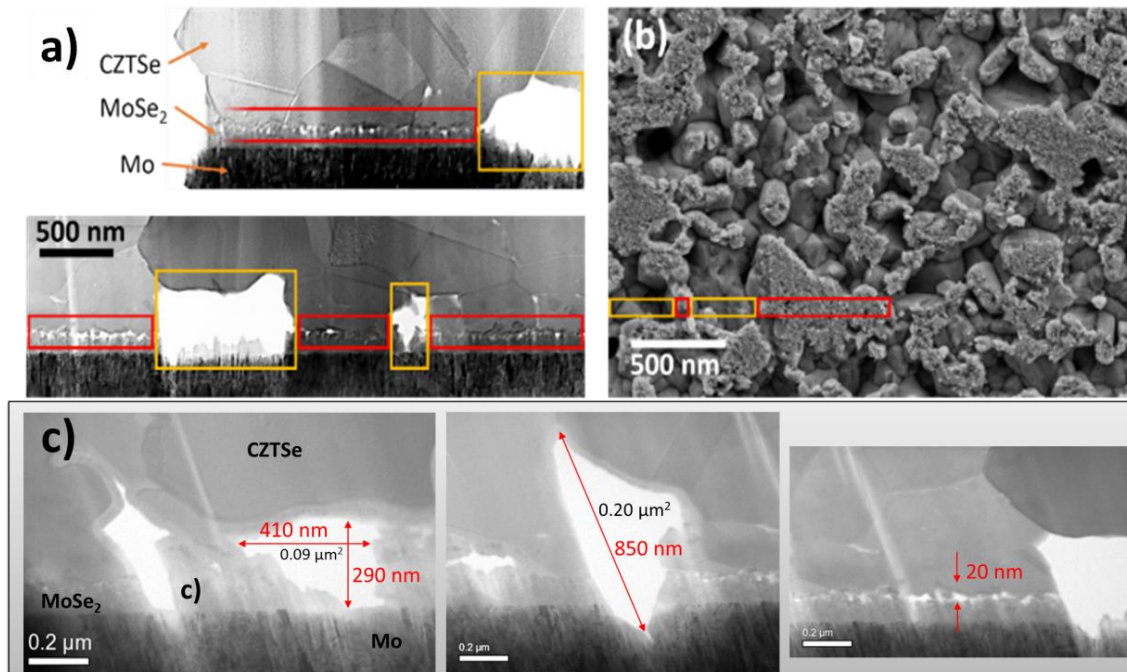


Figure 5.13.- a) Collage image of a series of cross-sectional STEM images of the CZTSe device. The CZTSe, MoSe₂ and Mo layers in the back interface are indicated. **b)** Planar view SEM image of the CZTSe rear interface. Red squares indicate regions with nano-voids, and yellow/orange squares indicate micro-voids. STEM images representing the **c)** Micro (left), Sub-micro (center) and nano (right) voided rear contact enlarged areas for the CZTSe/MoSe_x/Mo interface.¹⁵

Basically, two different types of voids can be distinguished in Figure 5.13: large micrometric voids (orange rectangles) and small nanometric voids (red rectangles). The micrometric voids observed in cross-section SEM and STEM collage images can achieve sizes up to $0.5 \mu\text{m}^2$.¹⁵ This represents approximately the 10% of the cross-section area of the CZTSe absorber layer and $\sim 40\%$ of the contact interface length between CZTSe and MoSe_x/Mo . A different perspective of the micrometric voids can be obtained from the planar view SEM image of the back interface of the absorber (acquired after mechanical lift-off) presented in Figure 5.13b.

Figure 5.13 shows that the presence of large voids spreads over the whole back surface of the CZTSe absorber decreasing the contact area with the back contact.

In particular, Figure 5.13b shows that the contact area between CZTSe and MoSe_x/Mo back contact is around 40% of the total area of the image (in agreement with the cross-sectional analysis). In the case of the small nanometric voids, the x-sectional STEM image shown in Figure 5.13a allows estimating their size to a radius of some tens of nanometers.

The presence of these small voids is also confirmed by the rough texture of the CZTSe grains observed in the planar SEM image of the back interface (See Figure 5.13b). These nanometric voids can create weak points that enable an easy and clean mechanical exfoliation process of the CZTSe absorber from the back contact layer. On the other hand, wettability is strongly suggested as responsible for the poor back interface.¹⁶ This way, once the rear (back) interface accessing process has been clarified, in before, further structural confirmation, compositional and morphological insights on the anionic graded CZTSSe films synthesized by distinct thermal profile scenarios are provided by Raman spectroscopy and cross sectional SEM micrographs. As it is represented in Figure 5.13a inset, by performing a lift-off thermo-mechanical process it was possible to perfectly access the back surface of the CZTSSe absorber layers. Therefore the 532 nm Raman spectra could be gathered for the front, back and substrate regions as it is shown in Figure 5.13b. Also, it is clearly observed that the lift-off process was severely clean applied since the Raman signals from the “substrate” piece mostly consist of a $\text{Mo}(\text{S},\text{Se})_2$ crystalline structure phase. But more importantly this figure shows a clear structural and compositional difference between the CZTSSe structures synthesized by the distinct S-shoot introduction scenarios.

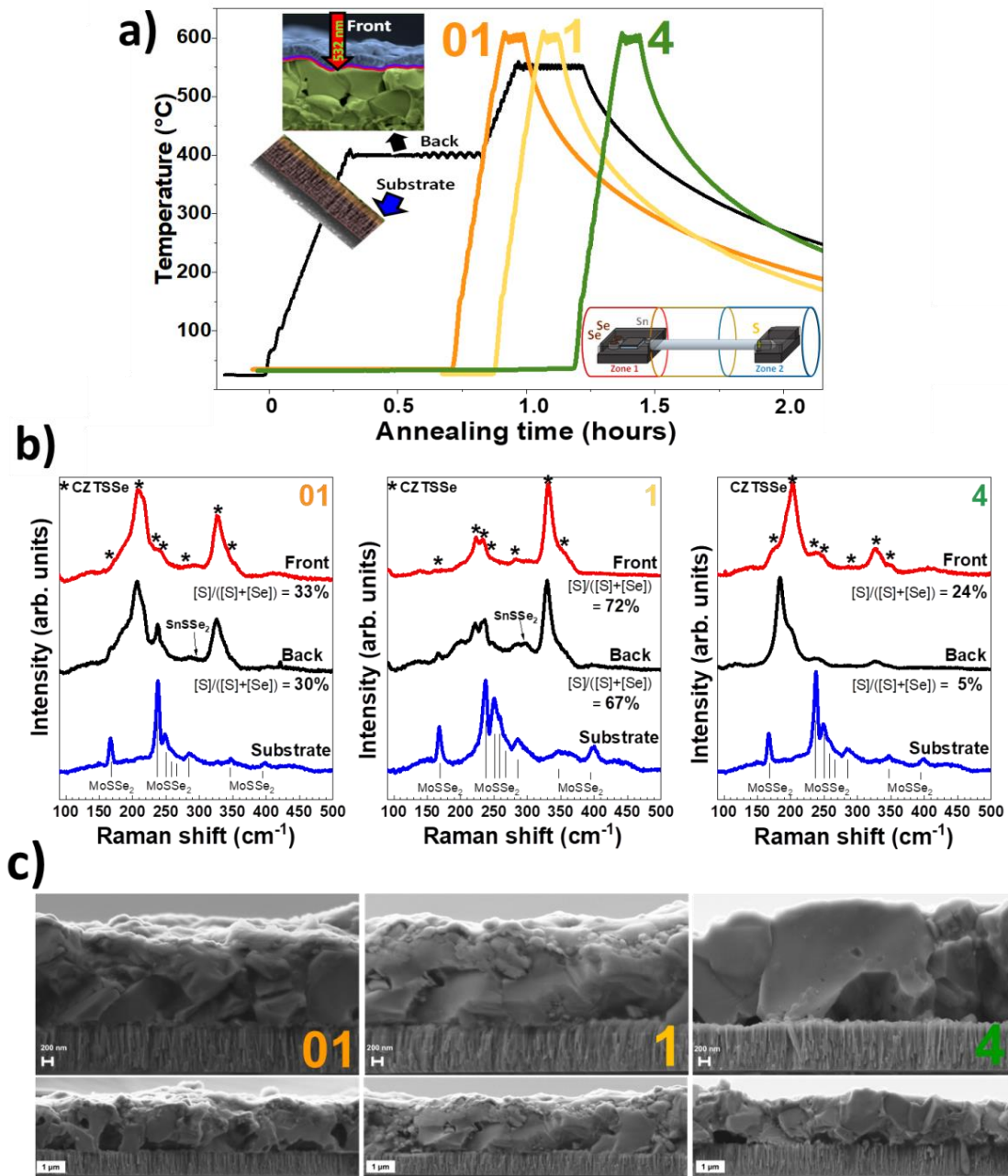


Figure 5.14.- a) Distinct thermal profile scenarios (01, 1 and 4) utilized for the superficial chalcogenization process. **b)** 532 nm Raman spectroscopy measurement regions displayed. **c)** Cross sectional SE2-SEM micrographs (WD = 3 mm, 5 kV).

It could be observed that before the re-crystallization step (Scenario 01), a very low S incorporation (due to a high S/Se competition) occurs, leading to a very low anionic gradient $\approx 3\%$. During 2nd step (1), since there is a high S incorporation (low pressure of Se, and high activation energy) a generation of a low anionic (S/S+Se) gradient $\approx 5\%$ takes place.

In a disruptive way, after the re-crystallization step (4) there is a low S incorporation (low activation energy) generating a high anionic gradient $\approx 20\%$ between front and back (rear) surfaces of the CZTSSe structural composition.

Moreover, correlating structural results with the morphological observations displayed in Figure 5.14c it is indisputably confirmed that the presence of an anionic gradient in the CZTSSe structure occur inside the same grain in the synthesized kesterite thin films.

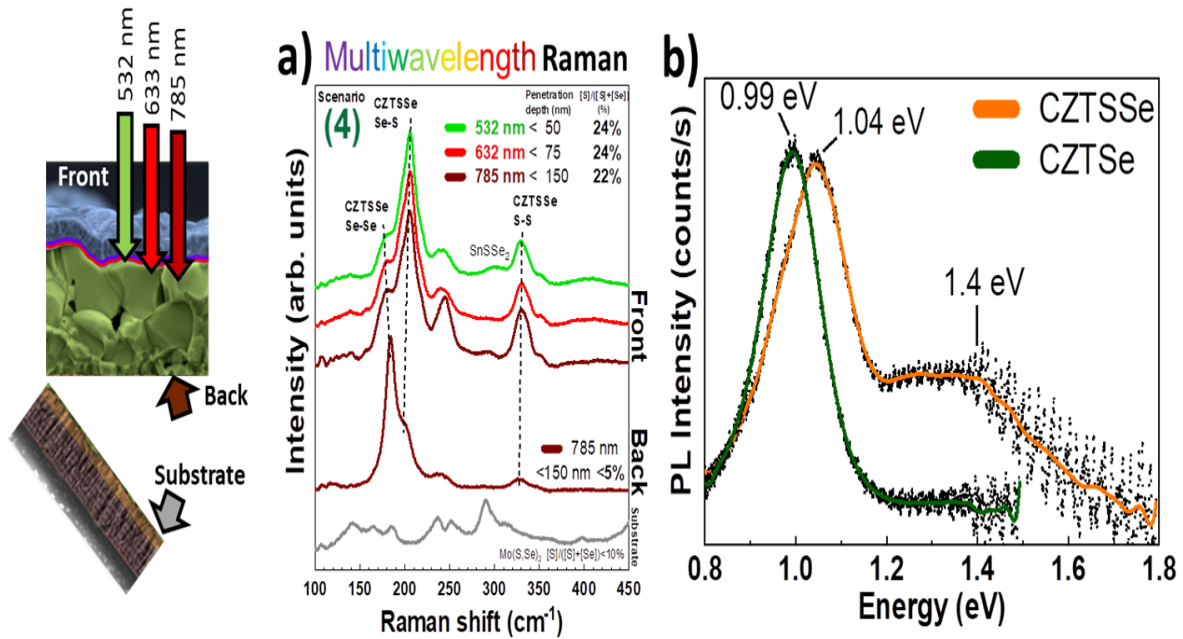


Figure 5.15.- a) Multiwavelength Raman spectra at front, back and substrate surfaces for CZTSSe synthesized by the S-Shoot at scenario 4. **b)** Front surface photoluminescence (PL) spectra.

Figure 5.15a shows the front surface multiwavelength (532, 632, and 785 nm) Raman spectra in which the laser penetration depth according to the material’s absorption coefficient is found to be ~ 50 , 75 , and 100 nm for each wavelength, respectively. Additionally it is shown the back (rear) and substrate 785 nm Raman spectra analysis.

Once again, both multiwavelength and rear analysis unequivocally demonstrates the anionic bandgap grading in the CZTSSe structure.

In this case, it could be observed a 20% difference between back and front surfaces.

Fact which shows absolutely correspondence with the photoluminescence (PL) spectra shown in Figure 5.15b as a comparison between a pure CZTSe (≈ 0.99 eV) reference thin film and the (Scenario 4 in Figure 5.14a) anionic graded CZTSSe sample, which corresponds to the maximum number of optical transitions between two Boltzmann distributions at 300 K (in the valence band and conduction band).

As follows in Figure 5.15, a first order estimation of differences is clearly evidenced the appearance of a band in between 1 eV and 1.4 eV for CZTSSe.

Last but not least, the implications on the front anionic graded profile CZTSSe are further *in-situ* confirmed by the power conversion efficiency (PCE) enhancement on solar cell devices. Figure 5.16a shows a four dimensional (PCE, open circuit voltage V_{OC} , short circuit current density J_{SC} , and fill factor FF) optoelectronic plots for the CZTSSe kesterite absorber devices synthesized by distinct S-Shoot introduction scenarios.

It is possible to note that despite the “reasonable” V_{OC} values (Up to 460 mV), due to the low J_{SC} values (Up to ~ 17 mA.cm⁻²), PCE are not higher than 2% when homogenously mixing the CZTSSe alloy (Scenarios from 00 to 3).

Disruptively, when the Type 2 S-shoot is introduced during the cooling down (Scenario 4) it an astonishing PCE enhancement from 0.1% to 7.2% occurs.

The main optoelectronic parameters for champion CZTSSe graded device are shown in the 1 Sun JV illuminated curve shown in Figure 5.16b.

On the other hand, the calculated bandgap values from the Internal Quantum Efficiency (IQE) curves are shown in Figure 5.16c, additionally, Figure 5.16d shows the External Quantum Efficiency (EQE) and IQE curves along with the estimated V_{OC} deficit for the champion anionic graded CZTSSe solar cell device.

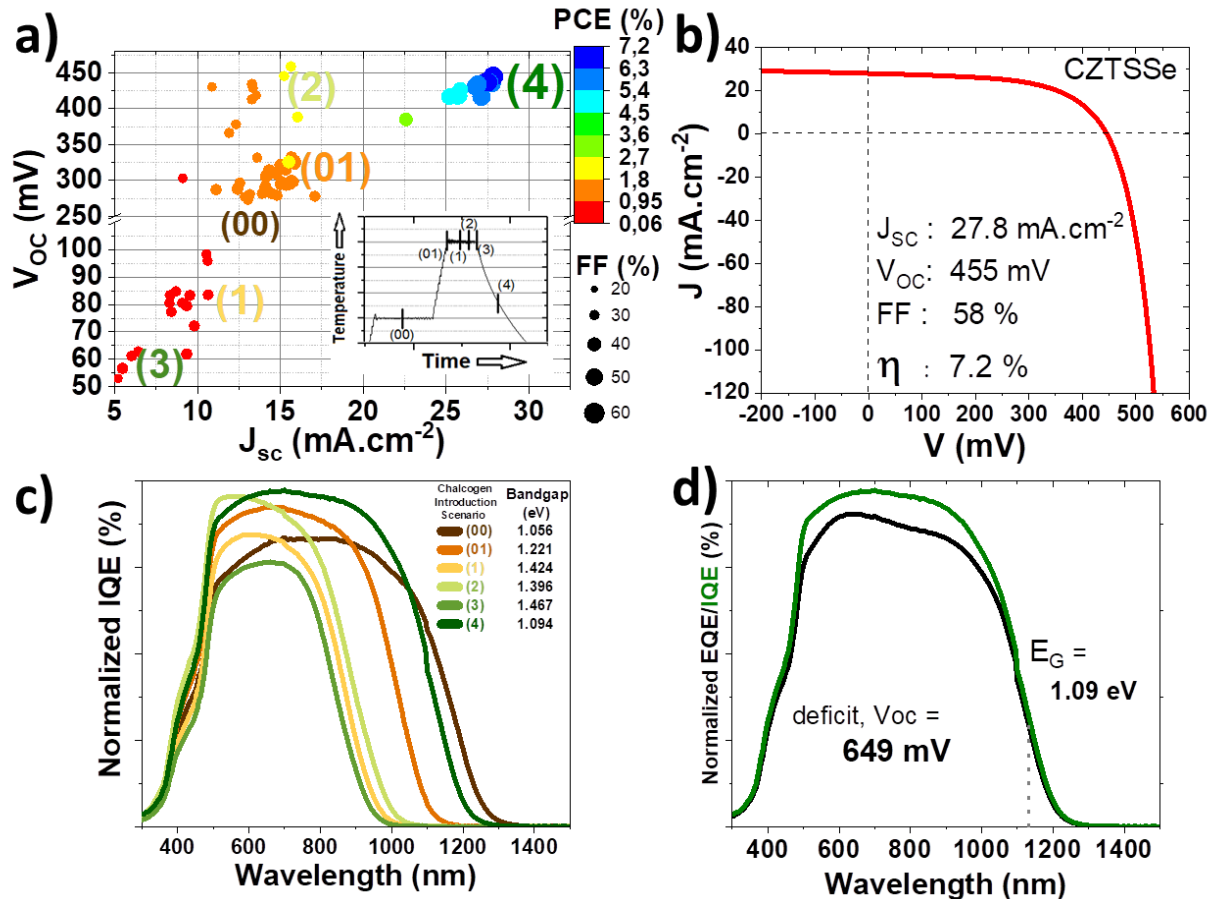


Figure 5.16.- a) 4D optoelectronic plots (PCE, V_{oc} , J_{sc} , and FF) for the CZTSSe synthesized by distinct S-Shoot introduction scenarios. b) 1 Sun JV illuminated curve and optoelectronic parameters for the champion CZTSSe graded device. c) Normalized IQE curves and bandgap estimation, d) Normalized EQE and IQE curves for the champion device.

Additionally, Figure 5.16c bandgap calculation evidences that there is a notable higher S inclusion when S-Shoots are introduced during the CZTSe formation process at zone 1, allowing an anionic (Se - S) interplay that posteriorly leads to a compositional homogenized CZTSSe structural matrix without generating a front surface shaped anionic graded bandgap.

Nevertheless, the introduction of the chalcogenide pulse (shoot) introduction during the cooling down after the CZTSe synthesis showed remarkable results and resulted to be the most promising and worth to further study scenario.

5.6.3 Case of SeS₂-Shoot Introduction at Different Cooling Down Times

Once the best S-shoot introduction scenario for generating front surface anionic graded profiles in CZTSSe has been identified and demonstrated to be during the cooling down process of the CZTSe formation, the next grading strategy moved towards the chalcogenide interplay by means of changing the chalcogenide (S source) shoot to selenium disulfide (SeS₂), and studying several cooldown introduction times (0, 3, 6, 9, and 12 minutes) after the CZTSe formation in zone 1 (selenization process) has finished (See Figure 5.17a). The study of this case pretends to enhance the PCE of the cells by means of optimizing the anionic bandgap profiling. Figure 5.17b presents the absorber and Mo layer thickness variations showing a dissimilar trend for both of the parameters as the cooling-down introduction time increased. Furthermore, Figure 5.17c shows how the S composition linearly decreases with the Type 2 sulfurization at cooling-down introduction times while the cationic XRF signals (Cu, Zn, and Sn) remain practically unaffected.

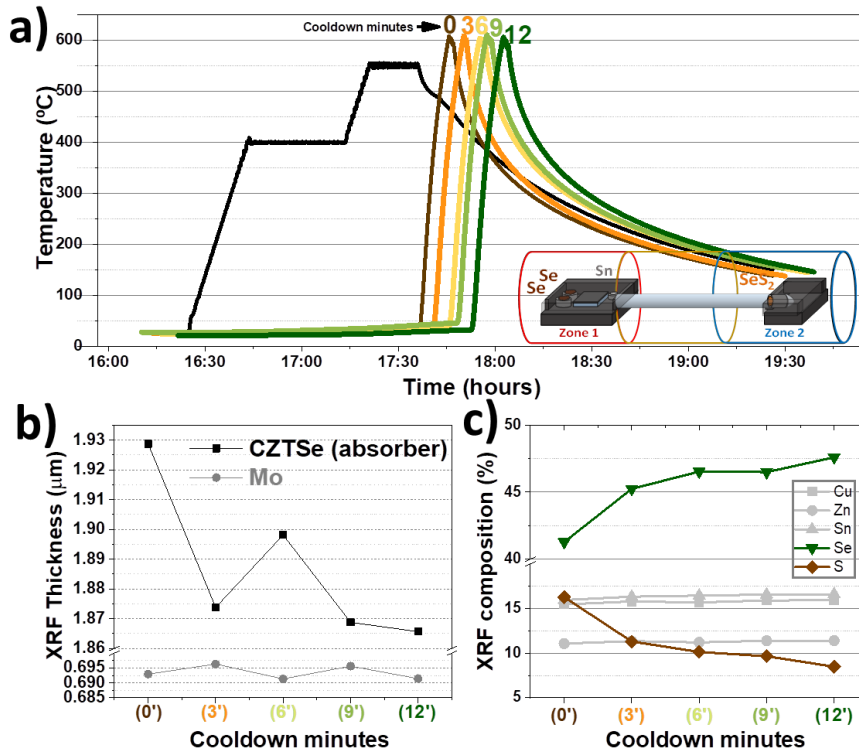


Figure 5.17.- a) Distinct thermal profiles for several cooling down S-Shoot introduction times. XRF of the **b)** Absorber and Mo layer thickness and **c)** Absorber atomic composition (Cu, Zn, Sn, Se and S) for the absorber material synthesized by the distinct cooling down times.

Further, Figure 5.18 shows the X-ray diffraction (XRD) patterns demonstrating the CZTSSe well crystallized structures, with an exception for the zero minutes (0') sample in which there is a high amount of thermal energy present in the system, possibly causing a disordered distribution of the S and Se atoms.

From this figure, it could be observed that an enhancement on the crystalline quality of the films is optimized for a 12' cooling down waiting time.

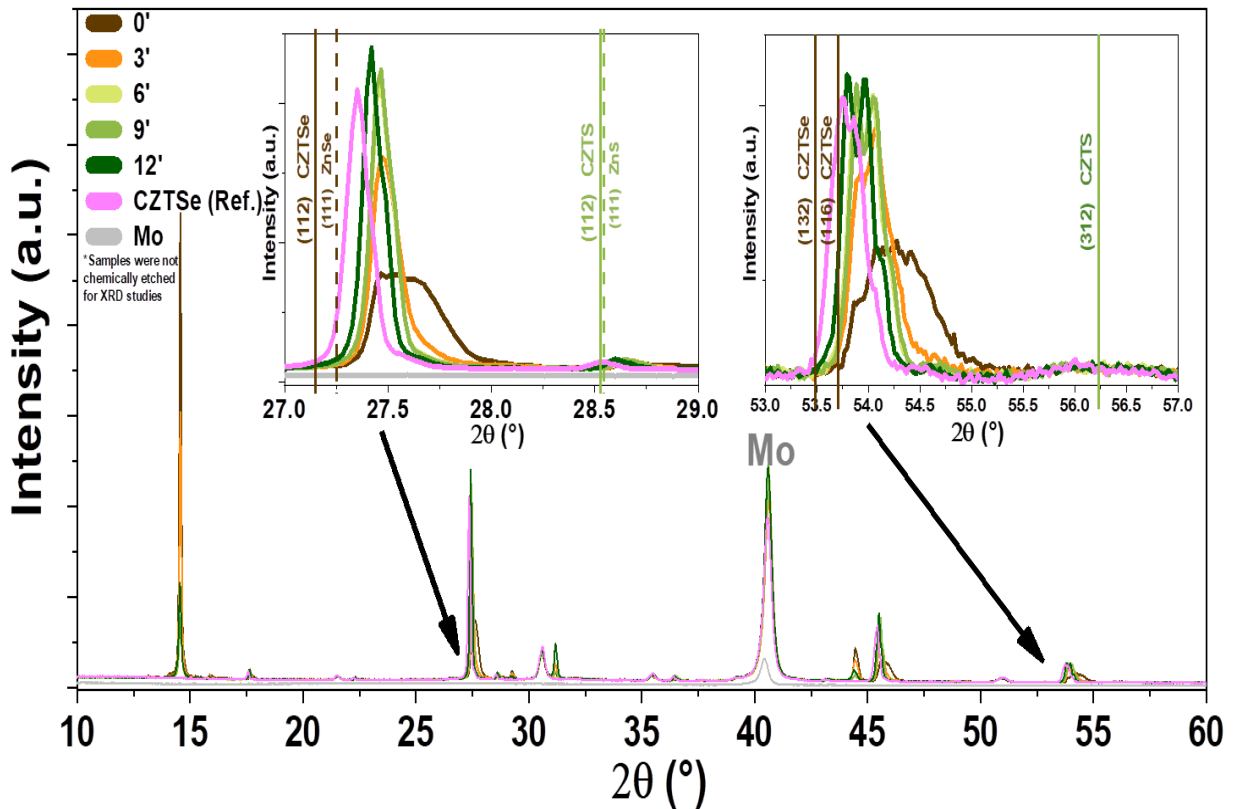


Figure 5.18.- XRD of the CZTSSe for several cooling down S-Shoot introduction times kesterite absorber thin films. Back contact (Mo) diffraction signals are also observed.

Additionally, complementary structural and lateral anionic compositional homogeneity tests are carried out by Raman spectroscopy as it is shown in Figure 5.19.

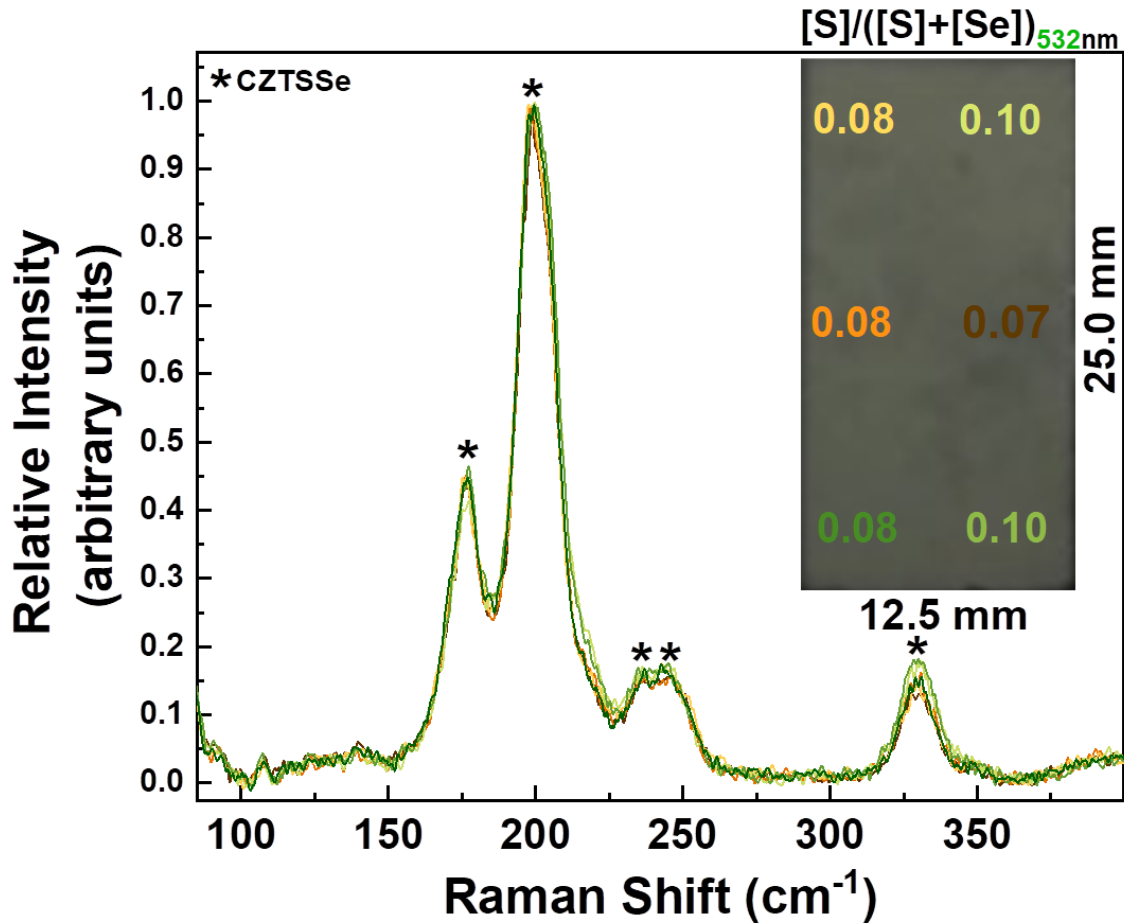


Figure 5.19.- 532 nm Raman spectroscopy structural and lateral compositional homogeneity tests for a graded CZTSSe thin film. The inset shows a photograph of the actual (1.25 x 2.50) cm² sized sample, the compositional anionic ratio is evaluated for each zone.

In Figure 5.19, it could be appreciated that there is a correct crystallization of the CZTSSe structure for the whole area of the thin film absorber material.

Additionally, it is inferred a lateral compositional homogeneity regarding the anionic ratio (S)/(S + Se) anionic compositional ratio calculation.

Furthermore, Figure 5.20a shows a further and deeper analysis by (532 nm and 785 nm) multiwavelength Raman spectroscopy at the front and rear (back) surfaces of the CZTSSe absorber material. Moreover, morphological insights are provided by the cross sectional SE2-SEM for cases 6' and 12'.

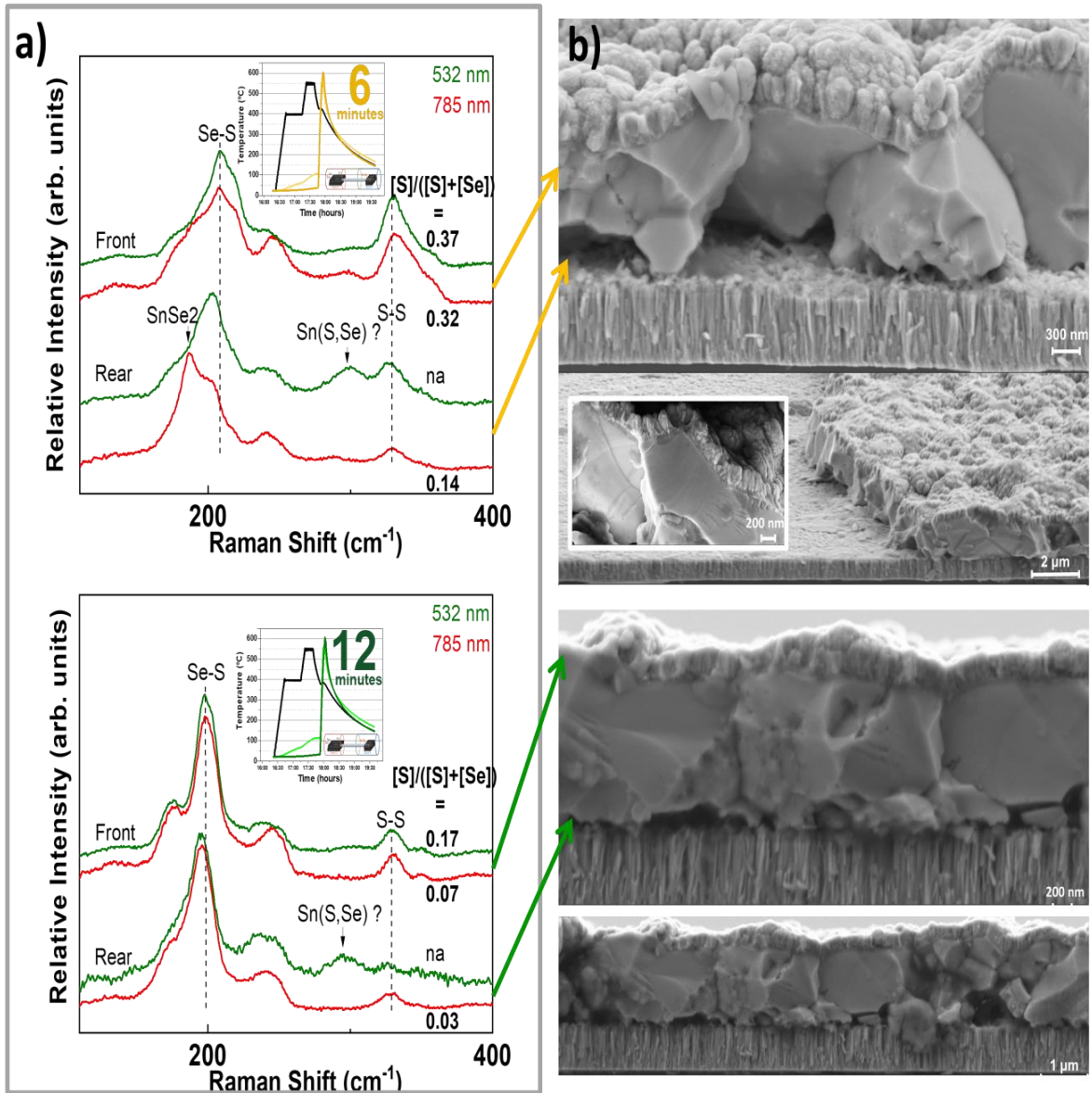


Figure 5.20.- a) Front/Rear multiwavelength Raman spectra for devices conformed by a SeS₂-Shoot occurring at 6 and 12 minutes during cooling down. **b)** Corresponding cross sectional SE2-SEM micrographs.

In this way, Figure 5.20 provides a strong structural, morphological and compositional correlational evidence of the subtlety on introducing a particularly desired complex superficial chalcogenization of the CZTSSe structure.

Also, Figure 5.20 might picture an idea of the graded bandgap profile from front to back surfaces of the CZTSSe absorber material.

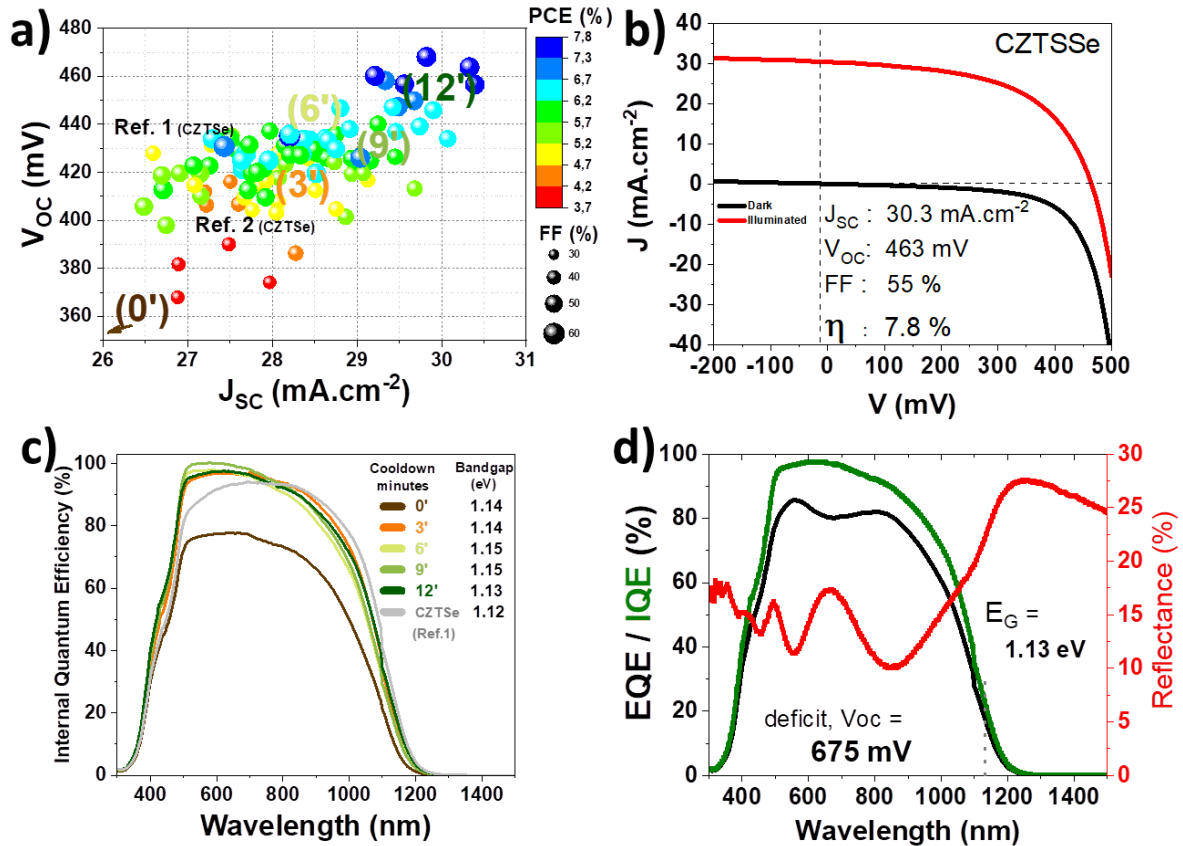


Figure 5.21.- a) 4D optoelectronic plots (PCE (η), V_{OC} , J_{SC} , and FF) for the CZTSSe synthesized by distinct SeS_2 -Shoot cooling down times. b) 1 Sun JV dark and illuminated curves, also the main optoelectronic parameters for champion CZTSSe graded device are shown. c) IQE curves and bandgap estimation, d) EQE/IQE/R curves for the champion device.

And once again, the positive impact of the front anionic graded profile in CZTSSe is further corroborated by the optoelectronic parameter comparison in Figure 5.21.

Particularly, Figure 5.21a shows the 4-dimensional plots for the CZTSSe absorbers devices synthesized by distinct SeS_2 -shoot introduction at distinct cooling down times.

It could be clearly observed that there is a quasi-linear optoelectronic parameter enhancement trend as function of the cooling down SeS_2 -Shoot introduction time.

From a chaotic introduction scenario at (0') in which PCE do not exceed a 4%, once again but in a softer disruptively manner, when the Type 2 SeS₂-shoot is introduced after (12') on the cooling down, a remarkable PCE enhancement from 4% to \approx 8% happens.

On one side, the main optoelectronic parameters for champion CZTSSe graded device are shown in the 1 Sun JV dark and illuminated curves shown in Figure 5.21b. On the other hand, the calculated bandgap values from the Internal Quantum Efficiency (IQE) curves are shown in Figure 5.21c, while Figure 5.21d shows the External Quantum Efficiency (EQE), Reflectance (R) and IQE curves along with the estimated V_{OC} deficit for the champion anionic graded CZTSSe solar cell device.

Therefore, by comparing these results (See Figure 5.21) with Section 5.6.1 (See Figure 5.16), i.e., S- with SeS₂-Shots; it could be observed that for the latter (SeS₂), the PCE of the CZTSSe device is slightly enhanced mainly due to J_{SC} (+2.5 mA.cm⁻²) improvements. However, the CZTSSe superficial anionic strategy by pure S-Shoots remarks lower V_{OC} deficit values (-26 mV).

5.7 Sulfur Introduction and Creation of Sharp Compositional Gradients by Distinct Chalcogenide Materials

As it is shown in Figure 5.21b, two different case studies were evaluated: sulfur introduction during the crystallization stage (sulfur pulse Type 1) and during the cooling down stage (sulfur pulse Type 2). In Type 1, sulfur is introduced during quasi-equilibrium conditions (P–T constant) and at high temperature (550 °C).

This leads to homogeneous absorbers with very limited S/(S + Se) grading (less than 5%) in agreement with previous studies.^{17,18}

However, as shown in Figure 5.22, although Type 1 sulfurization is not useful for creating sharp anionic gradients, it produces absorber materials with controllable and homogeneous S/(S + Se) ratios.

Figure 5.22 shows the front and back Raman spectra taken onto samples produced with a Type 1 S pulse, together with the S/(S+Se) ratio estimated by using Equation 5.1 and Equation 5.2.

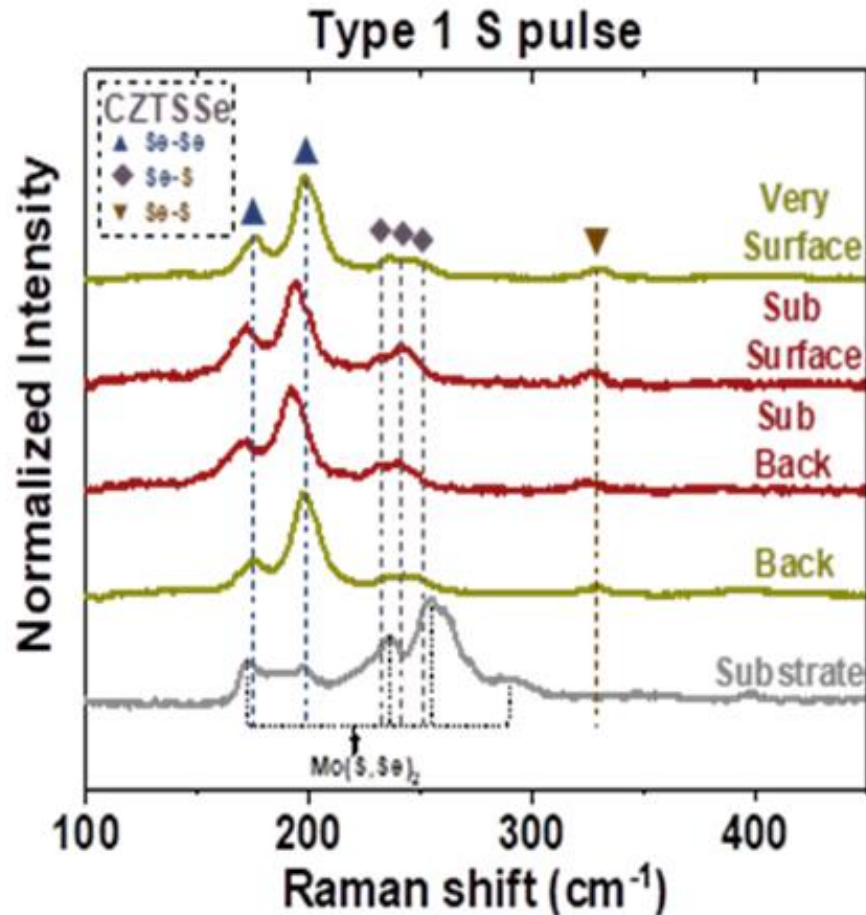


Figure 5.22.- Raman spectra taken at the front (532, and 785 nm) and back (785, and 532 nm) regions, of a kesterite (CZTSSe) sample produced with a Type 1 S pulse (See Figure 5.8). The 532 nm Raman spectra of the substrate ($\text{Mo}(\text{S,Se})_2$ signals) are also indicated.³

Similar results are obtained when the S pulse is introduced during the synthesis processes in the plateau at 400 °C, or during the crystallization process in the plateau at 550 °C in Figure 5.9, confirming that when the S-Se systems are subjected to a high temperature thermal process, the anionic composition and structure tends to be highly homogenized.

This is somehow expectable as a result of the high miscibility of the CZTS and CZTSe phases, especially at high temperatures.

Thus, it is necessary to work in out (far) of equilibrium conditions as well as to avoid high temperatures (to the extent possible) for creating sharp composition gradients in CZTSSe films. As such, the cooling down stage after the selenization appears as an appealing moment to introduce the sulfur pulse and selectively introduce S at the very surface.

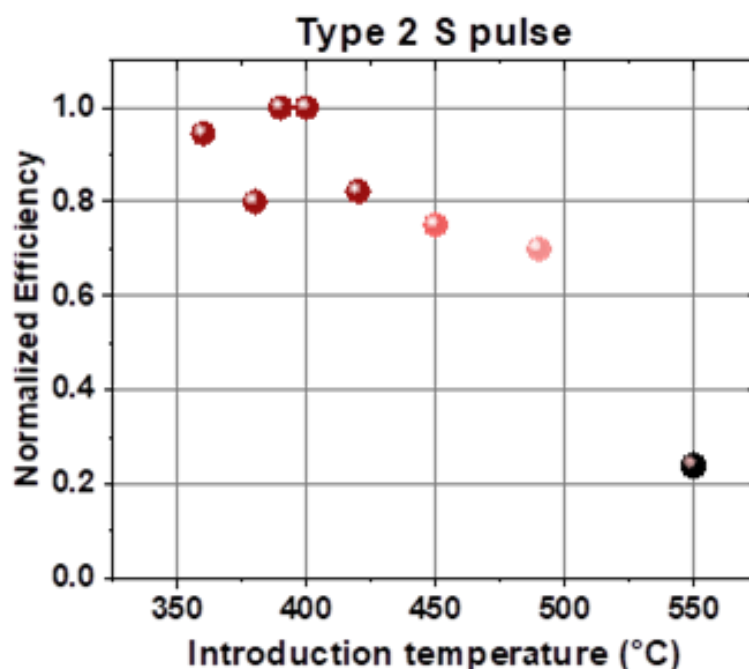


Figure 5.23.- Normalized efficiency of solar cell devices using absorbers produced introducing Type 2 S pulses during different temperatures of the cooling down process.

However, taking into account that the miscibility temperature of CZTSSe has been estimated in less than 300 K,¹⁹ the mixed S–Se phase can be expected to be stable in the whole temperature range of a typical cooling down process.

Additionally, the introduction of sulfur at low temperatures can imply a very slow reaction with the risk of undesired S diffusion toward the bulk of the absorber or even of partial surface condensation of unreacted chalcogenide. In this challenging context, two different types of sulfurization experiments were performed in order to identify the best temperature range during the cooling down stage to induce S/(S + Se) surface gradients.

In this way, Figure 5.23 shows the conversion efficiency of the devices fabricated with the CZTSSe absorbers prepared by introducing the sulfur pulses at different cooling down temperatures.

Based on these pure experimental observations, 380 °C seems to be the **sweet spot** for generating effective anionic gradient profiles in kesterite absorber material. Once the sulfur introduction temperature was fixed, the effectivity of sulfur pulses arising from different S sources (Elemental S, thiourea, SnS, and SeS₂) for the creation of front surface anionic graded compositional profiles was investigated (See Figure 5.24).

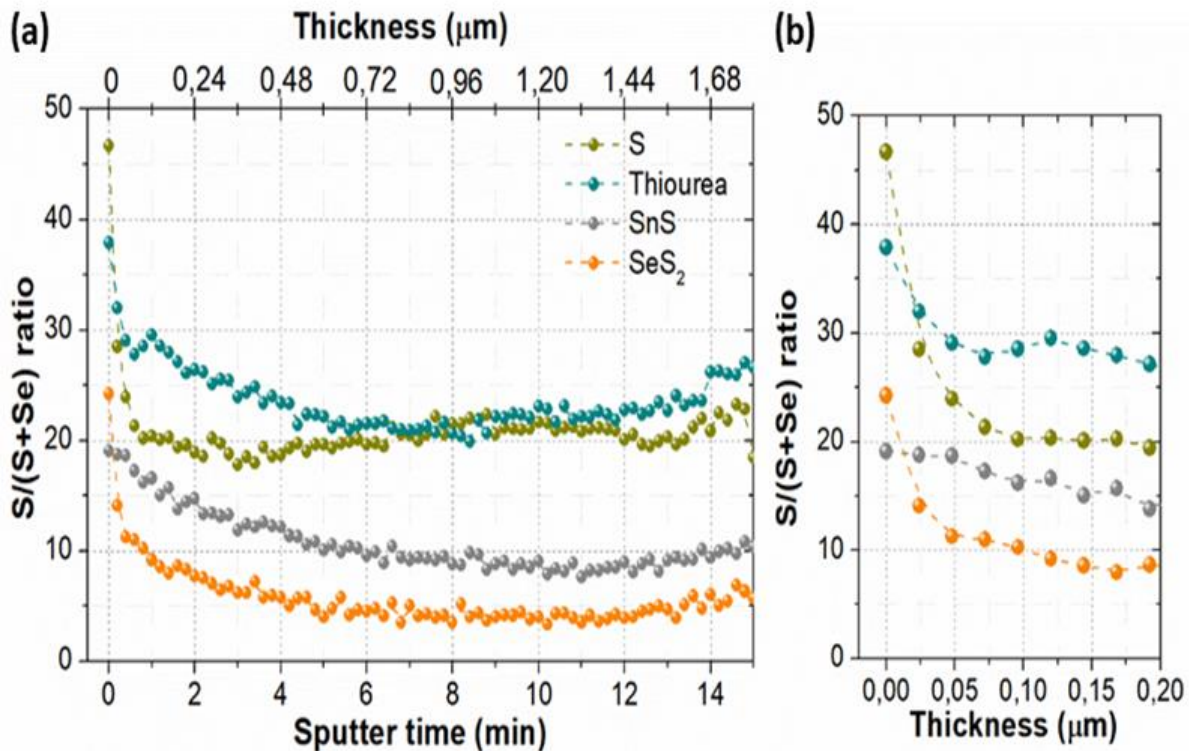


Figure 5.24.- a) In-depth Auger S/(S+Se) profiles of absorbers sulphurized with pulses of elemental S, thiourea, SnS and SeS₂. **b)** Detail of the Auger S/(S+Se) profiles at the very surface (First 200 nm) for the 4 previous S sources, showing the achieved graded composition.

Figure 5.24a shows the S/(S + Se) compositional profile extracted from in-depth Auger spectroscopy throughout the whole thickness of the absorber, while Figure 5.24b shows more in detail the profiles at the very surface region (First 200 nm, See Figure 4.11).

Impressively, it is possible to produce a pronounced surface S gradient with most of the sulfur sources under investigation while keeping an almost constant S/(S + Se) ratio within bulk of the absorber layer! This indicates that, quite probably, sulfur quickly accumulates at the surface of the absorbers during the introduction of the sulfur pulse and then starts to diffuse toward the back side during the rest of the cooling down process.

Interestingly, Figure 5.24 also shows that it is possible to control both the S concentration at the very surface and the S/(S + Se) ratio in the bulk by varying the chalcogen source.

This gospel opens promising perspectives for customized anionic gradients in kesterite absorbers.

More in detail, the main characteristics of the gradient profiles obtained for each different S source and shown in Figure 5.24 could be discussed as follows:

- **Elemental S:** Assuming that at $T > 400$ °C a considerable amount of S will be forming $S_{2(g)}$ molecules² and that the dissociation energy of disulfide is 425 kJ.mol^{-1} ,²⁰ elemental S can be considered to be one of the most reactive species employed in this experiment. In terms of the compositional profile of the resulting CZTSSe layer, the surface presents a 47% sulfur content that quickly drops down to 20% in the first 100 nm and then remains almost constant within the bulk. Clearly, sulfur can create very sharp surface anionic gradients under the investigated annealing conditions.²¹

- **CH₄N₂S:** The C=S bond dissociation energy in thiourea can be estimated in approximately 410 kJ.mol^{-1} , so it is comparable to elemental S. In this case, 38% sulfur content is found at the surface, rapidly dropping to approximately 30% in the first 50 nm and smoothly decreasing down to 20% in the following 700 nm. Nevertheless, in the case of thiourea, it should also be borne in mind that this chalcogenide could produce H₂S gas during thermal decomposition which can alter the reactivity of this compound.²²

- **SnS:** Tin and sulfur atoms form a strong bond with a bond-dissociation energy of 467 kJ.mol^{-1} .²⁰ Accordingly, it was obtained the least pronounced gradient with 19% sulfur content at the surface that slightly decreases to 9–10% toward the bulk, stabilizing in this value for the first 600 nm. Probably, the lower availability of S and/or the necessity of a direct reaction between SnS and Cu₂ZnSnSe₄ (e.g., through the following reaction: $\text{Cu}_2\text{ZnSnSe}_4 + \text{SnS} \rightarrow \text{Cu}_2\text{ZnSnS}_4 + \text{SnSe}$), may be at the origin of the remarkably lower S incorporation with respect to elemental S and thiourea and of the relatively smooth anionic gradient. Therefore, it can be inferred that SnS is not a good candidate to create sharp anionic gradients (at least with annealing conditions employed), in consonance with the TGA presented in Figure 5.3.

• **SeS₂**: In principle, with a dissociation energy of about 375 kJ.mol⁻¹,²⁰ SeS₂ is identified as the most reactive chalcogen specie under investigation and, in consequence, the sharpest surface anionic gradient could be expected. Nevertheless, and as it is shown in Figure 5.24, although this compound produces a pronounced compositional profile, only a 25% sulfur content is achieved at the surface, it drops down relatively quickly to only 10% in the first 200 nm and then stabilizes at approximately 5% in the bulk. This can be related to the fact that this compound contains both S and Se introducing a competition between both chalcogenides at the surface.

Thus, the presence of S and Se at the same time in the atmosphere during the SeS₂ pulse explains the possibility to achieve sharp gradients at the surface (due to the high reactivity of S) but low bulk S content (due to the mere presence of Se).

In order to provide an insight about the S incorporation dynamics into the CZTSe matrix, we have developed a phenomenological model considering a figure of merit (FM_x) related to the expected reactivity of the different chalcogen sources. For this purpose, and as a way of defining such FM_x, it is necessary to identify the main factors that may affect the reactivity of the different S compounds. First, as presented above, the bond dissociation energy (enthalpy change) of the different molecules is a very relevant parameter regarding the reactivity of the distinct S sources; **In particular, it can be expected that the lower the dissociation energy, the higher the reactivity. Thus, the FM_x should be inversely proportional to this parameter.**

Additionally, the availability of sulfur within the molecule is another important factor. Therefore, the FM_x should be proportional to the ratio between the molar mass of sulfur divided by the molar mass of the compound. Finally, it should be taken into account if during the decomposition of the molecule a competing chalcogen is produced (for example, when employing SeS₂ which generates both Se and S upon decomposition).

$$\text{Reactivity } FM_x = \frac{M_S}{E_x \cdot M_x} \cdot f_x \quad (\text{Eq. 5.3})$$

In this case, the FM_x should include a factor that accounts for the molecular ratio between sulfur and the other competing chalcogenides.

Bearing this in mind, the FM_x related to the reactivity of the sulfur sources can be defined by equation 5.3, where reactivity FM_x is defined for the reactivity of compound X [mol.kJ^{-1}], M_S is the molar mass of S [g.mol^{-1}], E_x is the energy formation of the compound X [kJ.mol^{-1}], M_x is the molar mass of the compound X [g.mol^{-1}], and f_x is a factor that accounts for the ratio of sulfur to all the chalcogenides produced during the decomposition of the compound X.

Table 5.1. Summary of the parameters used in Equation 5.3 to estimate a figure of merit related to the reactivity of the different sulphur compounds.

Compound	E_x (kJ.mol^{-1})	M_S/M_x	f_x	Reactivity FM (mol.kJ^{-1})
Elemental S	425	1	1	2.4×10^{-3}
CH₄N₂S (Thiourea)	410	0.42	1	1.0×10^{-3}
SnS	467	0.21	1	4.5×10^{-4}
SeS₂	375	0.45	0.67	8.0×10^{-4}

Table 5.1 summarizes the different parameters for the four sulfur sources employed in this work together with their estimated reactivity FM. Thus, it becomes crystal clear that elemental sulfur is the most reactive compound, followed by thiourea, SeS₂, and, finally, SnS.

Figure 5.25 shows the sulfur concentration (As it could be estimated from Auger measurements) of the samples as a function of the reactivity FM for both the surface (See Figure 5.25a) and the whole thickness (See Figure 5.25b) of the CZTSSe layers.

A direct correlation between the concentration of S at the surface of the absorbers and the reactivity FM of the different sulfur sources can be clearly observed in Figure 5.25a. In general, the higher the reactivity of the sulfur source, the higher the concentration of sulfur found at the surface of the CZTSSe thin film layers.

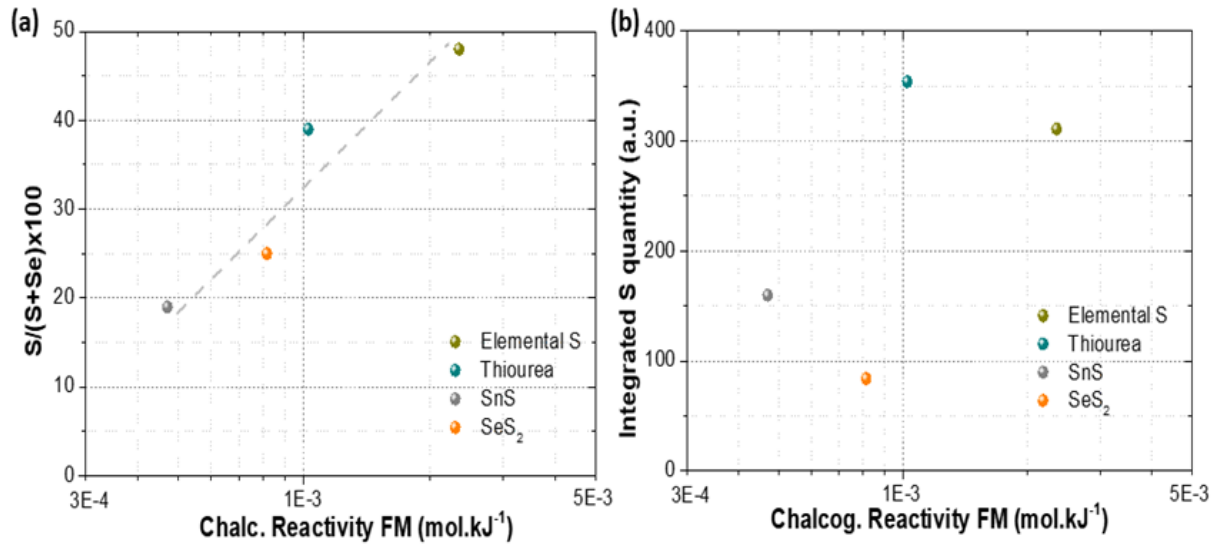


Figure 5.25.- a) Superficial S composition obtained by Auger spectroscopy as a function of the chalcogen reactivity FM for elemental S, thiourea, SnS and SeS₂. **b)** Integrated S quantity obtained by Auger spectroscopy as a function of the chalcogen reactivity FM for elemental S, thiourea, SnS and SeS₂.

This suggests that the methodology presented here based on the introduction of a sulfur pulse involves a very fast reaction of sulfur with the surface of the CZTSe absorber, which creates a sulfur enriched region. Then, sulfur seems to slightly diffuse toward the bulk of the absorbers while being accumulated at the surface. This diffusion process should be similar for all the sulfur sources because it should basically depend on the temperature of the diffusion media ($T > 300\text{ }^{\circ}\text{C}$ in all cases) and on the diffusion time.

Thus, the only difference between the samples fabricated with the different S sources would be the rate at which S is incorporated on the surface of the absorbers. Figure 5.25b shows the global S content of the absorbers synthesized with the different sulfur sources.

Although no clear correlation is found, there seems to be a S incorporation activation threshold. For low reactivity sources (SnS and SeS₂), the amount of S that reaches the surface of the absorbers is not high enough to keep a substantial S diffusion toward the bulk.

This way, creating a strong concentration gradient between the vapor phase and the solid, and, as a result, lower sulfur bulk concentrations are obtained.

Once the threshold is overcome (this can be very roughly estimated to happen for chalcogen sources with a reactivity of $1 \times 10^{-3} \text{ mol.kJ}^{-1}$, the amount of sulfur at the surface of the absorbers is enough to create a strong chalcogen depletion at the surface and activate S diffusion toward the bulk.

This would result in higher concentrations of sulfur in the layer as in the case of elemental sulfur and thiourea. These observations are strongly relevant because of the following:

1. Using the FM_x defined in this Thesis, it is possible to classify different surface selective chalcogen sources in order to anticipate possible desired anionic gradients in possible and suggested by the author, further experiments.

2. They demonstrate that high chalcogen reactivity is necessary not only to keep high sulfur content at the surface and create sharp compositional gradients but also to obtain higher concentrations of this chalcogen in the bulk if necessary.

From the collective of the previous characterization analysis, it can be concluded that working in out-of-equilibrium conditions (i.e., during the cooling down process) allows creating pronounced $S/(S + Se)$ gradient profiles using relatively highly reactive S-species.

As explained above, the highest S contents are obtained using elemental S with a 30% difference in the S content between the surface and the bulk. Fact which is significantly higher than the previously reported gradient profiles.^{23–25}

In the case of thiourea and SeS_2 , a difference in S content of around 20% between the surface and the bulk is achieved. However, SeS_2 leads to much lower global incorporation of S within the absorber. Finally, for SnS just a limited gradient is obtained, with S content softly decreasing a 10% from the surface to the back of the absorber.

This confirms that by optimizing both the sulfur pulse introduction during the cooling down stage (out-of-equilibrium conditions) and the chalcogen source, it may be possible to create different anionic compositional profiles.

To further confirm these profiles and corroborate that S is effectively being incorporated into the kesterite structure and not into secondary phases, multiwavelength Raman spectroscopy was performed at the front and rear (back) regions of the absorber by performing the before mentioned (Section 5.6.2) lift-off process.

Figure 5.26a (right) shows a typical SEM cross-sectional image of a graded CZTSSe device fabricated using elemental S. Further topographical, morphological and compositional details for the four distinct chalcogenide processed anionic graded CZTSSe structures are provided by the secondary electron microscopy (SEM) complete observations in Figure 5.27 and Figure 5.28.

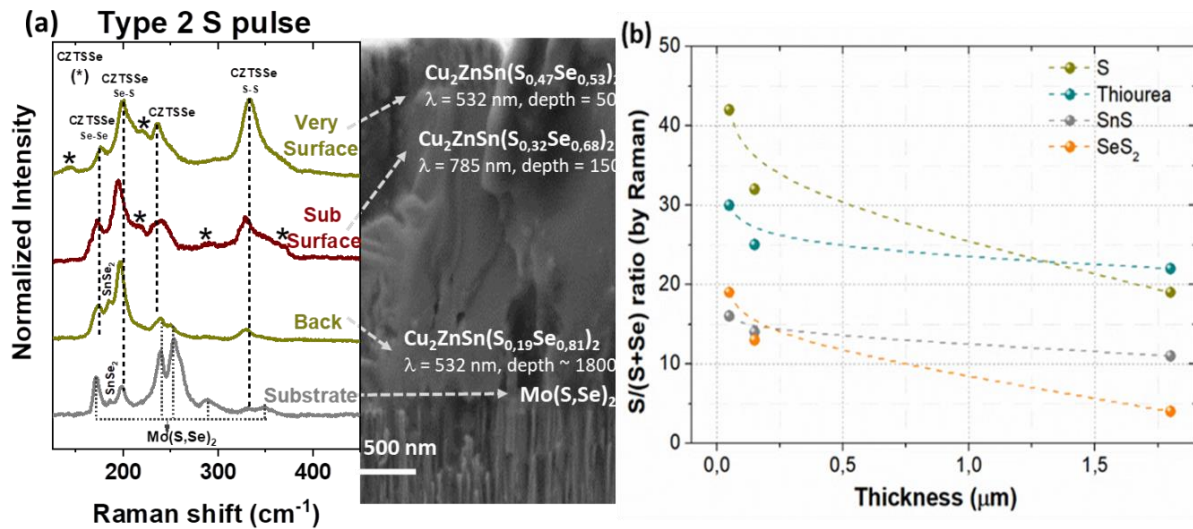


Figure 5.26.- a) Raman spectra of absorber prepared using an elemental S pulse during the cooling down process (at 380 °C): front characterization with 532 nm and 785 nm excitation wavelengths, and back/substrate characterization using 532 nm excitation wavelengths.⁴ Cross sectional SEM micrograph of the absorber, showing the different composition at different depths. **b)** Estimated S/(S+Se) compositional ratio at different penetration depths for the four S-sources utilized in this work.

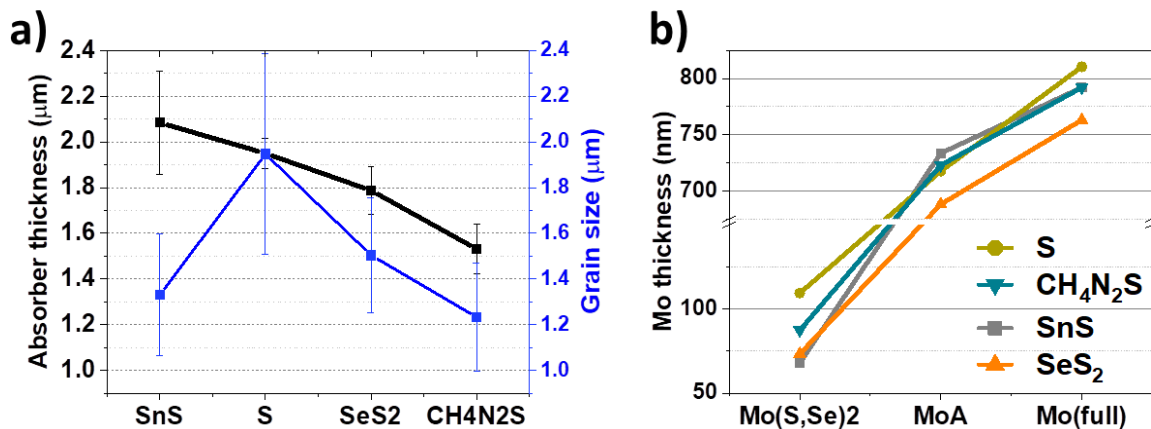


Figure 5.27.- a) Absorber thickness and grain size, while **b)** shows the Mo layer thickness for the 4 chalcogenide processed anionic graded CZTSSe absorber layers.

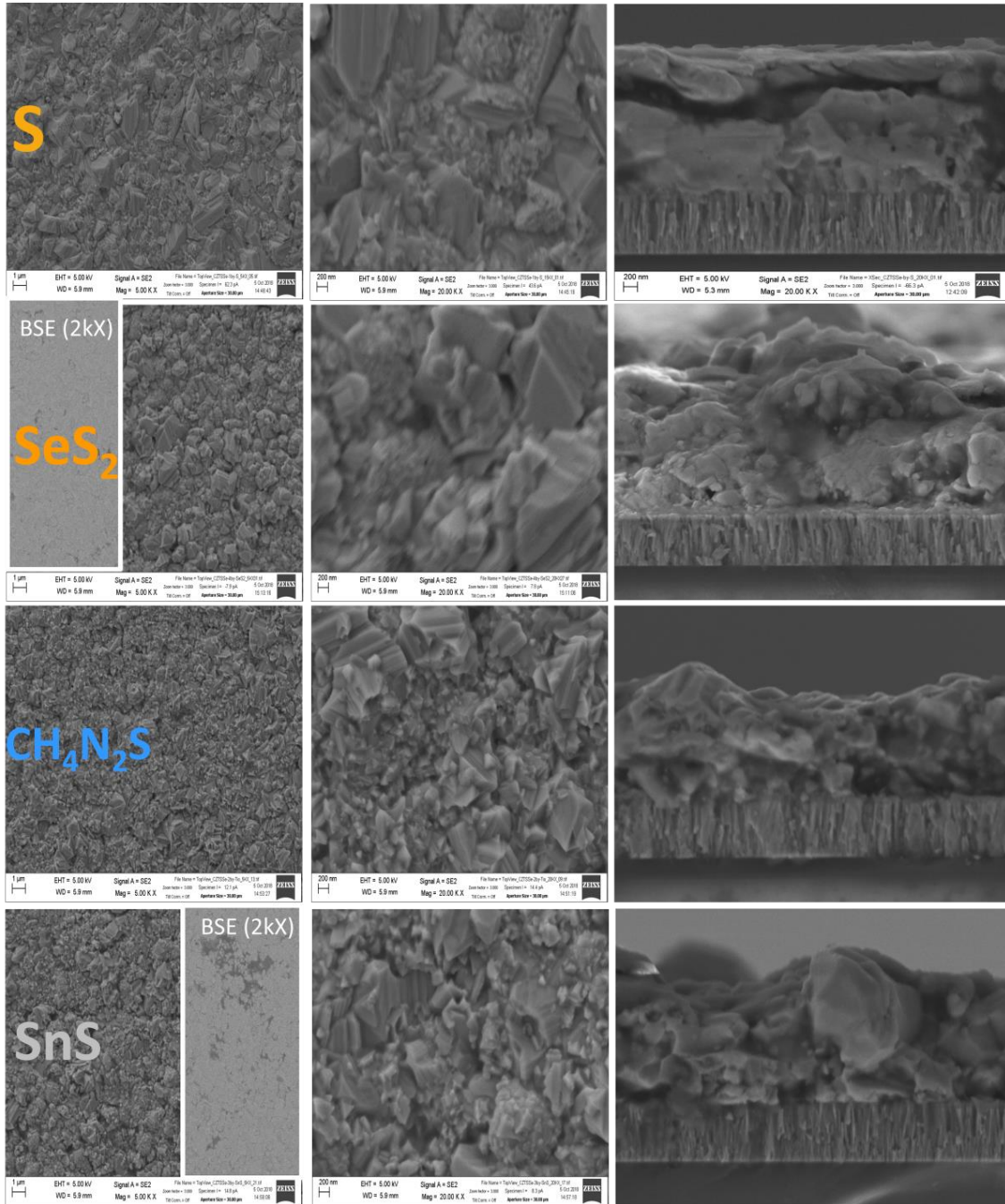


Figure 5.28.- SEM analysis for the four chalcogenide (S, SeS₂, CH₄N₂S, and SnS) processed anionic graded CZTSSe absorber layers. For selenium disulfide (SeS₂) and tin sulfide (SnS), the 2 kX BSE signals are also shown.

In before, from Figure 5.26, the composition estimated from Raman measurements using Equations 5.1 and 5.2 for different penetration depths is included in this figure.

In addition, the corresponding Raman spectra are shown in Figure 5.26a (left) where a large change in the S content at the very surface, at the subsurface, and at the back of the CZTSSe absorber can be clearly observed.³

On the other hand, Figure 5.26b shows the estimated $S/(S + Se)$ ratio at the very surface, subsurface, and back regions as determined by Raman spectroscopy.

A strong agreement between Auger and Raman spectroscopies is observed, corroborating the existence of steep or very sharp anionic gradients at the surface of the kesterite absorbers.

A key factor is to remark that few quantities of secondary phases are detected (mainly ZnS and ZnSe), which are almost completely removed after a Type B (HCl + KCN) chemical reactive etchings (See Figure 5.29)²⁶ confirming, thus, that the $S/(S + Se)$ gradient measured by Auger spectroscopy is due solely to S incorporation within the kesterite structure.

Figure 5.29 shows the Raman spectra obtained with UV (325 nm) and blue (442 nm) excitation wavelengths, confirming the absence of Zn(S,Se) secondary phases that can potentially affect the $S/(S+Se)$ ratio estimated by Auger spectroscopy.

In particular, only very low intensity peaks can be assigned to Zn(S,Se) phase as it is indicated in Figure 5.29, which are present in very low quantities as is indicated by the very low Raman signal.

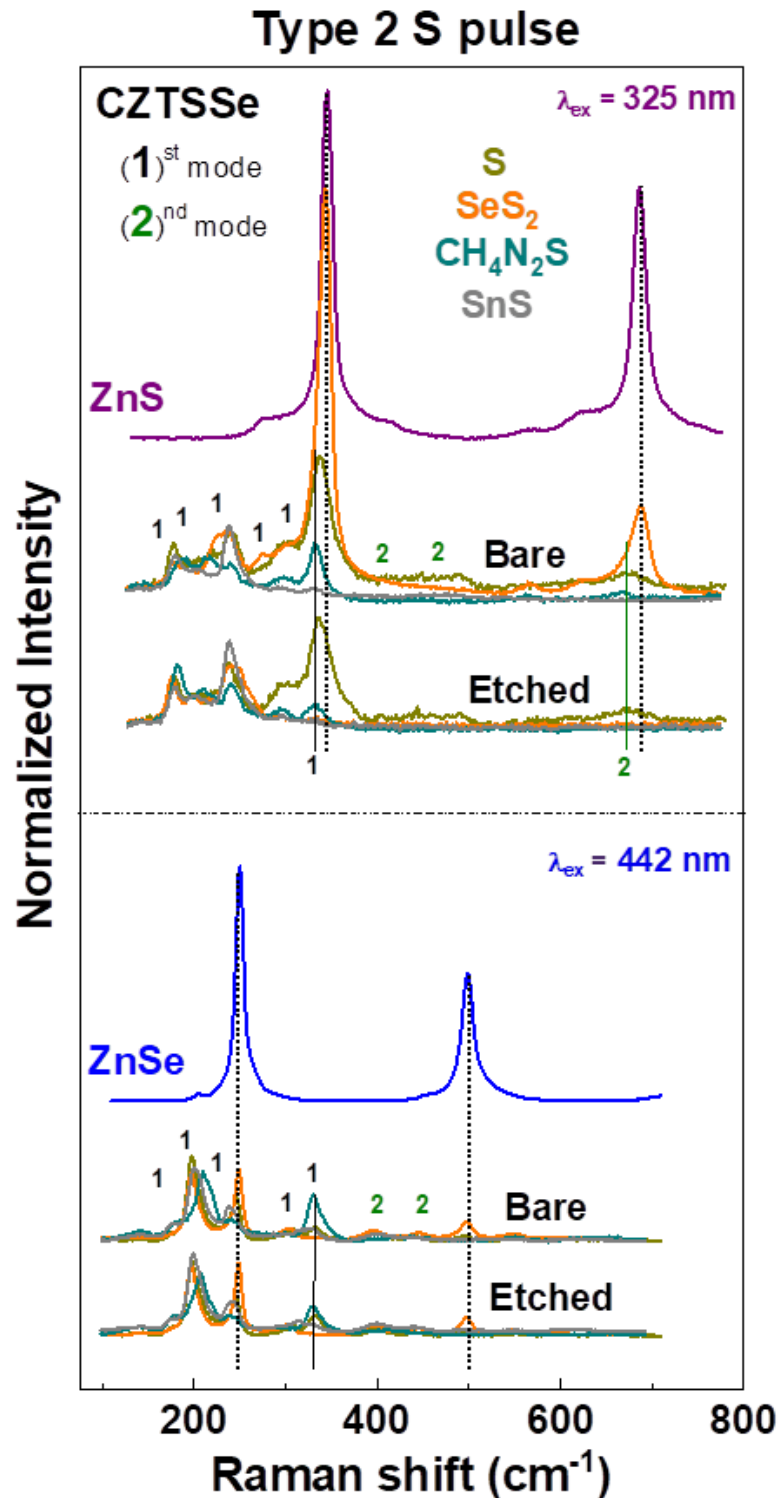


Figure 5.29.- Raman spectra obtained using UV (325 nm) and blue (442 nm) excitation wavelengths for kesterite (CZTSSe) absorber samples produced with a Type 2 chalcogenide (S, SeS_2 , $\text{CH}_4\text{N}_2\text{S}$, and SnS) pulse. Bare absorber and after etching Raman spectra are shown for both wavelengths. Raman reference spectra of ZnS and ZnSe are also depicted.^{3,4,27}

5.7.2 Raman Analyses of Zn(S,Se) Presence in CZTSSe Samples

Additionally, in this report, CZTSSe samples are analyzed by Raman spectroscopy in order to determine the impact of two different surface cleansing chemical etching agents (See Thesis Chapter III and Appendix) on the presence of possible secondary phases such as Zn(S,Se) in the CZTSSe samples obtained by sulfurization utilizing the abovementioned distinct sulfur sources.

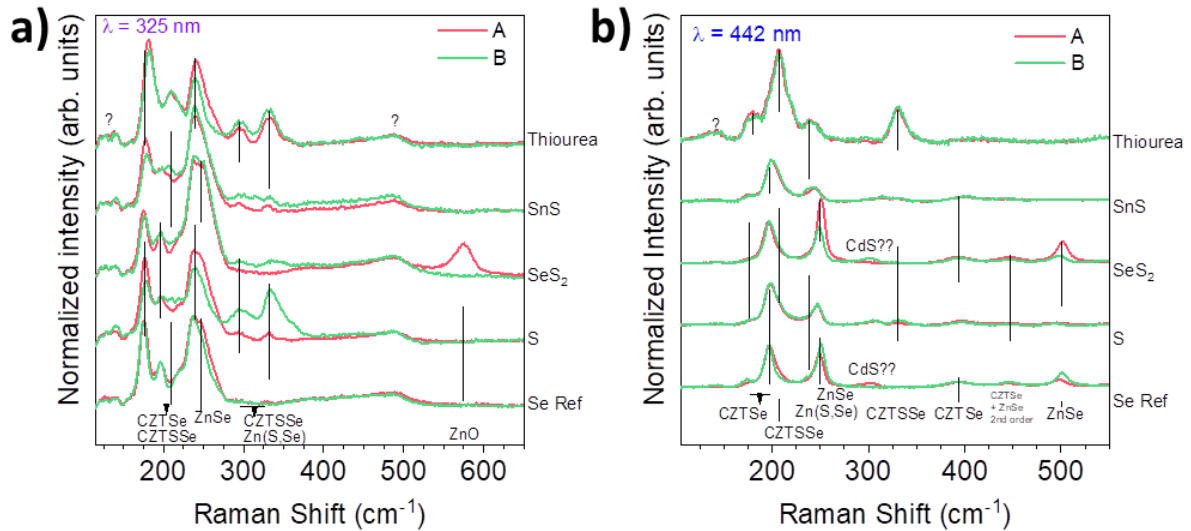


Figure 5.30.- Raman spectra obtained using **a)** 325 nm and **b)** 442 nm excitation wavelengths of different CZTSSe samples etched with two different agents (Type A = $\text{KMnO}_4 + (\text{NH}_4)_2\text{S}$ and Type B = $\text{HCl} + \text{KCN}$).

Figure 5.30 shows the Raman spectra of the different CZTSSe samples obtained with 325 and 442 nm excitation wavelengths, respectively. The presence of CZTSSe in all samples is confirmed by the presence of 172 cm^{-1} peak, which corresponds to Se-Se vibrations, 196 cm^{-1} peak, which corresponds to Se-S vibrations and shifts towards higher frequencies as the content of sulfur increases, and 330 cm^{-1} peak, which corresponds to S-S vibrations²⁷. Additionally, 250 cm^{-1} peak indicates the presence of ZnSe secondary phase, and this peak shifts towards lower frequencies as the content of sulfur increases resulting in a Zn(S,Se) phase²⁷.

However, no ZnS is detected in any sample. ZnO can be detected in sample A- SeS_2 , but its absence in the other samples probably indicates an accidental oxidation of the sample. Finally, several low intensity unidentified Raman peaks could be observed on these spectra.

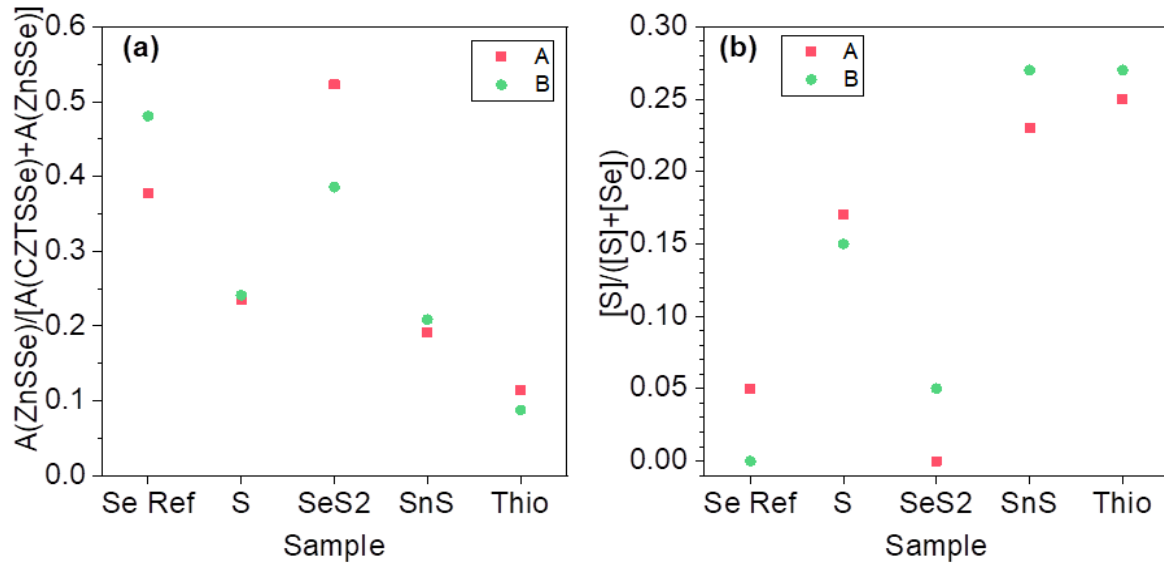


Figure 5.31.- a) Ratio of area under 250-240 cm^{-1} peak with respect to 196 cm^{-1} peak for different CZTSSe samples. Area under the peak is obtained by a Lorentzian fit of the 442 nm spectra. **b)** Anionic composition of Zn(S,Se) secondary phase present in CZTSSe samples according to the type of etching and source of sulfur ²⁷.

Figure 5.31 shows that the relative presence of Zn(S,Se) with respect to CZTSSe is higher in CZTSe reference samples and in samples sulfurized from SeS_2 source, while it is lower in samples sulfurized from thiourea.

A possible explanation for this fact is that the sulfurization stage introduces part of the ZnSe into the CZTSSe structure, while the low available S is mainly introduced into the CZTSSe structure too, thus reducing the sulfurization of the remaining ZnSe into Zn(S,Se). In the case of SeS_2 samples, the presence of Se in the sulfur source prevents the reduction of ZnSe. Regarding the type of etching, in samples sulfurized from S, SnS, and thiourea the relative amount of Zn(S,Se) does not change between etchings Type A and B. In the case of CZTSe reference samples, etching Type A reduces the presence of ZnSe more, while in the case of SeS_2 samples, etching Type B is the one that produces better results regarding secondary phase removing. Thus, no definitive conclusion can be reached regarding which type of etching is better.

However, it could be hypothesized from the Raman and compositional studies, that when introducing S to the CZTSSe crystalline matrix at film's surface via SeS_2 , the secondary phases such as ZnS could be easily removed when applying a Type B reactive chemical etching.

Figure 5.31 shows that the content of sulfur in Zn(S,Se) of samples Se reference (Ref) and SeS₂ is zero or negligible, while it represents around 25% of the anionic composition in samples sulfurized from SnS and thiourea sources. This is explained by the presence or lack of Se in the sulfur source.

For a more complete analysis, an additional comparison of the in-depth compositions obtained with the different sulfur sources measured with different techniques is presented in Figure 5.32, including the overall S/(S + Se) ratio measured by XRF, showing coherent results.

As such, it is unequivocally confirmed that the introduction of S pulses employing highly reactive precursors during the cooling down process is very effective to create sharp superficial anionic compositional gradients in kesterite absorbers.

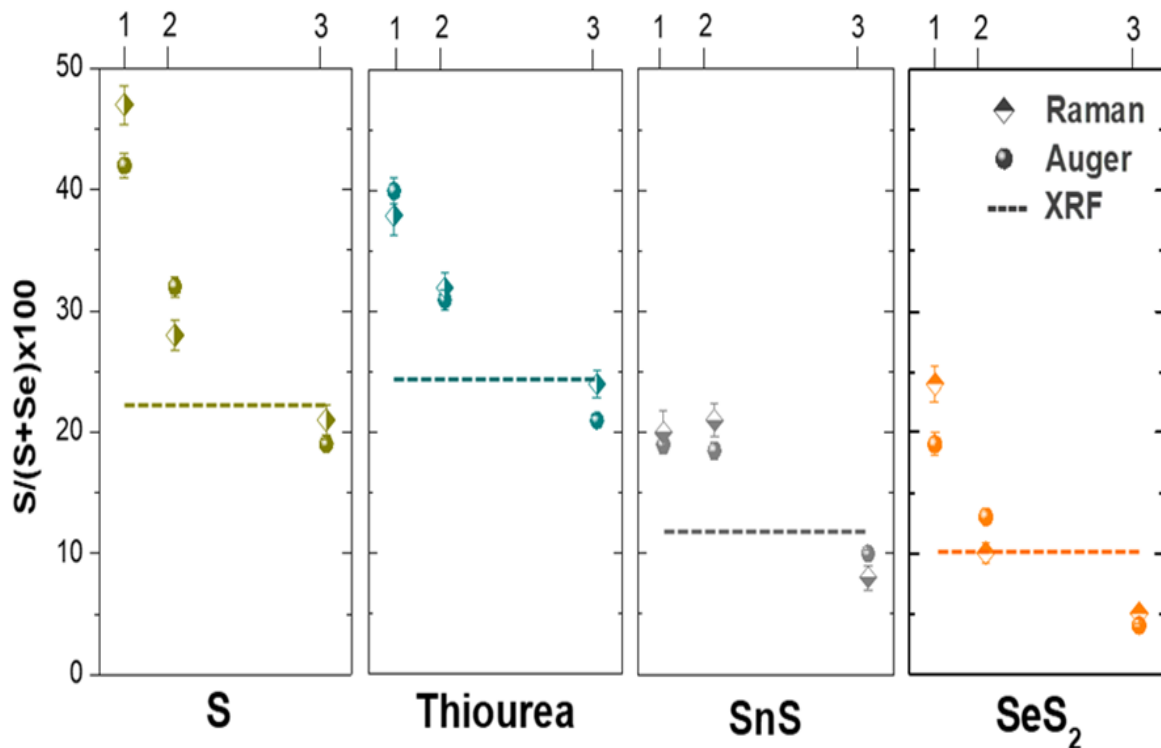


Figure 5.32.- Comparison of the S/(S+Se) compositional ratio obtained with different techniques (Raman spectroscopy, Auger spectroscopy and XRF) for the four chalcogenide precursors under analysis. Point 1 represents the very top surface (First 50 nm), Point 2 the sub-surface (First 150 nm), and Point 3 the very surface (First 50 nm) at the back (rear) surface.

5.8 Fabrication and Analysis of CZTSSe Solar Cell Devices

In this way, representative absorbers obtained with the different sulfur precursors were employed to fabricate solar cell devices.

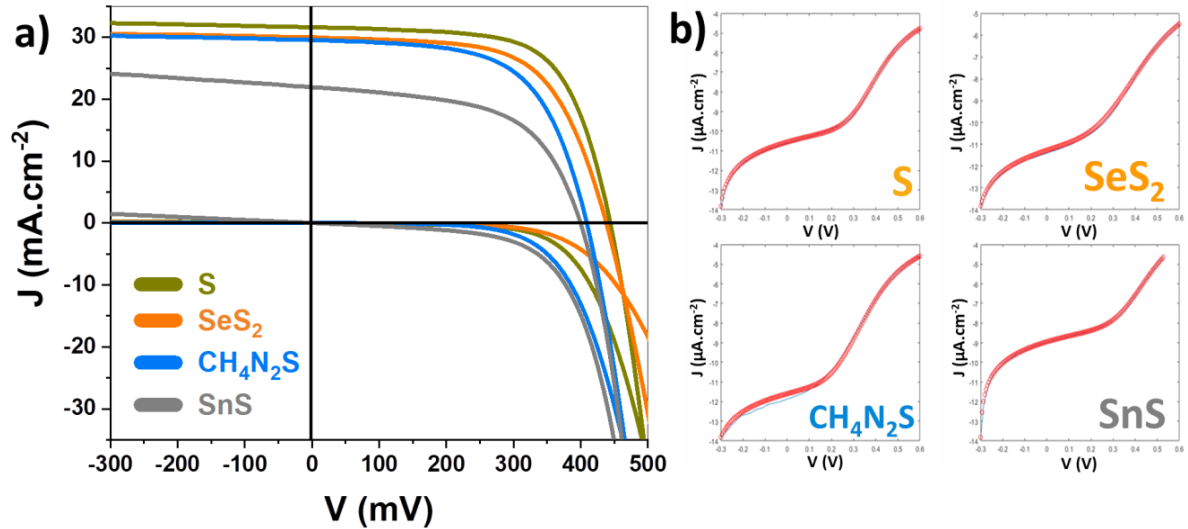


Figure 5.33.- a) Dark and illuminated JV curves of the best behaved SLG/Mo/MoSSe_x/CZSSe/CdS/iZnO/ITO for the four chalcogenide processed anionic graded CZTSSe thin film solar cells. b) Corresponding dark curve fittings.

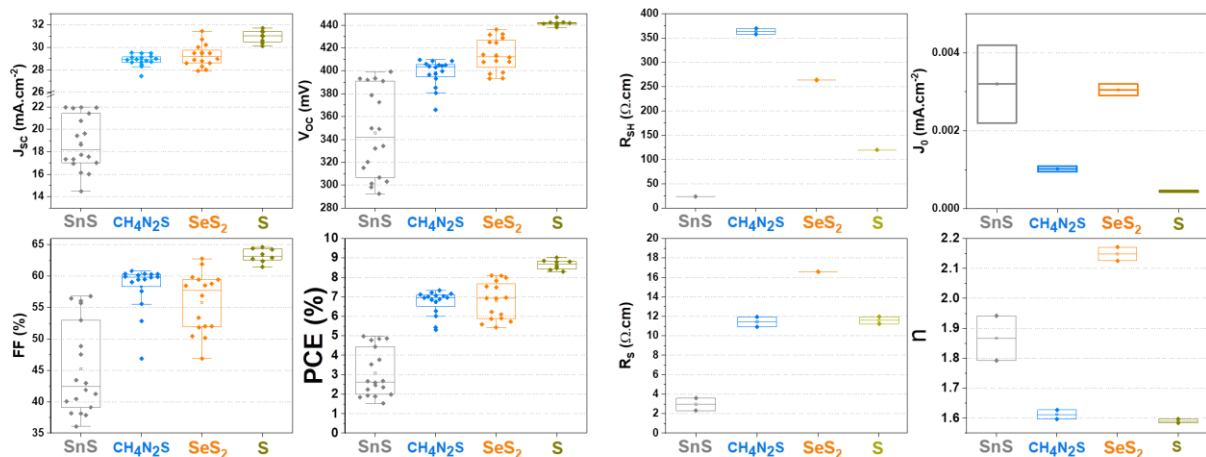


Figure 5.34.- Eight (4) Measured and (4) calculated optoelectronic solar cell parameters boxplots derived from the JV measurements.

Table 5.2. Optoelectronic parameters of selected samples obtained introducing S pulses with different precursors.

Device	J_{sc} [mA. cm ⁻²]	V_{oc} [mV]	FF [%]	Eff. (η) [%]	n	W [nm]	N [cm ⁻³]	E_g [eV]	SQ- Voc, deficit [mV]	Integrated J_{sc} (IQE) [mA. cm ⁻²]
S	31.6	444	65.8	9.23	1.60	271	5.8×10^{15}	1.064	384	34.38
SeS ₂	30.0	438	62.2	8.16	2.13	354	3.7×10^{15}	1.094	422	34.04
CH ₄ N ₂ S	29.5	408	60.9	7.34	1.63	10	6.9×10^{18}	1.090	444	32.69
SnS	21.9	399	56.8	4.97	1.94	110	1.2×10^{17}	1.072	437	23.00

Figures 5.33 and 5.34 as well as Table 5.2, show the JV illuminated curves (AM1.5) and a selection of the most representative optoelectronic parameters of the best devices fabricated with each of the S sources, respectively. As (later discussed) and expected from CV and IQE analysis, the best results in terms of efficiency are obtained for the devices fabricated with elemental S and SeS₂ with remarkable 9.2% and 8.2%, respectively. Figure 5.35a shows simultaneously the EQE and IQE curves of the devices fabricated with the different S sources, which provide information about the photogenerated carrier collection. Additionally, Figure 5.35a shows that the solar cell device fabricated with a SnS–sulfur pulse displays a significant lower collection than the other devices, which is in good agreement with the CV analysis (Figure 5.41). The rest of the devices exhibit rather similar IQE profiles at short wavelengths with the main differences observed in the long wavelength region (> 900 nm).

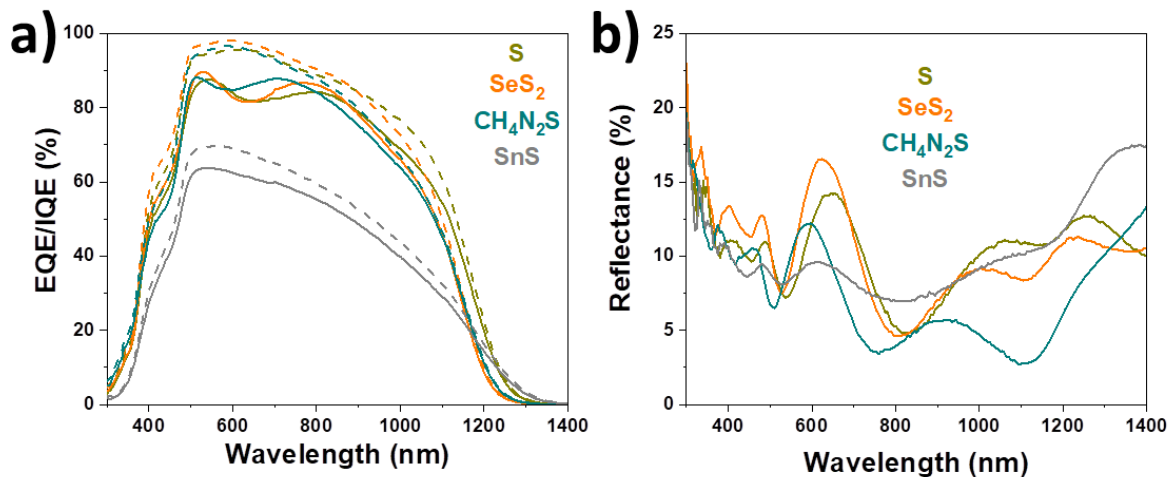


Figure 5.35.- a) EQE/IQE curves, and **b)** Reflectance curves for the best behaved device on each of four chalcogenide processed anionic graded CZTSSe solar cell devices.

This fact indicates slightly different collection of the charges generated within the bulk of the absorber. The band gap (E_G) values of the absorbers were estimated from the EQE and IQE curves by the Tauc plots. The extracted bandgap ranges between 1.064 eV and 1.094 eV depending on the chalcogen source.

By using the dependence between the band gap and $S/(S + Se)$ ratio reported by He et al.²⁸ with a bowing constant $b = 0.08$ eV, it is possible to estimate the anionic composition for the different chalcogen sources as follows: $S/(S + Se)_S = 0.22$ ($E_G = 1.064$ eV), $S/(S + Se)_{SeS_2} = 0.28$ ($E_G = 1.064$ eV), $S/(S + Se)_{CH_4N_2S} = 0.27$ ($E_G = 1.090$ eV), and $S/(S + Se)_{SnS} = 0.23$ ($E_G = 1.072$ eV). In the case of S and thiourea, these values agree very well with the overall composition obtained by XRF. In the case of SeS_2 and SnS, the composition obtained using the E_G values from the IQE is quite different from the values obtained by XRF, and in particular, the $S/(S + Se)$ ratio is estimated higher than the real value. It could be therefore concluded that this feature can be related to the higher influence of the surface grading in the band gap obtained by the IQE in the case of SeS_2 because the Se content in the layer is notably lower than in the other cases. For SnS, the bad characteristics of the devices make complicated a good estimation of the band gap introducing large uncertainties in the evaluation of this parameter.

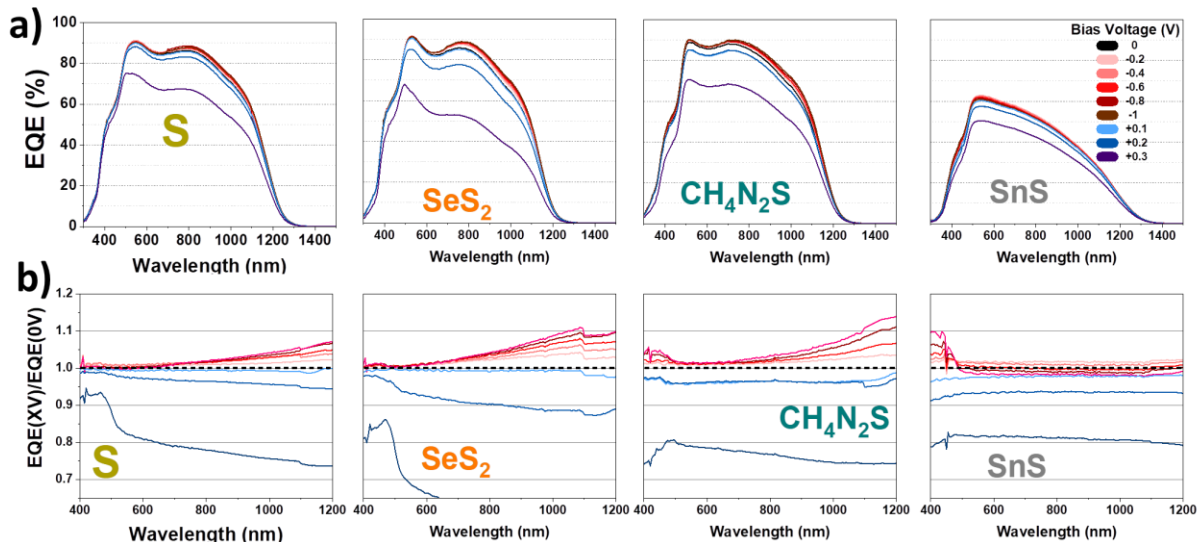


Figure 5.36.- Voltage (-1 to +0.3) Biased a) EQE curves and b) EQE(XV)/EQE(0V) ratio for the distinct anionic graded CZTSSe solar cell devices.

From Figure 5.36, it could be observed that the IQE shape and intensity strongly depends on the space charge region width $W(V)$.

Therefore, not collecting charge carriers that are generated beyond $(W(V) + L)$ represents a significant loss in the photogenerated current.

By applying a bias voltage (See Figure 3.18 to the solar cell during EQE measurement, it is possible to modify $W(V)$, thus by comparing biased with unbiased QE measurements, it is possible to gather information regarding the completeness of the current collection and possible loss mechanisms in the device (Figure 5.37).

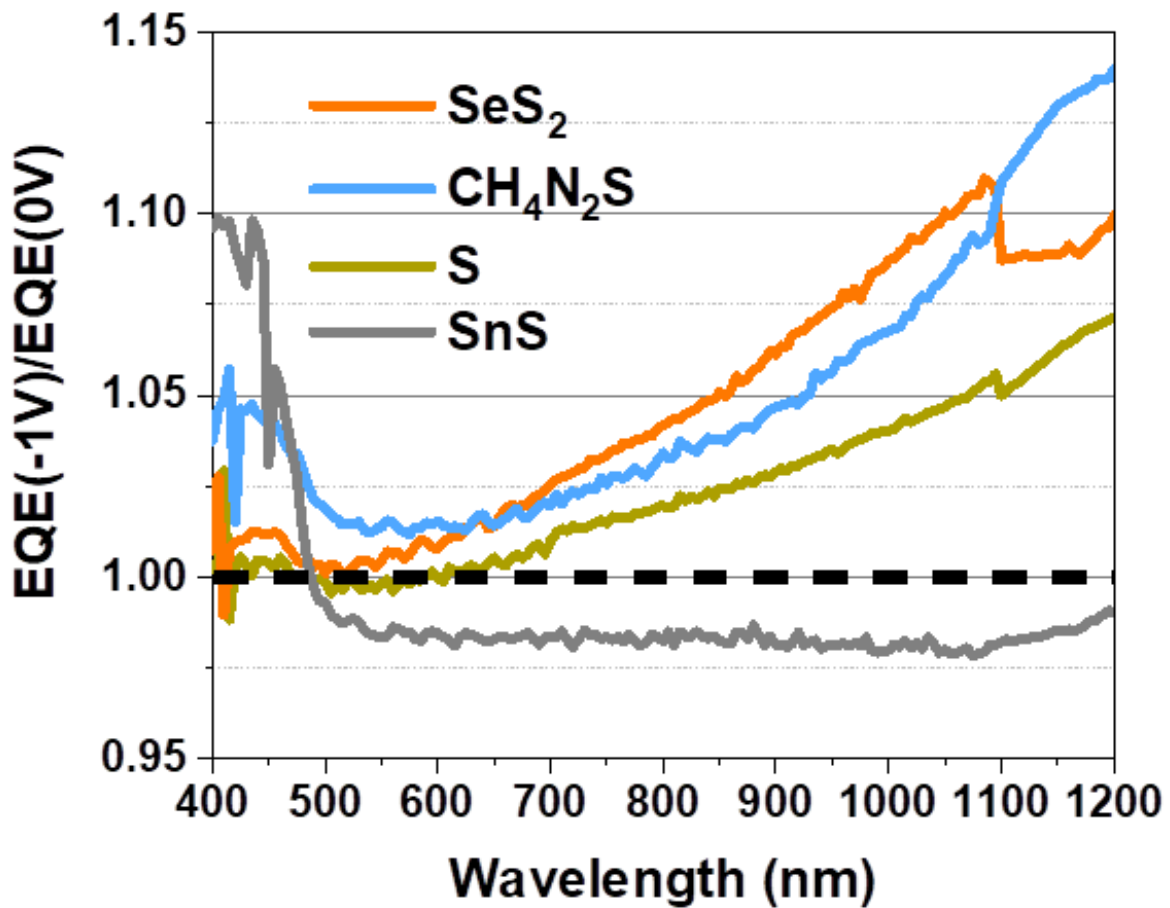


Figure 5.37.- $EQE(-1V)/EQE(0V)$ ratio for the distinct anionic graded CZTSSe solar cell devices.

5.9 Device Impedance spectroscopy analyses

Capacitance-Voltage (CV) measurements were performed on the devices in order to determine the width of the SCR and calculate if the band gap grading profiles are located within it (Figures 5.38 to 5.40).

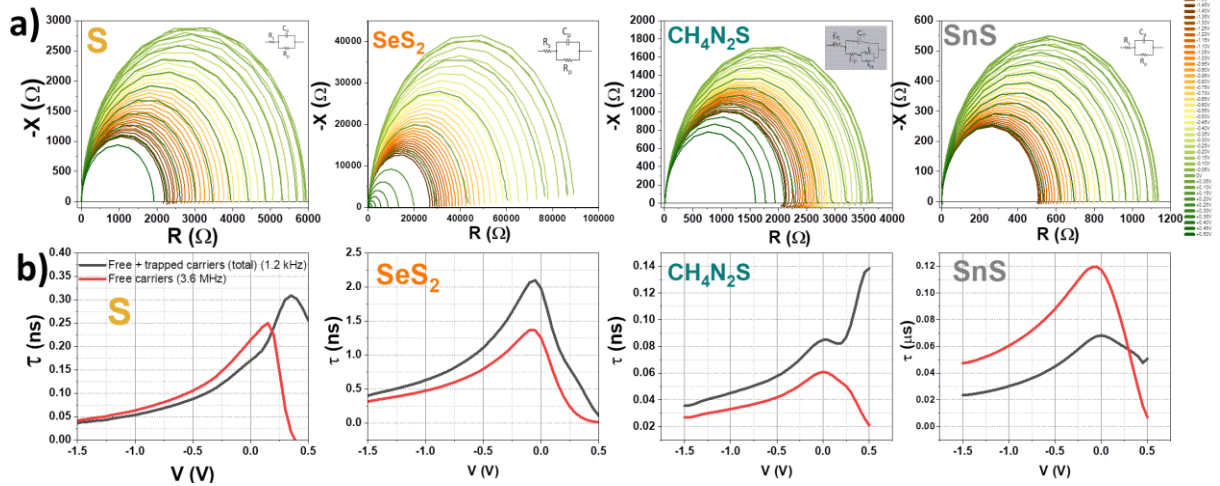


Figure 5.38.- a) Frequency swept impedance measurements of the CZTSSe graded bandgap solar cell devices. **b)** CV-calculated minority charge carrier lifetime.

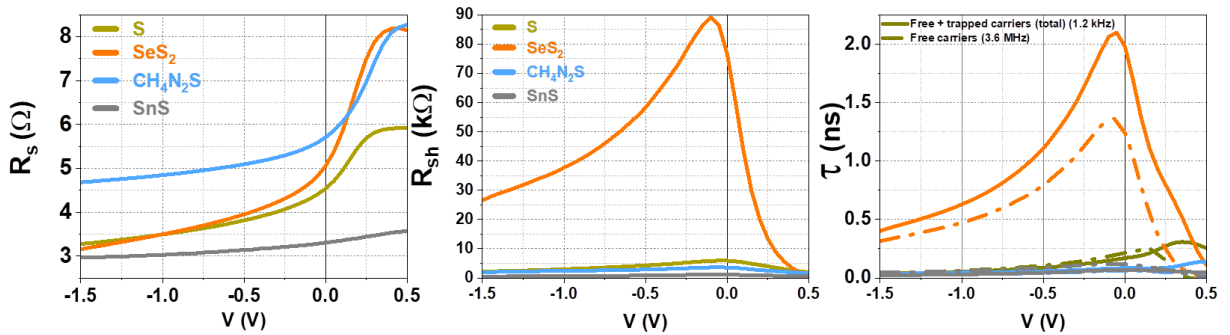


Figure 5.39.- Series and Shunt Resistance and lifetime calculation derived from the impedance measurements.

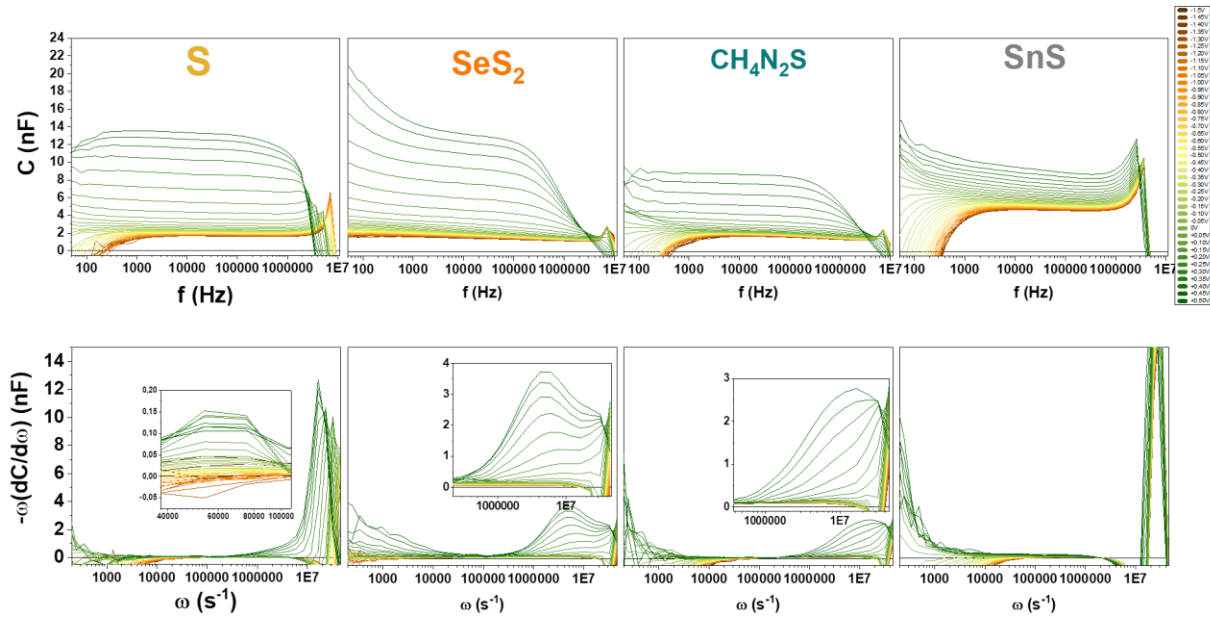


Figure 5.40.- Impedance spectroscopy analysis for the 4 chalcogenide (S, SeS₂, CH₄N₂S, and SnS) processed anionic graded CZTSSe absorber layers.

Figure 5.41b shows the minority carrier concentration as function of the depletion width of different CZTSSe samples measured with an (AC) frequency of 1 MHz, calculated from room-temperature CV measurements. The sample fabricated with a thiourea S pulse shows exceptionally high capacitance values with a large carrier concentration ($\sim 7 \times 10^{18} \text{ cm}^{-3}$) and an extremely narrow SCR ($\sim 10 \text{ nm}$), suggesting the presence of an abrupt junction as it was tested in three different devices. Despite this, the device exhibited a decent PV performance.

Thus, it might be possible that the presence of carbon-related residues and/or phases arising from the decomposition of the thiourea attenuates the capacitor behavior of the device. Thus, the CV characterization of these devices is discarded for further discussion.

On the other hand, the device fabricated with a SnS–sulfur pulse presents high capacitance values (Although 2 whole orders of magnitude above those of the thiourea-based device) with a carrier concentration of 10^{17} cm^{-3} and a SCR width just above 100 nm.

Finally, samples fabricated with elemental S and SeS₂ sulfur pulses show lower capacitances carrier concentrations below 10^{16} cm^{-3} and wider space charge carrier region widths (270–350 nm). These values are in good agreement with previous results.^{29,30}

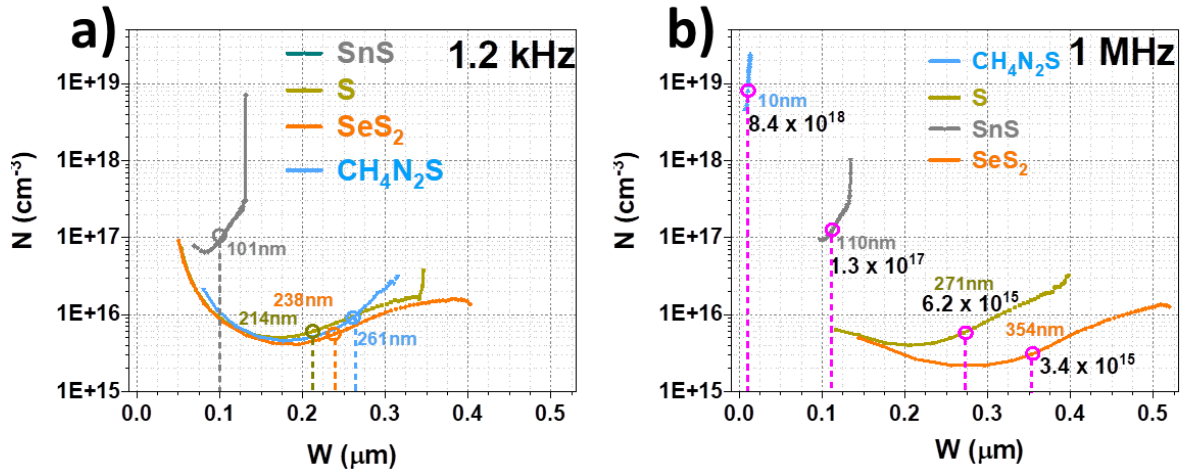


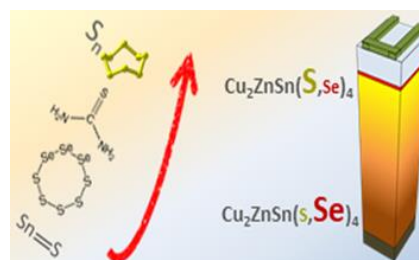
Figure 5.41.- a) Minority charge carrier density (N) vs. voltage vs. profiling positioning (W) at **a)** 1.2 kHz and **b)** 1MHz for the best SLG/Mo/MoSe_x/CZTSSe/CdS/iZnO/ITO thin film solar cells.

By comparing the results obtained from the CV analysis with the Auger compositional profiles (See Figure 5.41), it is possible to infer that the SCR lies inside the S/(S + Se) front grading region at least for S and SeS₂ (estimated in 100 and 200 nm, respectively). A high doping level should bring the fermi level closer to the valence band in the absorber, and thus increase the built in voltage. Hence, the samples with larger SCRs (those fabricated with elemental S and SeS₂) are expected to exhibit higher energy conversion efficiencies. As expected from CV and IQE analysis, the best results in terms of efficiency are obtained for the devices fabricated with elemental S and SeS₂ with remarkable 9.2% and 8.2%, respectively. For the devices prepared with the optimized graded band gap using sulfur, a V_{OC} deficit of 384 mV with respect to the Shockley–Queisser limit is estimated, which can be considered among the best values reported in the literature for all kesterites independently on the composition and one of the lowest ones considering the band gap of the absorber (see Table 3 of reference ³¹ for comparison). This demonstrates the feasibility of fabricating working devices with good efficiencies and improved V_{OC} deficit using the grading strategy developed in this Thesis. In addition, these devices exhibit the most pronounced S/(S + Se) compositional gradients. Thus, the superior performance of the devices correlates with sharp gradients obtained in these samples. ²³ These promising results open interesting perspectives for the future optimization and customization of anionic compositional gradient profiles in kesterites using the methodology proposed in this work and based on the introduction of chalcogen pulses during out-of-equilibrium conditions of the kesterite synthesis process.

5.10 Chapter Main Conclusions

In a conclusive way to the superficial anionic graded bandgap in (CZTSSe) kesterite thin film solar cells, a friendly “the take home message”:

- Sharp S/Se anionic graded bandgap can be created by considering:
 - The introduction of S under out-of-equilibrium conditions and after crystallization process.
 - Using highly reactive sulphur precursors.
 - S content at the bulk seems to be controlled by the volatility of the S precursor.
- Higher S concentration at the very surface (~300 nm) ensure:
 - Reduction of surface recombination.
 - Reduction of the V_{OC} deficit.
- Higher S concentration at the back interface (towards the Mo back contact): S/Se gradient is revealed as relevant for front interface but it is therefore urged to look after another solution for back interface engineering.



Last but not least, noteworthy is to mention that the utilization of the superficial chalcogenization methodology developed during this Thesis has also been successfully applied to solar cell devices based on chalcogenide materials such as **Ci(S,Se)** and **Sb₂(S,Se)₃** demonstrating remarkable results even in SLG or ceramic type substrates. Further details and examples are provided in **Thesis Appendix: Additional and Supporting Information (Figure i.6)**.

5.10 Chapter References

1. Lyons, J. R. An estimate of the equilibrium speciation of sulfur vapor over solid sulfur and implications for planetary atmospheres. *J. Sulfur Chem.* **29**, 269–279 (2008).
2. Jackson, A. J., Tiana, D. & Walsh, A. A universal chemical potential for sulfur vapours. *Chem. Sci.* **7**, 1082–1092 (2016).
3. Dimitrievska, M. *et al.* Multiwavelength excitation Raman scattering of $\text{Cu}_2\text{ZnSn}(\text{S}_x\text{Se}_{1-x})_4$ ($0 \leq x \leq 1$) polycrystalline thin films: Vibrational properties of sulfoselenide solid solutions. *Appl. Phys. Lett.* **105**, 031913 (2014).
4. Dimitrievska, M. *et al.* Raman scattering quantitative analysis of the anion chemical composition in kesterite $\text{Cu}_2\text{ZnSn}(\text{S}_x\text{Se}_{1-x})_4$ solid solutions. *J. Alloys Compd.* **628**, 464–470 (2015).
5. Oliva, F. *et al.* Optical methodology for process monitoring of chalcopyrite photovoltaic technologies: Application to low cost $\text{Cu}(\text{In,Ga})(\text{S,Se})_2$ electrodeposition based processes. *Sol. Energy Mater. Sol. Cells* **158**, 168–183 (2016).
6. Fairbrother, A. *et al.* Development of a Selective Chemical Etch To Improve the Conversion Efficiency of Zn-Rich $\text{Cu}_2\text{ZnSnS}_4$ Solar Cells. *J. Am. Chem. Soc.* **134**, 8018–8021 (2012).
7. Neuschitzer, M. *et al.* Optimization of CdS buffer layer for high-performance $\text{Cu}_2\text{ZnSnSe}_4$ solar cells and the effects of light soaking: elimination of crossover and red kink: CdS and effects of light soaking: elimination of crossover and red kink. *Prog. Photovolt. Res. Appl.* **23**, 1660–1667 (2015).
8. Dimitrievska, M. *et al.* Role of S and Se atoms on the microstructural properties of kesterite $\text{Cu}_2\text{ZnSn}(\text{S}_x\text{Se}_{1-x})_4$ thin film solar cells. *Phys. Chem. Chem. Phys.* **18**, 8692–8700 (2016).
9. Garcia-Llamas, E. *et al.* Multiwavelength excitation Raman scattering of $\text{Cu}_2\text{ZnSn}_{1-x}\text{Ge}_x(\text{S,Se})_4$ single crystals for earth abundant photovoltaic applications. *J. Alloys Compd.* **692**, 249–256 (2017).
10. Wang, Y. P. *et al.* Composition Dependent Band Gaps of Single Crystal $\text{Cu}_2\text{ZnSn}(\text{S}_x\text{Se}_{1-x})_4$ Solid Solutions. *Solid State Phenom.* **194**, 139–143 (2012).
11. PRIGOGINE, I., STENGERS, I., & PRIGOGINE, I. (1984). *Order out of chaos: man's new dialogue with nature.* Boulder, CO, New Science Library.
12. Prigogine, I. Irreversibility and randomness. *Astrophys. Space Sci.* **65**, 371–381 (1979).
13. Chen, S., Gong, X. G., Walsh, A. & Wei, S.-H. Electronic structure and stability of quaternary chalcogenide semiconductors derived from cation cross-substitution of II-VI and I-III-VI₂ compounds. *Phys. Rev. B* **79**, 165211 (2009).
14. Chen, S., Gong, X.-G., Walsh, A. & Wei, S.-H. Structural, Electronic and Defect Properties of $\text{Cu}_2\text{ZnSn}(\text{S,Se})_4$ Alloys. *MRS Proc.* **1370**, mrs11-1370-yy0-06 (2011).
15. Robert Fonoll-Rubio *et al.* Insights into interface and bulk defects in a high efficiency kesterite-based device. *Energy Environ. Sci.* **14**, 507–523 (2020).
16. Kim, S.-Y. *et al.* Secondary Phase Formation Mechanism in the Mo-Back Contact Region during Sulfo-Selenization Using a Metal Precursor: Effect of Wettability between a Liquid Metal and Substrate on Secondary Phase Formation. *ACS Appl. Mater. Interfaces* **11**, 23160–23167 (2019).
17. Englund, S., Saini, N. & Platzer-Björkman, C. $\text{Cu}_2\text{ZnSn}(\text{S,Se})_4$ from annealing of compound co-sputtered precursors – Recent results and open questions. *Sol. Energy* **175**, 84–93 (2018).
18. Grini, S., Ross, N., Persson, C., Platzer-Björkman, C. & Vines, L. Low temperature incorporation of selenium in $\text{Cu}_2\text{ZnSnS}_4$: Diffusion and nucleation. *Thin Solid Films* **665**, 159–163 (2018).
19. Chen, S. *et al.* Compositional dependence of structural and electronic properties of $\text{Cu}_2\text{ZnSn}(\text{S,Se})_4$ alloys for thin film solar cells. *Phys. Rev. B* **83**, 125201 (2011).
20. Luo, Y.-R. *Comprehensive Handbook of Chemical Bond Energies; CRC Press, 2007.*
21. Luo, Y.-R. *Handbook of Bond Dissociation Energies in Organic Compounds; CRC Press, 2002; Vol. 30.*
22. Wang, Z. D., Yoshida, M. & George, B. Theoretical study on the thermal decomposition of thiourea. *Comput. Theor. Chem.* **1017**, 91–98 (2013).
23. Yang, K.-J. *et al.* A band-gap-graded CZTSSe solar cell with 12.3% efficiency. *J. Mater. Chem. A* **4**, 10151–10158 (2016).
24. Hwang, D.-K. *et al.* Single-step sulfo-selenization method for achieving low open circuit voltage deficit with band gap front-graded $\text{Cu}_2\text{ZnSn}(\text{S,Se})_4$ thin films. *Sol. Energy Mater. Sol. Cells* **161**, 162–169 (2017).
25. Cai, C.-H. *et al.* Efficiency enhancement of $\text{Cu}_2\text{ZnSn}(\text{S,Se})_4$ solar cells by S-modified surface layer. *Sol. Energy Mater. Sol. Cells* **162**, 21–29 (2017).
26. Dimitrievska, M. *et al.* Raman scattering analysis of the surface chemistry of kesterites: Impact of post-deposition annealing and Cu/Zn reordering on solar cell performance. *Sol. Energy Mater. Sol. Cells* **157**, 462–467 (2016).
27. Xie, H. *et al.* Formation and impact of secondary phases in Cu-poor Zn-rich $\text{Cu}_2\text{ZnSn}(\text{S}_{1-y}\text{Se}_y)_4$ ($0 \leq y \leq 1$) based solar cells. *Sol. Energy Mater. Sol. Cells* **140**, 289–298 (2015).
28. He, J. *et al.* Composition dependence of structure and optical properties of $\text{Cu}_2\text{ZnSn}(\text{S,Se})_4$ solid solutions: An experimental study. *J. Alloys Compd.* **511**, 129–132 (2012).
29. Erkan, M. E., Chawla, V. & Scarpulla, M. A. Reduced defect density at the CZTSSe/CdS interface by atomic layer deposition of Al_2O_3 . *J Appl Phys* **9** (2016).
30. Zhong, J. *et al.* Sulfurization induced surface constitution and its correlation to the performance of solution-processed $\text{Cu}_2\text{ZnSn}(\text{S,Se})_4$ solar cells. *Sci. Rep.* **9**.
31. Giraldo, S. *et al.* Progress and Perspectives of Thin Film Kesterite Photovoltaic Technology: A Critical Review. *Adv. Mater.* **31**, 1806692 (2019).

An experiment is a question which science poses to Nature,
And a measurement is the recording of Nature's answer.

-Max Planck

Chapter VI

Results Part III, Case A: Experimental Rear Bandgap Grading Strategy in CZTGSe Alloyed Kesterite Solar Cells

6.1 Introduction and Chapter Presentation

In Chapter IV of the Thesis, a proven strategy of band engineering to assist charge carrier collection in kesterite, taking inspiration from chalcopyrite solar cells is demonstrated. For this purpose, a sequential process based on a combination of metallic precursor sputtering and chalcogenide reactive annealing, allowed the controlling of cationic substitutions by partly replacing Sn by Ge, hence tailoring several rear bandgap grading profiles along the absorber thickness. A complete set of structural (XRD), morphological and topographical (FESEM) and compositional (XRF, EDX) characterization techniques, with samples ranging from pure Sn to pure Ge compounds are firstly discussed. Therefore, the formation of a rear bandgap grading is determined through an advanced correlational characterization analysis, specifically through a combination of glow discharge optical emission (GDOES) and Auger spectroscopies along with multiwavelength Raman spectroscopy studies carried out at the front and back (rear) sides of the films using a lift-off process. As such, a preferential Ge enrichment toward the back of the absorber is unequivocally demonstrated in kesterite absorbers and further applied to complete devices for deliberately generating distinct rear bandgap profiles, leading to an efficient back surface field that potentially enhances the carrier selectivity of the back interface. In this way, the fabricated kesterite CZTGSe solar cells demonstrate a complex interplay between the benefits of bandgap grading and possible Ge-related defects in the absorber. By optimizing the synthesis conditions, an absolute increase in bare efficiency is obtained for the champion device (**≈10%**) **without any** antireflective coating (ARC) neither metallic grid.

However, the performance enhancement is mostly ascribed to the presence of a drift electric field assisting in the carrier collection while preventing back side recombination. Therefore, these results confirm the possibility of generating back bandgap grading in kesterite solar cells and open the way to a further development of the kesterite photovoltaic technology towards higher efficiencies through tailored bandgap engineering.

6.2 Tin (Sn) – Germanium (Ge) Alloyed Sputtered Layers

Thin film absorber layers were fabricated by the standardized sequential process developed at IREC, based on the thermal reactive annealing of DC-magnetron sputtered metallic precursors (See Chapter III) ¹⁻³.

In this part of this Thesis, Cu/Sn/Cu/Zn/Ge precursor structures were deposited on Mo-coated soda-lime glass (SLG) substrates. The sputtered Sn and Ge layer thicknesses were adjusted to produce the following Sn-Ge alloyed precursor materials: 0%, 20%, 40% and 100%.

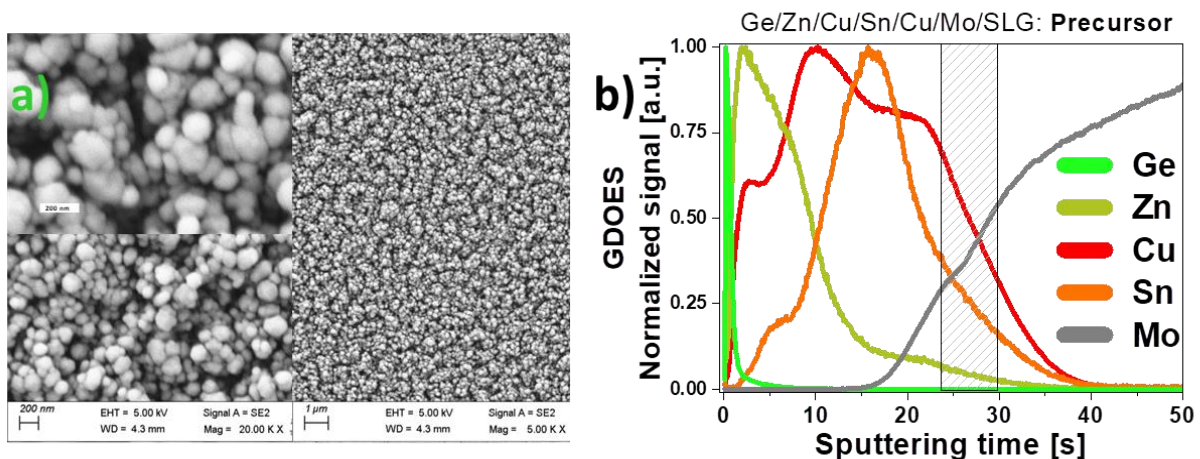


Figure 6.1.- CZTG sputtered precursor **a)** Planar view SEM micrograph and **b)** GDOES of the Ge, Zn, Cu, Sn, and Mo signals vs. sputtering time. The patterned area is an eye-guide to indicate the position of the precursor/Mo interface.

Figure 6.1 shows the GDOES spectra of a SLG/Mo/Cu/Sn/Cu/Zn/Ge precursor layer. In this figure, all the signals have been normalized to unity. A thin layer of Ge is visible on the top surface, followed by Cu/Sn/Cu/Zn metallic layers. The signals superposition, partially due to sputtering effect, seems to suggest some element atomic interdiffusion. The interface between the sample and the substrate (Mo) is depicted with a patterned area in Figure 6.1b.

6.3 Thermal annealing: Chalcogenization Process

The samples were labeled as CZTSe, CZTG20Se, CZTG40Se, and CZGSe according to these percentages. For the thermal annealing processes of this part of this Thesis, the precursor samples were introduced in graphite boxes (69 cm³ in volume) along with graphite crucibles containing elemental 100 mg of elemental Se and 10 mg of elemental Sn and placed in a tubular furnace to carry out the thermal reactive annealing (See Chapter III for further experimental details).

As it is shown in Figure 6.2, the annealing temperatures (T_1 and T_2) were adjusted depending on the $[Ge]/([Ge]+[Sn])$ ratio utilized for each precursor. Figure 6.2 also includes additional experimental details like the pressure along the synthesis and the amount of utilized elemental Sn and Se powders (See Chapter III).

In before, the thickness of the Sn and Ge layers in the sputtered CZTG metallic precursor were adjusted to produce the following Sn by Ge substitutions: 0%, 20%, 40% and 100%. The samples were labeled as CZTSe, CZTG20Se, CZTG40Se, and CZGSe according to these percentages.

The morphology and topographical characteristics of the CZTGSe absorber layers synthesized from the precursors with different $([Ge]/([Ge]+[Sn]) = GGT)$ ratios was analyzed by FESEM. Figure 6.3a and b show the top planar view micrographs of the CZTG and CZTGSe precursor and absorber layers, respectively.

For the absorber layers FESEM (See Figure 6.3b), it could be observed that the grain size gradually decreases as the Ge content increases.

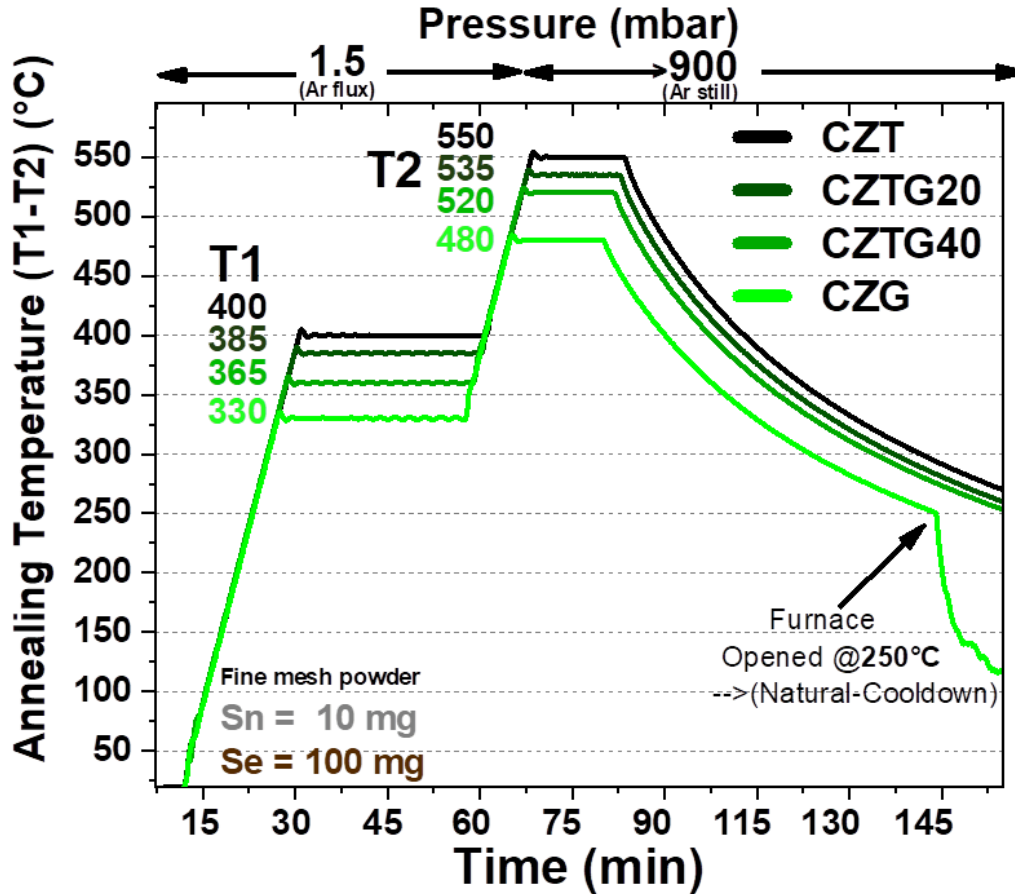


Figure 6.2.- Particular Experimental conditions of each CZTG metallic precursor layers during the thermal reactive annealing (selenization) in a tubular furnace.

6.4 Planar (Top) and Cross Sectional SEM Morphological Details on CZTG and CZTGSe

In this way, while CZTSe presents large and elongated platted grains, CZGSe exhibits a closed-packed agglomeration of smaller sized grains. In addition to the main grains, the samples that contain Ge display a surface covered by crystallites which may suggest the presence of secondary phases.

It should be noted that these are as-synthesized absorbers and that chemical etchings are applied to the absorbers when fabricating photovoltaic devices to remove this type of superficial secondary phases (See Chapter III and Thesis Appendix).

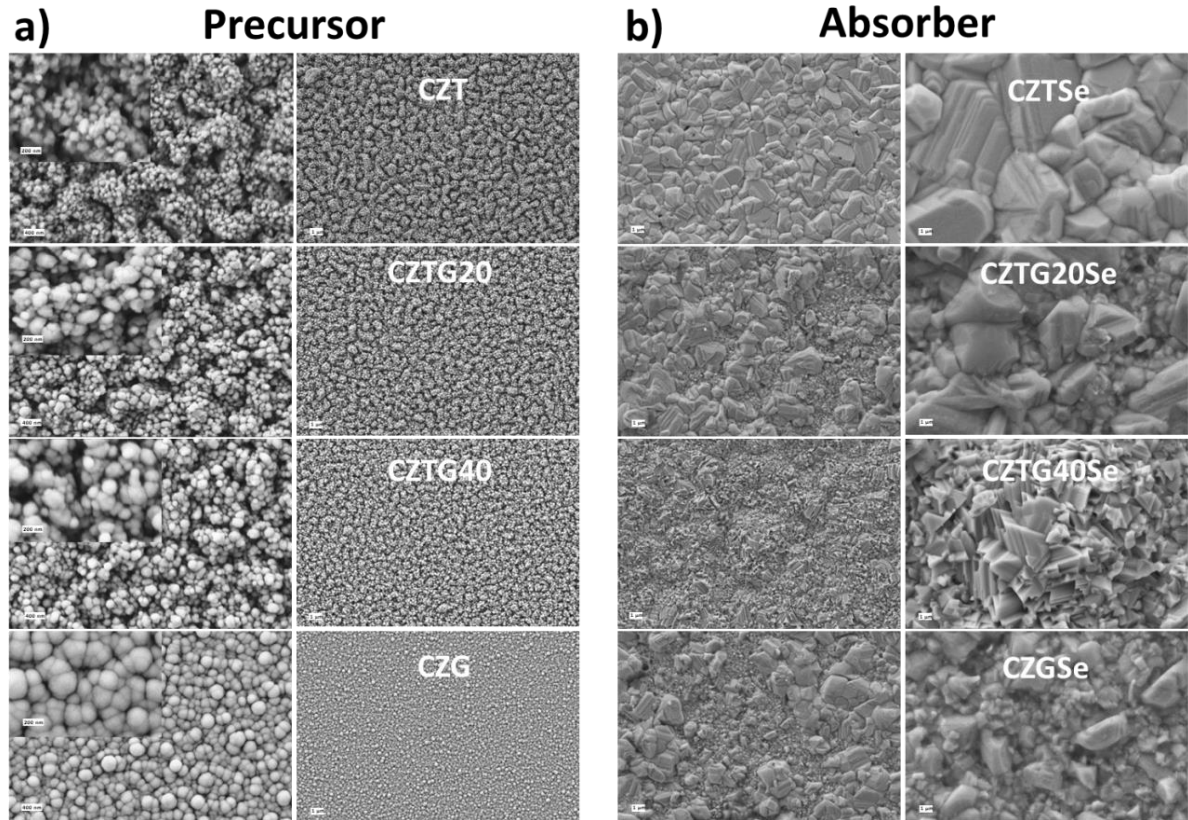


Figure 6.3.- Planar (top) view SE2-FESEM micrographs of the a) CZTG Precursor and b) CZTGSe Absorber materials.

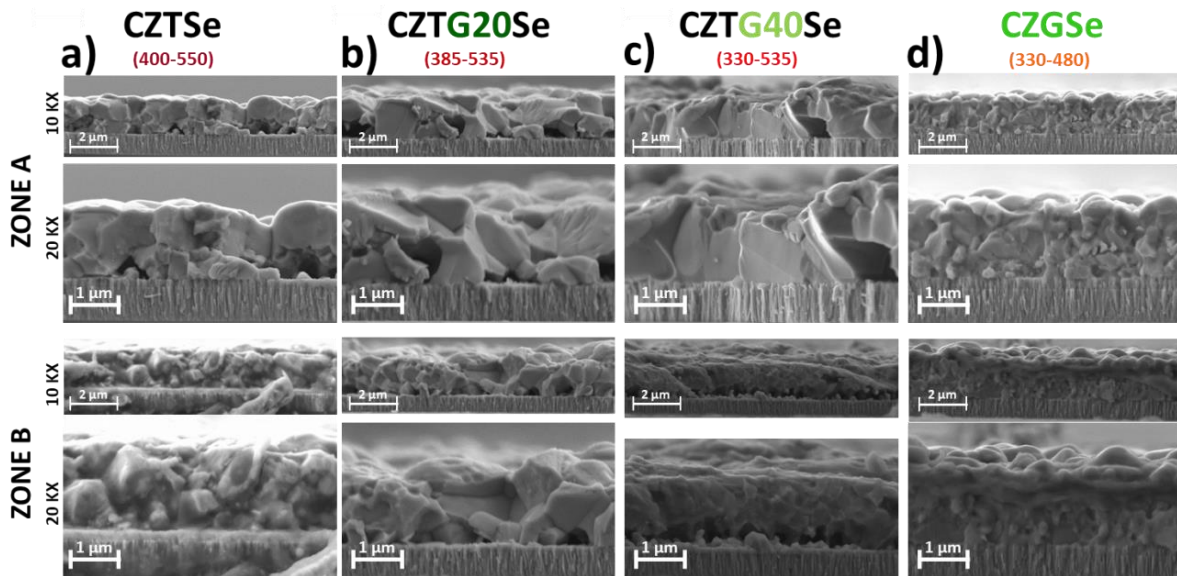


Figure 6.4.- Cross-sectional (2 Distinct Zones: A & B) FESEM micrographs. (T_1 - T_2) °C synthesis conditions are indicated for each of the depicted CZTGSe absorber layers.

6.5 XRD Structural Studies on CZTGSe

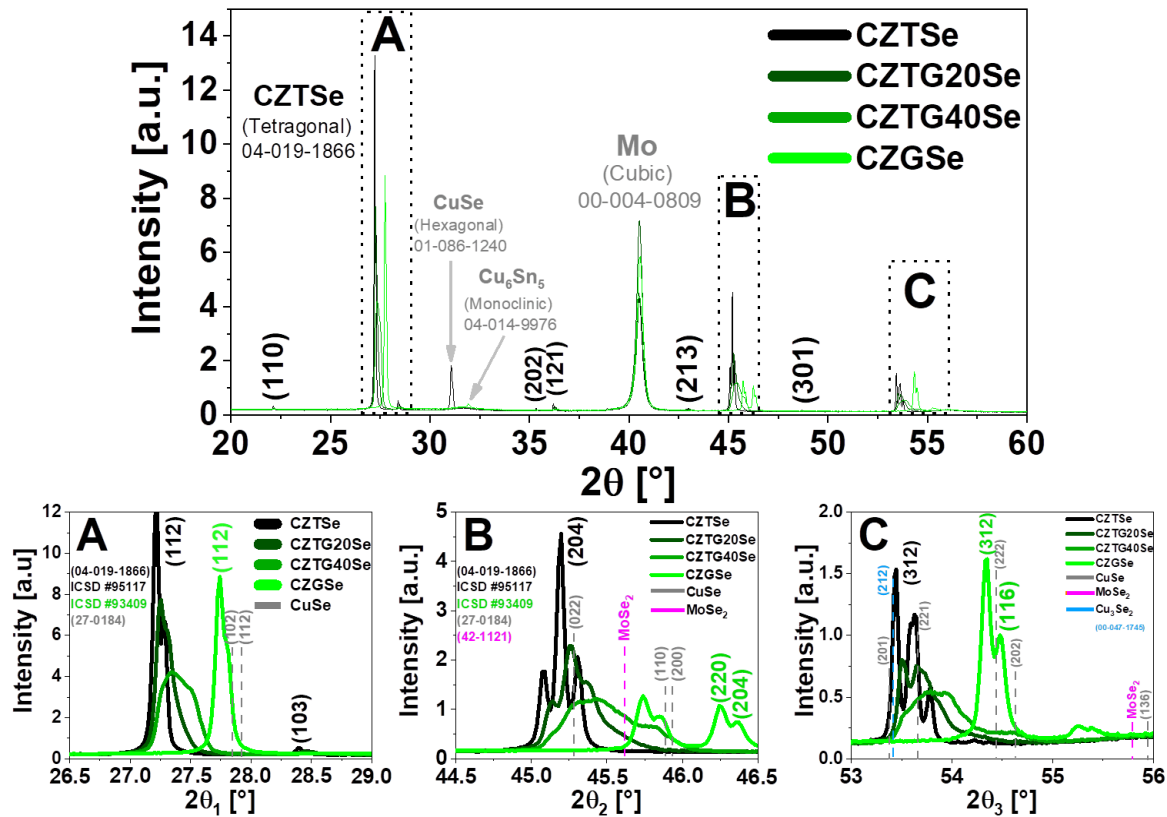


Figure 6.5.- XRD of the CZTGSe absorber thin films. Back contact (Mo) diffraction signals are also observed.

Additionally, cross-sectional SEM micrographs are shown in Figure 6.4. The Ge-free reference CZTSe (See Figure 6.4a) sample shows a larger density of voids at the CZTSe/MoSe_x interface in comparison to the Ge-containing absorbers. Moreover, the density of voids seems to decrease as the Ge content increases with no appreciable voids in the case of pure CZGSe sample. Fact which turns to find natural consistency with the hypothesis of Ge acting as a crystal flux agent proposed in literature.⁴

Moreover, a structural characterisation study of the absorbers with different GGT ratios was carried out by XRD. The acquired diffractograms (See Figure 6.5) show three of the main peaks corresponding to pure CZTSe, CZGSe and CZTGSe solid solutions at **A** = $2\theta_1 = (26.5 - 29.0)^\circ$, **B** = $2\theta_2 = (44.5 - 46.5)^\circ$, and **C** = $2\theta_3 = (53.0 - 56.0)^\circ$, in accordance with the different GGT ratios of the different absorber materials.

The large full width at half maximum (FWHM) of the peaks located at $50^\circ < 2\theta < 60^\circ$ may be due to the presence of mixed phases with different Ge contents. These observations confirm the feasibility of synthesizing absorbers with different GGT ratios with an adequate crystallographic structure for the fabrication of solar cells following the synthesis route employed in this work and based on thermal reactive annealing of sputtered metallic precursors.

Additionally, the diffraction peaks corresponding to the CZTGSe solid solution appear shifted towards higher diffraction angles (2θ) as the GGT ratio increases, due to Sn-replacement by smaller Ge atoms leading to shrinkage of the lattice. The crystallographic characteristics of the CZTGSe solid solution thin films were analyzed by a “plug and match” software (MDI Jade)⁵ in which a good correlation between the experimental peak positions and those previously reported for the crystallographic, X-ray and neutron diffraction data is observed.⁶⁻⁹

Still, the obtained XRD crystallographic data suggest the presence of secondary phases in the samples. However, some of the possible secondary phases, such as MoSe_2 ¹⁰, ZnSe ¹¹, Cu_2GeSe_3 ¹², Cu_2SnSe_3 ¹³, Cu_4SnSe_4 ¹⁴, Cu_xSe_y ¹⁴, GeSe_x ¹⁵, and GeO_x ^{16,17} are difficult to distinguish by XRD measurements due to a possible peak overlapping.

In Figure 6.5, it is possible to notice overlapping between the peaks corresponding to the CZ(T,G)Se structures and to the Cu_xSe_y phases which could be appearing into the thin films as secondary phases.

Furthermore, a Bragg peak attributable to MoSe_2 is also observed. These facts might be related to the appearance of the (112) Bragg peak corresponding to CZTSe and CZGSe samples. Conversely, while no position peak shifts are detected in the case of pure CZTSe and CZGSe samples (in which there is no GGT gradient) shifts are observed for peaks (112), (204), and (312) in the case of CZTG20Se and CZTG40Se samples.

This evidence, along with the widening of XRD diffraction maxima for the Ge-alloyed samples (CZTG20Se and CZTG40Se) might be pointing towards the existence of a structural/compositional induced bandgap grading.

6.6 Compositional Studies by GDOES and Auger Spectroscopy

Once that the morphological and structural properties of the samples confirmed a proper synthesis of CZTSe, CZGSe and CZTGSe absorber layers, the distribution of Ge and Sn throughout the whole thickness of the absorber was investigated by means of glow discharge optical emission spectroscopy (GDOES).

Figure 6.6 presents a closer and more detailed view of the Ge and Sn profile lines measured in each sample. The GDOES results show that the total amount of Ge in the different samples increases consistently with composition of the precursor films.

The complete GDOES profiles of the four CZTGSe samples with increasing Ge content are reported in Figure 6.7.

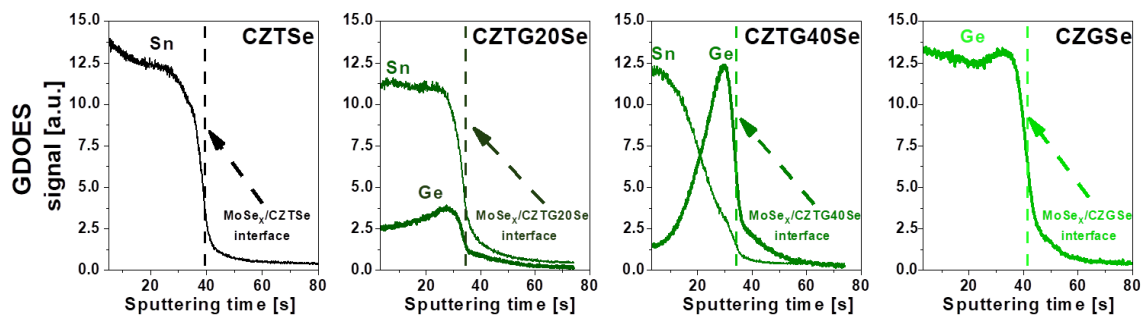


Figure 6.6.- GDOES of the Ge and Sn signals vs. sputtering time of the different CZTGSe absorber thin films. These profiles have been arbitrarily rescaled taking into account the typical/expected sample composition. The vertical dotted lines are an eye-guide to indicate the position of the CZTGSe/MoSe_x. The absorber/Mo interface position could not be accurately located due to the non-flatness of the sputtering crater, film roughness and the presence of a MoSe₂ layer.

Furthermore, in the case of the CZTG20Se and CZTG40Se samples, a graded GGT composition is clearly observed with Ge content increasing (and Sn content decreasing) toward the back side of the CZTGSe films.

This demonstrates that the synthesis route employed not only results in good quality absorbers with different controlled compositions but also enables the generation of an effective and reliable Ge-Sn compositional grading at the back/rear interface.

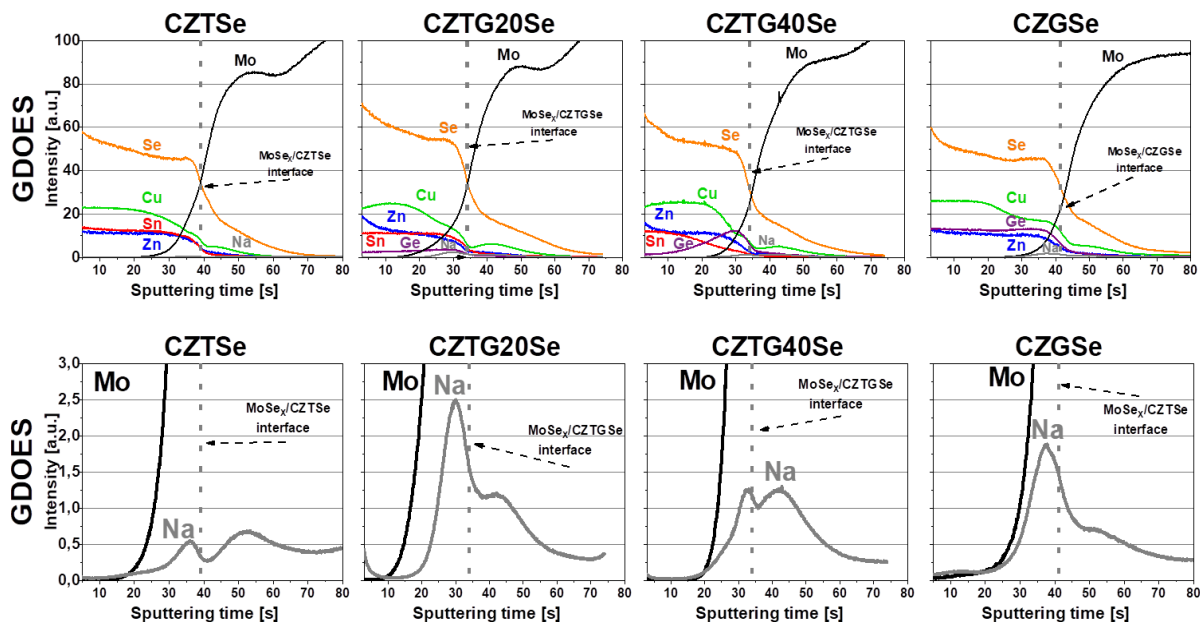


Figure 6.7.- GDOES of the Cu, Zn, Sn, Ge, Se, Na, and Mo signals vs. sputtering time of the different CZTGSe absorber thin films. The signals of Cu, Zn, Sn, Ge and Se have been arbitrarily rescaled taking into account the expected sample composition (top), whereas Na and Mo are simply plotted in a readable scale (bottom). The vertical dotted lines are an eye-guide to indicate the position of the CZTGSe/Mo interface.

Despite the difficulty of studying element interdiffusion due to the broad CZTGSe/Mo interface, the GDOES spectra also suggest that there exists Na diffusion and segregation at the MoSe_x/CZTGSe interface (See Figure 6.7).¹⁸ Further in-depth compositional profiling was performed on the samples by Auger spectroscopy. The results are reported in Figure 6.8 and Figure 6.9.

Particularly, Figure 6.8a depicts the Mo and O Auger atomic concentration signals for all the CZ(T,G)Se absorber samples. An inversed correlation is detected between the oxygen and Ge content which is negligible for the CZGSe sample. On one side, it can be observed that there is oxygen segregation at the back interface for the CZTG20Se sample.

On the other hand, Figure 6.8b represents the Mo and Sn Auger atomic concentration signals for CZTSe and CZTG40Se samples which give a glimpse of the presence of a rear graded composition that increases towards the kesterite/MoSe_x interface is confirmed. However, the data also demonstrated that the sensitivity of this technique to Ge is too low to accurately study the distribution of this element.

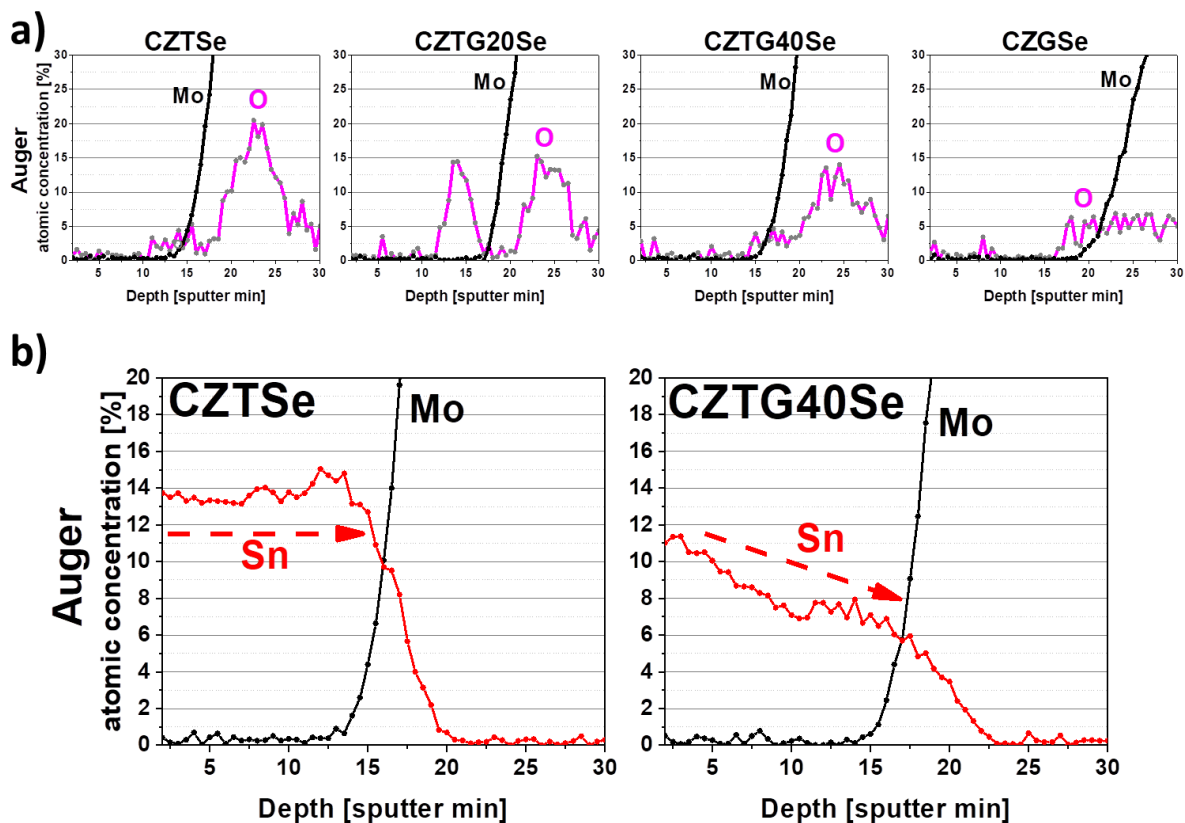


Figure 6.8.- a) Mo and O Auger atomic concentration signals for CZTSe, CZTG20Se, CZTG40Se and CZGSe absorber samples. **b)** Example of the Mo and Sn Auger atomic concentration signals for CZTSe and CZTG40Se samples.

Further relevant Auger spectroscopy related observations regarding the Se, Cu, Zn, Mo, and O signals can be highlighted from Figure 6.9:

- The Se and Cu “irregular” in-depth profile in the CZTG20Se point towards the possible presence of secondary phases.
- The abrupt Cu segregation at the back interface of the CZTG20Se sample may be related with the Na signal increment that can be observed in the full spectra in Figure 6.7.

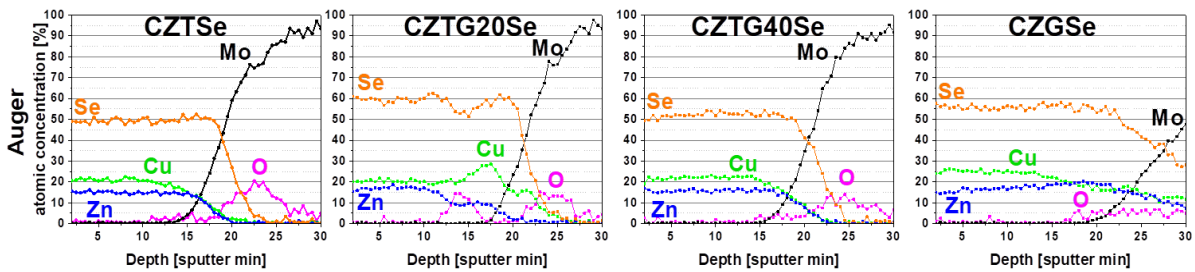


Figure 6.9.- Atomic concentration signals for Mo, Cu, Zn, Se and O by Auger spectroscopy of the four deposited CZTGSe thin films.

Despite providing useful “in-depth” information about the chemical composition (in particular, about species such as Na and O which are not trivial to detect by spectroscopic techniques), Auger and GDOES do not usually provide reliable information about the surface or the interfaces due to etching damage and layer roughness.

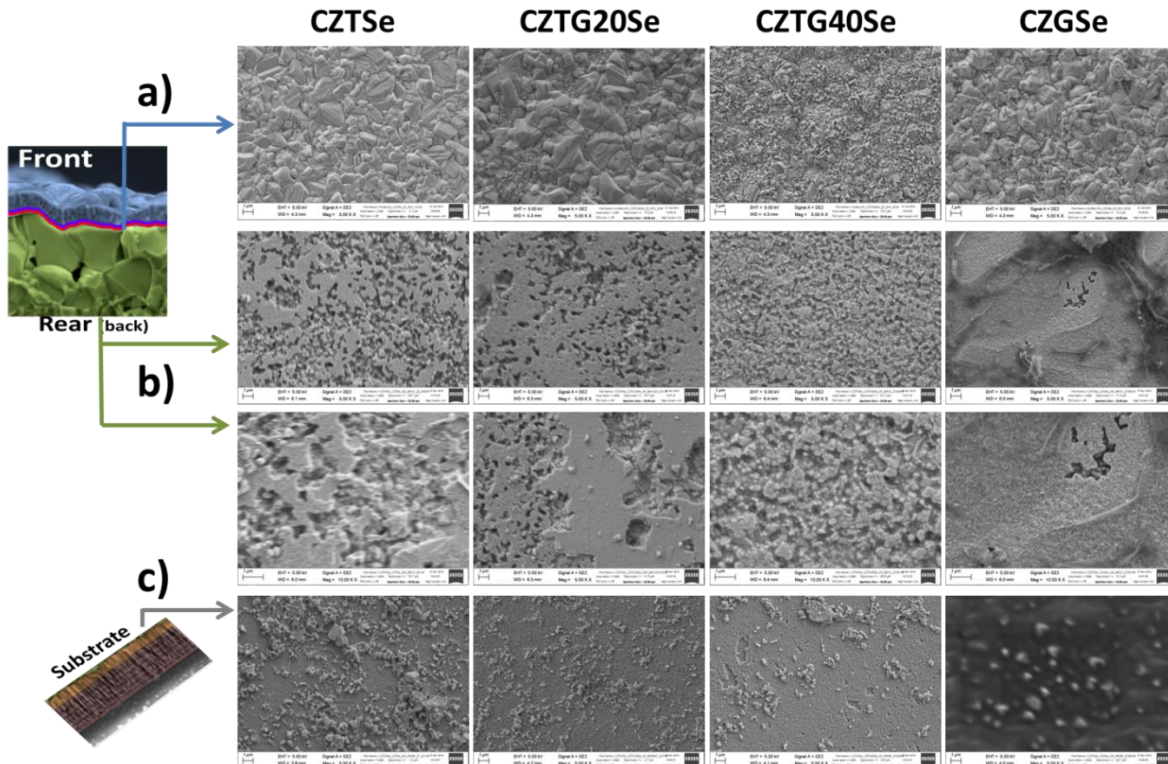


Figure 6.10.- a) SE2-SEM Planar-view of the **a)** Front, and **b)** Rear (back) interfaces after being by detached from the **c)** Substrate or back MoSSe_x/Mo back contact.

6.7 Structural and Compositional Analysis by Raman Spectroscopy

Raman spectroscopy measurements were performed on the samples to further investigate the surface and interfaces as well as the presence of secondary phases.

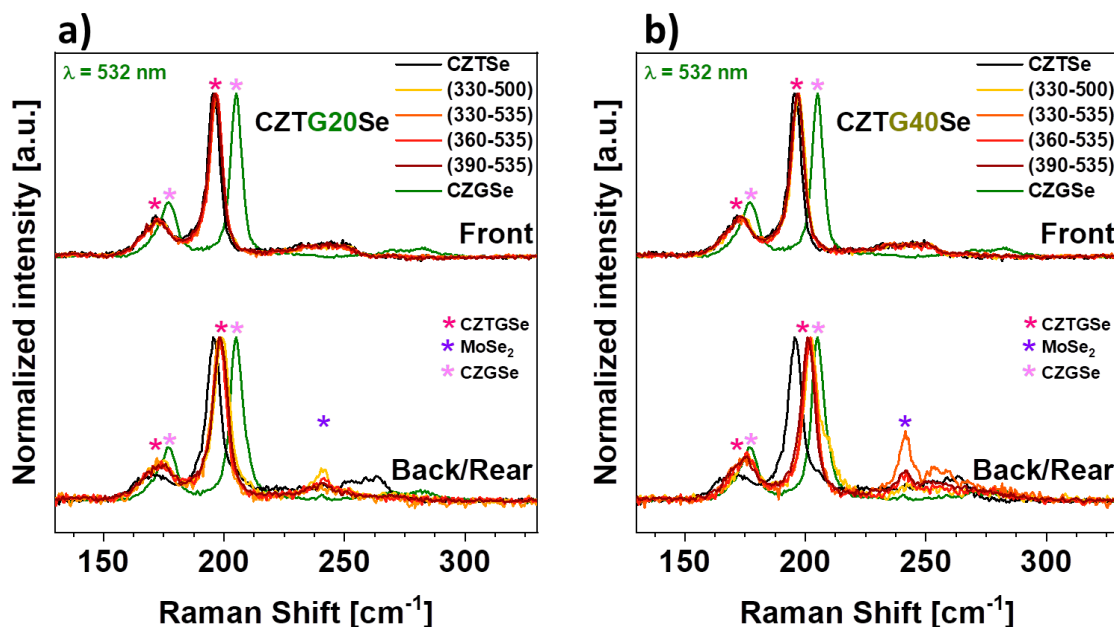


Figure 6.11.- Raman spectroscopy (532 nm) for the different (T_1 - T_2) annealing condition variations of the **a)** CZTG20Se and the **b)** CZTG40Se absorber materials. Different back bandgap profiles could be achieved by varying the (T_1 - T_2) thermal annealing conditions of the CZTGSe absorber synthesis.

In particular, in order to confirm the presence of a Ge gradient, an advanced multiwavelength (532 and 785 nm) Raman spectroscopy analysis was carried out both at the front side (air/CZTGSe interface) and, after a mechanical lift-off process¹⁹⁻²¹, at the rear side of all the processed films (See Figure 6.10).

The results are shown in Figure 6.12. On the other hand, Figures 6.11 and 6.12 show the Raman spectra of the different CZTGSe absorber materials. Both 785 and 532 nm lasers excitations were employed to analyze the samples due to their different penetration depths. However, since no clear differences in the vibrational Raman modes detected were found under both excitations, only the spectra obtained with the 532 nm laser are shown in the figures for the sake of clarity.

The spectra in Figure 6.12a show Raman bands that match very well with previous reports of CZTGSe polycrystalline thin films^{22,23}, in which no presence of secondary phases and a high crystalline quality is detected.

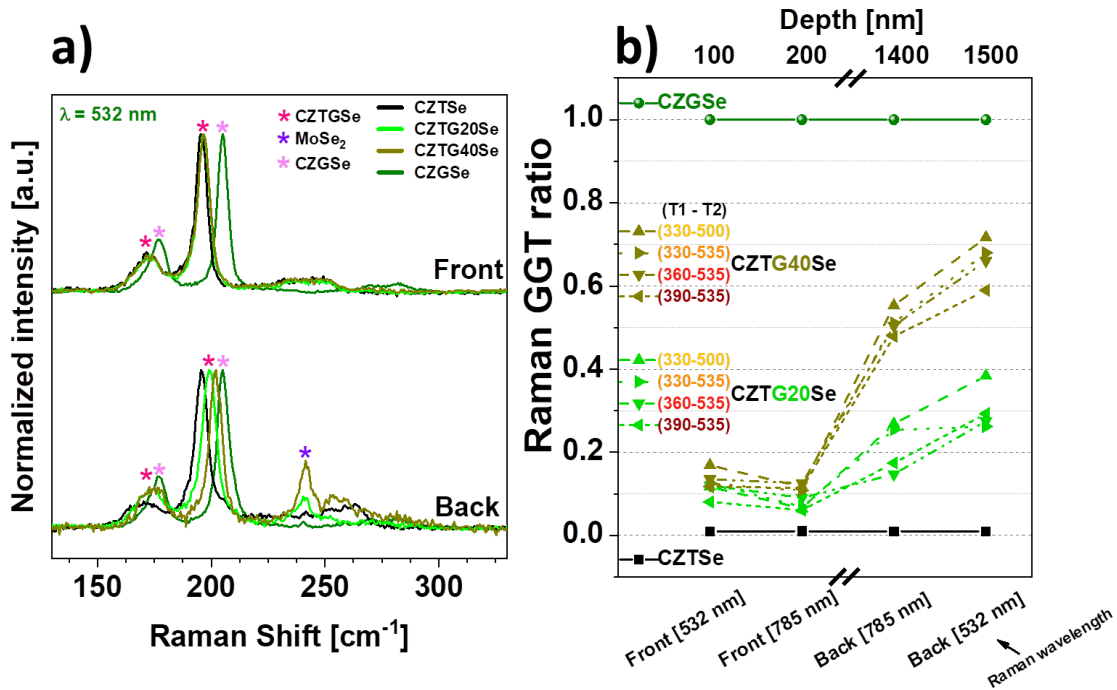


Figure 6.12.- a) Front and Back (after a mechanical lift-off process) 532 nm wavelength Raman spectroscopy of the CZTGSe absorber thin films. **b)** Front and back (rear) multiwavelength Raman spectroscopy of various CZTGSe absorber thin films. Different back bandgap profiles (GGT ratio) could be achieved by varying the (T1-T2) thermal annealing conditions (See Figure 6.11) of the CZTGSe absorber synthesis. Dashed and dotted lines serve just as a visual guide.

The fact that no prevalence of Ge-based secondary phases is observed at the back side of the films in Figure 6.12 combined with the results obtained by GDOES in which Ge content was found to increase towards the back interface (See Figure 6.11), allows concluding that this increase is due to Ge present in the kesterite matrix and not to Ge secondary phases. As such, it is thus possible to ascribe the Ge increase toward the back interface to a composition gradient existing within the film.

Moreover, these Raman results are consistent with the analysis of the XRD data (See Figure 6.5). A two mode (A1 and A2) behavior was found for most of the Raman bands.

However, the most intense band exhibited only a one mode behavior in the CZTGSe films. The Raman signals from the intense phonon symmetry mode (around 200 cm^{-1}) blue-shifts as the Ge content increases. The GGT ratio ($[\text{Ge}]/([\text{Ge}]+[\text{Sn}])$) of the absorbers at the front and back sides was estimated employing the following expression based on references^{22,23}:

$$\frac{[\text{Ge}]}{([\text{Ge}]+[\text{Sn}])} = \frac{\omega - 195.5}{9.4} \quad (\text{Eq. 6.1})$$

Where ω is the Raman band shift. Equation 6.1 empirically correlates the GGT ratio with the Raman signal resulting in a fast and non-destructive methodology for the estimation of the GGT ratio in CZTGSe solid-state solutions²². The estimated compositions are shown in Figure 6.12b and Table 6.1. The results indicate that the GGT ratio is different at the front and back sides for the CZTG40Se and CZTG20Se samples confirming the existence of a compositional Ge-grading in these absorbers. On top of that, it was found that the manipulation of the synthesis conditions (As it is shown in Figure 6.12b) also allows to deliberately engineer different graded rear bandgap profiles.

Table 6.1.- Front and Back GGT ratio derived from the multiwavelength Raman spectroscopy analysis of the CZTGSe absorber thin films. Different back bandgap profiles could be achieved by varying the ($T1-T2$) conditions of the CZTGSe absorber synthesis. *Considering experimental errors.

Sample	Annealing profile ($T1-T2$) [°C]	GGT compositional ratio			
		Front		Back	
Wavelength [nm] →		532	785	785	532
CZGSe	(330-480)	1	1	1	1
CZTG40Se	(330-500)	0.17	0.12	0.55	0.72
	(330-535)	0.12	0.11	0.51	0.68
	(360-535)	0.14	0.13	0.50	0.66
	(390-535)	0.12	0.11	0.48	0.59
CZTG20Se	(330-500)	0.12	0.07	0.27	0.38
	(330-535)	0.13	0.07	0.25	0.26
	(360-535)	0.12	0.09	0.15	0.28
	(390-535)	0.08	0.06	0.17	0.29
CZTSe	(400-550)	0.01*	0.01*	0.01*	0.01*

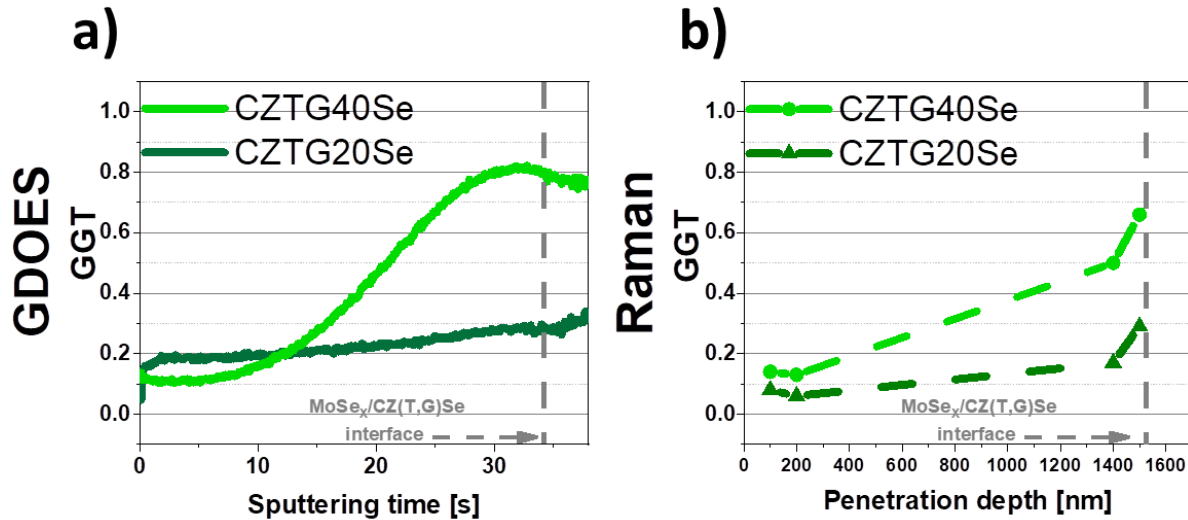


Figure 6.13.- a) GDOES vs. **b)** Raman spectroscopies derived (GGT = Ge/(Ge+Sn) ratios comparison for CZTG20Se and CZTG40Se absorber samples.

As it could be clearly observed, Figure 6.13 shows a strong correlation between the GGT ratios calculated from the Raman data and the ones directly measured by GDOES spectroscopy.

Since Raman is a structural sensitive technique, the predicted cationic compositions are found to be incorporated in the kesterite crystalline structure matrix.

6.8 Fabrication and Analysis of CZTGSe Solar Cell Devices

Once the presence of a Ge-grading at the back of the absorbers has been demonstrated, its influence on photovoltaic performance was investigated in completed solar cell devices.

The main optoelectronic parameters of the different samples and the illuminated *JV* curves of the best solar cells are depicted in Figure 6.14.

Additionally, Table 6.2 shows the optoelectronic parameters of the best devices obtained in each sample.

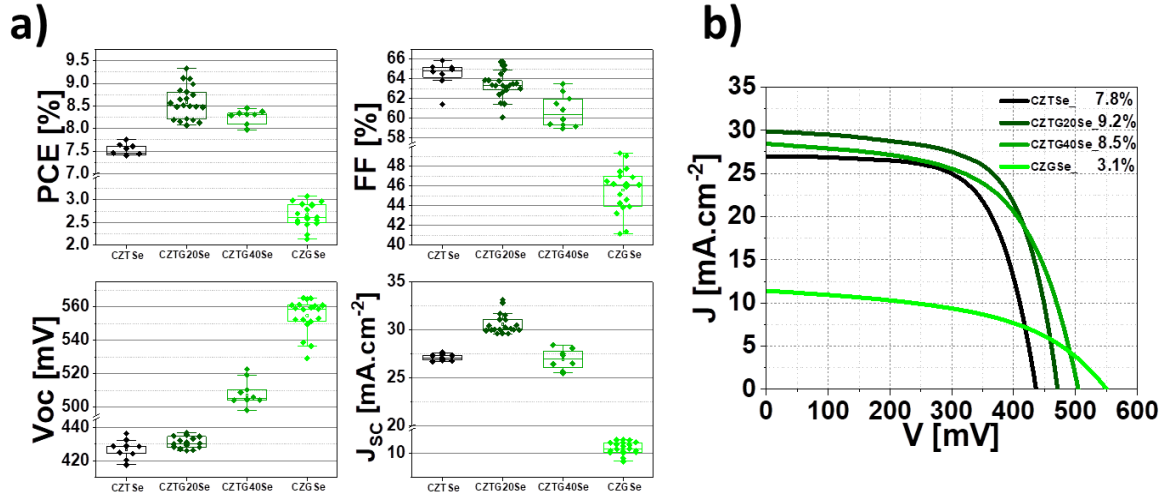


Figure 6.14.- a) Boxplots of the optoelectronic parameters and b) 1 Sun illuminated JV curves of the best behaved SLG/Mo/MoSe_x/CZ(T,G)Se/CdS/ZnO:i/ITO thin film solar cells.

Table 6.2.- Measured optoelectronic parameters (J_{SC} , V_{OC} , FF , and PCE), dark curve derived device parameters (n , R_S , R_{SH} , J_0), bandgap (E_G), $V_{OC,SQ}$ deficit and the short circuit current density (J_{SC}) calculated from the IQE values of the best behaved SLG/Mo/MoSe_x/CZ(T,G)Se/CdS/ZnO:i/ITO thin film solar cells. The dark JV curve of the CZGSe sample could not be properly fitted with a one diode model.

Best device	J_{SC} [mA· ⁻² cm]	V_{OC} [mV]	FF [%]	PCE [%]	n	R_S [Ω· ⁻² cm]	R_{SH} [kΩ· ⁻² cm]	J_0 [mA· ⁻² cm]	E_G [eV]	$V_{OC,SQ}$ deficit [mV]	Integra- ted J_{SC} [mA· ⁻² cm]
CZTSe	27.0	436	65.9	7.8	1.63	0.645	3.13	5.8×10^{-4}	1.05	377	29.7
CZTG20Se	29.9	471	65.1	9.2	1.70	0.246	0.61	1.2×10^{-3}	1.12	408	30.6
CZTG40Se	28.4	504	59.0	8.5	2.08	0.569	0.32	9.4×10^{-4}	1.14	393	29.3
CZGSe	11.4	550	49.3	3.1	-	-	-	-	1.46	653	14.9

As it was expected, higher open circuit voltage (V_{OC}) values were obtained with the increasing Ge content. Conversely, an opposite behavior is observed for the fill factor (FF) of the CdS/CZTGSe solar cells. This fact can possibly be attributed to resistive effects, in particular to a one order of magnitude in R_{SH} difference between CZTSe and CZTGSe samples (See Table 6.2).

Additionally, FF's behavior strongly correlates with the morphological evolution (See Figure 6.4) and with a possible worsening of the band alignment with the CdS buffer layer for alloys with Ge contents above 20%.²⁴

On the other hand, the short circuit current density (J_{SC}) values show a maximum value for sample CZTG20Se, followed by CZTG40Se. In both cases, the J_{SC} is higher than for the pure CZTSe (reference) and CZGSe samples, suggesting a positive impact of Ge-grading in kesterite solar cells through the creation of a back surface field (BSF) effect. Figure 6.14a shows that the power conversion efficiencies (PCE) follow the order: CZTG20Se($\approx 9.0\%$)>CZTG40Se($\approx 8.5\%$)>CZTSe($\approx 8.0\%$)>CZGSe($\approx 3.0\%$).

This trend indicates a performance improvement of the solar cell from the partial substitution of Sn by Ge with a record value obtained for 20% substitution. The optoelectronic properties of the best CdS/CZTGSe solar cell devices were further studied by means of external quantum efficiency (EQE, See Figure 6.15a) and biased voltage quantum efficiency ratio ($QE(-1V)/QE(0V)$, See Figure 6.15b) analyses.

The J_{SC} of the devices was also calculated from the integration of the EQE curves. In the case of the non-alloyed CZTSe the J_{SC} values obtained from the JV characterization are $\geq 90\%$ of those obtained from EQE.

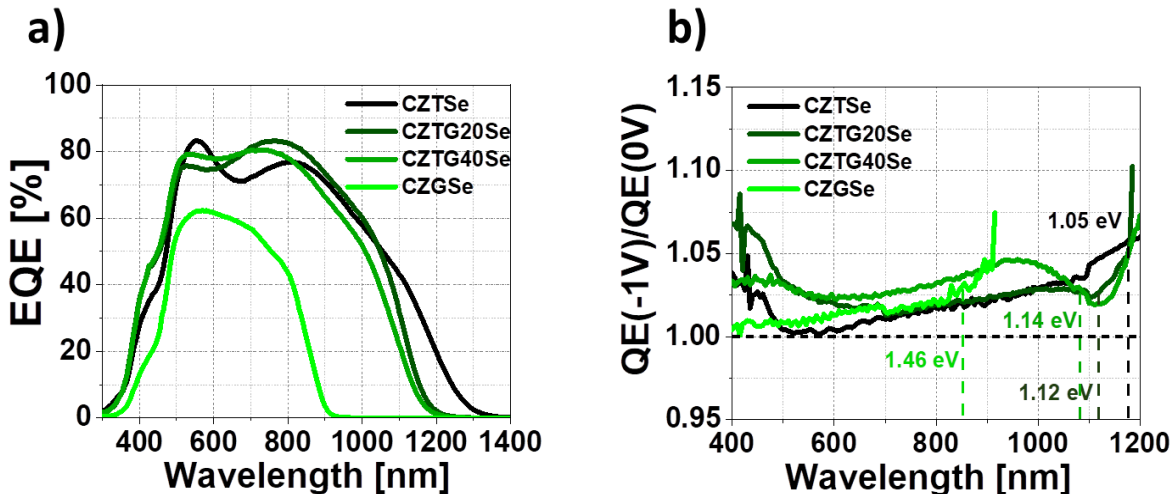


Figure 6.15.- a) External Quantum Efficiency (EQE) curves and biased voltage ($QE(-1V)/QE(0V)$) quantum efficiency ratio **b)** of the best behaved SLG/Mo/MoSe_x/CZ(T,G)Se/CdS/ZnO:i/ITO thin film solar cells. Bandgap (E_G) values are depicted in **b)**.

For the Ge alloyed samples, CZTS20Se and CZTG40Se, this value exceeds 95% while in the case of CZGSe this value is just around 75%. In this sense, the simultaneous increase of J_{SC} value, despite the bandgap increments in the Sn-Ge alloyed samples strongly suggest a back surface field reflector effect. The diode parameters extracted from the fitting (not shown) of the corresponding dark JV curves are also presented in Table 6.2. After the analysis results, the following observations can be highlighted:

- Ideality factor (n): It is comprised between 1.63 and 2.08 and increases with the increasing GGT ratio. This observation together with the admittance spectroscopy studies (later shown in Figures 6.18 to 6.21), suggests that the devices suffer from recombination within the SCR which correlates with the fill factor (FF) values observed between the different samples indicate it is not a limiting factor for the devices.
- Series resistance (R_S): the low differences ($0.25 \Omega \cdot \text{cm}^2$) observed between the different samples indicate it is not a limiting factor for the devices.
- Shunt resistance (R_{SH}): CZTSe device shows a 5-10 times higher value than the other samples. Since R_{SH} is related to the existence of a back interconnection, this parameter can be considered to be mostly related to fabrication issues rather than intrinsically linked to design of the heterostructure. This way, the differences observed might be explained by Ge inclusions generating electronic pathways bypassing the pn junction.
- Reverse saturation current (J_0): This parameter is mostly related to carrier recombination, often within the space charge region (at either sides of the junction) ²⁵ and mostly affects the voltage of the cells, which directly influences the V_{OC} deficit shown in Table 6.2. The values reported in this work are inconclusive in that regard, and temperature dependent characterizations would be more appropriate for the specific study of recombination processes.

Furthermore, Figure 6.15b represents the bandgap (E_G) values calculated from the $d(QE)/d(\lambda)$ curves. As expected, higher bandgap (E_G) values were obtained with the higher Ge content of the samples. Therefore, the $V_{OC,SQ}$ deficit $\left(\frac{E_{G,SQ}}{q} - V_{OC}\right)$ where q stands for the elemental charge, was calculated for the different devices. V_{OC} deficit values of ≈ 400 mV were obtained for the CZTSe, CZTG20Se, and CZTG40Se samples while a significantly higher value, (≈ 650 mV) was obtained for the CZGSe device (See Table 6.2).

In addition, the $QE(-1V)/QE(0V)$ ratio (See Figure 6.15b) presents increasing values with the increasing Ge-content at wavelengths above 700 nm, suggesting that the space charge region (SCR) width (W) has a pronounced effect on charge collection in the long spectral wavelength region (Between 5% and 10% deviation depending on the GGT ratio).

Moreover, the ratio of EQE response under the -1V and +0.3V (See Figure 6.16) range depicts the extent of the influence of W on charge collection.

The $EQE(-1V)/EQE(0V)$ ratio values of the Ge-content increasing cells rise more rapidly at wavelength values beyond 700 nm, suggesting W has more pronounced effect on charge collection of the cell in the long spectral wavelength region, i.e. in the region close to the rear contact, far from the junction.

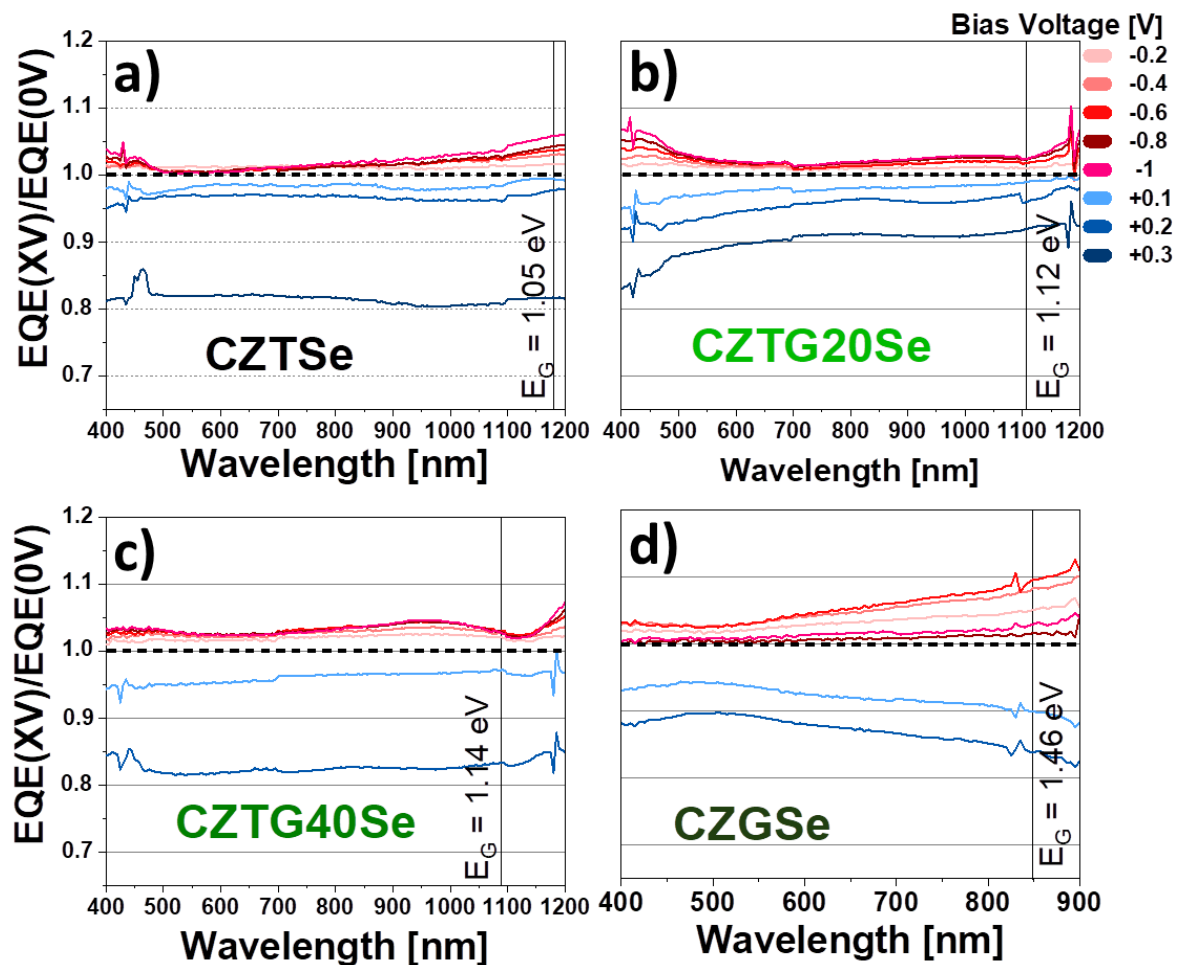


Figure 6.16.- Voltage biased (-1V to +0.3V) EQE curves for each best behaved a) CZTS, b) CZTG20Se, c) CZTG40Se, and d) CZGSe kesterite solar cell device.

On the other hand, Figure 6.17a shows the reflectance curves of the SLG/Mo/MoSe_x/CZ(T,G)Se/CdS/ZnO:i/ITO solar cells. The ratio of EQE response under the (-1 to +0.3)V range reflects the extent of the influence of the SCR width on the charge collection. Similar spectral positions of the reflectance maxima can be observed for the four devices studied with just slight shifts towards shorter wavelengths for the pure CZGSe and alloyed CZTGSe samples with respect to the pure CZTSe solar cell device.

However, a pronounced shift is detected for one of the maxima which appears at 700 nm for the pure CZTSe devices and is shifted towards 600 nm for the alloyed CZGSe devices. Conversely, there is observed an overall 5% reflectance intensity reduction at 500 nm when Ge present in the CZ(T,G)Se crystalline structures.

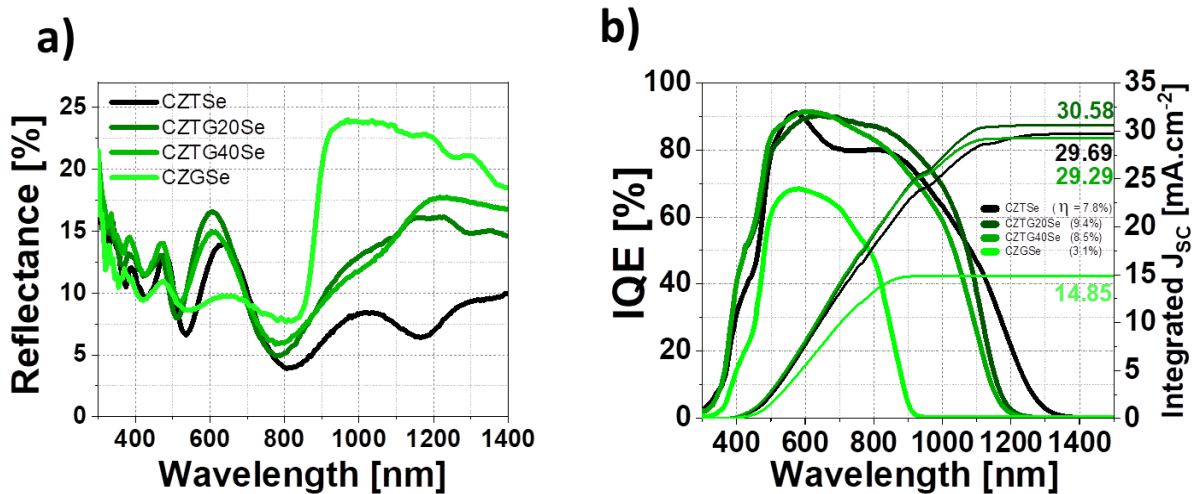


Figure 6.17.- a) Reflectance and b) Internal Quantum Efficiency (IQE) curves of the best SLG/Mo/MoSe_x/CZ(T,G)Se/CdS/ZnO:i/ITO thin film solar cells.

Both EQE (Figure 6.15a) and IQE (Figure 6.17b) curves show that the CZTG40Se sample has a steeper slope near the absorption edge, which serves as an indication of a better carrier collection at the vicinity of its bandgap, in the 800 – 1100 nm region, as compared to the other samples. Since this sample possesses the steepest conduction band gradient, this result is consistent with a stronger back surface field effect.

In terms of quantum efficiency, CZTG40Se seems like the best device. But this result is offset by its poor *FF* which can be attributed to a degradation of its diode properties as a consequence of the high Ge content that degrades the diode properties.

Therefore, it should be highlighted that there appears to be a “trade-off” between a strong BSF and good diode properties.

This would be the reason why the CZTG20Se yields the highest conversion efficiency since it would benefit from the BSF effect and not present Ge-induced diode degradation. In this way, Figure 6.18 shows the frequency-voltage swept impedance spectroscopy measurements of the CZTGSe absorber layers.

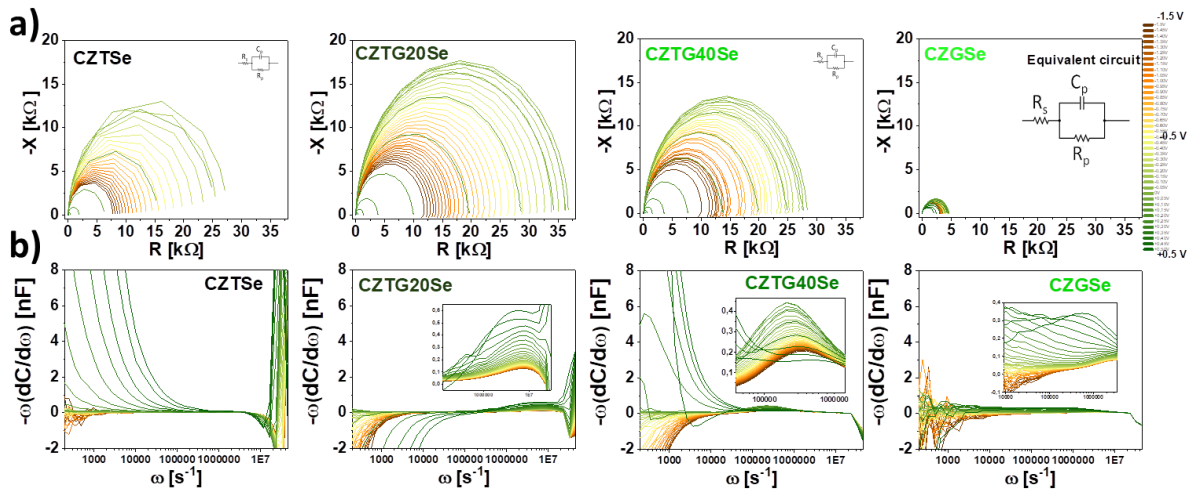


Figure 6.18.- Frequency-voltage swept impedance spectroscopy measurements of the CZTGSe absorber layers.

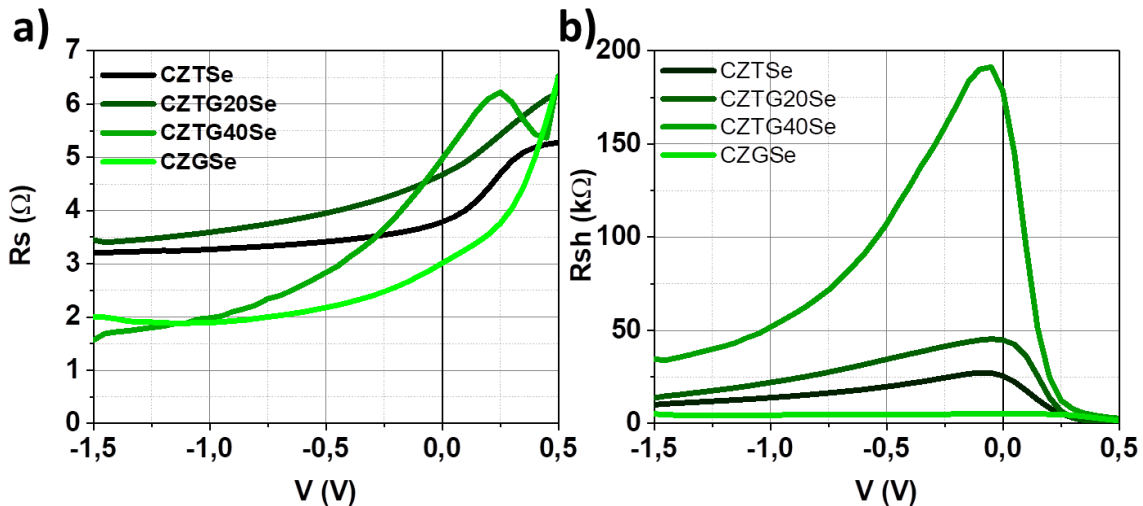


Figure 6.19.- a) Series and b) Shunt Resistances calculation derived from the impedance measurements.

Any significant differences are found for the CZTSe, CZTG20Se, and CZTG40Se solar cells with all of them showing values around ($1E+15 \text{ cm}^{-3}$ to $9E+15 \text{ cm}^{-3}$ at no bias voltage). However, the CZGSe device exhibits charge carrier density values one order of magnitude lower. Additionally, the calculations of the series and shunt resistances derived from the impedance measurements (See Figure 6.19), clearly show that even if the Sn-Ge alloying (CZTG20Se and CZTG40Se) introduce a slightly higher series resistance (See Figure 6.19a) referenced to the CZTSe device.

A ludicrously ten-fold increasing in the shunting is observed (See Figure 6.19b) when adding a 20% of Ge to the alloyed kesterite material (CZTG20Se).

By analyzing the minority charge carrier dependence for with SCR width (W) of CV measurements at defect-influence avoiding frequencies (See Figure 6.20b), significantly differences are observed at 0V between the different samples with the following tendency:
 $W_{CZGSe} > W_{CZTG40Se} > W_{CZTG20Se} > W_{CZTSe}$.

Moreover, by calculating the available free vs. trapped carriers (See Figure 6.21), it was found that the density of traps increases towards the front interface only in the case of the CZTSe sample.

Therefore, it can be concluded that the grains of the CZTG20Se sample present a better photogenerated carrier collection properties as compared to the CZTSe absorber layer.

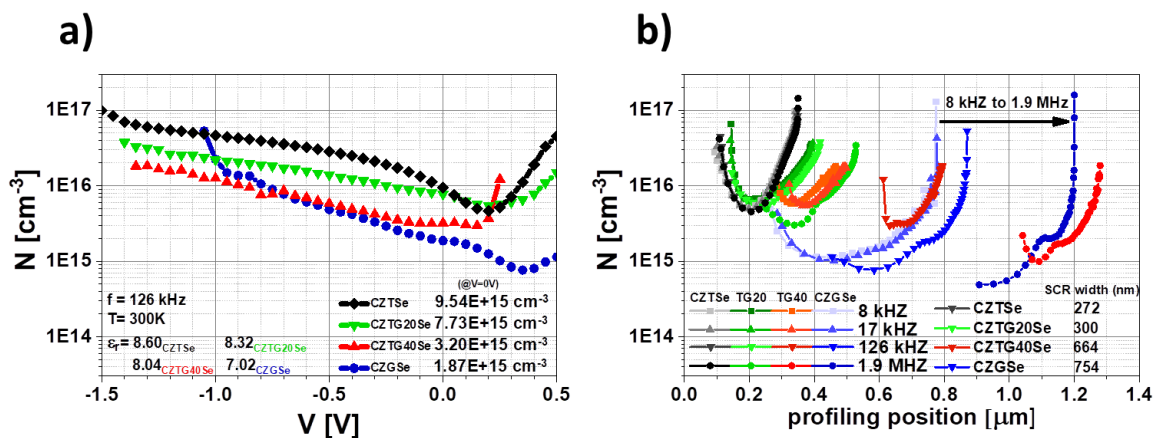


Figure 6.20.- a) Minority charge carrier density (N) vs. voltage. **b)** N vs. profiling positioning of the best SLG/Mo/MoSe_x/CZ(T,G)Se/CdS/ZnO:i/ITO thin film solar cells.

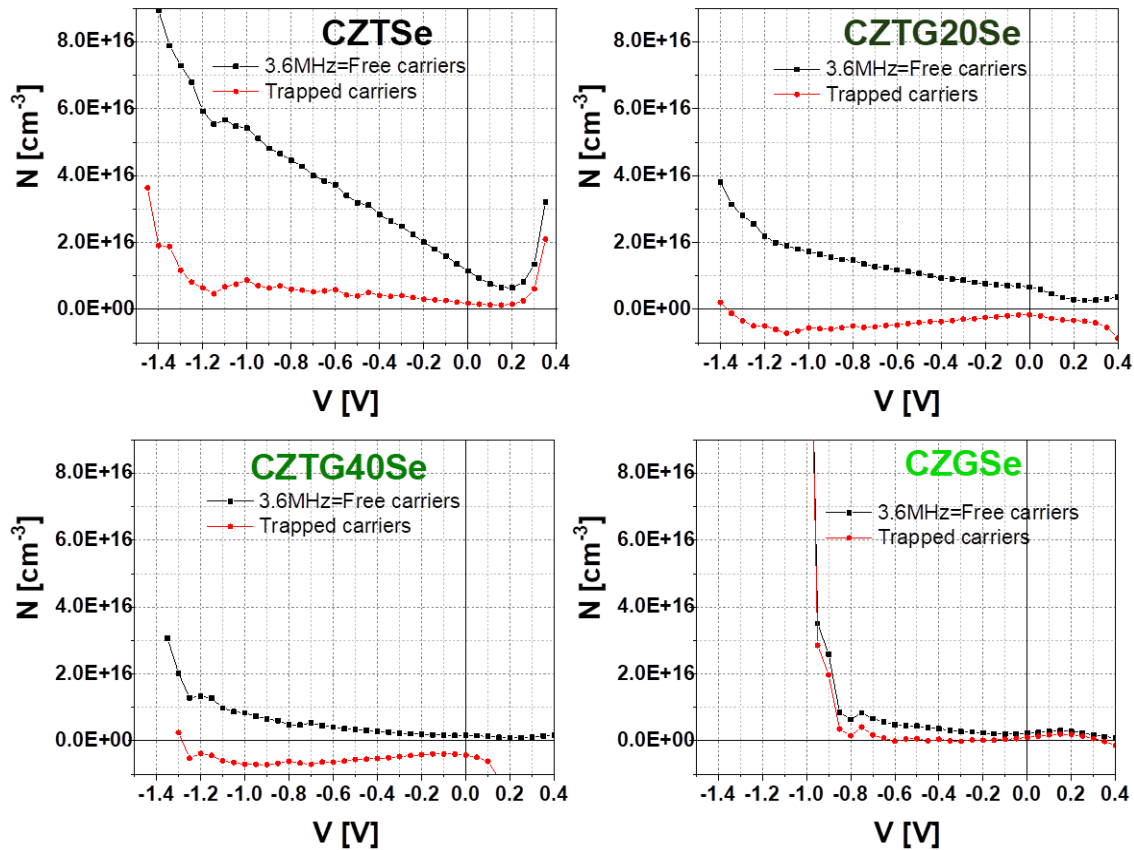


Figure 6.21.- Available free vs. trapped carriers determination for the different SLG/Mo/MoSe_x/CZ(T,G)Se/CdS/ZnO:i/ITO devices on the voltage vs. minority carrier density plots.

From Figure 6.21, it could be appreciated that the density of traps increases towards front interface apparently just for the CZTSe film, rather than «follow High frequencies, it virtually “decreases” for the trapped carriers (low frequencies) mostly sure due to an evidenced BSF. Finally, and for the sake of providing an unequivocal confirmation of a Ge back grading in the champion CdS/CZTG20Se solar cell device achieved in this work, further elemental spatial composition distribution analysis was carried out by means of cross-sectional high-angle annular dark-field scanning transmission electron microscopy (HAADF-STEM) images as an EDX compositional mapping, presented in Figure 6.22. The cross-sectional HAADF-STEM micrograph shows a similar void formation to that observed by SEM (See Figures 6.3 and 6.4). However, Ge-rich precipitates with a diameter of ~10 nm are observed at the rear side of the device which indicates that the morphology within the CZTG20Se absorber layer is less homogenous than for the Ge-free CZTSe sample.

In addition, two distinct grain morphologies and sizes are observed along the thickness of the absorber in the cross-sectional HAADF-STEM micrograph of the CZTG20Se absorber.

The main compositional difference between these two types of grains lies at the Ge content, with the smaller grains at the rear possessing a higher Ge content with respect to the larger grains at the front.

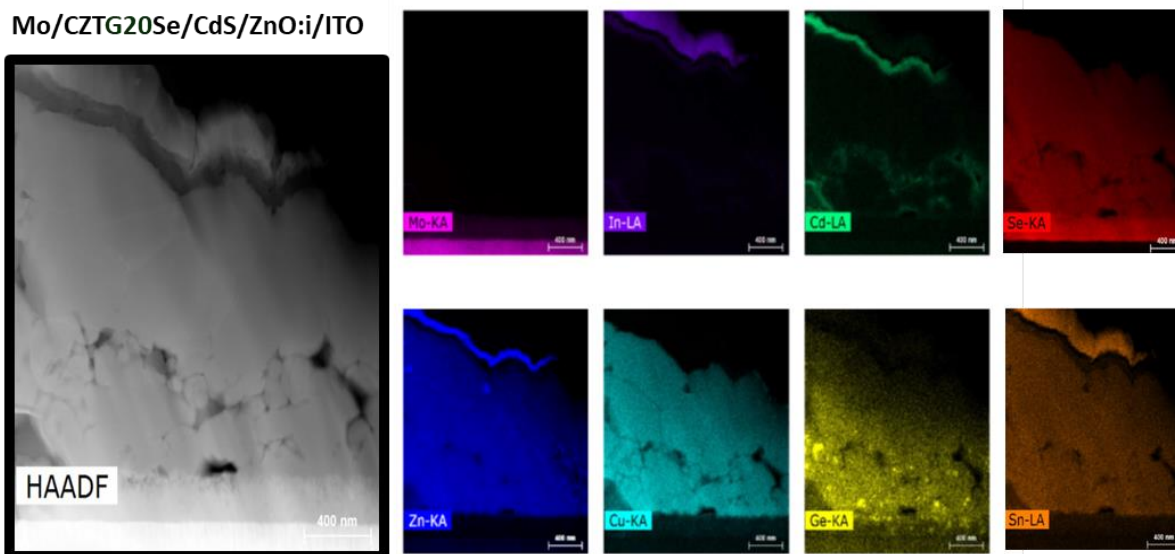


Figure 6.22.-Cross-Sectional HAADF-STEM micrographs and EDX compositional mapping of the champion SLG/Mo/MoSe_x/CZTG20Se/CdS/ZnO:i/ITO solar cell device.

Figure 6.22 also reveals that some of the grains are separated by Zn rich and Cu poor grain boundaries. Zn_{Cu} defects at the grain boundaries may be detrimental for the solar cell performance²⁶. Similarly, the presence of ZnSe-rich precipitates can be observed inside the larger at the front and Cd clusters (with a possible Ge enrichment) are found to aggregate on the walls of voids at the vicinity of the back contact. The latter indicates a possible detrimental migration of elements from the buffer layer along the grain boundaries of the absorber. The two types of grains observed at the front and the bottom of the sample seem to be interconnected by a third type of smaller round shaped grains, similar to those observed at the MoSe_x/CZTG20Se interface.

Finally, the HAADF-STEM analysis also reveals a possible segregation of Ge, GeO_x, and/or Cu₂GeSe₃ precipitates at the back interface of the device.

6.9 Chapter VI, Part III, Case A Main Conclusions

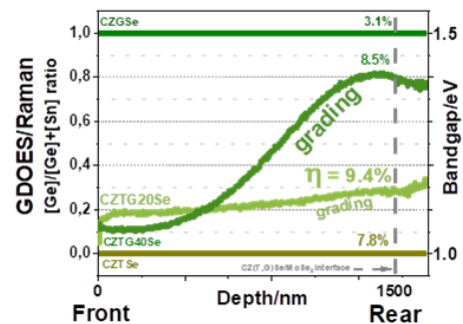
The STEM results confirm and expand all the previous conclusions made on the morphological, structural and compositional characteristics of the rear Ge grading in CZTGSe solar cells.

Moreover, its accurate relation with the spectroscopic techniques such as Raman spectroscopy provides a fast, non-destructive and reliable characterization technique for graded bandgap analysis. It was demonstrated that compositionally graded CZTGSe thin films might be favorable for reducing recombination towards the back contact.

In this regard, the feasibility of back side Ge grading, and a subsequent BSF effect, is unequivocally demonstrated in kesterite absorbers.

Material and electrical characterizations demonstrate that the inclusion of Ge in the matrix can also bring detrimental elements in the form of secondary phases or precipitates, and a fine tuning of the composition is necessary to improve the performance of the devices. A soft alloying with 20% Ge content is found to be the sweet spot in our experiments, with a BSF effect strong enough to improve the carrier collection while preserving the diode properties.

These results pave the way for a future complete band engineering strategy in kesterite absorbers, including both conduction and the valence band of the material. Finally, it is noteworthy to remark that in the case of Ga grading in CIGSe, the best devices only have a relatively small amount of Ga (20% or less)^{27,28}, and Ge in Kesterite seems to behave quite similarly.



Chapter VI

Results Part III, Case B:

Dual Anionic and Cationic Bandgap Grading Profiles in Kesterite

Conclusively from Chapter IV, it has been numerically modeled by mathematical simulations and later experimentally demonstrated in Chapter V, that by employing a disruptive and novel methodology based on the introduction of S pulses during the selenization process of CZTSSe, it was feasible to demonstrate that complex sharp anionic compositional gradients in kesterite might naturally occur when working in far from equilibrium conditions, that is, during the cooling down of the kesterite structures' recrystallization step.

Any attempt to selectively introduce sulfur during the synthesis or crystallization steps leads to a quasi-uniform complex in-depth anionic profile. Bearing this in mind, the influence of different sulfur sources including elemental S, thiourea, SnS, and SeS₂ were explored and classified them with regard to their predicted reactivity.

In this regard, it was found that the sulfur sources identified as more reactive, elemental S and thiourea, lead to sharper S/(S + Se) surface gradients with almost 30% and 20% more sulfur at the surface with respect to the bulk, respectively. In addition, the overall S quantity in the bulk is also higher, with a stabilized S/(S + Se) ratio around 0.2.

The presence of compositional gradients was confirmed using different techniques. The use of less reactive species such as SeS₂ and specially SnS leads to smoother compositional profiles and mainly to a lower S content in the bulk, with a S/(S + Se) ratio down to 0.1.

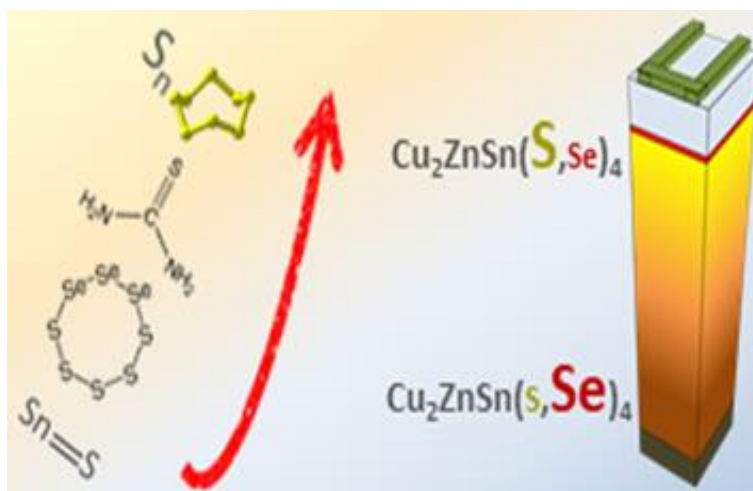


Figure 6.23.- Chapter V: Is It Possible To Develop Complex S–Se Graded Bandgap Profiles in Kesterite-Based Solar Cells? ²⁹

In agreement with the expected positive effect of these gradients on the solar cell performance, best devices are obtained with the samples exhibiting the sharpest anionic compositional profiles reaching efficiencies > 9% efficient devices with V_{OC} deficits amongst the lowest value so-far reported in literature.

Particularly, this work has demonstrated that the use of sulfur pulses during out of thermodynamically equilibrium conditions in the CZTSe system is a promising route for creating sharp anionic S/(S + Se) compositional gradients, which are key for the development of bandgap engineering in kesterite solar cells (The order out of chaos). ³⁰

On top of that, expanding the application range; this work developed sulfo-selenization methodology was successfully applied and positively impacted in other chalcogenides, rather than just for kesterite structured materials (See Thesis Appendix: Additional and Supporting Information).

On the other hand, the main conclusions of Chapter VI, Part III.A indicate and provide general insights into the feasibility of naturally generating complex back cationic (Sn-Ge) graded bandgap profiles in $Cu_2Zn(Sn_xGe_{1-x})Se_4$ absorber materials by a conventional thermal process. Such profiles have been obtained by varying the Sn and Ge layer thicknesses of the precursor material, leading to several graded compositions and bandgap profiles in the resulting absorbers (See Figure 6.24).

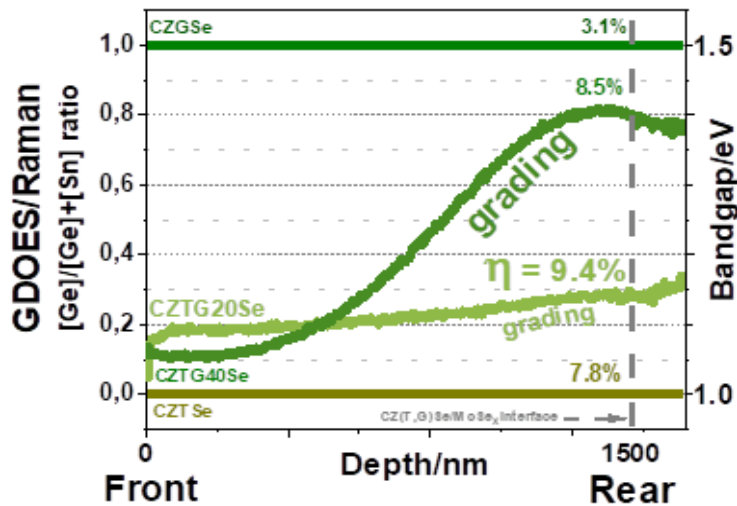


Figure 6.24.- Chapter VI: Rear Bandgap Grading Strategies on Sn–Ge Alloyed Kesterite Solar Cells.³¹

Moreover, a fine control of the grading at the back side of the absorbers is demonstrated by adjusting the conditions of the thermal reactive annealing. Using various composition analysis tools such as Auger, GDOES, and Raman spectroscopies, as well as the HAADF-STEM images, a ‘natural’ segregation of Ge atoms at the back interface of the films was demonstrated, though possible detrimental compounds are also observed.

The electrical characterization by means of current voltage analysis and IQE analysis revealed that a conversion efficiency without any antireflection coating or metallic grids around 10% in PCE ($J_{SC} \approx 30 \text{ mA}\cdot\text{cm}^{-2}$ and $V_{OC} > 470 \text{ mV}$) could be performed by a soft rear grading with Ge, optimizing the trade-off between back surface field effect and detriments from the Ge inclusion. Additionally, the admittance spectroscopy and capacitive analysis revealed that a slight substitution of Sn by Ge leads to an increased space charge region width without affecting the charge carrier density.

Finally, the structural characterization analysis along with the recorded optoelectronic parameters in the CZTGSe solar cell devices demonstrate an improved carrier collection improvement from the additional drift electric field, leading to a substantial increase in the J_{SC} values from the inhibition of recombination at the back contact side. This way, demonstrating that bandgap profile engineering can potentially lead to improved photovoltaic performances in kesterite thin film solar cells.

6.11 Experimental Double Graded U-Shaped Bandgap in CZTGSSe Solar Cells

One of the most advanced skills in contemporary western civilization is dissection: the split-up of problems into their smallest possible components. As humans, we became good at it. So good, we often forget to put the pieces back together again. This skill is perhaps most finely honed in science. There we not only routinely break problems down into bite-sized chunks and mini-chunks, we then very often isolate each one from its environment by means of a useful trick.

It is often said: *cæteris pãribus*- all other things being equal. In this way, it is possible to ignore (or not) the complex interactions between our specific dialogue with Nature and the rest of the Universe.³⁰

In this regards, thin film absorber layers were fabricated by the sputtering metallic layer sequential process (Chapter VI part III.B) developed at IREC along with this Thesis developed thermal annealing process the generation of complex sharp graded anionic compositional profiles (See Chapter V). Particularly, a described Cu/Sn/Cu/Zn/Ge precursor structures were deposited on Mo-coated soda-lime glass (SLG) substrates.

The sputtered Sn and Ge layer thicknesses were adjusted to produce a 20%Ge–80%Sn (GGT = 0.2) CZTG precursor (See Chapter VI part III.A) alloyed material (See Figure 6.25a). Therefore, by applying the adequate chalcongization process (See Chapter V), the CZTGSSe kesterite absorber material has been completed (See Figure 6.25b). On the other hand, compositional distribution throughout the whole thickness of the CZTG precursor (See Figure 6.26a) and CZTGSSe absorber (See Figure 6.26b) materials was investigated by means of glow discharge optical emission spectroscopy (GDOES).

For this case, dual front anionic ($S/(S+Se)$) and rear cationic ($Ge/(Ge+Sn)$) graded compositions are clearly observed with both S and Ge contents increasing (along with Sn and Se contents respectively decreasing) toward the back side of the CZTGSSe absorber thin film. This Thesis developed and employed material engineered routes, not only results in good quality absorbers with different controlled compositions but also enables the generation of an effective and reliable both S-Se and Ge-Sn compositional grading profiles at the at front and back interfaces, respectively.

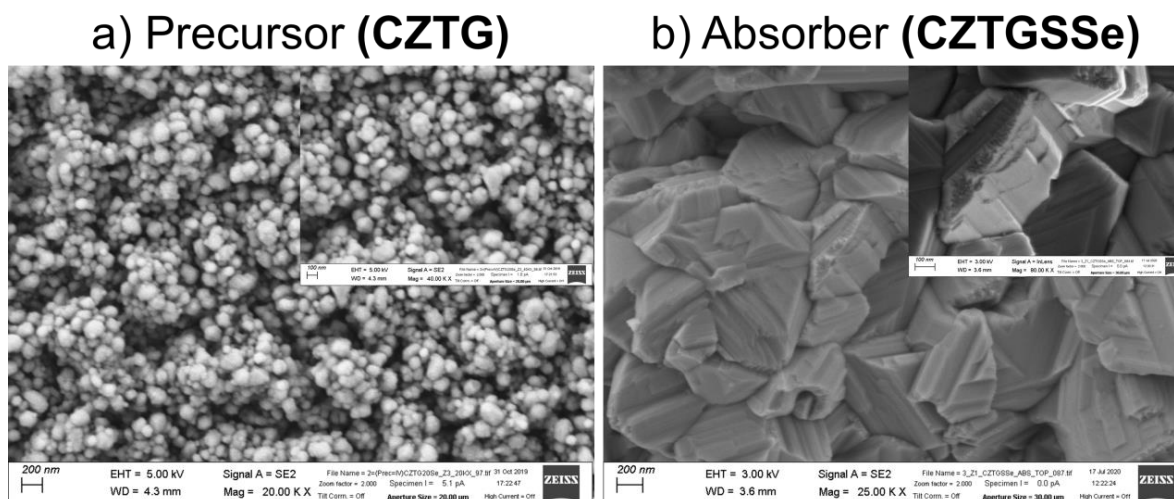


Figure 6.25.- Planar (Top) view SEM micrographs of the **a)** Precursor CZTG and **b)** Absorber CZTGSSe kesterite thin film materials.

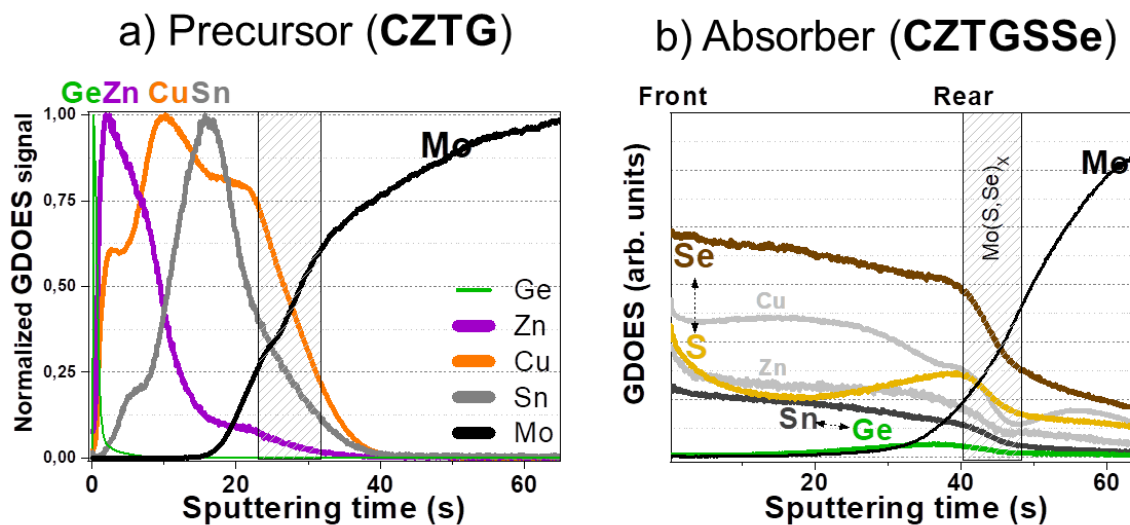


Figure 6.26.- **a)** CZTG Precursor GDOES of the Ge, Zn, Cu, Sn and Mo signals vs. sputtering time. **b)** CZTGSSe Absorber GDOES of the Ge, Zn, Cu, Sn, S, Se and Mo signals vs. sputtering time.

The main kesterite structural characteristics of the samples were revealed by multiwavelength Raman spectroscopy (See Figure 6.27). Therefore, by combining both GDOES and Raman spectroscopy it was allowed to further indulge on the surface and interfaces as well as the presence of a double graded bandgap in the CZTGSSe thin film kesterite absorber material.

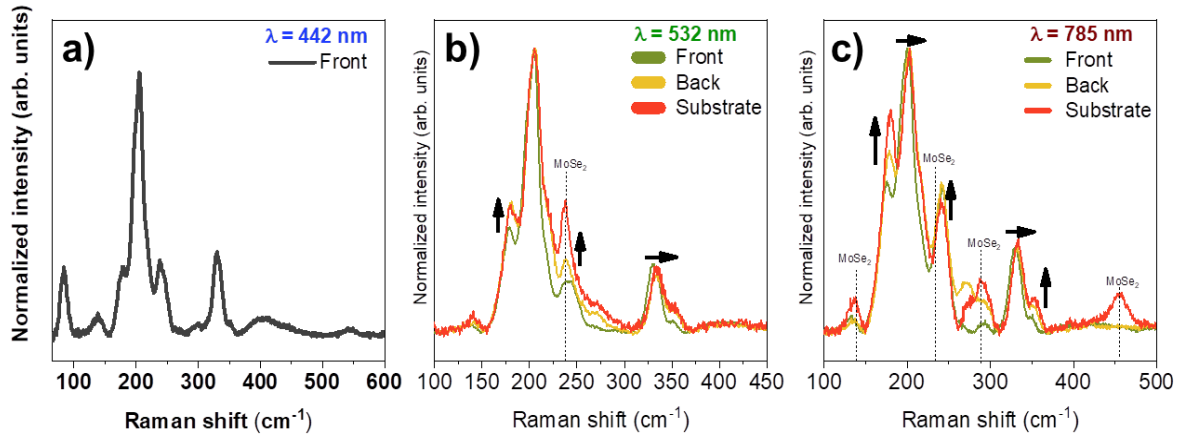


Figure 6.27.- Multiwavelength Raman spectroscopy **a)** 442 nm **b)** 532 nm, and **c)** 785 nm for the double graded U-Shaped bandgap absorber material (CZTGSSe) at front, back, and substrate interfaces (See Section 5.6.2).

In order to confirm the presence of both S-Se and Ge-Sn composition al gradients, an advanced multiwavelength Raman spectroscopy analysis was carried out both at the front side (Air/CZTGSSe interface) and, after a mechanical lift-off process,^{19–21} at the rear side of all the processed films (See Figure 6.27). 442, 785 and 532 nm wavelength lasers excitations were employed to analyze the samples due to their different penetration depths. Particularly, the 442 nm Raman analysis (See Figure 6.27a) aimed to demonstrate the non-existence of superficial ZnSe secondary phases. Also, the 532 nm Raman analysis (See Figure 6.27b) reveals a U-shape for S signal in GDOES (See Figure 6.26b). On top of that, 785 nm analyses (See Figure 6.27c) confirms a higher content of Se than S, along with a front-to-rear Ge enrichment in the entire CZTGSSe absorber sample.^{20,23}

Additionally, the spectra shown in Figure 6.27 demonstrate Raman bands that match very well with previous reports of CZTGSSe polycrystalline thin films, in which no presence of secondary phases and a high crystalline quality is detected.^{32,33} In this way, these results suggest that both anionic (SSe) and cationic (GGT) ratios are distinct at front and back interfaces for the synthesized CZTGSSe crystalline structure. In before, this Thesis has demonstrated the manipulation of the synthesis conditions allow to separately tune front (See Chapters IV and V) and rear (See Chapter VI) grading bandgap profiles. However, this (Chapter VII) results confirm the feasibility of combining both (front and back) strategies in order to engineer a double graded U-Shaped bandgap profile on kesterite (CZTGSSe) based thin film solar cells.

Figure 6.28 shows a comparison of the Raman spectroscopy signals of distinct kesterite (CZTSe= Flat, CZTSSe= Front, CZTGSe= Rear, and CZTGSSe= U-Shaped) graded bandgap profiles.

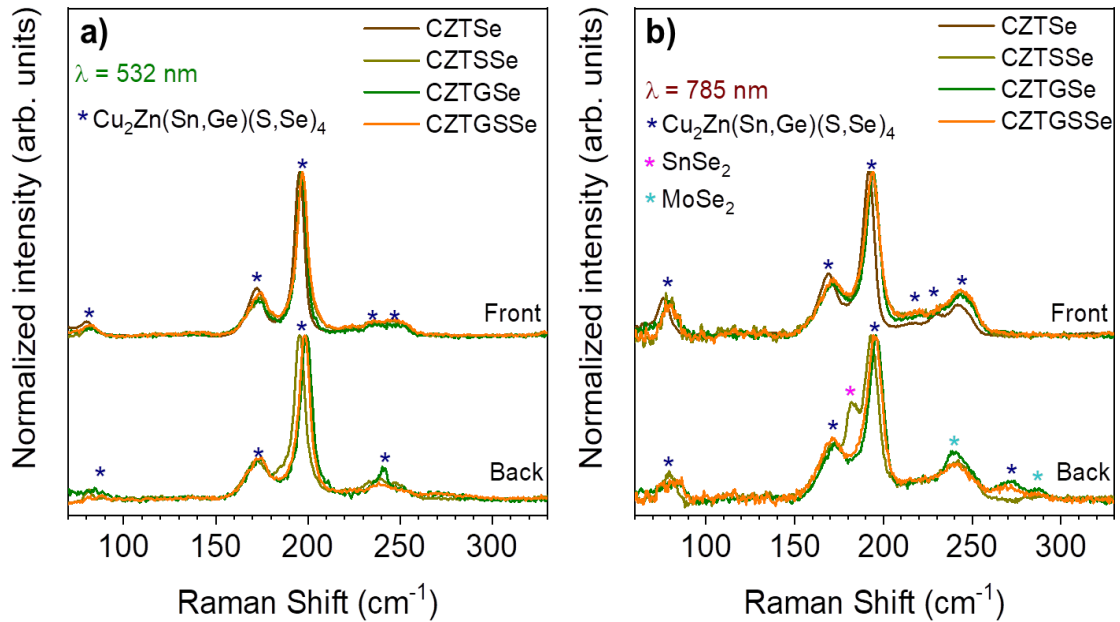


Figure 6.28.- Front and Back Raman spectra obtained using a) 532 nm and b) 785 nm excitation wavelengths of distinct bandgap profiles kesterite.

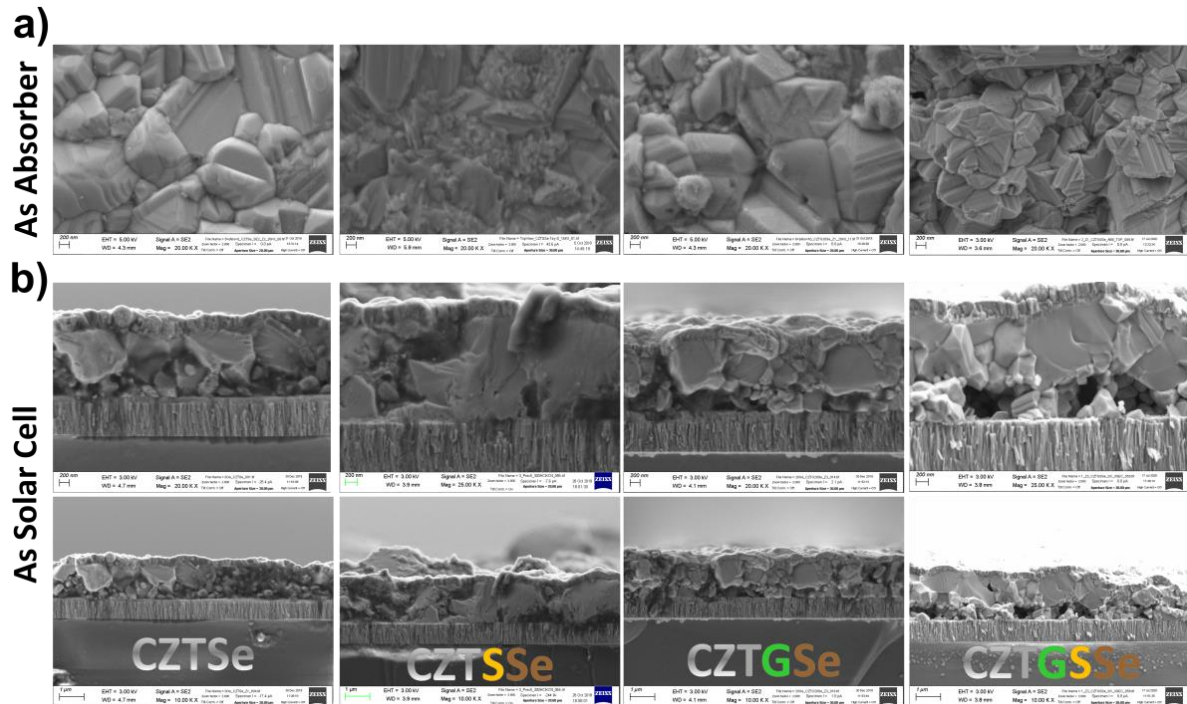


Figure 6.29.- a) Absorber material top (frontal) view SEM micrographs and b) Cross-sectional SEM micrographs of the CZTSe, CZTSSe, CZTGSe and CZTGSSe solar cell devices.

Moreover, the morphological details of the kesterite absorber materials can be observed in Figure 6.29a. On the other hand, Figure 6.29b shows a cross-sectional view of the CZTSe, CZTSSe, CZTGSe and CZTGSSe/CdS devices. Once that the presence of both S-Se and Sn-Ge grading profiles were confirmed, its influence on photovoltaic performance was investigated in full solar cell devices.

The main optoelectronic characteristics of the different type of both dark and the illuminated *JV* curves of the champion kesterite devices are depicted in Figure 6.30a. From this figure, it could be observed that the U-Shaped bandgap profile on CZTGSSe solar cells increases the power conversion efficiency (PCE) by an overall enhancement of the most relevant optoelectronic parameters (V_{OC} , J_{SC} , and FF) of the device.

Furthermore, Figure 6.30b show the bandgap (E_G) values were estimated from the Tauc plots derived from the Quantum Efficiency (IQE) curves. The extracted bandgap ranges between 1.08 and 1.13 eV depending on the bandgap profiles in each kesterite technology.

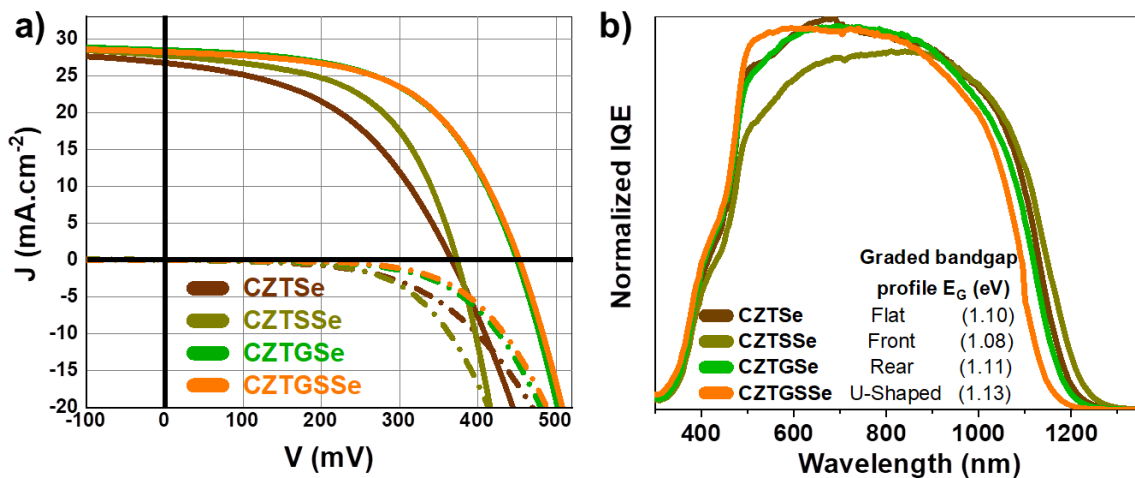


Figure 6.30.- a) JV and b) IQE curves of the CZTSe, CZTSSe, CZTGSe and CZTGSSe solar cell devices.

Therefore, the synergy between defect passivation and interface energetics-modification via bandgap grading strategies in kesterite lead to significantly improvements in stability and efficiency in solar cell devices. In the case of this particular alloy (CZTGSSe), the band energy offset can be independently controlled trough the S and Ge contents, which is explained by a double bandgap grading model.

6.12 Chapter References

1. Neuschitzer, M. et al. Optimization of CdS buffer layer for high-performance $\text{Cu}_2\text{ZnSnSe}_4$ solar cells and the effects of light soaking: elimination of crossover and red kink. *Prog. Photovolt. Res. Appl.* 23, 1660–1667 (2015).
2. López-Marino, S. et al. Inhibiting the absorber/Mo-back contact decomposition reaction in $\text{Cu}_2\text{ZnSnSe}_4$ solar cells: the role of a ZnO intermediate nanolayer. *J. Mater. Chem. A* 1, 8338 (2013).
3. Giraldo, S. et al. Study and optimization of alternative MBE-deposited metallic precursors for highly efficient kesterite CZTSe:Ge solar cells. *Prog. Photovolt. Res. Appl.* 27, 779–788 (2019).
4. Márquez, J. et al. Chemistry and Dynamics of Ge in Kesterite: Toward Band-Gap-Graded Absorbers. *Chem. Mater.* 29, 9399–9406 (2017).
5. MDI (2019). JADE Pro (Computer software), Materials Data, Livermore, CA, USA.
6. ICSD #95117.
7. ICSD #93409.
8. Mo (Cubic) 00-004-0809.
9. Morihama, M., Gao, F., Maeda, T. & Wada, T. Crystallographic and optical properties of $\text{Cu}_2\text{Zn}(\text{Sn}_{1-x}\text{Ge}_x)\text{Se}_4$ solid solution. *Jpn. J. Appl. Phys.* 53, 04ER09 (2014).
10. Anand, T. J. S. & Shariza, S. A study on molybdenum sulphoselenide ($\text{MoS}_x\text{Se}_{2-x}$, $0 \leq x \leq 2$) thin films: Growth from solution and its properties. *Electrochimica Acta* 81, 64–73 (2012).
11. Just, J. et al. Secondary phases and their influence on the composition of the kesterite phase in CZTS and CZTSe thin films. *Phys. Chem. Chem. Phys.* 18, 15988–15994 (2016).
12. Parasyuk, O. V., Gulay, L. D., Romanyuk, Ya. E. & Piskach, L. V. Phase diagram of the $\text{Cu}_2\text{GeSe}_3\text{–ZnSe}$ system and crystal structure of the $\text{Cu}_2\text{ZnGeSe}_4$ compound. *J. Alloys Compd.* 329, 202–207 (2001).
13. Delgado, G. E., Mora, A. J., Marcano, G. & Rincón, C. Crystal structure refinement of the semiconducting compound Cu_2SnSe_3 from X-ray powder diffraction data. *Mater. Res. Bull.* 38, 1949–1955 (2003).
14. Hsu, W.-C. et al. Growth mechanisms of co-evaporated kesterite: a comparison of Cu-rich and Zn-rich composition paths: Growth mechanisms of co-evaporated kesterite. *Prog. Photovolt. Res. Appl.* 22, 35–43 (2014).
15. Ross, L. & Bourgon, M. The germanium–selenium phase diagram. 47, 5 (1969).
16. Trukhin, A. & Capoen, B. Raman and optical reflection spectra of germanate and silicate glasses. *J. Non-Cryst. Solids* 351, 3640–3643 (2005).
17. Giri, P. K. & Dhara, S. Freestanding Core-Shell Nanocrystals with Varying Sizes and Shell Thicknesses: Microstructure and Photoluminescence Studies. *J. Nanomater.* 2012, 1–5 (2012).
18. Platzer-Björkman, C. et al. Back and front contacts in kesterite solar cells: state-of-the-art and open questions. *J. Phys. Energy* 1, 044005 (2019).
19. Giraldo, S. et al. Progress and Perspectives of Thin Film Kesterite Photovoltaic Technology: A Critical Review. *Adv. Mater.* 31, 1806692 (2019).
20. Andrade-Arvizu, J. et al. Is It Possible To Develop Complex S–Se Graded Band Gap Profiles in Kesterite-Based Solar Cells? *ACS Appl. Mater. Interfaces* 11, 32945–32956 (2019).
21. Antunez, P. D., Bishop, D. M., Luo, Y. & Haight, R. Efficient kesterite solar cells with high open-circuit voltage for applications in powering distributed devices. *Nat. Energy* 2, 884–890 (2017).
22. Shu, Q. et al. $\text{Cu}_2\text{Zn}(\text{Sn,Ge})\text{Se}_4$ and $\text{Cu}_2\text{Zn}(\text{Sn,Si})\text{Se}_4$ alloys as photovoltaic materials: Structural and electronic properties. *Phys. Rev. B* 87, 115208 (2013).
23. Garcia-Llamas, E. et al. Multiwavelength excitation Raman scattering of $\text{Cu}_2\text{ZnSn}_{1-x}\text{Ge}_x(\text{S,Se})_4$ single crystals for earth abundant photovoltaic applications. *J. Alloys Compd.* 692, 249–256 (2017).
24. Choubrac, L. et al. Sn Substitution by Ge: Strategies to Overcome the Open-Circuit Voltage Deficit of Kesterite Solar Cells. *ACS Appl. Energy Mater.* 3, 5830–5839 (2020).
25. Cuevas, A. The Recombination Parameter J_0 . *Energy Procedia* 55, 53–62 (2014).
26. Yin, W.-J. et al. Engineering Grain Boundaries in $\text{Cu}_2\text{ZnSnSe}_4$ for Better Cell Performance: A First-Principle Study. *Adv. Energy Mater.* 4, 1300712 (2014).
27. Kim, Y.-I. et al. The characteristics of $\text{Cu}(\text{In, Ga})\text{Se}_2$ thin-film solar cells by bandgap grading. *J. Ind. Eng. Chem.* 76, 437–442 (2019).
28. Lundberg, O., Edoff, M. & Stolt, L. The effect of Ga-grading in CIGS thin film solar cells. *Thin Solid Films* 480–481, 520–525 (2005).
29. Andrade-Arvizu, J. et al. Is It Possible To Develop Complex S–Se Graded Band Gap Profiles in Kesterite-Based Solar Cells? *ACS Appl. Mater. Interfaces* 11, 32945–32956 (2019).
30. PRIGOGINE, I., STENGERS, I., & PRIGOGINE, I. (1984). Order out of chaos: man's new dialogue with nature. Boulder, CO, New Science Library.
31. Andrade-Arvizu, J. et al. Rear Band gap Grading Strategies on Sn–Ge-Alloyed Kesterite Solar Cells. *ACS Appl. Energy Mater.* acsaem.0c01146 (2020) doi:10.1021/acsaem.0c01146.
32. Zhao, W., Pan, D. & Liu, S. (Frank). Kesterite $\text{Cu}_2\text{Zn}(\text{Sn,Ge})(\text{S,Se})_4$ thin film with controlled Ge-doping for photovoltaic application. *Nanoscale* 8, 10160–10165 (2016).
33. Sun, Y. et al. Non-vacuum prepared 9.1% efficient $\text{Cu}_2\text{Zn}(\text{Sn,Ge})(\text{S,Se})_4$ solar cells using a novel selenization process. *Mater. Lett.* 195, 76–78 (2017).

The flow of energy through a system,
Acts to organize that system.

-Harold Morowitz

Chapter VII

Thesis Conclusions, Closing Remarks and Outlook

7.1 Kesterite technologies optimized during the development of this Thesis:
CZTS, CZTSe, CZTSSe, CZTSe:Ge, CZTGSe, and CZTGSSe

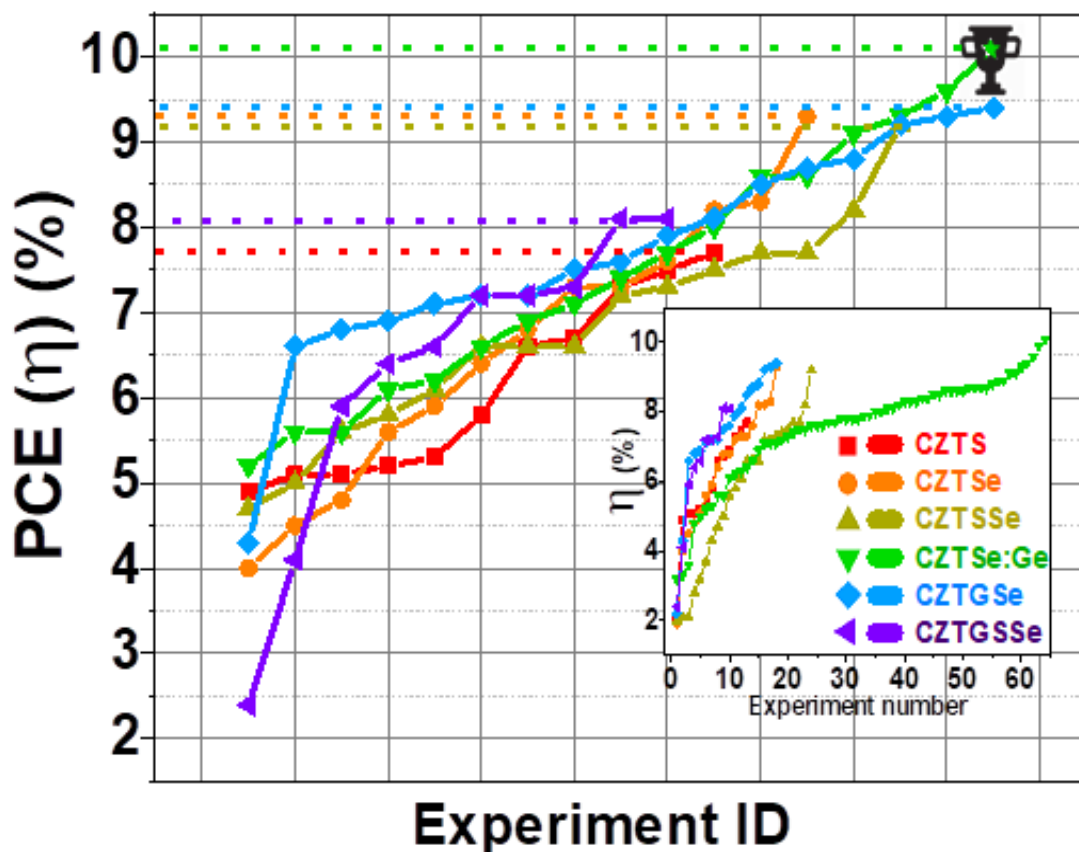


Figure 7.1.- Experimentally ID arranged Power Conversion Energy efficiency (PCE (η)) evolution for each kesterite technology developed and optimized during this Thesis.

Table 7.1a.- Solar cell optoelectronic parameters for the most relevant optimization key steps for each kesterite technology developed and optimized during this Thesis.

Kesterite Technology	EXP ID TAG	Technological Optimization Key Step Description	JV Curve Optoelectronic Parameters			
			PCE (η) (%)	V _{oc} (mV)	J _{sc} (mA·cm ⁻²)	FF (%)
CZTS	I.1	Compositional combinatorial analysis (25 cm ² Megasample)	5.2	720	13.0	56
	I.2	CZT precursor metallic thin layers from sputtering bronze targets	5.3	681	16.1	48
	I.3	Type-4 chemical etching + CZTS thermal annealing treatment	6.6	658	17.6	57
	I.4	Decreasing Cu content+1nm-Al ₂ O ₃ passivating layer	7.3	700	18.2	57
	I.5	Optimized process deposition over FTO substrates	7.7	677	17.8	64
CZTSe	II.1	Type-A chemical etching (CE)	5.6	345	29.9	54
	II.2	Type-3 CE	5.9	357	28.0	59
	II.3	Compositional combinatorial analysis (25 cm ² Megasample)	6.4	370	30.3	57
	II.4	Bandgap grading setup	6.8	371	30.3	61
	II.5	Annealing refinement	7.2	435	28.2	59
	II.6	Compositional upgrade	7.3	422	27.5	59
	II.7	Thermal reactor cleansing #1	8.2	396	34.1	61
	II.8	Thermal reactor and graphite box(es) cleansing #2	9.3	481	30.9	63
CZTSe:Ge	III.1	UV light physical etching + Type-1 CE	8.6	449	31.5	61
	III.2	Li-doping during CBD-CdS deposition process	9.1	449	30.3	67
	III.3	Soft-(controlled) cooldown during absorber synthesis	9.3	453	30.0	67
	III.4	Type-A CE	9.3	459	29.8	69
	III.5	Type-B CE + post deposition thermal treatment (Hot plate on solar cell device)	9.6	403	35.1	68
	III.6	2M of Na salt on CBD-CdS deposition	9.9	465	31.7	67
	III.7*	Optimized final tuned Ge (10-3) process	10.1	427	36.9	64

Table 7.1b.- Solar cell optoelectronic parameters for the most relevant optimization key steps for each kesterite technology developed and optimized during this Thesis.

Kesterite Technology	EXP ID TAG	Technological Optimization Key Step Description <i>(T1-T2)°C – (X)% Ge / (100-X)Sn alloy conditions during thermal annealing (selenization process)</i>	JV Curve Optoelectronic Parameters			
			PCE (η) (%)	V _{oc} (mV)	J _{sc} (mA·cm ⁻²)	FF (%)
CZTSse	IV.1	Bandgap grading setup (First experimental configuration)	4.7	469	19.7	50
	IV.2	Compositional combinatorial analysis (25 cm ² Megasample)	5.6	714	16.4	48
	IV.3	Decreasing synthesis pressure + Type-3 CE	6.6	436	27.2	56
	IV.4	Decreasing synthesis temperature on SeS ₂ Pulse-Shoot	6.6	444	27.3	54
	IV.5	Elemental S Pulse-Shoot synthesis parameter optimization	7.2	445	27.8	58
	IV.6	Thermal routine adjustment on SeS ₂ Pulse-Shoot	7.3	501	25.0	58
	IV.7	High pressure synthesis + Type-B CE	7.7	464	30.3	55
	IV.8	S Pulse-Shoot on already selenized CZTSe absorber	8.1	410	32.8	60
	IV.9	Increasing introduction temperature on SeS ₂ Pulse-Shoot	8.2	438	29.6	62
	IV.10	Is It Possible To Develop Complex S–Se Graded Bandgap Profiles in Kesterite-Based Solar Cells? ¹	9.2	442	32.2	64
CZTGSe	V.1	(300-500)-30 by GeSe ₂ powder	7.2	470	27.6	55
	V.2	(330-500)-20 + Type-A CE	7.6	434	28.2	62
	V.3	(380-535)-20 + Type-A CE	7.9	440	30.9	58
	V.4	(330-500)-20 + Type-B CE	8.1	456	28.2	63
	V.5	(330-500)-30 by GeSe powder	8.5	502	28.4	60
	V.6	(330-500)-20 by Sn powder	8.7	435	30.7	65
	V.7	(330-500)-10 by Sn powder	8.8	441	29.0	68
	V.8	(385-535)-20 by Sn powder	9.3	432	33.1	65
	V.9	Rear Bandgap Grading Strategies on Sn–Ge Alloyed Kesterite Solar Cells ²	9.4	470	30.9	65
CZTGSse	VI.1	(330-500)°C at a 50mg S Pulse-Shoot	2.4	359	20.3	34
	VI.2	Type-4 CE	4.1	399	23.4	44
	VI.3	(385-535)°C + Type-B CE	5.9	406	25.4	57
	VI.4	(330-500)°C at a 5mg S Pulse-Shoot	6.4	414	28.7	54
	VI.5	3mg S Pulse-Shoot	7.2	436	26.8	59
	VI.6	No Sn addition during selenization + Type-B CE	7.2	450	28.1	57
	VI.7	Type-A CE	7.3	485	28.9	52
	VI.8	Double Graded U-Shaped Bandgap on CZTGSse Solar Cells	8.1	456	28.2	63

Thesis Main Conclusions

First, it was possible to develop novel and disruptive anionic superficial substitutions at the front interface of kesterite (CZTSSe) thin film absorber layers. Thus, optimizing the band alignment by engineering a front semi U-Shaped graded bandgap profile.

Secondly, by means of generating a rear bandgap graded profile strategy mainly based on the spontaneous cationic substitution during the kesterite (CZTGSe) alloy synthesis, it was possible to reduce the effect of deep defect (Sn_{Cu}) formation and impose an additional drift (back surface) field within the quasi-neutral region. Additionally, this improves the crystallization quality of the absorber material by generating metallic Ge liquid phase fluxes.

And finally, by combining both strategies, it is feasible to synthesize a U-Shaped double graded bandgap profile kesterite (CZTGSSe) absorber thin film layer. Allowing a device performance enhancement by simultaneously down-shifting the absorber VBM at front interface and upshifting the CBM at back contact.

In this way, starting from an average energy Power Conversion Efficiency (PCE) $\leq 5\%$ for several **kesterite thin film solar cell technologies (CZTS, CZTSe, CZTSSe, CZTGSe and CZTGSSe)**, this Thesis studies allowed to double the PCE with values even higher than 10%.

7.2 Thesis Outlook: The Arrow of Time

How is it possible to justify the arrow of time from a probabilistic point of view?

According to Prigoginian's line of thoughts, the arrow of time appears with thermodynamics, and with the latter, entropy emerges.³ Entropy, or 'randomness' is an *in crescendo* function of time which is maximized for an isolated system. This particular state is commonly known as equilibrium. Also, and for the mere sake of convenience, it is often provoked to work with a particular function known as free energy. Literally, the free energy stands for the total energy minus the entropy times the temperature of the whole system. This represents a pure variational principle in which an *extremum* at the equilibrium occurs. In this way, at equilibrium the system resembles as immunized to internal fluctuations. At this state (equilibrium), if a small fluctuation occurs, the maximum (or minimum) conditional state of is lost, but the system <reacts> trying to reach an equilibrated state again. In a *grosso modo*, the system knows only one truth, and that true is that the truth of the maximum (or minimum) state of the entropy, or if you will, the free energy.

Nevertheless, a more interesting questioning might be:

What would happen "outside" or in far-from-equilibrium conditions?

As a first premisy; surprisingly, when a system is taken out from equilibrium, immediatly there happen to occur order phenomena, i.e., there is no increment in the degree of disorder, but conversely, ordering phenomena appear.

For example: the physiochemical phenomena of thermodiffusion. If one considers an isolated box containing at the same time two constituent species, hypothetically suppose: hydrogen and nitrogen atoms. Thus, if one side of the box is heated, it is immediately followed that it gets colder by the other side. On top of that, it will naturally happen to be a higher nitrogen content at the cold side, and logically, more hydrogen at the hot side. This constitutes order phenomena in which the gas molecules are separated by an irreversible process.

Following this line, nowadays we are convinced ⁴ that most of the complex structures that we find in the so far known Universe could only be created in (out) far from equilibrium conditions. Interestingly enough to be mentioned, outside from equilibrium there are no more maximum (or minimum) *in extremum* conditions, therefore there is no such a thing as an “ideal” or preferred state at which the system would necessarily tends to be. This is a fluctuation or bifurcation state where new solutions appear: the dissipative structure regime.

A dissipative structure is only sustained due its internal dynamical interaction with the external non-conformal environment, thus, its structure would be a reflection of its interaction. Amongst the conformal possibilities, an auto-organizational dissipative structure would be mostly defined by the probabilistically dependent bifurcations. At the same time, the constructive role of time appears. The fact of standing outside from the equilibrium, leads to the discovery of new structures. These structures are absolutely fundamental for a deeper comprehension of the world around us, from the ecosystem to precisely understand the weather conditions in Earth's life. In fact, for this *æon* the arrow of time leads to the general consideration that, perhaps, the direction of the arrow of time is the only common element in this known Universe. It is well known that what Sir Issac Newton sustained regarding classical mechanics principles is only applicable to particularly simplistic situations. ⁵ Of course that there is absolutely no doubt on the falling of the bodies phenomena or the movement of the Earth around the Sun. Nevertheless it is impossible to question the success of quantum mechanics, even though it is about simplifications, of ideal situations. Therefore, it is necessary a further consideration on something like the physics of populations which might not be reducible to the individuals.

Later, Sir Charles Darwin's biological evolutionary theories could not be reduced to a single specimen's behavior. ⁶ There must be a complete study of dynamic conditions irreducible to one single history (trajectory) in which it must be considered that the whole system's ensemble probability is not valid to what could be obtained for a single trajectory. This way, what could not be solved at a trajectory level, might be solved by probabilities. Since it was undoubtedly demonstrated that, despite stable systems like the harmonic oscillator; Newtonian systems are non-deterministic. The ideas of “free particle instantaneous interactions” are no longer enough lasting idealized resources to deal with far from equilibrium conditions.

Therefore, a physics of populations, statistically governed, must be implemented in order to provide a more complete vision in which the laws of Nature are re-signified at this stage of the human-Nature vast dialectics in which our science is fundamentally based-on.

The focus is anymore on the laws of individual events, but in the probabilistic ones. They express exactitude no more, but a probability instead. Thus, a constructing reality world is allowed. A non-given immediate future, but instead a dynamically developing one.

Essentially, the proposed theory of chaos is focused in something recently minted as “sensitive dependence” on the initial conditions, but rather more importantly, that reversibility a fundamental property of Nature.

Thus, it is suggested that Nature may be better understand in a statistical, rather than individual trajectory-based manner. The simplest of the possible scenarios is chaos in which an infinite precision to speak about trajectories would be needed.

The reality inside the arrow of time is the world in construction. This way, proposing time as the narrative element, which direction of propagation appears to be the only common element in the whole known Universe, and at all scales.

Thus, time is irreversible change, and of course imaging a one dimensional time may be a limitation of human interpretation of it. Since it is noteworthy to remark that our most scientific accurate and accepted cosmological approach is based on the conformal basis of biological organization by the Hierarchy of Life merely derived from The Big Bang Theory.

Hence, this work proposes to look after the complex manipulation and matter engineering as a dynamical action process of (auto) self-conformation driven by an attractive, rather than equilibrium state in order to reveal Nature very interesting properties. Thereby, serve this experimental Thesis as a extensive phenomenological evidence of dealing with fundamental complex conceptual problems that arise from the macroscopic and microscopic aspects of the second law of thermodynamics. Fact that has been previously theorized and outlined that non-equilibrium may become a source of order and that irreversible processes may lead to a new type of dynamic states of matter called “dissipative structures” by the Russian physicist-mathematician and awarded with the 1977 Chemistry Nobel Prize, Ilya Romanovich Prigogine.

Thus, a microscopic definition of irreversible processes is given and a transformation theory is developed that allows one to introduce non-unitary equations of motion that explicitly display irreversibility and approach to thermodynamic equilibrium.^{3,4,7}

From a brief review of Prigogine and the Brussels group, it could be clearly notified that the here exposed work serves as an experimental factual evidence of an application of the chaos theory, in which a new development of theoretical chemistry and physics in which -a new form of- Hierarchical Thermodynamics along with the adequate Lyapunov function derived coefficients as the most suitable mathematical tool, plays an ever increasing role as it is tackled in this work.

Grounding these ideas into direct materialistic applications urgency on scrutinizing Nature's complex properties, for example when it is subject of far from thermodynamic equilibrium conditions as this Thesis demonstrates.

7.3 Chapter References

1. Andrade-Arvizu, J. et al. Is It Possible To Develop Complex S–Se Graded Band Gap Profiles in Kesterite-Based Solar Cells? *ACS Appl. Mater. Interfaces* 11, 32945–32956 (2019).
2. Andrade-Arvizu, J. et al. Rear Band gap Grading Strategies on Sn–Ge-Alloyed Kesterite Solar Cells. *ACS Appl. Energy Mater.* acsaem.0c01146 (2020) doi:10.1021/acsaem.0c01146.
3. Prigogine, I., *Acad. Roy. Belg. Bull. Cl. Sc.* 31, 600, 1945. – Etude thermodynamique des phénomènes irréversibles. Thèse d'agrégation présentée en 1945 à l'Université Libre de Bruxelles. Desoer, Liège, 1947.
4. PRIGOGINE, I., STENGERS, I., & PRIGOGINE, I. (1984). *Order out of chaos: man's new dialogue with nature*. Boulder, CO, New Science Library.
5. Newton, Isaac, Sir, *Philosophiæ Naturalis Principia Mathematica* (author's personal copy) University of Cambridge. Consulted on 04/02/2021.
6. Darwin, Charles, Sir, 'Pencil Sketch of 1842', in Darwin, Francis (ed.), *The foundations of The origin of species: Two essays written in 1842 and 1844.*, Cambridge: Cambridge University Press, retrieved 15 December 2006, (published 1909).
7. Prigogine, I. Irreversibility and randomness. *Astrophys. Space Sci.* 65, 371–381 (1979).

Imaginary numbers are a fine and wonderful refuge of the divine spirit,

Almost an amphibian between being and non-being.

-Gottfried Wilhelm Leibniz

i Appendix:

Additional and Supporting Information

**i.1. Kesterite technologies optimized during the development of this Thesis:
CZTS, CZTSe, CZTSSe, CZTSe:Ge, CZTGSe, and CZTGSSe**

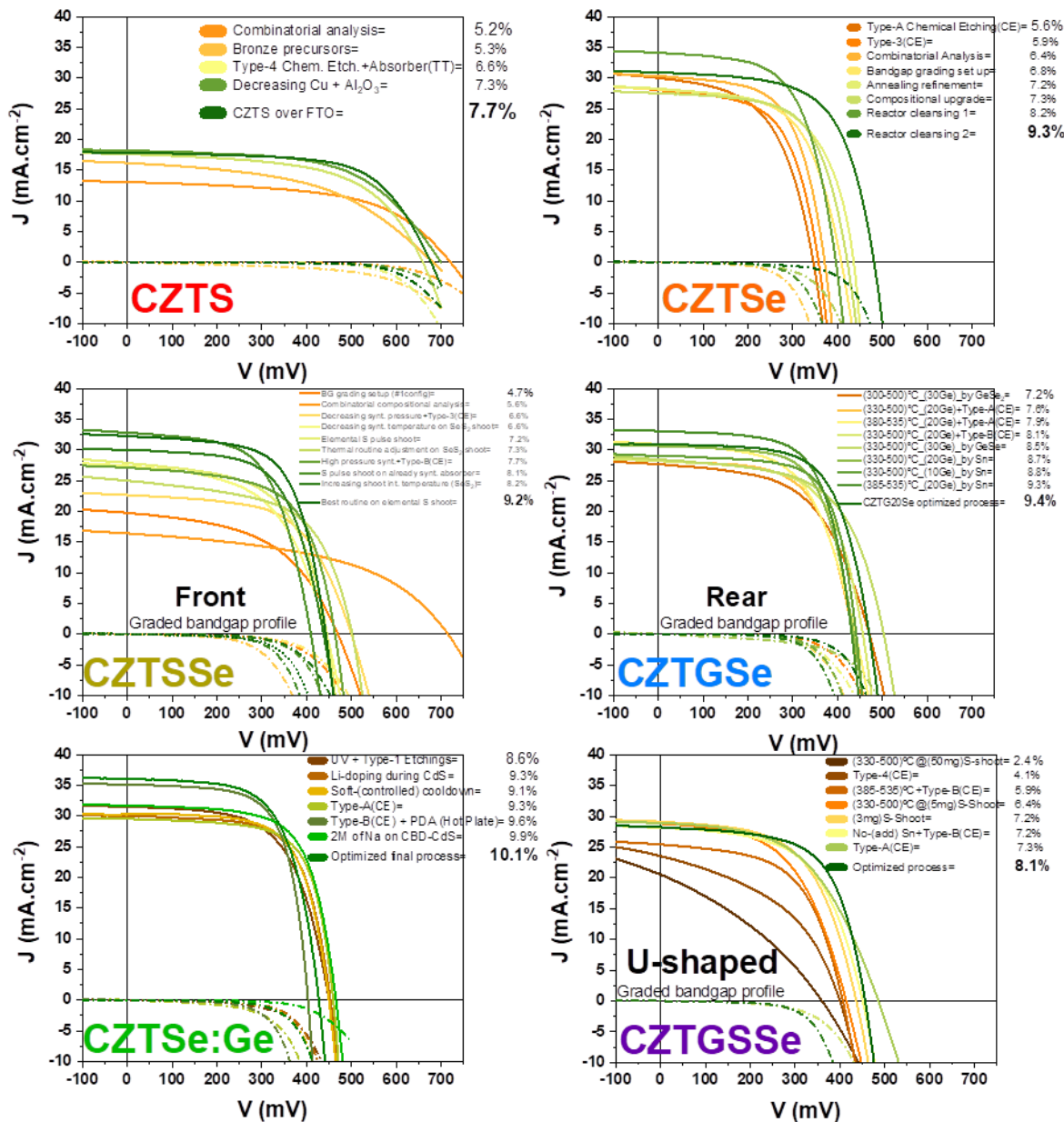


Figure i.1.- Champion device JV curves for each of the optimized kesterite technologies during this Thesis. ¹⁻³

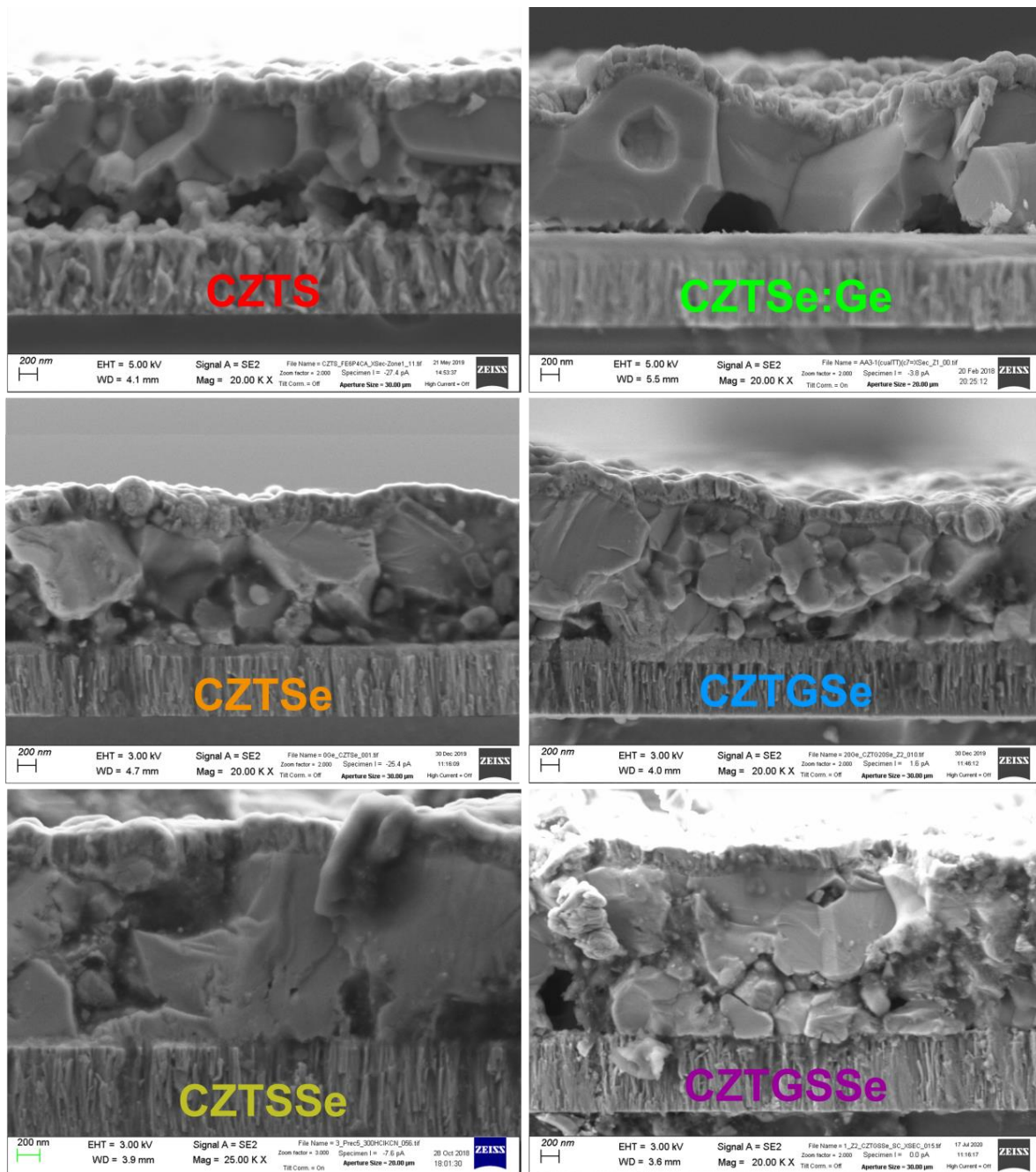


Figure i.2.- Cross-sectional SEM micrographs curves for the champion device for each of the optimized kesterite technologies during this Thesis.

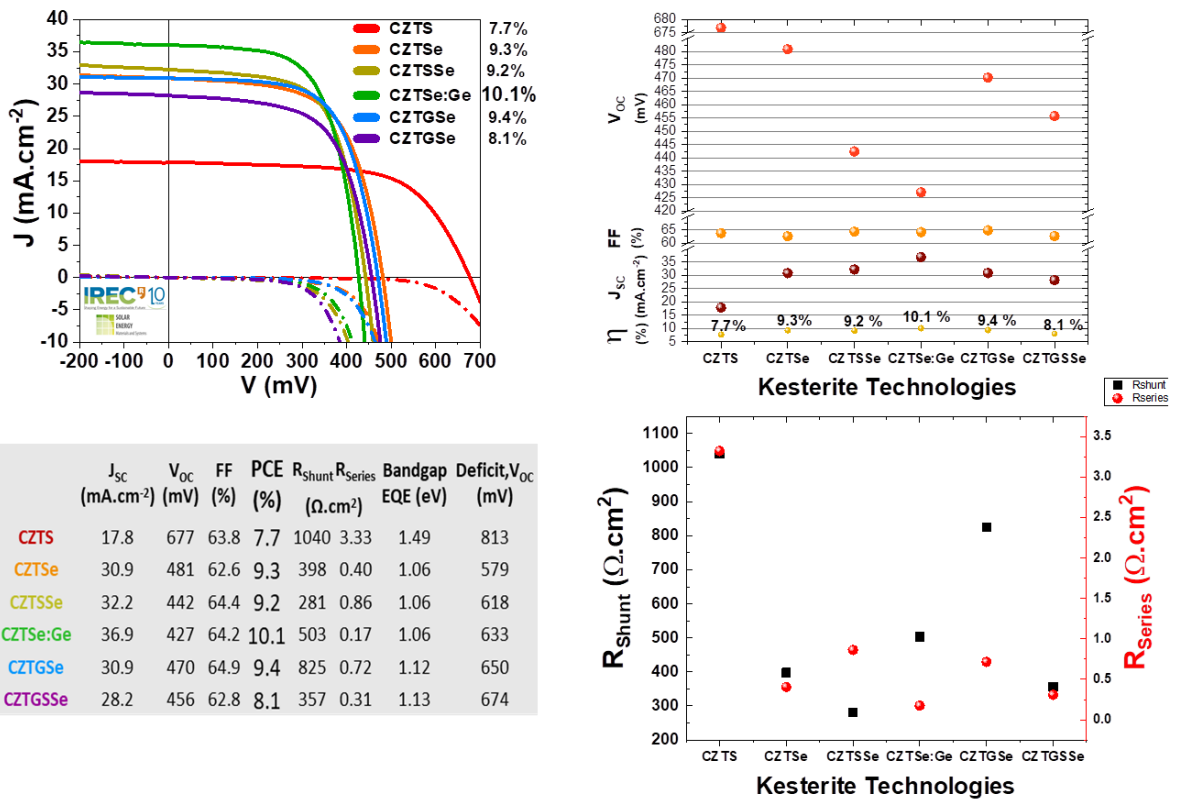


Figure i.3.- Champion device JV curves and optoelectronic parameters for each of the optimized kesterite technologies during this Thesis.

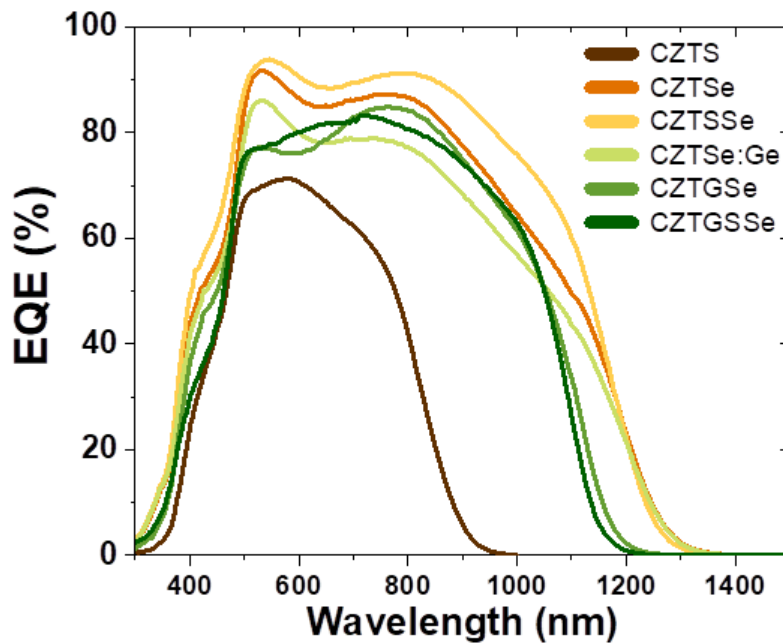


Figure i.4.- Champion device EQE curves for each of the optimized kesterite technologies during this Thesis.

i.2. Absorber Surface Cleaning: Chemical Etchings

The as-synthesized kesterite absorber materials were typically subjected to always fresh and new solutions by one or two wet-chemical etchings. Superficial passivation and removal of spurious secondary phases figured as the main purpose of this procedure.

- Potassium permanganate ($[KMnO_4] = 0.01M$, $[H_2SO_4] = 1M$): A standard magnetic stirred solution: 23.6 ml of miliQ-H₂O + 1.4 ml of H₂SO₄ (98% M/v) + 39.5 mg of KMnO₄ + 25 ml H₂O (miliQ) during 40 seconds. Application under room temperature (RT) conditions. ⁴
- Amonium sulfide ($[(NH_4)_2S] = 0.1M$): 22% M/v (NH₄)₂S concentrated solution, during 120 seconds. Application under RT conditions.
- Potassium cyanide (KCN): 2% KCN M/v solution applied during 60 to 120 seconds at 60 °C. ⁵
- Hydrochloric acid (HCl): 10% V/v solution during 120 seconds at 75 °C. ⁶

A purely empirical evidenced demonstration on the most adequate superficial cleaning chemical etching for each kesterite thin film solar cell technology fabricated in this Thesis is provided below in Figure i.1.

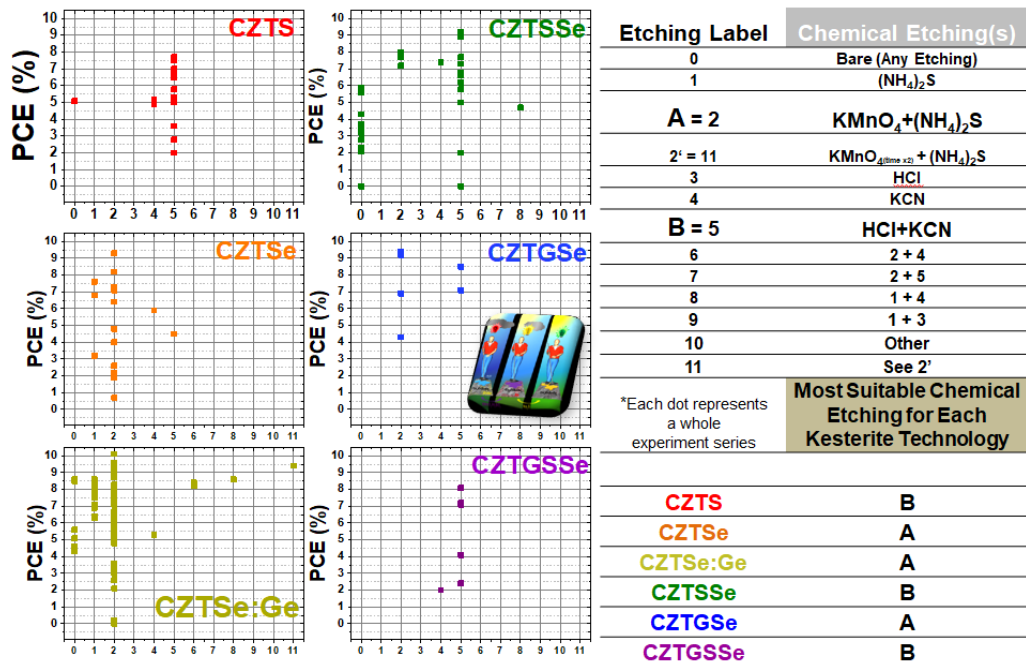


Figure i.5.- Best chemical etching (PCE enhancement) for each kesterite technology in this Thesis.

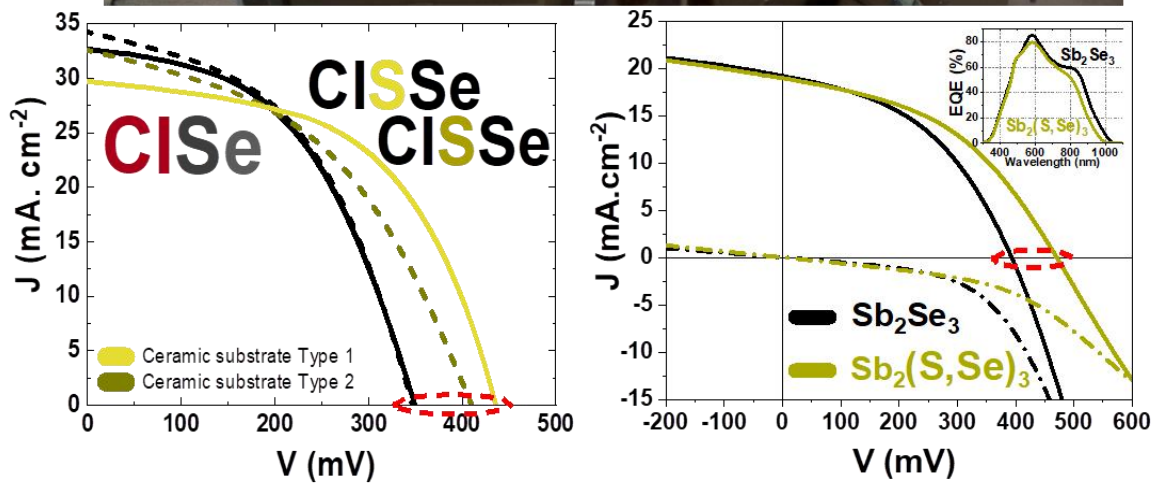
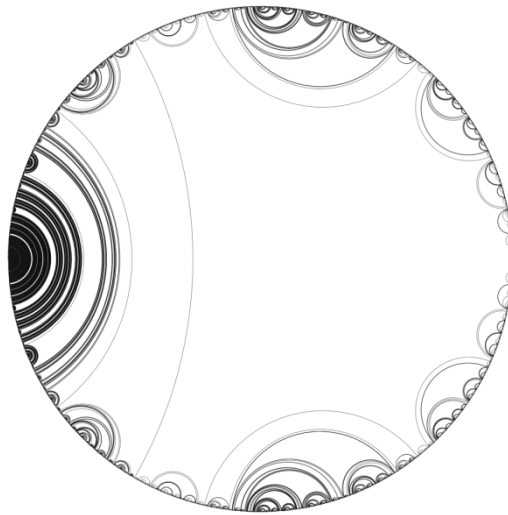
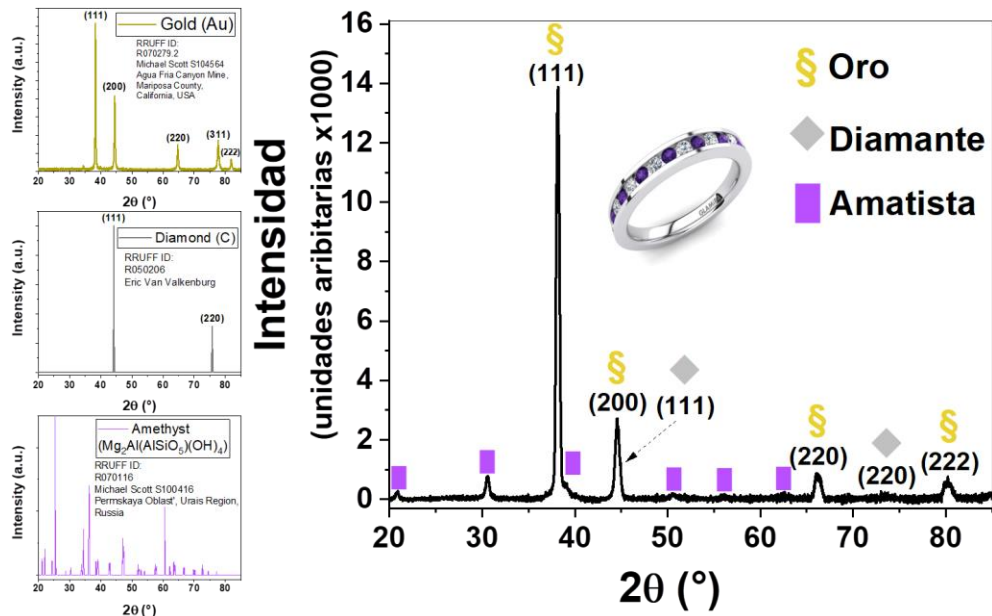


Figure i.6.- Superficial sulfurization methodology developed as product of this Thesis, applied to both chalcogenide materials: CISe and Sb₂(S,Se)₃.

Table i.1.- List of V_{OC} deficit identified failure modes for kesterite thin film solar cells (See Chapter II). The bold marked entries correspond to this Thesis failure mode focus.⁷

FOM #	Item/Function	Potential Failure Mode	Potential Cause / Mechanism of Failure	Ref.
1	Back Electrode	Carrier recombination in $MoSe_x$	Chunky $MoSe_x$ layer	8
6	Absorber (bulk)	Low mobility	Defect scattering	9
7			Carrier localization due to band gap fluctuations	10
8		Short carrier lifetime	SRH recombination on deep defect in the gap	26, 27
9			Tunneling assisted recombination	13
10			Non-radiative carrier recombination through bi-molecular recombination	29,30
11		Grain boundary recombination	Grains too small & poor grain boundary passivation	11, 16–18
12		Electrostatic potential fluctuations (Inhomogeneous distribution of defects)	Cu/Zn disorder + Band fluctuations	19
13			Very high concentration of compensated defect clusters + low dielectric constant	20,21
14		Band gap fluctuations	Presence of secondary phases in the bulk	22
15			Cu/Zn disorder	23
16			S/Se local inhomogeneities	1,24
17		Absence of internal electric field	No band gap gradient	1,2
18		Insufficient quasi Fermi-level splitting	Quasi-Fermi level pinning due to high defect density (Cu_{Zn})	23
19			Low doping level in absorber	11
28		Absorber (front interface)	Front interface recombination	Low interfacial band gap due to band gap narrowing (CZTS)
29	Presence of minor phases at front interface due to absorber decomposition (Sn-loss)			26,27
30	Fermi level position at the middle of hetero-interface (Fermi level pinning)			23
31	Poor/null charge inversion in kesterite absorber			28,29
32	High density of non-passivated surface defects			1,30
35	Buffer layer by sputtering	Front interface recombination	Insufficient buffer coverage + Conduction band offset positioning	31–33
36				
37				

Difracción de rayos X



Espectroscopía Raman

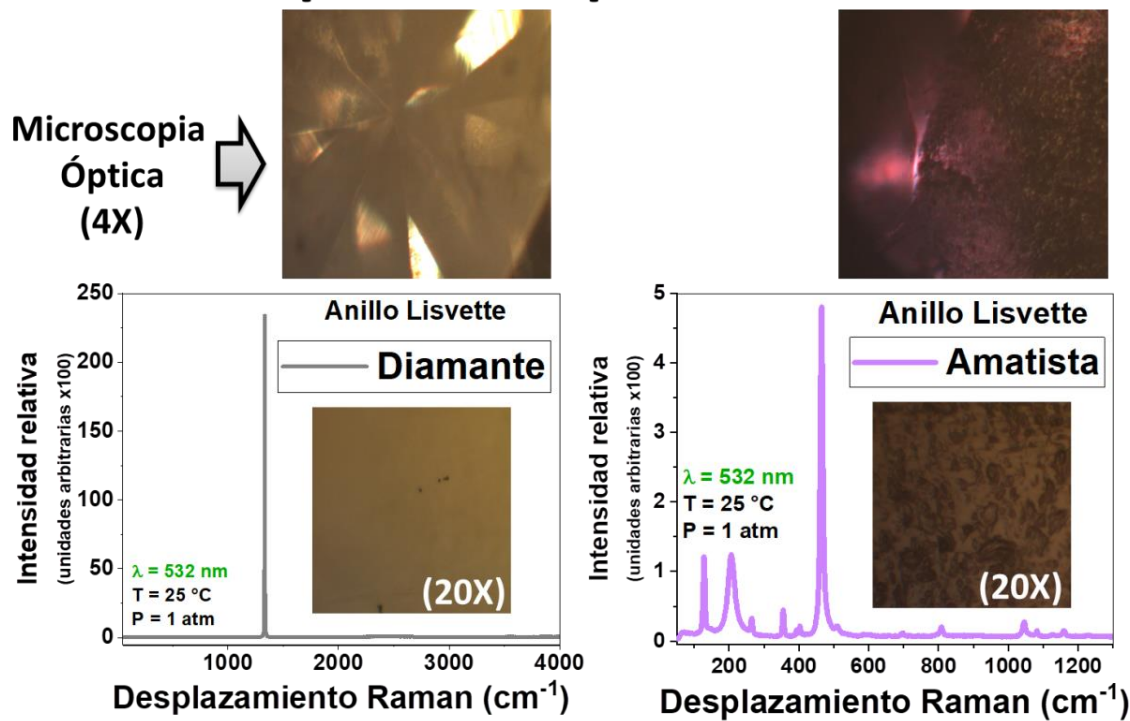
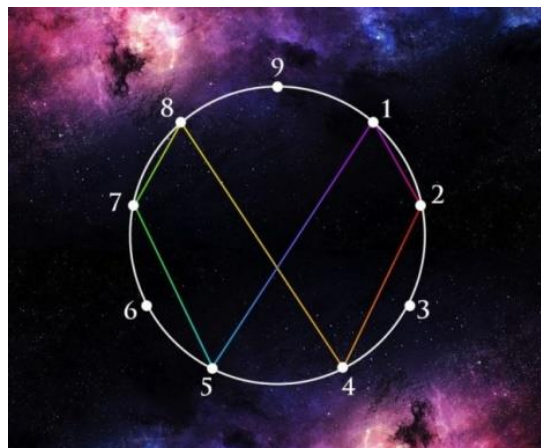


Figure i.7.- Irene (my amoh) weeding ring's chracterization. 201711252020062720201102 $\rightarrow\infty$

i.3 Appendix References

1. Andrade-Arvizu, J. *et al.* Is It Possible To Develop Complex S–Se Graded Band Gap Profiles in Kesterite-Based Solar Cells? *ACS Appl. Mater. Interfaces* **11**, 32945–32956 (2019).
2. Andrade-Arvizu, J. *et al.* Rear Band gap Grading Strategies on Sn–Ge-Alloyed Kesterite Solar Cells. *ACS Appl. Energy Mater.* *acsam.0c01146* (2020) doi:10.1021/acsaem.0c01146.
3. Jacob Andrade-Arvizu, Z. Jehl, M. Courel, R. Fonoll-Rubio, V. Izquierdo-Roca, Y. Sánchez, M. Guc, D. Sylla, I. Becerril, M. Placidi, A. Pérez-Rodríguez, Osvaldo Vigil-Galán and E. Saucedo. U-Shaped Graded Bandgap Profile on Kesterite Thin Film Solar Cells. Under Preparation.
4. López-Marino, S. *et al.* ZnSe Etching of Zn-Rich $\text{Cu}_2\text{ZnSnSe}_4$: An Oxidation Route for Improved Solar-Cell Efficiency. *Chem. - Eur. J.* **19**, 14814–14822 (2013).
5. Xie, H. *et al.* Impact of Sn(S,Se) Secondary Phases in $\text{Cu}_2\text{ZnSn(S,Se)}_4$ Solar Cells: a Chemical Route for Their Selective Removal and Absorber Surface Passivation. *ACS Appl. Mater. Interfaces* **6**, 12744–12751 (2014).
6. Fairbrother, A. *et al.* Development of a Selective Chemical Etch To Improve the Conversion Efficiency of Zn-Rich $\text{Cu}_2\text{ZnSnS}_4$ Solar Cells. *J. Am. Chem. Soc.* **134**, 8018–8021 (2012).
7. Grenet, L., Suzon, M. A. A., Emieux, F. & Roux, F. Analysis of Failure Modes in Kesterite Solar Cells. *ACS Appl. Energy Mater.* **1**, 2103–2113 (2018).
8. Schnabel, T. & Ahlswede, E. On the interface between kesterite absorber and Mo back contact and its impact on solution-processed thin-film solar cells. *Sol. Energy Mater. Sol. Cells* **159**, 290–295 (2017).
9. Nagaoka, A. *et al.* Effects of sodium on electrical properties in $\text{Cu}_2\text{ZnSnS}_4$ single crystal. *Appl. Phys. Lett.* **104**, 152101 (2014).
10. Hempel, H. *et al.* Intragrain charge transport in kesterite thin films—Limits arising from carrier localization. *J. Appl. Phys.* **120**, 175302 (2016).
11. Li, J. B., Chawla, V. & Clemens, B. M. Investigating the Role of Grain Boundaries in CZTS and CZTSSe Thin Film Solar Cells with Scanning Probe Microscopy. *Adv. Mater.* **24**, 720–723 (2012).
12. Lie, S. *et al.* Reducing the interfacial defect density of CZTSSe solar cells by Mn substitution. *J. Mater. Chem. A* **6**, 1540–1550 (2018).
13. Hages, C. J., Carter, N. J., Agrawal, R. & Unold, T. Generalized current-voltage analysis and efficiency limitations in non-ideal solar cells: Case of $\text{Cu}_2\text{ZnSn(S}_x\text{Se}_{1-x})_4$ and $\text{Cu}_2\text{Zn(Sn}_y\text{Ge}_{1-y})(\text{S}_x\text{Se}_{1-x})_4$. *J. Appl. Phys.* **115**, 234504 (2014).
14. Hages, C. J. *et al.* Identifying the Real Minority Carrier Lifetime in Nonideal Semiconductors: A Case Study of Kesterite Materials. *Adv. Energy Mater.* **7**, 1700167 (2017).
15. Kumar, M., Dubey, A., Adhikari, N., Venkatesan, S. & Qiao, Q. Strategic review of secondary phases, defects and defect-complexes in kesterite CZTS–Se solar cells. *Energy Environ. Sci.* **8**, 3134–3159 (2015).
16. Kim, J. *et al.* High Efficiency $\text{Cu}_2\text{ZnSn(S,Se)}_4$ Solar Cells by Applying a Double $\text{In}_2\text{S}_3/\text{CdS}$ Emitter. *Adv. Mater.* **26**, 7427–7431 (2014).
17. Liu, F. *et al.* Kesterite $\text{Cu}_2\text{ZnSn(S,Se)}_4$ Solar Cells with beyond 8% Efficiency by a Sol–Gel and Selenization Process. *ACS Appl. Mater. Interfaces* **7**, 14376–14383 (2015).
18. Gunawan, O., Gokmen, T. & Mitzi, D. B. Suns- V_{OC} characteristics of high performance kesterite solar cells. *J. Appl. Phys.* **116**, 084504 (2014).

19. Scragg, J. J. S. *et al.* Cu-Zn disorder and band gap fluctuations in $\text{Cu}_2\text{ZnSn}(\text{S},\text{Se})_4$: Theoretical and experimental investigations: Cu-Zn disorder and band gap fluctuations in $\text{Cu}_2\text{ZnSn}(\text{S},\text{Se})_4$. *Phys. Status Solidi B* **253**, 247–254 (2016).
20. Gokmen, T., Gunawan, O., Todorov, T. K. & Mitzi, D. B. Band tailing and efficiency limitation in kesterite solar cells. *Appl. Phys. Lett.* **103**, 103506 (2013).
21. Yin, L. *et al.* Limitation factors for the performance of kesterite $\text{Cu}_2\text{ZnSnS}_4$ thin film solar cells studied by defect characterization. *RSC Adv.* **5**, 40369–40374 (2015).
22. Siebentritt, S. Why are kesterite solar cells not 20% efficient? *Thin Solid Films* **535**, 1–4 (2013).
23. Yuan, Z.-K. *et al.* Engineering Solar Cell Absorbers by Exploring the Band Alignment and Defect Disparity: The Case of Cu- and Ag-Based Kesterite Compounds. *Adv. Funct. Mater.* **25**, 6733–6743 (2015).
24. Bourdais, S. *et al.* Is the Cu/Zn Disorder the Main Culprit for the Voltage Deficit in Kesterite Solar Cells? *Adv. Energy Mater.* **6**, 1502276 (2016).
25. Crovetto, A. *et al.* Interface band gap narrowing behind open circuit voltage losses in $\text{Cu}_2\text{ZnSnS}_4$ solar cells. *Appl. Phys. Lett.* **110**, 083903 (2017).
26. Weber, A., Mainz, R. & Schock, H. W. On the Sn loss from thin films of the material system Cu–Zn–Sn–S in high vacuum. *J. Appl. Phys.* **107**, 013516 (2010).
27. Scragg, J. J. *et al.* Effects of Back Contact Instability on $\text{Cu}_2\text{ZnSnS}_4$ Devices and Processes. *Chem. Mater.* **25**, 3162–3171 (2013).
28. Polizzotti, A., Repins, I. L., Noufi, R., Wei, S.-H. & Mitzi, D. B. The state and future prospects of kesterite photovoltaics. *Energy Environ. Sci.* **6**, 3171 (2013).
29. Barkhouse, D. A. R., Gunawan, O., Gokmen, T., Todorov, T. K. & Mitzi, D. B. Device characteristics of a 10.1% hydrazine-processed $\text{Cu}_2\text{ZnSn}(\text{Se},\text{S})_4$ solar cell: Characteristics of a 10.1% efficient kesterite solar cell. *Prog. Photovolt. Res. Appl.* **20**, 6–11 (2012).
30. Li, J., Mitzi, D. B. & Shenoy, V. B. Structure and Electronic Properties of Grain Boundaries in Earth-Abundant Photovoltaic Absorber $\text{Cu}_2\text{ZnSnSe}_4$. *ACS Nano* **5**, 8613–8619 (2011).
31. Grenet, L., Suzon, M. A. A., Emieux, F. & Roux, F. Analysis of Failure Modes in Kesterite Solar Cells. *ACS Appl. Energy Mater.* **1**, 2103–2113 (2018).
32. Englund, S., Saini, N. & Platzer-Björkman, C. $\text{Cu}_2\text{ZnSn}(\text{S},\text{Se})_4$ from annealing of compound co-sputtered precursors – Recent results and open questions. *Sol. Energy* **175**, 84–93 (2018).
33. Grenet, L. *et al.* Sputtered ZnSnO Buffer Layers for Kesterite Solar Cells. *ACS Appl. Energy Mater.* **3**, 1883–1891 (2020).



RESEARCH EXPERIENCE

Publications during Doctoral Thesis development:

1. "U-Shaped Graded Bandgap Profile on Kesterite Thin Film Solar Cells". **Jacob Andrade-Arvizu**, Z. Jehl, M. Courel, R. Fonoll-Rubio, V. Izquierdo-Roca, Y. Sánchez, M. Guc, D. Sylla, I. Becerril, M. Placidi, A. Pérez-Rodríguez, Osvaldo Vigil-Galán and E. Saucedo. Under Preparation.
2. "Insights into the role of the intrinsic zinc oxide buffer in chalcogenide photovoltaics". **J. Andrade-Arvizu**, R. Fonoll-Rubio, I. Becerril, M. Guc, K. Tiwari, D. Sylla, Y. Sanchez, S. Giraldo, V. Izquierdo-Roca, A. Pérez-Tomás, M. Espindola-Rodriguez, L. Calvo-Barrio, Z. Jehl Li-Kao, A. Pérez-Rodríguez, E. Saucedo, M. Placidi. Under Preparation.
3. "Controlling the anionic ratio and gradient in kesterite technology". **Jacob Andrade-Arvizu**, Robert Fonoll Rubio, Victor Izquierdo-Roca, Ignacio Becerril-Romero, Diouldé Sylla, Pedro Vidal-Fuentes, Zacharie Jehl Li-Kao, Angélica Thomere, Sergio Giraldo, Kunal Tiwari, Shahaboddin Resalati, Maxim Guc, Marcel Placidi. ACS Appl. Mater. Interfaces. Under review since 23/02/2021.
4. "High efficiency $\text{Cu}_2\text{ZnSnS}_4$ solar cells over FTO substrate and its CZTS/CdS interface passivation via thermal evaporated Al_2O_3 ". Esteban Ojeda-Durán, Karim Monfil-Leyva, **Jacob Andrade-Arvizu**, Ignacio Becerril-Romero, Yudania Sánchez, Robert Fonoll-Rubio, Maxim Guc, Zacharie Jehl Li-Kao, José A. Luna-López, Jesús Carrillo-López, Ana L. Muñoz-Zurita, Victor Izquierdo-Roca, Marcel Placidi, Edgardo Saucedo. Journal of Materials Chemistry C, 9, 5356-5361 (2021). DOI: 10.1039/D1TC00880C
5. "Insights on the limiting factors of $\text{Cu}_2\text{ZnGeSe}_4$ based solar cells". I. Anefnaf, S. Aazou, Y. Sanchez, P. Vidal-Fuentes, R. Fonoll-Rubio, K. Tiwari, S. Giraldo, Z. J. Li-Kao, **Jacob Andrade-Arvizu**, M. Guc, E. Saucedo, Z. Sekkat. Solar Energy Materials and Solar Cells, 227, 111106 (2021). DOI: 10.1016/j.solmat.2021.111106

6. [“Insights into interface and bulk defects in a high efficiency kesterite-based device”](#). Robert Fonoll-Rubio, **Jacob Andrade-Arvizu**, Javier Blanco-Portals, Ignacio Becerril-Romero, Maxim Guc, Edgardo Saucedo, Francesca Peiró, Lorenzo Calvo-Barrio, Maurizio Ritzer, Claudia S. Schnohr, Marcel Placidi, Sònia Estradé, Víctor Izquierdo-Roca, Alejandro Pérez-Rodríguez. *Energy Environ. Sci.*, 2021, 14, 507-523. DOI: 10.1039/D0EE02004D
7. [“Rear Band gap Grading Strategies on Sn-Ge Alloyed Kesterite Solar Cells”](#). **Jacob Andrade-Arvizu**, R. Fonoll-Rubio, Y. Sánchez, I. Becerril-Romero, C. Malerba, M. Valentini, L. Calvo-Barrio, V. Izquierdo-Roca, M. Placidi, O. Vigil-Galán, A. Pérez-Rodríguez, Edgardo Saucedo, Z. Jehl Li-Kao. *ACS Appl. Energy Mater.* 3 (11), 10362–10375 (2020). DOI: 10.1021/acsaem.0c01146
8. [“Argon vs. air atmosphere in close spaced vapor transport deposited tin sulfide thin films”](#). **Jacob Andrade-Arvizu**, Maykel Courel, M. García-Sánchez, R. González, D. Jiménez, I. Becerril-Romero, A. Ramírez, O. Vigil-Galán. *Solar Energy* 208, 227-235 (2020). DOI: 10.1016/j.solener.2020.07.070
9. [“Investigation on limiting factors affecting \$\text{Cu}_2\text{ZnGeSe}_4\$ efficiency: Effect of annealing conditions and surface treatment”](#). Nada Benhaddou, Safae Aazou, Yudania Sánchez, **Jacob Andrade-Arvizu**, Ignacio Becerril-Romero, Maxim Guc, Sergio Giraldo, Victor Izquierdo-Roca, Edgardo Saucedo, Zouheir Sekkat. *Solar Energy Materials & Solar Cells* 216, 110701 (2020). DOI: 10.1016/j.solmat.2020.110701
10. [“Transition-Metal Oxides for Kesterite Solar Cells Developed on Transparent Substrates”](#). Ignacio Becerril-Romero, Diouldé Sylla, Marcel Placidi, Yudania Sánchez, **Jacob Andrade-Arvizu**, Victor Izquierdo-Roca, Maxim Guc, Alejandro Pérez-Rodríguez, Sigbjørn Grini, Lasse Vines, Benjamín Pusay, Rosa Almache, Joaquim Puigdollers, Paul Pistor, Edgardo Saucedo, Moisés Espíndola-Rodríguez. *ACS Appl. Mater. Interfaces* 12 (30), 33656–33669 (2020). DOI: 10.1021/acsaami.0c06992
11. [“Efficient Se-rich \$\text{Sb}_2\text{Se}_3/\text{CdS}\$ planar-heterojunction solar cells by sequential processing: control and influence of Se content”](#). Pedro Vidal-Fuentes, Marcel Placidi, Yudania Sánchez, Ignacio Becerril-Romero, **Jacob Andrade-Arvizu**, Zacharie Jehl, Alejandro Pérez-Rodríguez, Víctor Izquierdo-Roca, and Edgardo Saucedo. *RRL Solar* 4 (7), 2000141 (2020). DOI: 10.1002/solr.202000141

12. "[CZTS solar cells and the possibility of increasing \$V_{OC}\$ using evaporated \$Al_2O_3\$ at the CZTS/CdS interface](#)". E. Ojeda-Durán, K. Monfil-Leyva, **J. Andrade-Arvizu**, I. Becerril-Romero, Y. Sánchez, R. Fonoll-Rubio, M. Guc, Z. Jehl, J.A. Luna-López, A.L. Muñoz-Zurita, J.A.D. Hernández-de la Luz, V. Izquierdo-Roca, M. Placidi, E. Saucedo. *Solar Energy* 198, 696-703 (2020). DOI: 10.1016/j.solener.2020.02.009
13. "[Sputtered ZnSnO Buffer Layers for Kesterite Solar Cells](#)". Louis Grenet, Fabrice Emieux, **Jacob Andrade-Arvizu**, Eric De Vito, Géraldine Lorin, Yudania Sánchez, Edgardo Saucedo, and Frédéric Roux. *ACS Applied Energy Materials* 3(2), 1883–1891 (2020). DOI: 10.1021/acsaem.9b02329
14. "[Structural and vibrational properties of \$\alpha\$ - and \$\pi\$ -SnS polymorphs for photovoltaic applications](#)". Maxim Guc, **Jacob Andrade-Arvizu**, Ibbi Y. Ahmet, Florian Oliva, Marcel Placidi, Xavier Alcobé, Edgardo Saucedo, Alejandro Pérez-Rodríguez, Andrew L. Johnson, Victor Izquierdo-Roca. *Acta Materialia* 183, 1-10 (2020). DOI: 10.1016/j.actamat.2019.11.016
15. "[Is It Possible To Develop Complex S–Se Graded Band Gap Profiles in Kesterite-Based Solar Cells?](#)". **Jacob Andrade-Arvizu**, Víctor Izquierdo-Roca, Ignacio Becerril-Romero, Pedro Vidal-Fuentes, Robert Fonoll-Rubio, Yudania Sánchez, Marcel Placidi, Lorenzo Calvo-Barrio, Osvaldo Vigil-Galán, and Edgardo Saucedo. *ACS Applied Materials & Interfaces* 11 (36), 32945-32956 (2019). DOI: 10.1021/acsaem.9b09813
16. "[Study and optimization of alternative MBE-deposited metallic precursors for highly efficient kesterite CZTSe:Ge solar cells](#)". Sergio Giraldo, Shinho Kim, **Jacob Antonio Andrade-Arvizu**, Xavier Alcobé, Claudia Malerba, Matteo Valentini, Hitoshi Tampo, Hajime Shibata, Victor Izquierdo-Roca, Alejandro Pérez-Rodríguez, Edgardo Saucedo. *Progress in Photovoltaics* 27(9), 779-788 (2019). DOI: 10.1002/ppa.3147
17. "[An innovative alkali doping strategy for \$Cu_2ZnSnSe_4\$ through the CdS buffer layer](#)". Y. Sánchez, S. Giraldo, **J. A. Andrade-Arvizu**, M. Neuschitzer, L. Calvo-Barrio, V. Izquierdo-Roca, A. Pérez-Rodríguez, E. Saucedo. 2018 IEEE 7th World Conference on Photovoltaic Energy Conversion (WCPEC). DOI: 10.1109/PVSC.2018.8547417

18. "[Influence of Ge content on \$\text{Cu}_2\text{Zn}\(\text{SnGe}\)\text{Se}_4\$ physical properties deposited by sequential thermal evaporation technique](#)". J. R. González-Castillo, F. A. Pulgarín-Agudelo, Eugenio Rodríguez-González, O. Vigil-Galán, Maykel Courel-Piedrahita, **J. A. Andrade-Arvizu**. Materials Science in Semiconductor Processing 83, 96-101 (2018). DOI: 10.1016/j.mssp.2018.04.024
19. "[Cu content dependence of \$\text{Cu}_2\text{Zn}\(\text{SnGe}\)\text{Se}_4\$ solar cells prepared by using sequential thermal evaporation technique of Cu/Sn/Cu/Zn/Ge stacked layers](#)". F. A. Pulgarín-Agudelo, O. Vigil-Galán, **Jacob A. Andrade-Arvizu**, J. R. González-Castillo, Eugenio Rodríguez-González, Maykel Courel, Y. Sánchez, E. Saucedo. Journal of Materials Science: Materials in Electronics 29, 18, 15363-15368 (2018). DOI: 10.1007/s10854-018-8915-5
20. "[Preparation and characterization of \$\text{Cu}_2\text{ZnSnSe}_4\$ and \$\text{Cu}_2\text{ZnSn}\(\text{S,Se}\)_4\$ powders by ball milling process for solar cells application](#)". Fabian Andres Pulgarín-Agudelo, Osvaldo Vigil-Galán, M. M. Nicolás-Marín, Maykel Courel, R. González, Héctor Mendoza-Leon, S. Velumani, M. Rohini, **Jacob A. Andrade-Arvizu**, F. Oliva, Victor Izquierdo-Roca. Materials Research Express 4, 12 (2017). DOI: 10.1088/2053-1591/aa9a8d
21. "[Assisted laser ablation: silver/gold nanostructures coated with silica](#)". J. R. González-Castillo, Eugenio Rodríguez-González, Ernesto Jiménez-Villar, Carlos Lenz Cesar, **Jacob Antonio Andrade-Arvizu**. Applied Nanoscience 7, 8, 597-605 (2017). DOI: 10.1007/s13204-017-0599-2
22. "[Study of CBD-CdS/CZTGSe solar cells using different Cd sources: behavior of devices as a MIS structure](#)". O. Vigil-Galán, **J. A. Andrade-Arvizu**, Maykel Courel-Piedrahita, C. Mejía-García, E. Valencia-Resendíz, Y. Sánchez-González, M. Espíndola-Rodríguez, E. Saucedo-Silva, R. González-Castillo, E. Rodríguez-González, D. Seuret-Jiménez, D. Jiménez-Olarte. Journal of Materials Science: Materials in Electronics 28, 24, 18706-18714 (2017). DOI: 10.1007/s10854-017-7820-7
23. "[Processing pathways of \$\text{Cu}_2\text{Zn}\(\text{SnGe}\)\text{Se}_4\$ based solar cells: The role of CdS buffer layer](#)". O. Vigil-Galán, Maykel Courel, **J. A. Andrade-Arvizu**, Y. Sánchez, M. Espíndola-Rodríguez, E. Saucedo, D. Seuret-Jiménez, R. González. Materials Science in Semiconductor Processing 67, 14-19 (2017). DOI: 10.1016/j.mssp.2017.05.003

24. [“Study and application of colloidal systems for obtaining CdTe+Te thin films by spray pyrolysis”](#). Antonio Arce-Plaza, **Jacob A. Andrade-Arvizu**, Maykel Courel, José Alberto Alvarado, Mauricio Ortega-López. Journal of Analytical and Applied Pyrolysis 124, 285-289 (2017). DOI: 10.1016/j.jaap.2017.01.022

Journal Reviewer at:

- Journal of Materials Science: Materials in Electronics
- Solar Energy Materials and Solar Cells
- **Solar Energy**
- Material Research Express
- Journal of Physics D: Applied Physics
- Materials Science in Semiconductor Processing
- Physica Status Solidi (RRL) - Rapid Research Letters
- Inorganic and Nano-Metal Chemistry
- Boletín de la Sociedad Española de Cerámica y Vidrio
- Journal of Alloys and Compounds
- Thin Solid Films
- Nanomaterials
- Materials Letters



Oral lectures at congresses and conferences:

Oral Lectures:

- “Rear Bandgap Grading Strategies on Sn-Ge Alloyed Kesterite Solar Cells”. 11th European Kesterite Online Workshop. Oldenburg, Germany, November 26th - 27th, 2020.
- “Status of graded bandgap concepts for kesterite”. Asia-Pacific Workshop on Kesterite Structured Thin Film Solar Cells. Xi’han, China, November 8th, 2019.
- “Graded bandgap engineering on S-Se Kesterite Solar Cells”. Nanotechnology and Next Generation High Efficiency Photovoltaics International School & Workshop (NEXTGEN). Palma, Mallorca, Balearic Islands, October 1st – 4th, 2019.
- “Suitable complex S-Se graded bandgap profiles on kesterite-based solar cells”. Materials Research Society, Spring Meeting & Exhibit 2019 (MRS-2019). Phoenix, Arizona, United States of America, April 22nd – 26th, 2019.
- “Is it possible to obtain a complex S-Se graded bandgap on $\text{Cu}_2\text{ZnSn}(\text{S},\text{Se})_4$ absorbers?”. 9th European Kesterite Workshop. Ghent, Belgium, November 29th - 30th, 2018.
- “Experimental set-up regarding a complex graded bandgap on $\text{Cu}_2\text{ZnSn}(\text{S}_x\text{Se}_{(1-x)})_4$ Solar Cells”. European Materials Research Society, Spring Meeting 2018 (EMRS-2018). Strasbourg, France, June 18th – 22nd, 2018.
- “Towards a Complex Graded Band Gap on $\text{Cu}_2\text{ZnSn}(\text{S}_x\text{Se}_{(1-x)})_4$ Solar Cells”. 8th European Kesterite Workshop. Barcelona, Catalunya, Spain, November 8th - 10th, 2017.
- “Pressure induced morphological and directional transformations on closed space vapor transport deposited SnS thin films”. Research Workshop for Young Researchers Thin Film Emerging Photovoltaic and Optoelectronic Technologies (EMTECH 2017). Barcelona, Catalunya, Spain, April 28th - 29th, 2017.

Conference attendance, poster presentation and collaborative lectures:

* “11th European Kesterite Online Workshop”. Oldenburg, Germany,
November 26th-27th, 2020.

Collaborative lecture: Controlling the anionic ratio and gradient in kesterite technology.

* “Virtual Chalcogenide PV Conference 2020”. Online, May 25th-28th, 2020.

Attendance.

* “10th European Kesterite Workshop”. Uppsala, Sweden, November 20th-22th, 2019.

Collaborative lecture: Characterization of defects presence at the interfaces on
9.4% efficiency CZTSe device.

Collaborative poster: On the Se distribution at atomic level in Sb₂Se₃ Q-1D PV
absorbers.

* “XXVIII International Materials Research Congress (IMRC-2019)”.
Cancún, Quintana Roo, México, August 18th-23th, 2019.

Collaborative lecture: Cu₂ZnSnS₄ SOLAR CELLS ONTO FTO SUBSTRATES AND THE
USE OF FRONT PASSIVATION BY EVAPORATED Al₂O₃.

* “European Materials Research Society, Fall Meeting 2019 (EMRS-2019).
Warsaw, Poland, September 16th-19th, 2019.

Collaborative lecture: Efficient Cu₂ZnSnS₄ solar cells developed onto transparent
substrates.

* “Materials Research Society, Spring Meeting & Exhibit 2019 (MRS-2019)”.
Phoenix, Arizona, United States of America, April 22-26, 2019.

Collaborative lecture: The Challenges to Develop Sb₂Se₃/CdS Based Solar Cells in
Substrate Configuration.

* “IEEE Photovoltaic Specialist Conference (46th IEEE PVSC)”.
Chicago, Illinois, United States of America, June 16th-21th, 2019.

Collaborative lecture: THE USE OF Al₂O₃ DEPOSITED BY EVAPORATION ON THE
INTERFACE OF CZTS/CdS AND ITS BENEFITS IN THE SOLAR CELLS.

* “9th European Kesterite Workshop”. Ghent, Belgium, November 29th-30th, 2018.
Collaborative lecture: The photoluminescence efficiency of kesterite based photovoltaic materials.

Collaborative lecture: Understanding the synthesis of $\text{Cu}_2\text{ZnGeSe}_4$: a comparative analysis with pure Sn compound.

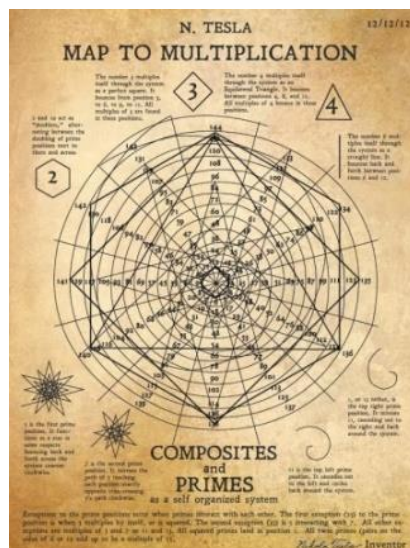
Collaborative lecture: Alkali migration from doped-CdS buffer layer as a novel strategy for controlled doping of kesterite solar cells.

* “WORLD CONFERENCE ON PHOTOVOLTAIC ENERGY CONVERSION (WCPEC-7)”. Waikoloa, Hawaii, United States of America, June 10th-15th, 2018.
Collaborative lecture: An innovative alkali doping strategy for $\text{Cu}_2\text{ZnSnSe}_4$ through the CdS buffer layer.

* “Nanotechnology and Next Generation High Efficiency Photovoltaics International School & Workshop”. Palma, Mallorca, Spain. Sept 12 – 15, 2017.

Poster presentation:

- Superficial passivating oxides on CZTSe:Ge/CdS solar cells.
- CZTGeSe layers deposited by sequential thermal vacuum evaporation: influence of the Cu and Ge thickness and post thermal annealing on the properties of thin films and solar cells.

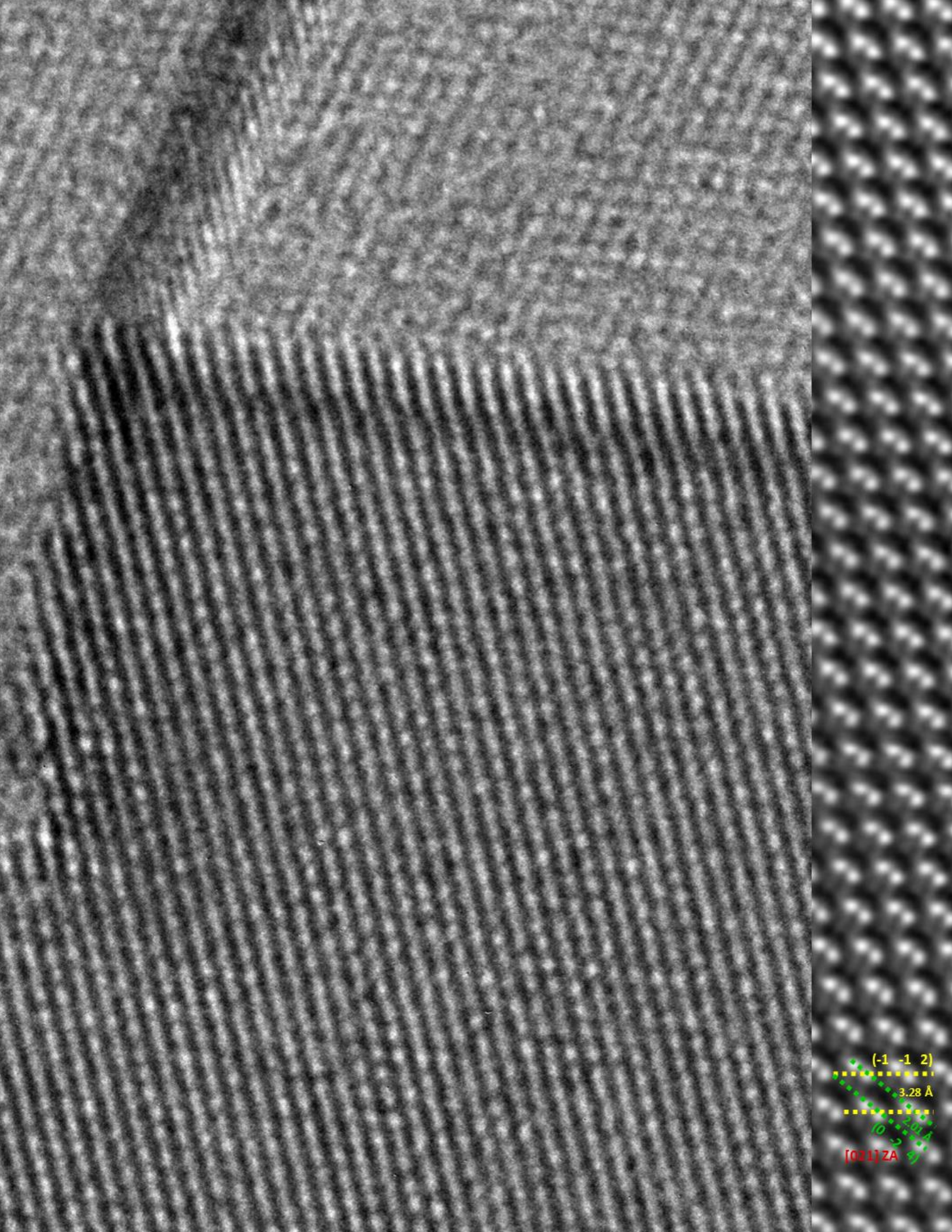


Miscellaneous Thesis derivatives

- Assistance and participation (Seminars and Personnel formation) of the Solar Energy Materials System (SEMS) group at the Catalonia Institute for Energy Research (IREC).
- Project meeting assistances of the European project STARCELL “Advanced strategies for substitution of critical raw materials in photovoltaics”
(H2020-NMBP-03-2016-720907, 2017-2021
<http://www.starcell.eu>)
- Proactive participation in the integration and human resources formation of international researchers for the European project INFINITE-CELL “International cooperation for the development of cost-efficient kesterite/c-Si thin film next generation tandem solar cells”
(H2020-MSCA-RISE-2017-77968, 2017-2021
<http://www.infinite-cell.eu/>)
- Proactive participation in the integration and human resources formation of international researchers for the European project MASTER-PV “Innovative manufacturing solutions for cost-efficient semi-transparent BIPV”
(MICINN-PCI-2018-092945, 2018-2021,
<http://www.master-pv.eu/>)
- Participation and formerly part of the organizing committee of the Pre-student day at the 9th European Kesterite Workshop, Ghent, Belgium, November 29th – 30th, 2018.
- Participation and formerly part of the organizing committee of the Pre-student day at the 8th European Kesterite Workshop, Barcelona, Spain November 8th - 10th, 2017.

Thesis Book Front and Rear Covers from:

*“Insights into interface and bulk defects in a high efficiency kesterite-based device”. Robert Fonoll-Rubio, Jacob Andrade-Arvizu, Javier Blanco-Portals, Ignacio Becerril-Romero, Maxim Guc, Edgardo Saucedo, Francesca Peiró, Lorenzo Calvo-Barrio, Maurizio Ritzer, Claudia S. Schnohr, Marcel Placidi, Sònia Estradé, Víctor Izquierdo-Roca, Alejandro Pérez-Rodríguez. **Energy and Environmental Science**, (2021), 14, 507-523. DOI: 10.1039/D0EE02004D



$(-1 \ -1 \ 2)$
 3.28 \AA
 2.01 \AA
 $[011]_{ZA}$